

# **Development of Prediction Tools for Improved Wear Assessment of Pipelines and Complex Geometries**

By

Oluwaseun Ezekiel Adedeji

A thesis submitted in partial fulfillment of the requirements for the degree of

Doctor of Philosophy

in

Chemical Engineering

Department of Chemical and Materials Engineering  
University of Alberta

©Oluwaseun Ezekiel Adedeji, 2021

# Abstract

Particle-laden flows such as pneumatic conveying or slurry transport are common in the minerals processing and oil sands industries. These industries face the challenge of erosion wear due to the repeated impact of the entrained particles, and subsequent damage to pipelines and equipment. Many economic losses such as equipment replacement cost, start-up and shutdown cost, and loss in production are associated with this erosion wear. An estimated \$1 billion/year in losses has been reported for the Canadian oil sands industry alone. It is, therefore, important for industries to know when and where failure will occur, as well as how much material is lost in order to take proactive steps to reduce these losses. The goal of this thesis is to develop more accurate predictive tools and methodologies that industries can use to assess the wear performance of their processes. Bench-scale devices and wear models are the typical predictive tools which will be explored in this thesis.

Part I of this thesis focuses on the development of a bench-scale device known as the toroid wear tester (TWT) as a slurry pipeline wear prediction tool. An initial Computational Fluid Dynamics (CFD) analysis and flow visualization experiments were conducted to study the hydrodynamics in the TWT. The results revealed regions of strong secondary flows in the TWT, and further identified possible operating conditions for wear testing which may be scalable to horizontal slurry pipelines applications. A subsequent experimental investigation

studied how the bed of particles respond to the TWT hydrodynamics. Coulombic stress was correlated to measured wear rate in the device over a range of operating conditions. It was found that a fully settled slurry flow regime occurs in the TWT when the ratio of the linear wheel speed to the particle terminal settling velocity (i.e.  $V/v_{\infty}$ ) is less than 7, and that there is a linear correlation between the measured wear rate and Coulombic stress in this region. However, to apply this correlation to slurry pipelines, the amount of wear due to Coulombic stress in pipelines must also be calculated. A CFD and experimental data analysis was therefore conducted on slurry pipeline wear data as a follow-up study. The results revealed that a correlation similar to that obtained for the TWT also exists in slurry pipelines between Coulombic stress and the associated wear rate. More slurry pipeline wear data are needed to further develop and support the correlation that would allow the use of the TWT for the prediction of wear in slurry pipelines.

Part II of this thesis presents studies on the improvement of wear model performance in complex geometries, and for effective decision-making in industrial process operations. The first study used CFD modelling to develop a geometry correction factor function (GCFF) for a standard 90 degree elbow. The GCFF provides factors that correct the effect of geometry-induced secondary flows not originally accounted for in the development of traditional single particle erosion models. The GCFF in this study was combined with the Oka erosion model and it performed better than the model alone. Another CFD analysis was conducted on a Once-Through Steam Generator (OTSG) system used in *in situ* oil sands extraction. Superheated steam transports precipitated fine particles ( $10\ \mu\text{m}$ ) at very low concentration ( $3\ \text{ppm}$ ) in the OTSG boiler tubes. Contrary to previous assumptions, the investigation showed severe erosion wear damage in the boiler tubes due to these fine particles. Additional analysis showed that the API RP 14E industrial guideline used in the design of OTSGs cannot adequately capture the effect of operational changes such as an increase in steam

production rate. The CFD analysis performed was, however, able to show that a 10% increase in OTSG operating velocity would cause failure in the OTSG boilers two times faster.

In summary, a significant step towards accurate wear prediction in slurry pipelines and other particle-handling systems was made through the research presented.

# Preface

This thesis is an original work by me, Oluwaseun Ezekiel Adedeji, with support from my supervisor, Professor R.S. Sanders, my colleagues at the Pipeline Transport Processes (PTP) Research Group, and partners from other institutions and the industry.

A part of Chapter 3 of this thesis has been submitted as

*Oluwaseun E. Adedeji, Lisheng Zhang, Nitish R. Sarker, David E.S. Breakey, R. Sean Sanders, Characterization of the flow field in a Toroid Wear Tester*

to the Canadian Journal of Chemical Engineering. Some of this material was presented at the 67th Canadian Chemical Engineering Conference in Edmonton, AB, Canada, 23-25 October, 2017.

A part of Chapter 4 of this thesis has been submitted as

*"Oluwaseun Ezekiel Adedeji, Lisheng Zhang, David E.S. Breakey, R. Sean Sanders, Investigation of abrasive wear in contact load-dominated slurry flows using a toroid wear tester"*

to the 23rd International Conference of Wear of Materials, Banff, Canada, April 24-29 2021 and will be published in Wear Journal. The manuscript was submitted for peer review on September 07, 2020.

A part of Chapter 5 has been accepted for presentation at the Hydrotransport Conference 2021 as

*Oluwaseun E. Adedeji, R. Sean Sanders, Estimation of wear loss related to Coulombic and kinematic friction in dense slurry flow in horizontal pipelines.*

The complete manuscript is ready for submission to Particle Science and Technology journal.

A part of Chapter 6 of this thesis has been published as

*"Adedeji O.E., Yu W., Sanders R.S., Analysis of local wear variables for high-precision erosion modelling in complex geometries. Wear. 2019;426-427:562-569. doi:<https://doi.org/10.1016/j.wear.2018.12.071>".*

The paper was also presented at the 22rd International Conference of Wear of Materials, Miami, USA, April 13-19th, 2019.

A part of Chapter 7 will be submitted as

*"Oluwaseun E. Adedeji, Anupam Kumar, Perdikcakis Basil, R. Sean Sanders, Investigation of erosion-related failure in SAGD OTSG boiler tubes and the limitations of API RP 14E"*

to the Journal of Engineering Failure Analysis.

# Dedication

You can move mountains. You can bring down walls!

# Acknowledgements

I want to first of all express my gratitude to God who gave me the potential and strength to complete this thesis. I also want to appreciate my parents, especially my mother. I know your sacrifices and they will never be forgotten. I want to specially thank my wife, Dupe, for her support, prayers, belief, and encouragement throughout this journey. To my pastor, Samuel Adeyemi, thank you for all your prayers and support. To everyone in my family who has supported in one way or the other, I am indeed very grateful.

To my supervisor, Prof. Sean Sanders, thank you very much for this opportunity to be a student under you. To me, it is more than a PhD study but a chance to create a new life. Thank you for all your guidance, directions, and lessons. Besides having the best interest of your students, you also bring out the best in them. I have learned a lot from your technical prowess and I have been equipped with tools that will make me succeed in future pursuit. Thank you also for the funding and financial support provided throughout my study.

To all the people that helped me through out this degree, I am very grateful. Dr David Breakey, thanks for providing support and making yourself available. Lisheng (Brad) Zhang, thanks for your help in the laboratory while conducting experiments. Thank you Terry Runyon for all your administrative support. To all my friends and colleagues at the Pipeline Transport Processes (PTP) Research Laboratory, and in the department of Chemical and Materials Engineering, thank you for being a part of this wonderful story I will someday share.

Finally, I will like to thank everyone that has inspired me and pushed me to go on to the

next level. To my undergraduate supervisor, Dr Dauda Araromi, thanks for all your help and fatherly advice. To my MSc supervisor, Professor Chris Rielly, I am glad you introduced me to CFD which became a tool I used throughout this PhD degree. To all my teachers, thanks for the lessons. To all the people I taught, know that I learned from you as well. I may not have mentioned your name but know that if you are a part of my life, you are deeply appreciated.

# Contents

<b>Abstract</b>	<b>ii</b>
<b>Preface</b>	<b>v</b>
<b>Dedication</b>	<b>vii</b>
<b>Acknowledgements</b>	<b>viii</b>
<b>Contents</b>	<b>x</b>
<b>List of Tables</b>	<b>xvi</b>
<b>List of Figures</b>	<b>xix</b>
<b>1 Introduction</b>	<b>1</b>
1. 1 Project background and motivation . . . . .	1
1. 2 Project scope and objectives . . . . .	6
1. 3 Author’s contribution . . . . .	9
1. 4 Thesis outline . . . . .	9
References . . . . .	11
<b>2 Literature review</b>	<b>16</b>
2. 1 Introduction . . . . .	16
2. 2 Slurry flow modelling . . . . .	17
2. 2.1 Frictional pressure gradient . . . . .	17

2. 2.2	Deposition velocity . . . . .	23
2. 3	Solid particle erosion (SPE) wear models . . . . .	25
2. 3.1	Finnie’s model . . . . .	25
2. 3.2	Oka et al. model . . . . .	26
2. 3.3	E/CRC or Tulsa model . . . . .	27
2. 3.4	DNV model . . . . .	28
2. 3.5	Comparison of the erosion models . . . . .	29
2. 3.6	Huang et al. model . . . . .	30
2. 4	Experimental wear testing devices . . . . .	35
2. 4.1	Recirculating pipe loop tester . . . . .	36
2. 4.2	Impingement jet tester . . . . .	37
2. 4.3	Toroid wear tester . . . . .	38
2. 5	Computational fluid dynamics modelling . . . . .	39
2. 5.1	CFD modelling steps . . . . .	41
2. 5.2	Turbulence modelling . . . . .	43
2. 5.3	Multiphase flow modelling . . . . .	47
2. 5.4	Implementation of erosion models in CFD . . . . .	51
	References . . . . .	53
<b>I</b>	<b>Part 1</b>	<b>65</b>
<b>3</b>	<b>Characterization of the flow field in a Toroid Wear Tester</b>	<b>66</b>
3. 1	Introduction . . . . .	69
3. 1.1	Background . . . . .	69
3. 1.2	Operation and development of the TWT . . . . .	70
3. 1.3	Scope and objectives . . . . .	71
3. 2	Experiment and method . . . . .	73
3. 2.1	Details of the experimental rig . . . . .	73
3. 2.2	Torque measurement . . . . .	74
3. 2.3	Quantitative flow visualization . . . . .	76
3. 3	Numerical Modelling . . . . .	77
3. 3.1	Model equations . . . . .	77
3. 3.2	Boundary conditions . . . . .	78

3. 3.3	Geometry and meshing . . . . .	78
3. 3.4	Solution procedure . . . . .	79
3. 4	Results and discussion . . . . .	81
3. 4.1	Measured and predicted torque data . . . . .	81
3. 4.2	Fluid flow pattern and velocity profile . . . . .	84
3. 5	Implications for Wear Testing . . . . .	89
3. 6	Conclusions . . . . .	90
	References . . . . .	91
<b>4</b>	<b>Investigation of abrasive wear in contact load-dominated slurry flow regime using a toroid wear tester</b>	<b>96</b>
4. 1	Introduction . . . . .	99
4. 1.1	Background . . . . .	99
4. 1.2	History and operation of the TWT . . . . .	101
4. 2	Modelling Coulombic friction in the TWT . . . . .	102
4. 3	Experiments and Methods . . . . .	104
4. 3.1	Wear experiment . . . . .	104
4. 3.2	Torque measurement . . . . .	108
4. 3.3	Flow visualization . . . . .	109
4. 4	Results and discussion . . . . .	109
4. 4.1	Identification of contact-load dominated flow in the TWT . . . . .	109
4. 4.2	Wear in contact load-dominated slurry flow . . . . .	114
4. 5	Conclusions . . . . .	118
	References . . . . .	118
<b>5</b>	<b>Estimation of wear loss related to Coulombic and kinematic stress in dense slurry flow</b>	<b>123</b>
5. 1	Background . . . . .	127
5. 2	The SRC two-layer model . . . . .	129
5. 3	Methodology . . . . .	131
5. 3.1	Development of method . . . . .	131
5. 3.2	Preliminary analysis . . . . .	134
5. 4	Experimental Details . . . . .	136
5. 5	Computational Fluid Dynamics (CFD) Modelling . . . . .	137

5. 5.1 Model description and equations . . . . .	137
5. 5.2 CFD model validation . . . . .	138
5. 6 Results and discussion . . . . .	139
5. 6.1 Predicted slurry hydrodynamics . . . . .	139
5. 6.2 Analysis of experimental data . . . . .	140
5. 6.3 Validation of method . . . . .	142
5. 6.4 Wear-Friction loss relationship . . . . .	147
5. 7 Conclusions . . . . .	150
References . . . . .	150
<b>II Part 2</b>	<b>155</b>
<b>6 Analysis of local wear variables for high-precision erosion modelling in complex geometries</b>	<b>156</b>
6. 1 Introduction . . . . .	159
6. 2 Background . . . . .	159
6. 3 Methodology . . . . .	160
6. 4 Description of experimental case . . . . .	164
6. 5 Numerical formulation . . . . .	166
6. 5.1 Model equations . . . . .	166
6. 5.2 CFD set-up and solution . . . . .	169
6. 6 Results and discussion . . . . .	172
6. 6.1 Flow validation . . . . .	172
6. 6.2 Wear rate and local wear variables predictions . . . . .	173
6. 6.3 GCFF development and validation . . . . .	178
6. 7 Conclusions and future works . . . . .	182
References . . . . .	183
<b>7 Investigation of erosion damage and the limitations of API RP 14E guideline in SAGD OTSG operations</b>	<b>188</b>
7. 1 Introduction . . . . .	191
7. 2 Background . . . . .	195
7. 2.1 Review of API RP 14E industrial guideline . . . . .	195

7. 2.2 OTSG case study . . . . .	197
7. 3 CFD Model Development . . . . .	199
7. 3.1 Model equations . . . . .	199
7. 3.2 Erosion model . . . . .	201
7. 3.3 CFD code validation case . . . . .	202
7. 3.4 OTSG model set-up and solution . . . . .	204
7. 4 Results and Discussion . . . . .	206
7. 4.1 Effect of target material hardness . . . . .	206
7. 4.2 Effect of particle size . . . . .	208
7. 4.3 Effect of superficial flow velocity . . . . .	211
7. 4.4 Effect of solids volume concentration . . . . .	213
7. 4.5 Performance of 2D CFD erosion models . . . . .	214
7. 5 Conclusions . . . . .	216
References . . . . .	217
<b>8 Conclusions and recommendations for future works</b>	<b>223</b>
8. 1 Summary of contributions and conclusions . . . . .	223
8. 2 Recommendations for future work . . . . .	227
References . . . . .	229
<b>Global References</b>	<b>231</b>
. . . . .	231
<b>Appendices</b>	<b>252</b>
<b>A Experimental Data</b>	<b>252</b>
A.1 Liquid-related torque data . . . . .	252
A.2 Solid-related torque data . . . . .	254
A.3 TWT experimental wear data . . . . .	261
<b>B MATLAB codes</b>	<b>262</b>
B.1 SRC Two-Layer Model Code . . . . .	262
B.2 Coulombic friction code for the toroid wear tester . . . . .	274
B.3 PipeMeshStarter MATLAB App Code . . . . .	276
B.4 Contracer code for TWT surface profile contour . . . . .	279

<b>C ANSYS UDF Codes</b>	<b>288</b>
C.1 Velocity profile inlet boundary condition . . . . .	288
C.2 Particle tracking for local wear variables and UDF erosion (DNV model) . . .	289
<b>D Additional material</b>	<b>293</b>
D.1 Proof of Geometry Correction Factor . . . . .	293
D.2 OTSG failure mechanisms investigation steps . . . . .	295

# List of Tables

2.1	Impact angle function coefficients for E/CRC erosion model . . . . .	28
2.2	Comparison between the described erosion models . . . . .	30
3.1	Viscosity and density of tested liquid samples . . . . .	75
3.2	Simulation time step sizes . . . . .	81
4.1	Properties of erodent particles used in the experiments of this study (All particles have a true density, $\rho_s$ , of $2650 \text{ kg/m}^3$ ) . . . . .	106
4.2	Properties of carrier fluid used to prepare the slurries tested in this study . .	106
5.1	Experimental wear data and conditions simulated in CFD . . . . .	136
5.2	Models selected for CFD simulations . . . . .	138
6.1	Experimental conditions [12] . . . . .	164
6.2	Morsi and Alexander drag law constants . . . . .	167
6.3	Numerical values of GCFF model constants . . . . .	179
7.1	OTSG system specifications and conditions . . . . .	198
7.2	Target materials properties with API RP 14E constants and velocity limits . .	199
7.3	Morsi and Alexander drag law constants . . . . .	200
A.1	Liquid-only torque data: water . . . . .	252
A.2	Liquid-only torque data: 20% corn syrup-water mixture . . . . .	253
A.3	Liquid-only torque data: 35% corn syrup-water mixture . . . . .	253
A.4	Liquid-only torque data: 20% glycerin-water mixture . . . . .	253

A.5 Liquid-only torque data: 40% glycerin-water mixture . . . . .	254
A.6 Solid-related torque data (Nm): 4 mm gravel in water (1 mPa·s) . . . . .	254
A.7 Solid-related torque data (Nm): 2 mm gravel in water (1 mPa·s) . . . . .	254
A.8 Solid-related torque data (Nm): 1 mm gravel in water (1 mPa·s) . . . . .	255
A.9 Solid-related torque data (Nm): 0.425 mm sand in water (1 mPa·s) . . . . .	255
A.10 Solid-related torque data (Nm): 0.250 mm sand in water (1 mPa·s) . . . . .	255
A.11 Solid-related torque data (Nm): 0.125 mm sand in water (1 mPa·s) . . . . .	256
A.12 Solid-related torque data (Nm): 4 mm gravel in 20% glycerin-water mixture (2.3 mPa·s) . . . . .	256
A.13 Solid-related torque data (Nm): 2 mm gravel in 20% glycerin-water mixture (2.3 mPa·s) . . . . .	256
A.14 Solid-related torque data (Nm): 1 mm gravel in 20% glycerin-water mixture (2.3 mPa·s) . . . . .	257
A.15 Solid-related torque data (Nm): 0.425 mm sand in 20% glycerin-water mixture (2.3 mPa·s) . . . . .	257
A.16 Solid-related torque data (Nm): 0.250 mm sand in 20% glycerin-water mixture (2.3 mPa·s) . . . . .	257
A.17 Solid-related torque data (Nm): 0.125 mm sand in 20% glycerin-water mixture (2.3 mPa·s) . . . . .	258
A.18 Solid-related torque data (Nm): 2 mm gravel in 40% glycerin-water mixture (5.12 mPa·s) . . . . .	258
A.19 Solid-related torque data (Nm): 1 mm gravel in 40% glycerin-water mixture (5.12 mPa·s) . . . . .	258
A.20 Solid-related torque data (Nm): 0.425 mm sand in 40% glycerin-water mixture (5.12 mPa·s) . . . . .	259
A.21 Solid-related torque data (Nm): 0.250 mm sand in 40% glycerin-water mixture (5.12 mPa·s) . . . . .	259
A.22 Solid-related torque data (Nm): 20% v/v 2 mm glass beads . . . . .	259
A.23 Solid-related torque data (Nm): 20% v/v 0.425 $Al_2O_3$ in 40% glycerine-water mixture(5.12 mPa·s) . . . . .	260
A.24 Experimental wear data- New data plus data from Sarker (2016) and Zhang (2018) . . . . .	261

B.1 Experimental data to test the SRC two layer model code in the run file that following . . . . . 265

# List of Figures

1.1	Possible avenues for losses due to erosion-related failures in process industries	2
1.2	A visual layout of project objectives and studies conducted as part of this PhD thesis research	8
2.1	Theoretical layers for the development of SRC friction loss model	19
2.2	Predictions from SRC two-layer model programmed into MATLAB for Gillies et al. [10] data: $d_{50c} = 270\mu m$ , $D = 103mm$ , $\rho_p = 2650kg/m^3$ , $C = 20\%$ , $\rho_f = 998kg/m^3$ , $\mu_f = 0.00096Pa.s$ , (left) frictional pressure drop, (right) Coulombic friction	22
2.3	Observed vs predicted particle deposition velocity for data from Gillies [35] and Spelay et al. [15] in the interval defined by Equation 2.16	24
2.4	Particle shape factor [47, 48]	28
2.5	Response surface plots of different wear models (a) Ductile, Cutting, Finnie (b) Ductile, Deformation + Cutting, Oka et al. (c) Brittle, DNV	31
2.6	Control surface for model derivation [52]	34
2.7	Schematic of the recirculating pipe-loop wear tester (based on [7])	36
2.8	Schematic of impingement jet tester	38
2.9	Schematic of toroid wear tester	39
3.1	Illustration of the TWT operation [4].	70
3.2	Photograph of the TWT rig at the PTP Research Laboratory.	74
3.3	The toroid wheel (a) 3D geometry and (b) mesh generated.	79

3.4	Mesh independence study using four mesh sizes (225k, 360k, 545k and 880k), testing three key parameters (Wall shear stress, $\tau_w$ ; Torque, $T$ ; Turbulent kinetic energy, $k$ ). . . . .	80
3.5	Experimental torque data for the liquid samples tested. . . . .	82
3.6	Comparisons of CFD-predicted and experimental torque. . . . .	83
3.7	Data planes considered for flow pattern analysis. . . . .	84
3.8	Flow patterns and water interface from visualization experiments: downstream. . . . .	85
3.9	Flow patterns and water interface predicted by CFD: mid-plane $S_0$ , downstream . . . . .	85
3.10	Comparison of experimental and predicted axial velocity profile at plane $F_{+45}$ : air-water flow. . . . .	86
3.11	Comparison of velocity vector and colour plots for middle plane $F_0$ at $Re = 35000$ for the three liquid cases. . . . .	87
3.12	Velocity colour plots for planes (a) $F_{-45}$ , (b) $F_0$ , and (c) $F_{+45}$ . . . . .	88
3.13	Velocity vector plots for planes (a) $F_{-45}$ , (b) $F_0$ , and (c) $F_{+45}$ . . . . .	89
3.14	Particle response to the TWT hydrodynamics: Image shows 15 vol.% 1 mm gravel in water at (a) 30 rpm, $T=0.14 Nm$ , and (b) 90 rpm, $T=0.82 Nm$ . . . . .	90
4.1	Illustration of the TWT operation. Adapted from Sarker [23]. . . . .	101
4.2	Schematic of Coulombic friction formulation for torque prediction in the TWT (a) cross section of wheel channel (b) wetted arc length. . . . .	103
4.3	The TWT device set up: schematic and photograph of the installation. . . . .	105
4.4	Coupon-wheel contact with edge clearance in the TWT. . . . .	107
4.5	Effect of fluid properties on the measured solids-related torque . . . . .	110
4.6	Visualization of slurry bed behavior under different system condition . . . . .	112
4.7	Parity plot for the measured and predicted Coulombic friction for sand-water slurry . . . . .	113
4.8	TWT test coupons wear map distribution. . . . .	115
4.9	Correlation for abrasive wear at fully settled slurry condition in the TWT . . . . .	117
5.1	Types of slurry flow condition and the related wear mechanism . . . . .	127
5.2	Schematic representation of the SRC two layer model . . . . .	130
5.3	Wear rate vs particle flux for 180 $\mu m$ particles at slurry flow velocity of $V = 3$ m/s, solids volume concentration of $C = 20\%$ in a 50 mm horizontal acrylic pipe [1] . . . . .	132

5.4	Schematic for estimating mean local wear rate . . . . .	133
5.5	Visual representation of variation of the two layers (SRC model) and pipe wall thickness loss with velocity . . . . .	135
5.6	Predicted concentration distribution for Gillies et al. [3] experimental data . .	139
5.7	Predicted concentration distribution for (a) Run 4 (b) Run 5 and (c) Run 7 in Table 5.1 . . . . .	140
5.8	Measured average wear rate against (a) mean slurry velocity (b) slurry friction loss . . . . .	141
5.9	Particle flux ratio versus contact load fraction . . . . .	143
5.10	Total wear rate for the bottom layer of the pipe: CFD estimate versus Huang's model estimate . . . . .	144
5.11	Comparison of bottom layer wear rate for 450 $\mu\text{m}$ and 250 $\mu\text{m}$ . . . . .	145
5.12	Ultrasound thickness measurement - 450 $\mu\text{m}$ , 2.28 m/s, 20% v/v, ID = 87 mm [5]	146
5.13	Relative wear rate: mass loss ratio for bottom-to-top layer (a) Comparison with experiment (b) All estimates from CFD method . . . . .	146
5.14	Wear ratio (a) Abrasion-to-erosion (b) Erosion-to-total wear and Abrasion-to-total wear . . . . .	148
5.15	Wear relationships versus velocity (a) Erosion (b) Abrasion . . . . .	149
6.1	Geometry correction factor function (GCFF) development methodology . . . . .	161
6.2	Elbow definition using (a) radius of curvature (b) characteristic angles $\beta_1$ and $\beta_2$	163
6.3	Geometry of experimental facility showing test elbow [12] . . . . .	165
6.4	Erosion depth profile from experimental measurement [12] . . . . .	165
6.5	Mesh grid for (a) geometry inlet (b) test elbow . . . . .	170
6.6	Mesh independence analysis- Turbulence intensity predicted at elbow extrados	170
6.7	Comparison of CFD prediction and experimental data for normalized particle velocities [32, 36] . . . . .	173
6.8	Particle-wall interaction simulation cases . . . . .	173
6.9	Contour plots of erosion depth calculated for smooth wall (Case 1), rough wall (Case 2), and rough wall with particle rotation (Case 3) versus experimental data	174
6.10	Elbow centre line profiles of erosion depth calculated for smooth wall (Case 1), rough wall (Case 2), and rough wall with particle rotation (Case 3) versus experimental data . . . . .	175

6.11 Comparison of particle impact variables (a)-(c) particle impact angle for smooth wall, rough wall, and rough wall with particle rotation respectively (d)-(f) particle impact velocity for smooth wall, rough wall, and rough wall with particle rotation respectively (g)-(i) particle mass rate for smooth wall, rough wall, and rough wall with particle rotation respectively . . . . .	176
6.12 Particle tracks for smooth wall (Case 1), rough wall (Case 2), and rough wall with particle rotation (Case 3) . . . . .	177
6.13 Surface plot of the fitted geometry correction factor function, $G(\beta_1, \beta_2)$ . . . .	179
6.14 Contour plot of the fitted geometry correction factor function, $G(\beta_1, \beta_2)$ . . . .	180
6.15 Performance of Oka model versus Oka model with the developed GCOFF model .	181
7.1 Schematic of an OTSG system for SAGD bitumen recovery (based on Gwak and Bae [2]) . . . . .	191
7.2 Wear damage mechanisms observed in tube samples from OTSGs used in SAGD oil sands extraction (a) From Godfrey et al. [4] (b) Recent Images . . . .	193
7.3 Single U-bend system geometry for CFD simulation . . . . .	198
7.4 Comparison between (a) experimental wear map [12] and (b) CFD predictions for the particle-impact related wear of an elbow in a gas-solid flow . . . . .	203
7.5 Trajectory of particles through the gas-solid elbow . . . . .	204
7.6 Unstructured grid for the OTSG U-bend: <i>left</i> (inlet surface), <i>right</i> (U-bend wall)	205
7.7 Erosion rate for A106C vs P22 for (a) all simulation conditions (b) 10 $\mu\text{m}$ particles	206
7.8 CFD Predicted failure time for A106C and P22 for 10 $\mu\text{m}$ particles . . . . .	207
7.9 Predicted erosion rate for different particle diameters at $V=20$ m/s for A106C	209
7.10 Erosion rate heatmaps for 60 $\mu\text{m}$ particles at 20m/s for A106C (a) saturated steam at 0.1 MPa (b) saturated steam at 11 MPa . . . . .	210
7.11 Extent of wear damage caused by individual particle size . . . . .	211
7.12 Erosion rate predictions for (a) P22 and (b) A106C, with the vertical dashed line representing the API RP 14E limit velocity . . . . .	212
7.13 Predicted failure times for (a) P22 and (b) A106C alloys, with the vertical dashed line representing the API RP 14E limit velocity . . . . .	212
7.14 Predicted maximum wear rate for different particle sizes at two different concentrations- target material: A106C, operating velocity: 20 m/s . . . . .	214

7.15 Comparison between 3D CFD-Oka model calculations and 2D-CFD Parsi model calculations for (a) different particle sizes at 20 m/s, and (b) different flow velocities for 10 $\mu\text{m}$ particles . . . . .	215
B.1 MATLAB App (PipeMeshStarter) developed to estimate first layer thickness for a pipe mesh for a target $y^+$ value . . . . .	279
D.1 Investigation steps for identifying the dominant wear mechanisms for the OTSG295	

# Introduction

## 1.1 Project background and motivation

Particle-laden flows such as pneumatic conveying or slurry transport are an integral part of minerals processing and oil sands industries operations. A primary concern for these industries is the energy requirement to transport materials through their pipelines i.e. to overcome additional friction loss due to the presence of particles and to avoid the formation of deposits or blockage [1–3]. Another concern, which presents even as a greater challenge in these industries, is the phenomenon known as erosion wear.

Erosion wear occurs when material is removed from the surfaces of pipelines and process equipment after repeated impact by the solid particles transported in the process fluid stream. This phenomenon affects the efficiency and reliability of process equipment, and has significant economic implications. An estimated one billion dollars is spent annually on erosion-related failures in the Canadian oil sands industry alone [4]. Sometimes, these failures can occur over a relatively short duration. For example, severe erosion rates of about 20 mm/yr has been reported for hydrotransport pipelines in the oil sands industries [5]. Figure 1.1 shows the possible avenues through which these economic losses can be incurred. The primary/direct implication for process industries is the loss in production, maintenance cost, and cost of equipment replacement. It is critical that the predictions of material loss through erosion wear for specific operating conditions are needed to provide industries with both time-to-failure and the specific failure location. There is, therefore, a need *to develop more accurate predictive tools and methodologies by which industries can assess the wear*

*performance of their processes, pipelines, and equipment.*

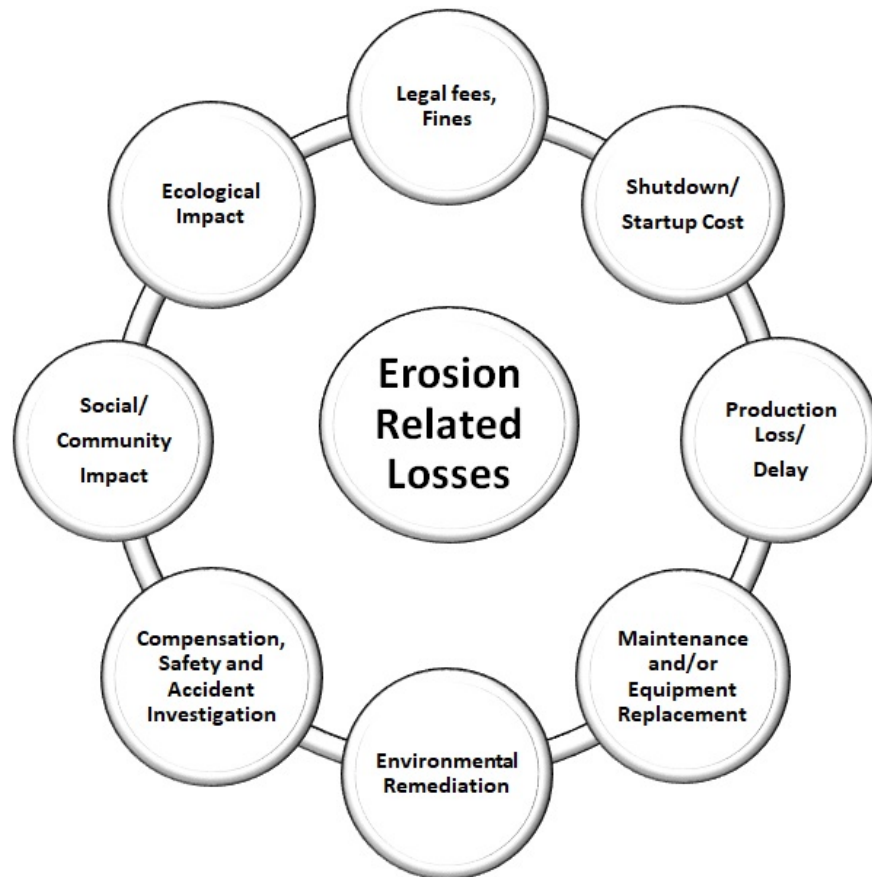


Figure 1.1: Possible avenues for losses due to erosion-related failures in process industries

Erosion, however, is a complex multi-physics phenomenon that involves fluid-particle-wall interactions and is dependent upon many parameters, such as the impact angle and velocity of the particles, the solids concentration, particle size, shape, abrasiveness and density, fluid properties (viscosity and density), roughness of the target surface, and the relative hardness of particles and of the target materials [6–8]. Geometrical factors such as pipe diameter or bend curvature have also been reported to influence erosion rate [8–12]. The ability to accurately predict erosion wear has, therefore, remained a bottleneck for industries despite over six decades of research and development in wear studies. Two major approaches have been used over time to address erosion wear challenges. The first approach is through experiments using wear testers which are bench- or pilot-scale devices that expedite the wear process under controlled environment. The second approach is through numerical modelling

and simulation which is a more recent development [13]. It is important to note that the two methods are not mutually exclusive and one is often used in support of the other. For example, because no industrially relevant erosion model is based purely on first principle physics, erosion wear experiments are often needed to determine empirical constants for erosion models.

There are several bench-scale devices that have been used for erosion wear studies. Examples include the slurry pot tester [10, 14], the recirculating pipe loop tester [9, 10, 14, 15], impingement jet tester [16, 17], and the toroid wear tester [18–21]. These devices are often used to rank pipeline and process equipment materials for wear resistance or develop and tune erosion wear models. There are underlying challenges that accompany the use of these experimental techniques, such as the difficulty to replicate the exact industrial conditions in the lab device. Many of the devices have a significantly different hydrodynamics (flow field) from that of a pipeline. There is, therefore, a question of the suitability of these devices to represent industrial pipeline processes. Even for the recirculating pipe loop tester that has a comparable hydrodynamics to industrial pipelines, there is excessive particle degradation (i.e. loss of abrasiveness of particles) due to the shearing action of the pump [4, 10, 22]. This condition is not representative of what happens in an industrial system where fresh slurry is supplied at all times. Collecting wear data is also very time-consuming and expensive [10] in the recirculating pipe loop tester. Finally, wear rates measured in the recirculating pipe loop have been shown to depend on pipe diameter; hence, scaling up for industrial use is also questionable [9, 10]. In the toroid wear tester, the challenge of very long experiment duration and particle degradation effect have been minimized, thereby making it a more economically viable choice [18–20]. However, a major drawback is that there is little knowledge of the hydrodynamics in the toroid wear tester and how they may influence the measured wear rate. Until the TWT hydrodynamics can be better quantified and compared with slurry pipeline flow, the TWT cannot be assumed to provide wear data directly applicable to pipelines.

Many models and correlations have been developed by researchers to describe the relationship between material loss due to erosion and the fluid-particle-material properties and operating conditions [7, 11, 14, 23–27]. Some correlations like the API RP 14E guideline [23], which is widely used in industry, is very conservative and does not provide the basic information such as the erosion wear rate (in mm/yr) experienced in a pipeline [28]. Other models like the Oka model [7] or the E/CRC model [27] provide wear rate information after inputting the fluid-particle-material properties e.g. particle impact angle and velocity,

target material hardness. However, these models do not account for the effect of fluid turbulence on particle impact and cannot provide details about the distribution of wear on a surface. Numerical methods including Computational Fluid Dynamics (CFD) simulations have become increasingly popular as tools to evaluate wear performance of systems; in particular, the capability to use CFD to resolve fluid-particle-wall interactions locally and generate a wear map or distribution [6, 29–32]. Computational Fluid Dynamics captures the dispersive effects of turbulence, geometrical-influence, surface wall roughness, and the resultant particle dynamics to determine the location and distribution of wear in the system [8, 30, 31]. This means industries can visualize more realistically, the erosion hot spots in their systems and can take more proactive steps to mitigate the damage. There are three steps usually involved in CFD calculations for erosion prediction; flow hydrodynamics calculation, particle trajectory calculations, and the implementation of the semi-mechanistic erosion models in the computational domain [33]. The latter is usually done via User-Defined Functions (UDFs), if the models are not already available in the CFD code [6, 34–38].

It can be inferred from the discussion of these two approaches that erosion is indeed complex both from investigation and application perspectives. The following provides a list of challenges to erosion wear studies:

- *Erosion models are system-specific*: This means that erosion wear models perform best in systems from which they were developed or in other systems similar in characteristics [8]. If a model is to be used in another system, a new set of experiments will be needed to determine empirical coefficients for the model.
- *Limited data available*: Especially for slurry pipeline systems, there is limited wear data both from industrial operations and laboratory experiments [10, 19]. Some available data are not representative of the industrial system e.g. the use of acrylic pipes in the lab to test for failure of carbon steel pipe in the industrial process can give misleading conclusions.
- *Erosion experiments are expensive*: Wear-testing facilities for slurry pipeline erosion are very expensive to run [4, 10]. The large volume of slurry needed, the prolonged run time, and the power requirement all contribute significantly to overall cost.
- *Limited capacity*: Most erosion wear devices are limited in their operating capacity e.g. Hydrotransport pipelines move particles of mean diameter as large as 10 mm,

however, pumping a slurry made up of even 2 mm particles might not be possible in a recirculating pipe loop wear-testing facility.

- *Difference in hydrodynamics*: Other than the recirculating pipe loop wear tester, most wear testing devices are fundamentally different in their hydrodynamics when compared to pipelines e.g. slurry pot tester vs pipeline [20, 21, 39]. Erosion is a local phenomenon and changes in fluid structures such as the presences of swirls, rotations, and other secondary flows will greatly affect the trajectory and energy of a particle as it approaches the surface to impact. This means both erosion wear severity and distribution will be affected. If a model is developed in a system such as the jet impingement tester, effects of such secondary flows will not be captured; hence, the model may perform poorly in another system such as a cyclone where the particle velocities and angles of attack are poorly represented in the jet impingement tester.
- *System geometry*: This is somewhat related to the previous point on difference in hydrodynamics between systems. Geometrical form and layout can play a significant role in determining the extent of damage [8, 12]. For example, a pipe bend curvature and its direction of flow (horizontal-to-horizontal vs vertical-to-horizontal) can influence the level of erosion damage in the system.
- *Multiphase flow behaviour*: The presence of other phases e.g. bubbles, liquid droplets, annular or slug flow can greatly influence the level of wear damage experienced in the system [40–42].
- *Erosion and fluid-particle hydrodynamics are not independent*: Many wear studies have been conducted in which erosion wear is measured while hydrodynamic parameters like particle concentration distribution have not been measured. This sometimes poses a challenge to validation of erosion models especially when it comes to numerical simulations. Most CFD studies for erosion wear prediction validate their hydrodynamics calculations using another system's data. Once this is done, they use the set model to validate erosion in the system of interest. Ideally, both hydrodynamics and erosion wear should be validated using data from the same system.
- *Other synergistic damage mechanisms*: Erosion mostly occurs simultaneously with other wear damage mechanisms e.g. corrosion, thermal fatigue [43, 44]. Usually, there

is a synergistic effect of one damage mechanism enhancing the severity of the other, although there are times when one mechanism is dominant. Therefore, it is very difficult to truly quantify the extent of damage due to pure erosion alone in certain industrial systems.

- *Erosion should be studied from a local and global lens*: While erosion is a local phenomenon and requires analysis at a micro-scale for proper assessment (i.e. particle trajectory information), many industries require their input variables to relate directly to their operational parameter e.g mass flow rate. A balance these two requirement is a challenge in the application of erosion models, and perhaps, this is the reason standards like the API RP 14E is still widely used in the industry.

## 1.2 Project scope and objectives

The primary objective of this thesis research is *to provide improved tools and methodologies by which industries can assess the wear performance of their processes, pipelines, and equipment*. The investigations in this thesis address this primary objective through:

- a) The development of a cost-effective and efficient bench-scale experimental device that can be used to tune the empirical coefficients of erosion models used for industrial slurry pipelines wear prediction
- b) The improvement of the performance of traditional erosion wear models for use in complex geometries e.g. bends, and for better decision-making in industrial processes e.g. choosing production flowrate

Figure 1.2 shows a summary of the contents of this thesis and highlights the studies that have been conducted (per chapter) to address these objectives. As can be inferred from Figure 1.2, the toroid wear tester (TWT) has been selected as the bench-scale experimental device to be investigated. The TWT is found to be a suitable candidate because there are precedents that suggest it simulates slurry pipeline wear damage flow conditions efficiently and cost effectively, at least under some specific, limited operating conditions [18–21, 45]. To support the studies conducted on the TWT, Computational Fluid Dynamics (CFD) has also been selected as a tool for investigation. The advantage of CFD to the ability to provide

details about the different flow fields and their interactions with particles in the system [8]. The power of CFD simulations combined with experimental investigations and data analysis will be used to provide more insights on how to use the TWT to understand wear behaviour in a slurry pipeline system as well as improve the performance of erosion wear models in other particle-laden systems.

In summary, the corresponding activities of the objectives are

- To use CFD simulations to study and understand the hydrodynamic features of the TWT, and to inform its suitability for use as a prediction tool for slurry pipeline wear (Chapter 3).
- To perform experimental wear and hydrodynamics investigations to understand the flow behaviour and wear mechanisms in the TWT system relative to those in the pipeline (Chapter 4).
- To perform CFD simulations and experimental data analysis to identify the dominant erosion wear mechanisms in slurry pipelines (i.e. kinematic or Coulombic friction dominated wear) with the aim of being able to interpret pipeline wear data using the TWT (Chapter 5).
- To use CFD simulations to improve the performance of traditional erosion models (e.g. the Oka model) when used to predict wear in a complex geometry such as a standard 90° elbow (Chapter 6).
- To use CFD simulations to predict failure in an industrial process such as a Once Through Steam Generator (OTSG), and to show the limitations of the API RP 14E guideline as a design and operation tool for such processes (Chapter 7).

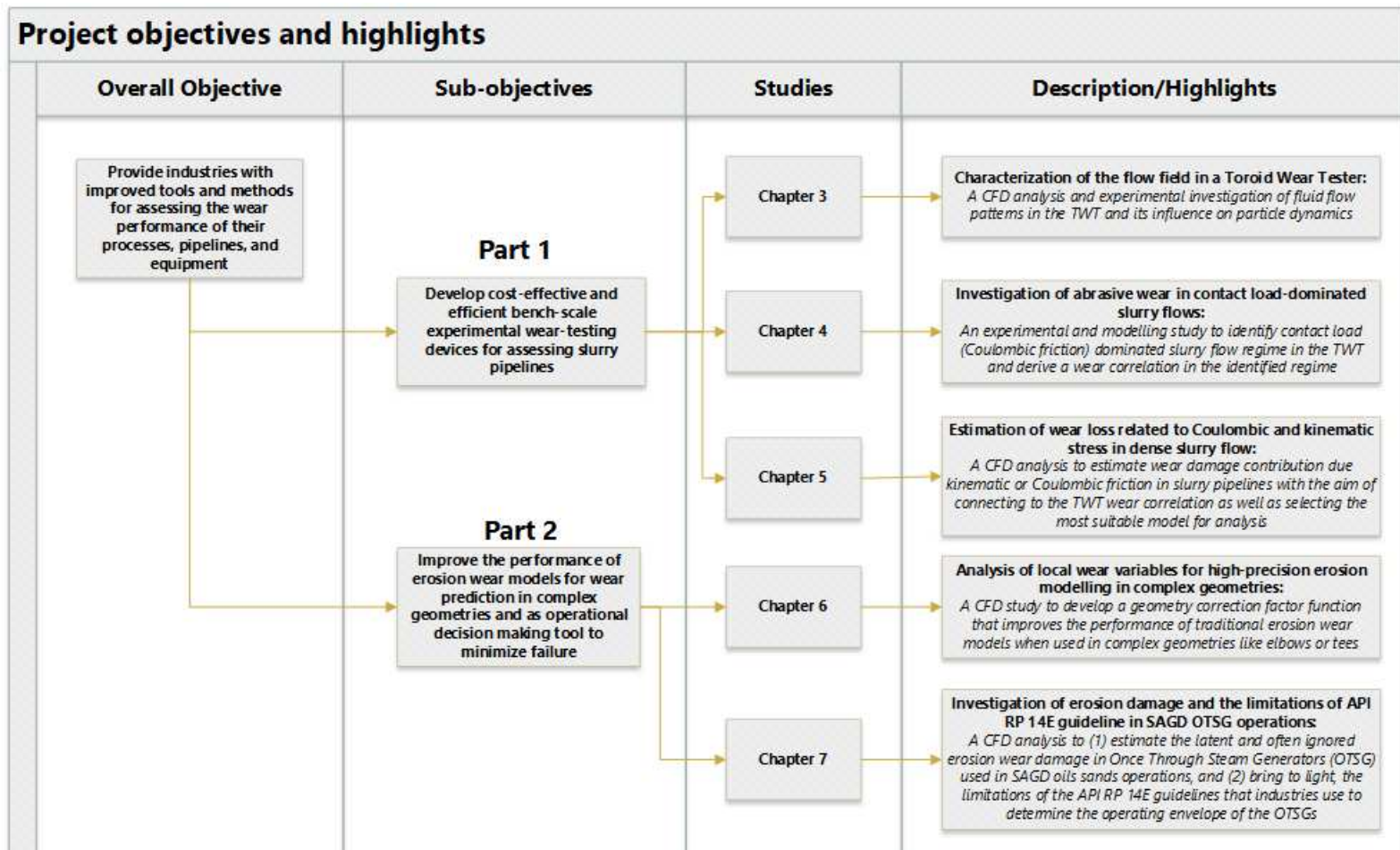


Figure 1.2: A visual layout of project objectives and studies conducted as part of this PhD thesis research

### 1.3 Author's contribution

In this thesis, all Computational Fluid Dynamics (CFD) modelling and simulations were done by the author. This includes developing CAD models in SolidWorks and SpaceClaim, meshing of geometries in ICEM CFD or ANSYS Meshing, and post-processing of results. All the User-Defined Functions (UDFs) written in C++ programming language for the CFD code i.e. ANSYS Fluent were also done by the author. The MATLAB programs for the SRC two-layer model, pipe mesh calculations, curve fitting, and data visualization were done by the author. The MATLAB code to process Particle Tracking Velocimetry (PTV) images in Chapter 3 was written by Dr David Breakey and that for plotting of surface contours for the TWT test coupons in Chapter 4 were previously written by Nitish Sarker, updated by Dr David Breakey, and then adapted for this PhD research by the author. Prof. R. Sean Sanders provided the project ideas, scope and definition. The conceptualization and development of the ideas, methodologies implemented, approach of analysis, and results presentation were done by the Prof. R. Sean Sanders and the author. All design of experiment (wear, torque, visualization, surface profile measurement) and selection of materials for the experiments were done by the author with support from Prof. R. Sean Sanders and Dr David Breakey. Thanks to Lisheng Zhang for helping out in the laboratory during most of the experiments, and Dr David Breakey during the visualization experiments. All analysis of experimental simulation data and interpretation of results were done by the author. All the novel models and methodologies reported in this thesis were also developed by the author.

### 1.4 Thesis outline

Chapter 1 presents the background, motivation, and current challenges of erosion studies, the scope and objectives of this thesis, and the contributions made by the author. It highlights the tools, resources, and techniques used to complete this project i.e. the lab-scale device known as the toroid wear tester (TWT), CFD simulations, experimental data from literature [10, 22, 30], and advanced analysis using engineering tools.

Chapter 2 presents a review of literature for covering the major subject areas that form the basis of this thesis. First, detailed description of the Saskatchewan Research Council (SRC) Pipe Flow Model, often called the SRC two-layer model [1] is presented. This is followed

by a review of selected solid particle erosion (SPE) models and a comparison between these models. A brief description of wear-testing devices is also presented. This is then followed by a discussion of CFD modelling steps, turbulence models, and the different multiphase flow methods.

Chapter 3 presents a report of the initial study of the toroid wear tester (TWT) hydrodynamics. Torque measurement and flow visualization experiments are conducted to characterize friction loss and provide details of the flow field in the TWT system. Computational fluid dynamics (CFD) simulations are also conducted and compared with the experiments.

Chapter 4 presents an experimental investigation of erosion wear under fully-settled slurry flow conditions in the TWT. Experiments to visualize the behaviour of particle beds and determine solids-related torque are used to identify different slurry flow conditions in the TWT.

Chapter 5 presents a method to estimate the amount of wear damage due to kinematic and Coulombic friction losses in slurry pipelines. The method combines the Eulerian-Eulerian multiphase modelling approach with the formulation of the SRC two-layer model is presented. Ultrasound thickness loss (UTL) measurement from slurry pipeline wear experiments, and predictions from the Huang et al. [26] wear model are compared to the estimated wear rates from the aforementioned method. Coulombic stress-related wear losses estimated for the slurry pipeline wear data is found to have a similar relationship as those found in the TWT.

Chapter 6 presents an analysis of local wear variables, i.e. particle impact angle and velocity, to develop a geometry correction factor function (GCFF) which can be used to improve the performance of erosion models. The Eulerian-Lagrangian multiphase approach is used used to perform the analysis. The experimental wear data collected in a gas-solid elbow from the work of Solnordal et al. [30] is used in the investigation. The GCFF developed is different from previously existing ones because it adapts locally based on the spatial position of particle impact on the elbow.

Chapter 7 presents an investigation of failure due to erosive wear damage in a Once-Through-Steam-Generator (OTSG) used in Steam Assisted Gravity Drainage (SAGD) oils sands extraction. A series of CFD simulations are conducted to test the integrity of different OTSG construction materials to wear damage from very fine particles at low concentrations. Further analysis is also conducted to show that the API RP 14E guideline alone is not a

sufficient design and operation tool for the industrial OTSG system.

Chapter 8 presents summary, conclusions and recommendations for the studies in this thesis. Future directions for projects whose foundation will be built on the work presented are also provided.

## References

- [1] R. G. Gillies, C. A. Shook, K. C. Wilson, An improved two layer model for horizontal slurry pipeline flow, *Can. J. Chem. Eng.* 69 (1991) 173–178. URL: <http://doi.wiley.com/10.1002/cjce.5450690120>. doi:10.1002/cjce.5450690120.
- [2] R. G. Gillies, Pipeline Flow of Coarse Particle Slurries, Ph.D. thesis, University of Saskatchewan, 1993.
- [3] R. G. Gillies, J. Schaan, R. J. Sumner, M. J. McKibben, C. A. Shook, Deposition velocities for newtonian slurries in turbulent flow, *Can. J. Chem. Eng.* 78 (2000) 704–708. URL: <http://doi.wiley.com/10.1002/cjce.5450780412>. doi:10.1002/cjce.5450780412.
- [4] B. Fotty, M. Krantz, J. Been, J. Wolodko, Development of a pilot-scale facility for evaluating wear in slurry pipeline systems, in: *Proc. Hydrotransp.* 18, September, Rio de Janeiro, Brazil, 2010, pp. 431–443.
- [5] L. L. Parent, D. Y. Li, Wear of hydrotransport lines in Athabasca oil sands, *Wear* 301 (2013) 477–482. doi:10.1016/j.wear.2013.01.039.
- [6] D. R. Lester, L. A. Graham, J. Wu, High precision suspension erosion modeling, *Wear* 269 (2010) 449–457. doi:10.1016/j.wear.2010.04.032.
- [7] Y. I. Oka, H. Ohnogi, T. Hosokawa, M. Matsumura, The impact angle dependence of erosion damage caused by solid particle impact, *Wear* 203 (1997) 573–579.
- [8] O. E. Adedeji, W. Yu, R. S. Sanders, Analysis of local wear variables for high-precision erosion modelling in complex geometries, *Wear* 426-427 (2019) 562–569. doi:10.1016/j.wear.2018.12.071.

- [9] P. Goosen, I. Malgas, An Experimental Investigation into Aspects of Wear in Boiler Ash Disposal Pipelines, in: Proc. Hydrotransp. 14, September, Maastricht, The Netherlands, 1999, pp. 8–10.
- [10] A. Sadighian, Investigating Key Parameters Affecting Slurry Pipeline Erosion, Ph.D. thesis, University of Alberta, 2016. doi:[10.1017/CB09781107415324.004](https://doi.org/10.1017/CB09781107415324.004). arXiv:[arXiv:1011.1669v3](https://arxiv.org/abs/1011.1669v3).
- [11] DNV GL, Managing sand production and erosion, Technical Report August, 2015.
- [12] B. S. McLaury, J. Wang, S. A. Shirazi, SPE, J. R. Shadley, E. F. Rybicki, Solid Particle Erosion in Long Radius Elbows and Straight Pipes, Annu. Spe Tech. Conf. (San Antonio, 10/5-8/97) Proc. [Production Oper. Eng. (1997) 977–986.
- [13] J. Been, F. Ju, Prediction of Wear of Tailings Pipelines in Oil Sands Slurries, Technical Report, Alberta Innovates Technology Futures, 2013.
- [14] R. Gupta, S. N. Singh, V. Sehadri, Prediction of uneven wear in a slurry pipeline on the basis of measurements in a pot tester, *Wear* 184 (1995) 169–178. doi:[10.1016/0043-1648\(94\)06566-7](https://doi.org/10.1016/0043-1648(94)06566-7).
- [15] C. A. Shook, M. McKibben, M. Small, Experimental investigation of some hydrodynamic factors affecting slurry pipeline wall erosion, *Can. J. Chem. Eng.* 68 (1990) 17–23. URL: <http://doi.wiley.com/10.1002/cjce.5450680102>. doi:[10.1002/cjce.5450680102](https://doi.org/10.1002/cjce.5450680102).
- [16] R. J. K. Wood, The sand erosion performance of coatings, *Mater. Des.* 20 (1999) 179–191. URL: [http://dx.doi.org/10.1016/S0261-3069\(99\)00024-2](http://dx.doi.org/10.1016/S0261-3069(99)00024-2). doi:[10.1016/S0261-3069\(99\)00024-2](https://doi.org/10.1016/S0261-3069(99)00024-2).
- [17] H. Arabnejad, A. Mansouri, S. A. Shirazi, B. S. McLaury, Development of mechanistic erosion equation for solid particles, *Wear* 332-333 (2015) 1044–1050. doi:[10.1016/j.wear.2015.01.031](https://doi.org/10.1016/j.wear.2015.01.031).
- [18] R. Cooke, G. Johnson, P. Goosen, Laboratory Apparatus for Evaluating Slurry Pipeline Wear, Technical Report March, SAIT Seminar, Calgary, 2000.
- [19] N. R. Sarker, A Preliminary Study of Slurry Pipeline Erosion Using a Toroid Wear Tester, MSc thesis, University of Alberta, 2016.

- [20] L. Zhang, Relating slurry friction to erosion rate using a toroid wear tester, MSc thesis, University of Alberta, 2018.
- [21] N. R. Sarker, D. E. S. Breakey, M. A. Islam, S. Sun, B. A. Fleck, R. S. Sanders, Performance and Hydrodynamics Analysis of a Toroid Wear Tester to Predict Erosion in Slurry Pipelines, *Wear* (2019) 203068. URL: <https://doi.org/10.1016/j.wear.2019.203068>. doi:10.1016/j.wear.2019.203068.
- [22] R. Jami, Investigation Using Polymer Additives to Mitigate Erosion in Multiphase Turbulent Pipe Flow, Master's thesis, University of Alberta, 2019.
- [23] API RP 14E, Recommended Practice for Design and Installation of Offshore Production Platform Piping System, 5th editio ed., American Petroleum Institute, Washington DC, 1991.
- [24] I. Finnie, Erosion of surfaces by solid particles, *Wear* 3 (1960) 87–103. doi:10.1016/0043-1648(60)90055-7. arXiv:arXiv:1011.1669v3.
- [25] J. G. A. Bitter, A study of erosion phenomena part II, *Wear* 6 (1963) 169–190.
- [26] C. Huang, P. Minev, J. Luo, K. Nandakumar, A phenomenological model for erosion of material in a horizontal slurry pipeline flow, *Wear* 269 (2010) 190–196. URL: <http://dx.doi.org/10.1016/j.wear.2010.03.002>. doi:10.1016/j.wear.2010.03.002.
- [27] Y. Zhang, E. P. Reuterfors, B. S. McLaury, S. a. Shirazi, E. F. Rybicki, Comparison of computed and measured particle velocities and erosion in water and air flows, *Wear* 263 (2007) 330–338. doi:10.1016/j.wear.2006.12.048.
- [28] S. A. Shirazi, B. S. Mclaury, H. Arabnejad, T. Erosion, A Semi-Mechanistic Model for Predicting Sand Erosion Threshold Velocities in Gas and Multiphase Flow Production, *Soc. Pet. Eng. SPE-18147-* (2016).
- [29] X. Chen, B. S. McLaury, S. A. Shirazi, Application and experimental validation of a computational fluid dynamics (CFD)-based erosion prediction model in elbows and plugged tees, *Comput. Fluids* 33 (2004) 1251–1272. doi:10.1016/j.compfluid.2004.02.003.

- [30] C. B. Solnordal, C. Y. Wong, J. Boulanger, An experimental and numerical analysis of erosion caused by sand pneumatically conveyed through a standard pipe elbow, *Wear* 336-337 (2015) 43–57. URL: <http://dx.doi.org/10.1016/j.wear.2015.04.017>. doi:10.1016/j.wear.2015.04.017.
- [31] C. A. R. Duarte, F. J. de Souza, R. V. Salvo, V. F. dos Santos, The role of inter-particle collisions on elbow erosion, *Int. J. Multiph. Flow* 89 (2017) 1–22. doi:10.1016/j.ijmultiphaseflow.2016.10.001.
- [32] W. Yu, P. Fede, E. Climent, S. Sanders, Multi-fluid approach for the numerical prediction of wall erosion in an elbow, *Powder Technol.* 354 (2019) 561–583. URL: <http://www.sciencedirect.com/science/article/pii/S0032591019304504>. doi:https://doi.org/10.1016/j.powtec.2019.06.007.
- [33] M. Parsi, K. Najmi, F. Najafifard, S. Hassani, B. S. McLaury, S. A. Shirazi, A comprehensive review of solid particle erosion modeling for oil and gas wells and pipelines applications, *J. Nat. Gas Sci. Eng.* 21 (2014) 850–873. doi:10.1016/j.jngse.2014.10.001.
- [34] J. Wu, L. J. W. Graham, D. Lester, C. Y. Wong, T. Kilpatrick, S. Smith, B. Nguyen, An effective modeling tool for studying erosion, *Wear* 270 (2011) 598–605. doi:10.1016/j.wear.2011.01.016.
- [35] L. J. W. J. W. Graham, D. Lester, J. Wu, Slurry Erosion in Complex Flows : Experiment and CFD, in: *Seventh Int. Conf. CFD Miner. Process Ind.*, December, 2009, pp. 1–6.
- [36] J. K. Edwards, B. S. McLaury, S. A. Shirazi, Modeling Solid Particle Erosion in Elbows and Plugged Tees, *J. Energy Resour. Technol.* 123 (2001) 277. doi:10.1115/1.1413773.
- [37] X. Chen, B. S. McLaury, S. A. Shirazi, Numerical and experimental investigation of the relative erosion severity between plugged tees and elbows in dilute gas/solid two-phase flow, *Wear* 261 (2006) 715–729. doi:10.1016/j.wear.2006.01.022.
- [38] A. Gnanavelu, N. Kapur, A. Neville, J. F. Flores, An integrated methodology for predicting material wear rates due to erosion, *Wear* 267 (2009) 1935–1944. URL: <http://linkinghub.elsevier.com/retrieve/pii/S0043164809003986>. doi:10.1016/j.wear.2009.05.001.

- [39] O. E. Adedeji, L. Zhang, D. Breakey, R. S. Sanders, Investigation of abrasive wear in contact load-dominated slurry flows using a Toroid Wear Tester, *Manuscr. Submitt. to Wear* (2020).
- [40] M. Parsi, M. Kara, M. Agrawal, N. Kesana, A. Jatale, P. Sharma, S. Shirazi, CFD simulation of sand particle erosion under multiphase flow conditions, *Wear* 376-377 (2017) 1176–1184. URL: <http://dx.doi.org/10.1016/j.wear.2016.12.021>. doi:10.1016/j.wear.2016.12.021.
- [41] R. E. Vieira, M. Parsi, P. Zahedi, B. S. Mclaury, S. A. Shirazi, Electrical resistance probe measurements of solid particle erosion in multiphase annular flow, *Wear* 382-383 (2017) 15–28. URL: <http://dx.doi.org/10.1016/j.wear.2017.04.005>. doi:10.1016/j.wear.2017.04.005.
- [42] T. A. Sedrez, S. A. Shirazi, Y. R. Rajkumar, K. Sambath, H. J. Subramani, Experiments and CFD simulations of erosion of a 90° elbow in liquid-dominated liquid-solid and dispersed-bubble-solid flows, *Wear* 426-427 (2019) 570–580. URL: <https://doi.org/10.1016/j.wear.2019.01.015>. doi:10.1016/j.wear.2019.01.015.
- [43] B. Dooley, D. Lister, Flow-Accelerated Corrosion in Steam Generating Plants, *Powerpl. Chem.* 20 (2018) 194–244.
- [44] M. M. Stack, S. M. Abdelrahman, B. D. Jana, A new methodology for modelling erosion – corrosion regimes on real surfaces : Gliding down the galvanic series for a range of metal-corrosion systems, *Wear* 268 (2010) 533–542. URL: <http://dx.doi.org/10.1016/j.wear.2009.09.013>. doi:10.1016/j.wear.2009.09.013.
- [45] N. R. Sarker, L. Zhang, D. Breakey, B. A. Fleck, R. S. Sanders, Laboratory-Scale Erosive Wear Measurements Conducted with a Toroid Wear Tester (TWT), in: 8th Int. Conf. Transp. Sediment. Solid Part., September, 2017, pp. 295–303.

# Literature review

## 2.1 Introduction

Multiphase gas-solid and liquid-solid flows are commonly encountered in the transport lines of industries like the minerals processing and oil sands industries [1]. These industries are often faced with challenges such as pipeline blockage due to the presence of sand, increased energy/friction loss due to flow of the particulate phase, and erosion wear problems. These challenges compromise the integrity of major equipment, pumps, and pipelines, and often result in huge economics losses [2–4]. Several approaches or tools can be used to study and understand the multiphase flow behaviour related to these challenges in order to improve industrial system process design and operation. Modelling, which is the use of an equation or a set of equations to represent the physical system, is a widely used approach. The equations or models can be based entirely on physics-based theories or semi-mechanistic i.e. supplemented with empirical factors. Another approach is the use of bench-top or pilot-scale experimental facilities to understand the multiphase flow behaviour and guide modelling activities [5–7]. Usually, both approaches are used to complement each other through various validation and verification steps. Also, depending on the level of complexity of the model or on the level of detail required for the multiphase flow system under study, analytical or numerical methods can be used to solve the model equations. If the output from a model is at a macro-scale, an analytical method may be sufficient, however, whenever meso-scale analysis is required e.g. turbulence flow field, a numerical solution method is usually adopted [5, 8]. This is the advantage of methods like Computational Fluid Dynamics (CFD). This

chapter presents a literature review of a multiphase flow slurry friction loss model (the SRC two-layer model), CFD methods, erosion wear models, and relevant experimental techniques to provide a background knowledge for the work done in this thesis. This literature review will also present some preliminary analysis and discussion of the subject areas relevant to the investigations in this thesis. The analysis informed the selection of methods and techniques used to complete the research in this PhD thesis.

## 2. 2 Slurry flow modelling

The flow of slurry i.e. solid particles dispersed in a carrier liquid phase constitutes the hydrotransport processing systems of surface mining oil sands operation. Prediction of friction loss, deposition velocity, and concentration gradient are important slurry flow parameters needed for the optimal design and operation of these facilities [9]. In the following sections, the aforementioned parameters will be discussed.

### 2. 2.1 Frictional pressure gradient

Slurry flow pressure gradient is the energy loss generated as a result of friction from fluid-particle, particle-particle, fluid-wall, and particle-wall interactions. Depending on the size of the suspended solid particles, slurry friction loss mechanisms can be classified as either homogeneous or heterogeneous [1, 10]. For the homogeneous or non-settling slurries, the particles are uniformly dispersed and totally suspended by fluid turbulence due to the small size the particles [10, 11]. The slurry thus behaves like a single phase fluid with the frictional pressure gradient estimated based on bulk mean fluid properties i.e. average mixture density, viscosity, and flow velocity. The mean density of the slurry is determined by

$$\rho_m = C_v \rho_s + (1 - C_v) \rho_f \quad (2.1)$$

where  $C_v$  is the particle volume fraction,  $\rho_f$ ,  $\rho_s$ , and  $\rho_m$  are the liquid, solid, and mixture density respectively. Also, particle size alone cannot determine if a slurry system is truly homogeneous (or heterogeneous). The system flow conditions and the geometry length scale e.g. pipe diameter, are also contributing factors [12].

For heterogeneous slurry systems, the fluid turbulence does not fully suspend the

particles due to their larger size; hence, a fraction of the entire solid content is supported by the pipe wall [13]. The particles are, therefore, not evenly distributed over the pipe cross section. One of the most widely used models for friction loss prediction for heterogeneous slurry is the Saskatchewan Research Council (SRC) two-layer model [1, 9, 10, 13, 14].

The SRC two-layer model consists of a kinematic friction component and a Coulombic friction component [13]. The kinematic friction is the sum of the friction losses due to the carrier fluid and a Bagnold-like dispersive stress term due to the particles [14, 15]. The dispersive stress tends to drive the particles towards the pipe wall [16]. There is, however, a particle-wall lubrication effect or near wall lift which is a tempering effect that tends to drive particles away from the wall at certain conditions e.g. high velocities and lower solids volume concentrations [17, 18]. The kinematic friction is strongly dependent on slurry velocity, particle size, and solids volume concentration. The Coulombic friction, also known as contact-load or sliding bed friction results from the immersed weight of the particles being supported by the pipe wall. This friction is the cause of the asymmetric distribution of wall shear stress (and erosion wear) in slurry pipelines [14, 19] and is strongly dependent on the particle size and slurry mean velocity.

In the formulation of the SRC two-layer model, two theoretical layers were assumed as shown in Fig. 2.1. The upper layer (layer 1) consists of suspended particles contributing only kinematic friction while the lower layer (layer 2) consists of both suspended and contact load particles contributing to kinematic and Coulombic friction, respectively. The two layers are separated by an hypothetical interface as shown in the figure and they both have different mean solids concentration and slurry velocity. The upper layer solids concentration,  $C_1$  is less than that in the lower layer i.e.  $C_2$ , however, the reverse is the case for the slurry mean velocity i.e.  $V_1 > V_2$ . From writing a force balance equation for the two layers in a horizontal pipe, the frictional pressure gradient for layer 1 is given by

$$\frac{dP}{dz} = \frac{\tau_{k1}S_1 + \tau_{12}S_{12}}{A_1} \quad (2.2)$$

and for layer 2

$$\frac{dP}{dz} = \frac{\tau_{k2}S_2 - \tau_{12}S_{12} + \tau_c S_2}{A_2} \quad (2.3)$$

where  $\tau_k = \tau_f + \tau_s$  is the kinematic friction contribution,  $\tau_{12}$  is the interfacial stress and  $\tau_c$  is the Coulombic friction contribution.

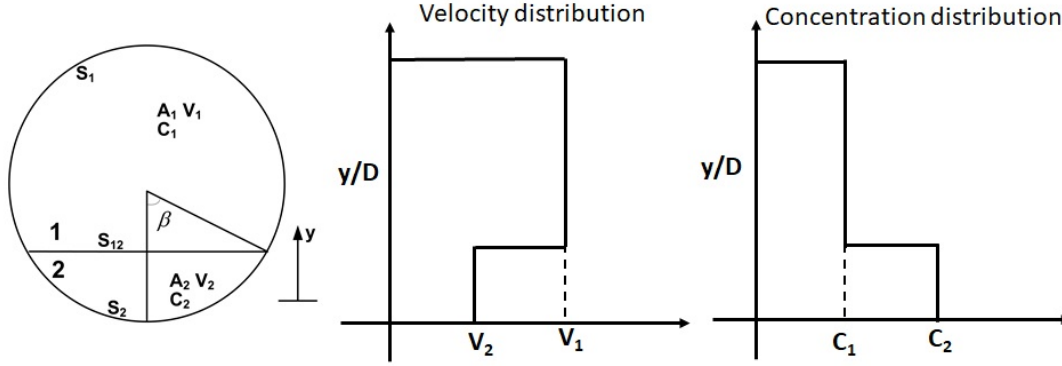


Figure 2.1: Theoretical layers for the development of SRC friction loss model

The friction loss due to the carrier fluid is defined as

$$\tau_f = \frac{1}{2} f_f \rho_f V^2 \quad (2.4)$$

where  $f_f$ , the Fanning friction factor can be determined using correlations like that of Swamee-Jain [12, 20] which is given by

$$f_f = \frac{0.0625}{\log_{10} \left[ \frac{k}{3.75D} + \frac{5.74}{Re^{0.9}} \right]^2} \quad (2.5)$$

where  $D$  is the pipe diameter,  $k$  is the pipe hydrodynamic roughness, and  $Re = \rho_f DV / \mu_f$  is the Reynolds number. The variable  $\mu_f$  is the fluid viscosity which should account for the presence of fines in the slurry. Other correlations like that of Churchill [21] also provide very good estimates of the Fanning friction factor.

The particle-related friction loss [14] is given by

$$\tau_s = \frac{1}{2} f_s \rho_s V^2 \quad (2.6)$$

where  $f_s$ , is the solids friction factor. A correlation based on numerous pipe flow experiments at SRC was developed for the solids friction factor and is given by [14]

$$f_s = \lambda^{1.25} [k_o \ln(d^+) + k_1] \quad (2.7)$$

where  $\lambda$  is the linear concentration, which represents the ratio of the mean particle diameter to the mean distance between neighboring particles and is given by

$$\lambda = \left[ \left( \frac{C_{max}}{C_r} \right)^{1/3} - 1 \right]^{-1} \quad (2.8)$$

where  $C_{max}$  is the limiting or maximum solids concentration (i.e. concentration of a settled bed of the particles). In Equation 2.8,  $C_{max}$  must be measured to obtain accurate predictions from the SRC two-layer model. The *in-situ* solids concentration  $C_r$  is the area-averaged solids concentration [7] which is given by

$$C_r = \frac{1}{A} \int_A c dA \quad (2.9)$$

The dimensionless particle diameter, which relates the particle diameter to the viscous sublayer thickness is given by

$$d^+ = \frac{d_{50c} \rho_f u^*}{\mu_f} \quad (2.10)$$

where  $d_{50c}$  is the mass median diameter of the coarse particles in the slurry (subscript "c" indicates coarse),  $u^* = V \sqrt{f_f/2}$  is the shear velocity. The fitting constants in Equation 2.7 are determined based on the value of the dimensionless particle diameter.

For  $d^+ < 21$ :  $k_o = -1.1 \times 10^{-4}$ ;  $k_1 = 4.2 \times 10^{-4}$

For  $21 \leq d^+ \leq 100$ :  $k_o = -5.6 \times 10^{-5}$ ;  $k_1 = 2.6 \times 10^{-4}$

For  $d^+ > 100$ :  $k_o = 0$ ;  $k_1 = 0$

It can be seen from the classification above that for large particles and at high slurry velocity, the kinematic friction is mainly due to the contribution of the carrier fluid.

The Coulombic friction,  $\tau_c S_2$ , is given by [14]

$$2 \int_0^\beta \tau_c dS_2 = 0.5 g D^2 \eta_s (\rho_s - \rho_f) (C_2 - C_1) (\sin \beta - \beta \cos \beta) \quad (2.11)$$

where  $\eta_s$  is the coefficient of sliding friction between the particles and the pipe wall, which is usually taken as 0.5 for sand and gravel [1]. This coefficient of sliding friction is preferably measured for a more accurate prediction from the SRC two-layer model. The parameter  $\beta$  is defined as shown in Fig. 2.1 and is the angle defining the hypothetical interface between the upper and lower layers. The difference in lower and upper layer solids concentrations in Equation 2.11 can be determined from the ratio of the Coulombic ( $C_c$ ) to the *in-situ* solids concentrations i.e. the contact load fraction. This is defined by

$$\frac{C_c}{C_r} = \frac{(C_2 - C_1)A_2}{C_r A} \quad (2.12)$$

The contact load fraction has been reported [1, 10, 12, 22] to be a function of the ratio of the bulk flow velocity and particle terminal settling velocity. The correlation for the contact load fraction is defined by

$$\frac{C_c}{C_r} = \exp[-0.062 \left( \frac{V}{v_\infty} \right)^{0.81} Fr^{-0.38}] \quad (2.13)$$

where  $Fr = V/\sqrt{gD(\rho_s/\rho_f - 1)}$  is the particle Froude number. The lower layer or limiting solids concentration  $C_2$  is found iteratively by solving the force balances (to get V1 and V2) and then the contact load (Equation 2.13 until there is convergence on either  $C_r$ ).

The contact load fraction increases with the ratio of particle-to-pipe diameter and with the solids concentration while it decreases with increase in slurry flow velocity. The particle terminal settling velocity  $v_\infty$  in Equation 2.13 can be calculated iteratively or from a direct method [12, 17, 23, 24]. A direct method using Archimedes number is as follows [22];

For  $Ar \leq 4.8$ :  $Ar = 24Re_p$  : Stokes regime

For  $4.8 < Ar < 4 \times 10^5$ :  $Ar = 24Re_p + 3.6Re_p^{1.687}$  : Transition regime

For  $Ar \geq 4 \times 10^5$ :  $Ar = 0.44Re_p^2$  : Newton's regime

where

$$Ar = \frac{4d^3 \rho_f (\rho_s - \rho_f) g}{3\mu_f^2} \quad (2.14)$$

and

$$Re_p = \frac{v_\infty \rho_f d}{\mu_f} \quad (2.15)$$

The particle terminal settling velocity can then be calculated from Equation 2.15. In order to obtain the solution to the SRC two-layer model, a balance equation written as  $AV = (A_2V_2 + A_1V_1)$  along with Equations 2.2 and 2.3 must be solved. The solution algorithm and other required correlations can be found in the literature [1, 9, 10]. Since the SRC model will be used extensively in some of the studies in this thesis, a MATLAB<sup>®</sup> code was written to implement this solution algorithm. This can be found in Appendix B.1. Sample data from the work of Gillies et al. [10] was used to validate the code and this is shown in Fig. 2.2.

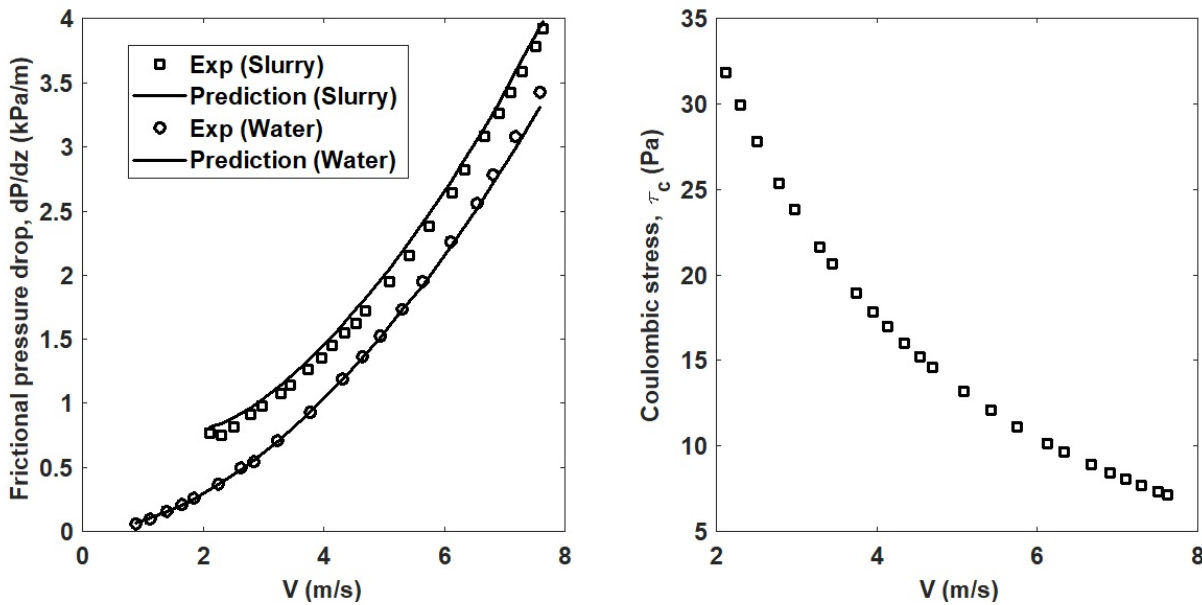


Figure 2.2: Predictions from SRC two-layer model programmed into MATLAB for Gillies et al. [10] data:  $d_{50c} = 270\mu m$ ,  $D = 103mm$ ,  $\rho_p = 2650kg/m^3$ ,  $C = 20\%$ ,  $\rho_f = 998kg/m^3$ ,  $\mu_f = 0.00096Pa.s$ , (left) frictional pressure drop, (right) Coulombic friction

For the data, pipe diameter is 103 mm, particle mass median diameter is 270  $\mu m$ , and solids volume concentration is 20%. The slurry is a sand-water mixture with the sand particles

having a density of  $2650 \text{ kg/m}^3$ . It can be seen from Fig. 2.2 that the model prediction matched the experimental data. As expected, the presence of particles will increase the frictional pressure drop due to collisions with one another and with the walls of the pipe. This is apparent in the experimental data as well as the model predictions when compared to the pressure drop from water alone. The Coulombic friction is also shown to decrease with increasing slurry flow velocity. This is reasonable since the particles become more efficiently suspended in the carrier fluid as the fluid velocity increases.

## 2. 2.2 Deposition velocity

The transport of settling slurry in pipelines requires that the slurry mean flow velocity is above a certain operational limiting velocity to avoid the formation of a stationary bed of particles. This limiting velocity is the particle deposition velocity [25]. The accurate prediction of particle deposition velocity is important to pipeline operators because of its economic implications. The formation of a stationary bed of particles increases the pressure gradient in the pipe because the effective pipe diameter has been reduced [26, 27]. In addition, the mass throughput of the material being transported is reduced, indicating a reduced production efficiency. In other words, there is increase in energy consumption and an accumulation of the particles being transported in the system. Several researchers who have worked on determining the deposition velocity found that (1) the particle-to-fluid density ratio, (2) the particle size, (3) the fluid viscosity, (4) the particle-to-pipe diameter ratio, (5) the particle size to laminar sublayer thickness ratio, (6) the solids volume concentration, (7) the particle shape, (8) the pipe wall roughness, and (9) the inclination of the pipe can greatly affect the predicted deposition velocity [15, 25, 28–35]. For coarse particle slurry conditions often found in mining and hydrotransport pipelines, a correlation was developed for predicting the particle deposition velocity at the SRC Pipe Flow Technology Centre™ based on deposition Froude number ( $Fr$ ) which is given by [15]

$$V_c = Fr \sqrt{gD \left( \frac{\rho_s - \rho_f}{\rho_f} \right)} \quad (2.16)$$

where

$$Fr = a + b \ln(Ar) \quad (2.17)$$

The value of the deposition Froude number is determined from a piece-wise relationship with the Archimedes number which is given by

For  $125 \leq Ar < 2690$ :  $a = 1.27$ ;  $b = 0.049$

For  $2690 \leq Ar < 86000$ :  $a = 2.35$ ;  $b = -0.088$

For  $Ar \geq 86000$ :  $a = 1.35$ ;  $b = 0.0$

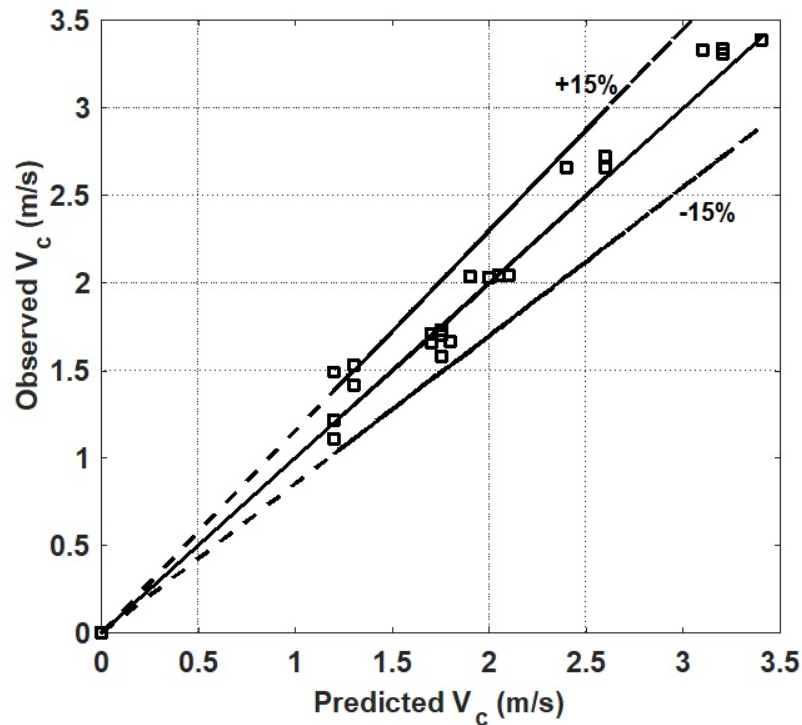


Figure 2.3: Observed vs predicted particle deposition velocity for data from Gillies [35] and Spelay et al. [15] in the interval defined by Equation 2.16

The above correlation is suitable only for conditions where  $Ar > 125$ . For certain conditions where  $Ar < 125$ , a limiting Archimedes  $Ar_0$  is defined by [15]

$$Ar_0 = 48(C_{max} - C_r)^{0.88} \quad (2.18)$$

for the interval  $Ar_0 \leq Ar \leq 125$ . A linear relationship suitable for interpolation is said to exist between  $V_c \sqrt{f_f/2}$  and  $Ar$  in this interval, where  $f_f$  is the carrier fluid Fanning friction factor [15].

The correlation defined in Equation 2.16 was used to predict the deposition velocity for some data collected from Spelay et al. [15] and Gillies [35]. These data can be found in Appendix B.1. The model prediction and the experimental data agree within a maximum error of  $\pm 15\%$  as can be seen in Fig. 2.3. Usually, industries will set their operating velocity to  $1.2V_c$  for their slurry pipeline design and operation [12].

## 2.3 Solid particle erosion (SPE) wear models

The development of solid particle erosion (SPE) wear models has been ongoing for over six decades. However, the accurate prediction of erosion wear is still not possible for many industries. This is because erosion wear is complex, involving fluid-particle-wall interactions and system-specific characteristics such as geometry and relative particle-target material hardness [36–38]. Therefore, there is no single SPE model available for general practical use across industries [39]. For most applications, erosion models are "tuned" to fit a specific system i.e. new empirical coefficients suitable for the system are determined for the erosion models. There are some erosion models that have been used across many industries. This section presents a description of four commonly used erosion models. A comparison is made between these erosion models to highlight their strengths and limitations.

### 2.3.1 Finnie's model

One of the earliest SPE wear models that is still being used by industries is Finnie's erosion model [40–42]. Finnie's model was developed based on a single particle impact causing a cutting damage on ductile materials. Finnie's model is the first to introduce the basic concept of erosion wear that subsequent erosion models build on. The basic concept is that the extent of erosion wear damage depends mainly on the incident angle and velocity of the eroding particle, and system-specific constants that represent a complex interaction of hydrodynamics and material properties. The model is defined by

$$ER = KV_p^n f(\alpha) \quad (2.19)$$

where ER is the dimensionless erosion rate reported as the mass of material lost to the mass of particle impacting the surface i.e.  $kg/kg$ . The particle impact angle function is given by

$$f(\alpha) = \begin{cases} f(\alpha) = \sin(2\alpha) - 3\sin^2(\alpha), & \text{if } \tan(\alpha) \leq \frac{1}{3} \\ f(\alpha) = \frac{1}{3}\cos^2(\alpha), & \text{if } \tan(\alpha) > \frac{1}{3} \end{cases} \quad (2.20)$$

The particle impact angle is given by  $\alpha$  and particle impact velocity by  $V_p$ . The velocity exponent and the coefficient  $K$  are system-specific and depend on the particle mass and target material flow stress at the given operating temperature of the system. Finnie's model is the foundation of many often-applied SPE wear models, but the model itself, as a single-particle model, has found minimal applications.

### 2.3.2 Oka et al. model

The Oka et al. model is also one of the most widely used SPE models that accounts for the effect of target material hardness and the particle diameter [43–45]. The Oka et al. erosion model shows the dependency of erosion rate on the impact velocity at normal incident angle i.e.  $90^\circ$ . The model is defined by

$$ER = E_{90}f(\alpha) \quad (2.21)$$

where the erosion rate at normal incidence angle is given by

$$E_{90} = K_p(H_v)^{k_1} \left( \frac{V_p}{V_{p,ref}} \right)^{k_2} \left( \frac{d_p}{d_{p,ref}} \right)^{k_3} \quad (2.22)$$

and the impact angle function is given by

$$f(\alpha) = (\sin \alpha)^{n_1} [1 + H_v(1 - \sin \alpha)]^{n_2} \quad (2.23)$$

The impact angle function consists of two parts. The first part with the exponent  $n_1$  represents the plastic deformation mechanism which increases with the particle impact angle. The second part with the exponent  $n_2$  represents the cutting mechanism which reaches a maximum value when the particle impacts the target surface tangentially i.e. at a particle impact angle of  $0^\circ$ . The parameters in the equation are defined as follows:

$d_p$  = Erodent particle diameter

$d_{ref}$  = Reference particle diameter (326  $\mu\text{m}$ )

$V_{ref}$  = Reference velocity (104 m/s)

$H_v$  = Vickers hardness of the target material

The exponents in the model are a function the target material hardness and are given by

$$n_1 = 0.71(H_v)^{0.14} \quad (2.24a)$$

$$n_2 = 2.4(H_v)^{-0.94} \quad (2.24b)$$

$$k_2 = 2.3(H_v)^{0.038} \quad (2.24c)$$

The coefficient  $K$  and exponents  $k_1$  and  $k_3$  are constants which strongly depend on the specific system characteristics, the particle properties and the target material hardness. Therefore, they may vary for different erodent-target materials combination. The Oka et al. model has been applied in many industrial processes, however, most often it is applied in gas-solid systems.

### 2. 3.3 E/CRC or Tulsa model

The Erosion/Corrosion Research Center at the University of Tulsa, USA also developed a SPE wear model that can also account for the target material hardness [46]. The model does not account for the effect of particle diameter but incorporates a particle shape factor. The erosion equation is given by

$$ER = C(BH)^{-0.59} F_s V_p^n f(\alpha) \quad (2.25)$$

The impact angle function is given by

$$f(\alpha) = \sum_{i=1}^5 A_i \alpha^i \quad (2.26)$$

where  $C$  is a system specific constant,  $BH$  is Brinell hardness number of the target material,

$F_s$  is the particle shape factor, and  $A_i$  are the fitting coefficients for the impact angle polynomial correlation. The values of the fitting coefficients are given in Table 2.1. The particle impact angle in the correlation is in radians while the velocity exponent  $n = 2.41$ .

Table 2.1: Impact angle function coefficients for E/CRC erosion model

		$A_i$				
i	1	2	3	4	5	
Value	5.4	-10.11	10.93	-6.33	1.42	

The particle shape factor  $F_s$  is based on the work of Powers [47][48] and ranges from well rounded to very angular as shown in Fig. 2.4. Usually, when sand particles are considered, the particle shape factor for sub-rounded particles is used in the wear model.

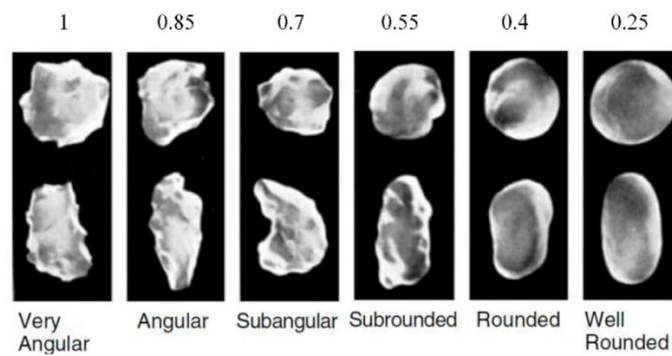


Figure 2.4: Particle shape factor [47, 48]

The E/CRC model is very popular in the oil and gas industry. The model has been successful in many multiphase applications (gas-solid, liquid-solid, gas-liquid solid); hence, its popularity.

### 2. 3.4 DNV model

In 2007, the Norwegian company Det Norske Veritas (DNV) Group developed an erosion wear model as an industrial guideline DNV RP O501 for piping systems [49]. The wear model has then been updated to a more recent version with separate correlations for ductile and brittle material through the impact angle relationship [50]. The model equation is given by

$$ER = KV_p^n f(\alpha) \quad (2.27)$$

where for brittle material, the impact angle function is given by

$$f(\alpha) = \frac{2\alpha}{\pi} \quad (2.28)$$

and for ductile materials, the impact angle function is given by

$$f(\alpha) = A[\sin(\alpha) + B(\sin\alpha - \sin^2\alpha)]^k [1 - e^{-C\alpha}] \quad (2.29)$$

The velocity exponent  $n = 2.6$ . The value of the constants are  $A = 0.6$ ,  $B = 7.2$ ,  $C = 20$ , and  $k = 0.6$ .

The coefficient  $K$  depends on the target material and a list of values for different materials type can be found in the DNV RP O501 industrial guideline manual [50]. It is important to note the brittle material impact angle function has a linear behaviour and should be considered an approximation suitable for most practical applications. The ductile material impact angle function behaves like the previously described erosion models where both plastic deformation and cutting damage mechanisms are captured.

### 2. 3.5 Comparison of the erosion models

All the erosion models previously described have limitations and advantages which best suits them for certain applications. A comparison made between the erosion models is summarized in Table 2.2. It can be seen from the comparison that most of the erosion models are only suitable for ductile material, except for the DNV model that has an impact angle function approximated for brittle materials. Cutting and plastic deformation damage were also accounted for by the erosion models except for the Finnie model which is based only on a cutting damage mechanism. A surface response diagram was plotted to demonstrate the erosion ratio for the two damage mechanisms and the two types of materials mentioned earlier. A case of impact angle between 0 and  $\pi/2$  rads and impact velocity between 0 m/s and 20 m/s was considered. Empirical constants for carbon steel was used for ductile material case and PSZ ceramic for brittle material. The plots are shown in Fig. 2.5.

Table 2.2: Comparison between the described erosion models

Parameters/Mechanism	Erosion model			
	Finnie	Oka et al.	E/CRC (Tulsa)	DNV RP O501
Particle impact angle	✓	✓	✓	✓
Particle impact velocity	✓	✓	✓	✓
Particle shape factor	×	×	✓	×
Hardness of target material	×	✓	✓	×
Hardness of erodents	×	×	×	×
Particle diameter	×	✓	×	×
Geometry factor (elbows)	×	×	✓	✓
Mass of particles	✓	×	×	×
Concentration of particles	×	×	×	×
Density of particles	×	×	×	×
Carrier fluid density	×	×	×	×
Carrier fluid viscosity	×	×	×	×
Ductile material	✓	✓	✓	✓
Brittle material	×	×	×	✓
Cutting damage	✓	✓	✓	✓
Deformation damage	×	✓	✓	✓

It can be seen from Fig. 2.5a that for the case of erosion wear due cutting mechanism on ductile materials (Finnie's model), maximum wear will occur at the minimum particle impact angle and maximum impact velocity. However, for the case of a brittle material as in Fig. 2.5c demonstrated via the DNV model, maximum wear will occur at normal (maximum) impact angle and maximum impact velocity. For models such as the Oka et al. model that accounts for both cutting and plastic deformation mechanism (Fig. 2.5b), maximum wear will occur at maximum impact velocity but at an impact angle between  $30^\circ$  and  $45^\circ$  [44]. The power law relationship between wear rate and particle impact velocity is also apparent in the response surface plots shown in the figures. The particle impact velocity exponent is usually between 2-3 [51] making erosion wear rate strongly dependent on the operating velocity of systems.

### 2. 3.6 Huang et al. model

The Huang et al. [52] erosion model is a modification of the initial model published in 2008 [53] for impingement jet flow. It is discussed in much detail here, and separate from the previously described erosion models because of how it will be implemented in the investigations conducted in Chapter 5. Also, the derivation of the Huang et al. [52] is based on analysis of turbulence quantities which is different from the previously described erosion

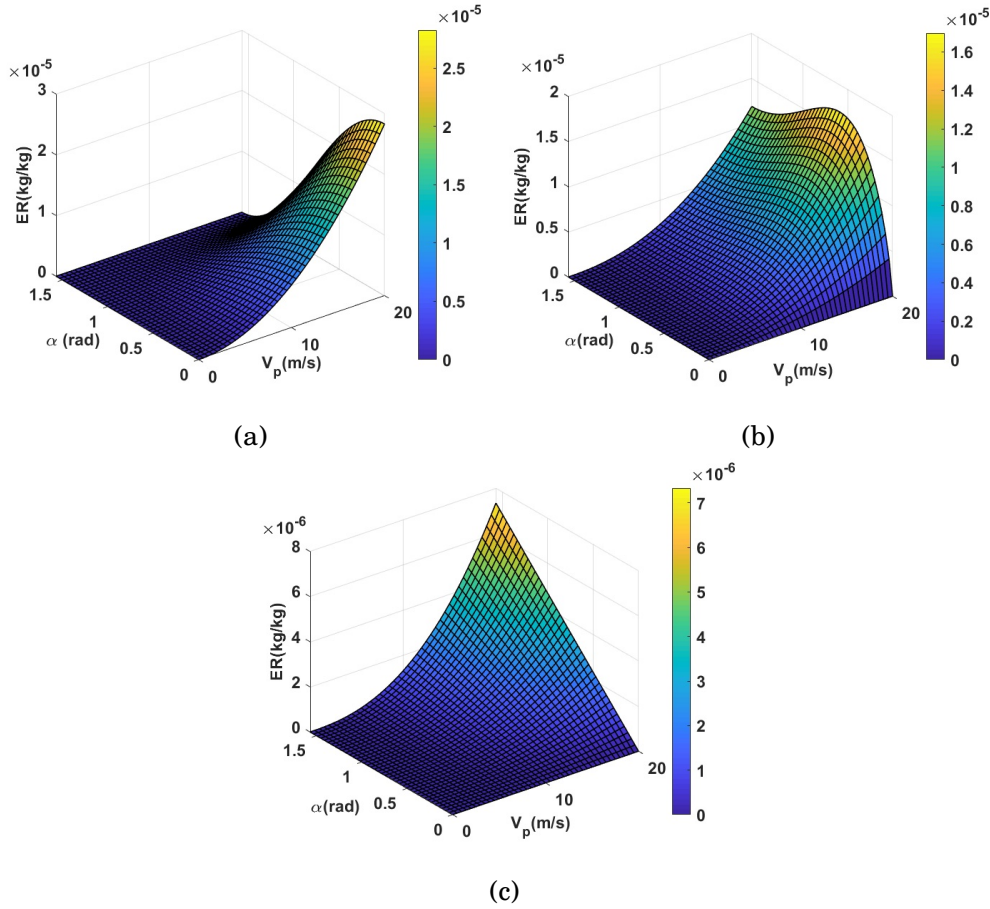


Figure 2.5: Response surface plots of different wear models (a) Ductile, Cutting, Finnie (b) Ductile, Deformation + Cutting, Oka et al. (c) Brittle, DNV

models. However, just like Bitter's erosion model [54], the Huang et al. [53] erosion model was developed based on deformation and cutting damage removal mechanisms for a single particle erosion. The initial model is given by

$$\Delta Q_E = \frac{Bm_p\rho_p^{1/4b}(V_p\sin\theta)^{2+1/2b}}{\varepsilon_c^{1/b}P_n^{1+1/4b}} + \frac{Cm_p^{1+3(1-n)/4}V_p^{2+3(1-n)/2}(\cos\theta)^2(\sin\theta)^{3(1-n)/2}}{d_p^{(1-n)/4}\varepsilon_0^iP_tP_n^{3(1-n)/4}} \quad (2.30)$$

where  $n$  is a constant with a value depending on the type of cutting mechanism and particle shape ( $n=0.5$  for line cutting,  $n=1$  for area cutting). The constants  $b, i, B, C$  are determined by experiments,  $\varepsilon_c$  is the critical strain,  $\varepsilon_0$  is the material ductility,  $P_n, P_t$  are normal and tangential pressures,  $\rho_p, m_p, V_p, \theta$  are particle density, mass, impact velocity, and impact

angle, and  $\Delta Q_E$  is the volume removed due to erosion from a single particle.

The first expression on the right hand side of the equation represents the deformation damage removal. It results from analysis of normal impact force acting on the target surface, the volume of indentation, and the deformation volume removal based on critical strain and Coffin-Manson equation [55]. The second expression on the right hand side of the equation represents the cutting damage removal. This results from analysis of tangential force (oblique particle impact) on the target material and the change in kinetic energy of particles after cutting.

In the derivation of the Huang et al. [52] model for slurry flow in horizontal pipe flows from this initial model, an assumption was made that most particles impacting the wall in a slurry pipeline flow have an oblique angle; hence, cutting damage will be significant while deformation damage will be negligible. Equation 2.30 was reduced to

$$\Delta Q_E = \frac{Cm_p^{1+3(1-n)/4}V_p^{2+3(1-n)/2}(\cos\theta)^2(\sin\theta)^{3(1-n)/2}}{d_p^{(1-n)/4}\epsilon_0^i P_t P_n^{3(1-n)/4}} \quad (2.31)$$

With further mathematical simplification, Equation 2.31 was multiplied with  $(\cos\theta)^{3(1-n)/2}$ , thereby replacing the particle impact velocity  $V_p$  with the axial component of the velocity  $V_{px}$  in the flow direction, thereby, reducing the equation to

$$\Delta Q_E = \frac{Cm_p^{1+3(1-n)/4}V_{px}^{2+3(1-n)/2}(\tan\theta)^{3(1-n)/2}}{d_p^{(1-n)/4}\epsilon_0^i P_t P_n^{3(1-n)/4}} \quad (2.32)$$

Further simplification was carried out by assuming that particle velocity in a turbulent pipe flow is similar to that of the fluid i.e. not greatly retarded and approximately follows the fluid path. This replaces the particle axial velocity  $V_{px}$  with the slurry mean velocity  $V$ . A summary and implication of this assumption is that

- The pipe flow must be turbulent
- For moderately turbulent flow, the particle diameter must be small enough for the assumption to hold.
- For highly turbulent flow, larger particle diameter can be used in the model.

- No metrics was put forward to support this assumption for the use of the model e.g particle Stokes number being less than or equal to 1 in the flow
- Attention was not drawn to the local slurry velocity in the vicinity of the pipe wall.
- From the assumption, and from the previous point, the model may just be suitable for pseudo-homogeneous slurry flows or flows with an almost symmetrical velocity and concentration profile.

Another assumption was also made that the particle impact angle is very small for cutting damage such that  $\tan\theta \approx \theta$ . With this, the equation reduces to

$$\Delta Q_E = \frac{C m_p^{1+3(1-n)/4} V^{2+3(1-n)/2} \theta^{3(1-n)/2}}{d_p^{(1-n)/4} \epsilon_0^i P_t P_n^{3(1-n)/4}} \quad (2.33)$$

The summary and implication of this assumption is that

- Abrasive erosion mechanism will dominate, which is as a result of Coloumbic stress or particle contact load resulting form a highly heterogeneous flow or a sliding bed flow. This however, contradicts the previous assumption that particles follow fluid path, which is a characteristics of kinematic friction dominated slurry flow.
- If the condition for this assumption holds, it will only be suitable for the pipe invert region because high impact angle deformation damage is significant at the top region of the pipe (pipe obvert).
- The exact need for this assumption is unclear, except for mathematical simplification. Further derivation of the model focuses mainly on finding an expression for the particle impact angle  $\theta$  as a function of position around the pipe perimeter based on turbulent flow analysis of particle normal and tangential fluctuating velocities, gravitational force, buoyant force, and drag force on the particle. The expression could have been substituted directly in the Equation 2.30 but with a drawback of greater complexity of the equation and more empirical constants, which may be tedious to obtain.

However, going further with the formulation of the model, the position angle  $\alpha$  around the pipe perimeter is defined as shown in Fig. 2.6

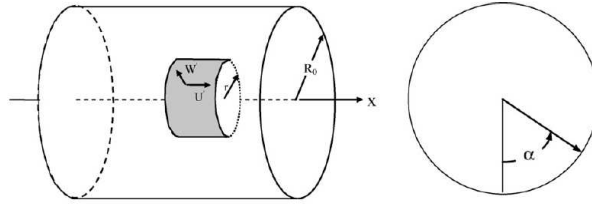


Figure 2.6: Control surface for model derivation [52]

The particle impact angle is defined as

$$\theta = \frac{w'_p + w_{pyn}}{V} \quad (2.34)$$

where  $w'_p$  is the component of the particle fluctuating velocity normal to the pipe wall,  $w_{pyn}$  is the component of the particle settling velocity normal to the pipe wall. Ideally, the expression should equal  $\tan\theta$ , which will essentially result in the same equation if the second assumption of  $\tan\theta \approx \theta$  was not made. From the force balance and turbulence analysis, Equation 2.34 was represented by

$$\theta = \frac{1}{V} \left[ \frac{b^*V}{Re_D^{m/2}} + \frac{d_p^2(1-C_v)(\rho_p - \rho_f)\cos\alpha}{18\mu_f(1+0.1Re_p^{0.75})} \right] \quad (2.35)$$

Where  $b$  is a coefficient reflecting the degree of turbulence. The coefficient  $m = 0.25$  for  $Re_D < 10^5$ , while  $m = 0.2$  for  $10^5 < Re_D < 10^6$ , where  $Re_D = \rho_f VD/\mu_f$ . From analysis of the model,  $m = 0.2$  was found to be suitable for both flow regimes. The particle diameter is  $d_p$ ,  $C_v$  is the slurry *in-situ* solid volume concentration, and  $D$  is pipe diameter. It is important to note here that the latter is not the local solid volume concentration. Another question is that, can this expression for impact angle be used in other single particle erosion models for application in horizontal pipeline?

Now substituting Equation 2.35 into 2.33, the material volume loss around the pipe perimeter due to single particle impact was derived as

$$\Delta Q_E = \frac{Cm_p^{1+3(1-n)/4}V^2}{d_p^{(1-n)/4}\epsilon_0^i P_t P_n^{3(1-n)/4}} \left[ \frac{b^*V}{Re_D^{m/2}} + \frac{d_p^2(1-C_v)(\rho_p - \rho_f)\cos\alpha}{18\mu_f(1+0.1Re_p^{0.75})} \right]^{3(1-n)/2} \quad (2.36)$$

For total amount of material removed by multiple impact of particles, the number of particles impacting a unit area is defined as

$$N = \frac{3(w'_p + w_{p,yn})C_v^t}{\pi d_p^3} \quad (2.37)$$

Where  $t$  is an exponent determined by experiment that reflects the local effective concentration. In the Huang et al. [52] model,  $t$  was selected based on material properties ( $t=0.516$  for brass, 0.556 for mild steel, taken from Gupta et al. [56]) while apparently, it should be based on pipeline flow conditions and should vary locally around pipe perimeter for heterogeneous slurry flows. This might have been done for simplicity sake, and the unavailability of data.

Now multiplying Equations 4.5 and 2.37, the equation for slurry flow in horizontal pipeline was derived and it is given by

$$ER = \frac{C^* \rho_p^{1+3(1-n)/4} V^2 d_p^{2(1-n)} C_v^t}{\varepsilon_0^i P_t P_n^{3(1-n)/4}} \left[ \frac{b^* V}{Re_D^{m/2}} + \frac{d_p^2 (1 - C_v) (\rho_p - \rho_f) \cos \alpha}{18 \mu_f (1 + 0.1 Re_p^{0.75})} \right]^{(5-n)/2} \quad (2.38)$$

Where  $C^*$  is a coefficient equal to  $(C/2)(\pi/6)^{3(1-n)/4}$ . In using the available development data to determine the constant coefficient for the model, Equation 2.38 was reduced to

$$ER = k \rho_p^{1+3(1-n)/4} d_p^{2(1-n)} V^2 C_v^t \left[ \frac{b^* V}{Re_D^{m/2}} + \frac{d_p^2 (1 - C_v) (\rho_p - \rho_f) \cos \alpha}{18 \mu_f (1 + 0.1 Re_p^{0.75})} \right]^{(5-3n)/2} \quad (2.39)$$

Where  $k = \frac{C^*}{\varepsilon_0^i P_t P_n^{3(1-n)/4}}$  is a coefficient that includes the target material properties.

## 2.4 Experimental wear testing devices

Erosion wear models are not based purely on first principle physics because of the complex nature of the erosion process. This means erosion models have empirical coefficients which must be determined using experiments. Several bench-top and pilot scale experimental testing devices exist, which can speed up the erosion process so that these empirical coefficients

can be determined. Also, the wear testing devices also serve as tools to study and understand the various parameters that affect erosion wear. A few of these wear testing experimental devices are discussed below.

### 2. 4.1 Recirculating pipe loop tester

The recirculating pipe loop (RPL) tester is a closed-loop system that has been used by many researchers to study slurry pipeline erosion wear [2, 3, 7, 22, 57–59]. The RPL tester has a unique advantage of having a similar hydrodynamics as that of industrial pipelines. A schematic of a typical closed-loop pipeline rig is shown in Fig. 2.7. As shown in the schematic, the system consists of a centrifugal slurry pump, a flow meter, a control valve, a heat exchanger, an observation section, pipe spools, and a slurry feed tank. To prevent settling, the slurry feed tank is continually agitated. The pump supplies energy to move the slurry around the pipe loop. Energy from the rotating action of the pump as well as friction causes the slurry temperature to rise, hence, the need for the heat exchanger to maintain the system at a constant temperature. Keeping temperature constant in the system is important because it affects the fluid viscosity which can introduce error to the wear measurement and change the flow behaviour of the settling slurry.

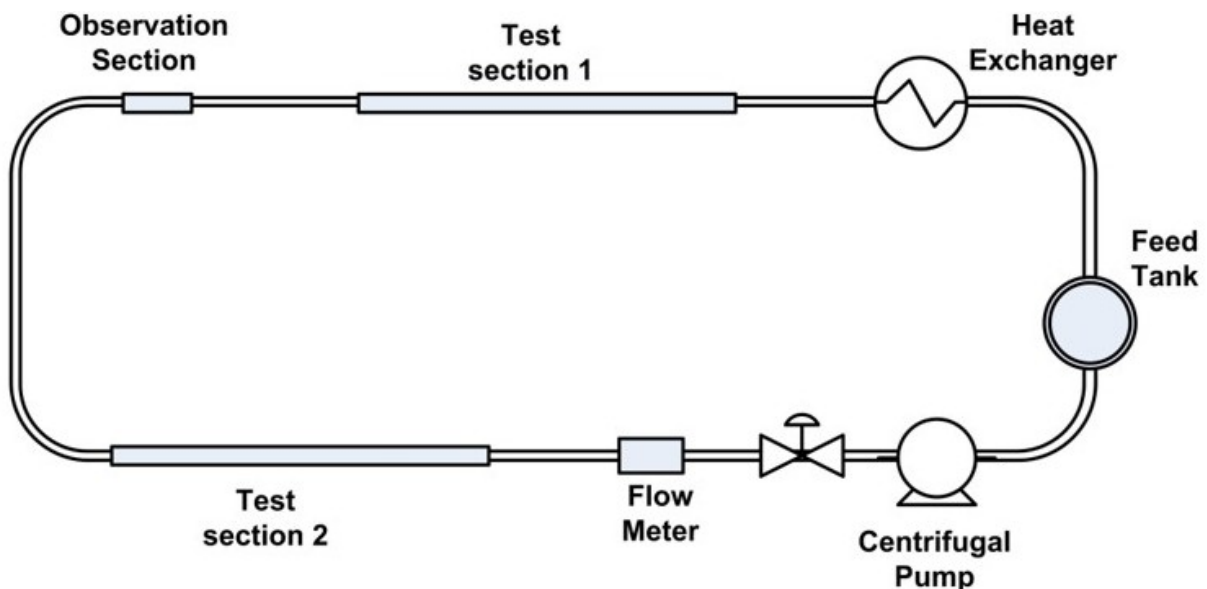


Figure 2.7: Schematic of the recirculating pipe-loop wear tester (based on [7])

The test sections are often pipes of different diameters so that erosion wear measurements can be taken at different mean slurry flow velocities. A simultaneous study of slurry friction loss can be carried out in the RPL by installing other instrumentation e.g. a differential pressure transducer. Generally, the RPL system best represents slurry pipeline wear studies, however, there are accompanying drawbacks. Particle degradation caused by continual passes through the pump and pipeline reduces the angularity of the particles and increases the amount of fines in the slurry [2, 7]. Consequently, the abrasiveness of the particles is compromised, the effective particle diameter is reduced, and the bulk fluid viscosity increased. These changes will result in a much lower wear rate that is not representative of the true slurry condition [60]. Particle degradation is addressed by replacing the slurry in the feed tank at intervals when the degradation is considered not to be significant [7, 61–63]. This activity can be expensive and time consuming. Also, experiments conducted in the RPL usually take a longer time, typically, 4-6 weeks before a reasonable mass loss can be measured on the test spools [7, 58]. The limitation on handling capacity is another drawback e.g. most pilot scale RPL cannot handle large particle sizes (e.g. 2 and 4 mm), whereas, industrial systems handle particles as large as 10 mm [2].

## 2. 4.2 Impingement jet tester

The impingement jet tester (IJT) is designed to intensely focus particles on a test specimen at high velocity. It is one of the most widely used wear testing device to estimate empirical coefficients for erosion models, and has been combined with computational fluid dynamics (CFD) methods to develop new erosion models [38, 43, 45, 46, 64–67]. The IJT can either be wet, submerged (liquid-solid) or dry (gas-solid). The components of the IJT include a specimen holder, a nozzle, a control valve, a sand or slurry feeder, and a pump or compressor depending whether it is wet or dry [68]. A schematic of the IJT is shown in Fig. 2.8. The design of the IJT facilitates easy control of the wear-influencing parameters like the particle impact velocity and the particle impact angle.

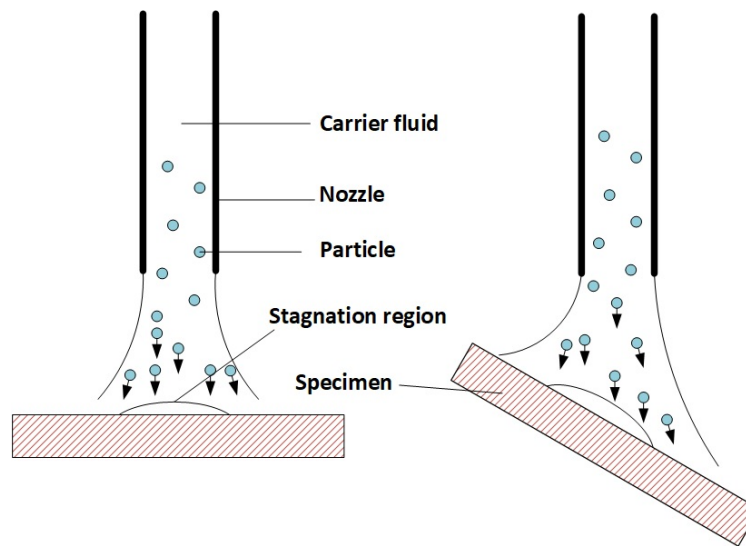


Figure 2.8: Schematic of impingement jet tester

For a slurry (liquid-solid) IJT system, a stagnation region exists as indicated in Figure 2.8 [69–71]. Also, the specimen can be tilted as shown in the schematic to obtain a desired range of particle impact angles. The particle impact velocity and impact angle in a jet tester can be measured using methods like Laser Doppler Velocimetry (LDV) or Particle Image Velocimetry (PIV) or in some other cases a combination of measurement and CFD prediction of the local wear variables [46, 68, 69, 72–75]. Impingement jet testers are not suitable to simulate the conditions inside a pipeline because the operating velocity of the jet tester is too high to realistically represent a pipe system. Jet testers are also best suited for dilute systems since inter-particle collisions are not accounted for in their analyses.

### 2. 4.3 Toroid wear tester

The toroid wear tester (TWT) is another device that can be used to accelerate wear rate on test materials. A TWT provides measurable wear results much more quickly than a recirculating pipe loop tester but not as rapidly as a jet impingement tester. A toroid is a closed loop system made from a pipe (or channel) shaped into a wheel and rotated about the wheel's axis to simulate pipe flow conditions. It has been used in several studies with the most common being emulsion inversion [76–79] and erosion wear of materials [51, 61–63, 76, 80–84]. Just like the impingement jet tester (IJT), the toroid wear tester (TWT) is also suitable for testing various materials for ranking purposes. It is, however, designed

to study erosion wear rate in contact load dominated slurry flow systems [62]. Hence, the mechanism of wear is predominantly due to abrasion and not high energy impact as in the IJT. A schematic of the toroid wear tester is shown in Fig.2.9. As the wheel rotates, the partially suspended slurry mixture is in contact with the test coupons, thereby creating the abrasive action that results in the wear. Some other advantages of the toroid wear tester include the reduced rate of particle degradation and the use of relatively small slurry volumes. Also, even though the TWT was made to simulate pipe flow, the hydrodynamics are different from those in pipelines [80]. This calls for the need to further understand this system if it is to be used as a tool for slurry pipeline wear prediction. The TWT wheel can also be made from a transparent material such that it facilitates visual observation of the behaviour of particles in the system, as discussed later in this thesis.

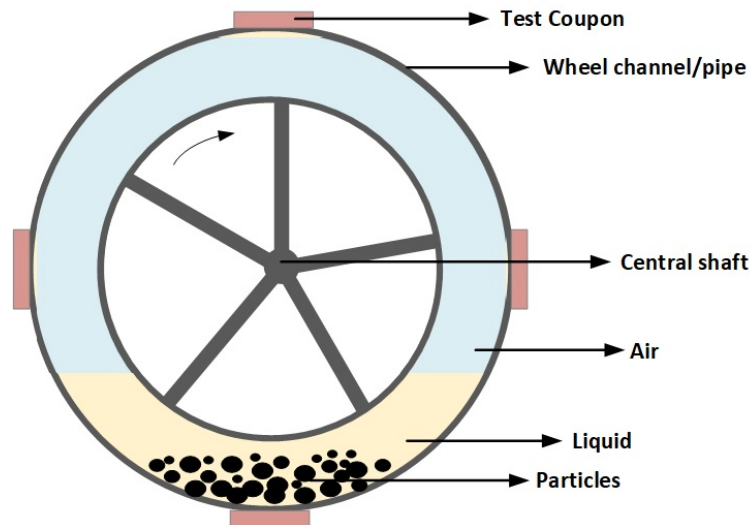


Figure 2.9: Schematic of toroid wear tester

## 2.5 Computational fluid dynamics modelling

Flow is an integral part of many processes ranging from natural convection of wind, flow of blood in the veins, transport of species in a reaction, mixing of substances in a tank, to transport of materials/particles in a pipeline [85–89]. The influence of fluid flow on these processes needs to be understood if optimal design and performance is to be achieved [85]. Computational Fluid Dynamics (CFD) is a powerful and sophisticated computer-based design

and analysis tool developed in the late 1960's to solve fluid flow problems [85–88]. Since the development of CFD, it has become a powerful modelling tool used to simulate design alternatives, providing solutions and operating strategies to fluid systems in many industry. CFD can reduce the overall cost of the design process by eliminating the need to invest in a pilot plant. The recent development in computational capacity has also extended the use of CFD to solve even more complex flow problems in very unusual geometries or systems. Many commercial computer programs or CFD codes such as ANSYS Fluent/CFX, Star CCM+, COMSOL, and OpenFOAM are now available to industries and academics for use. These CFD codes are based on certain governing equations which allow the solution of fluid flow problems to be possible. These are [85, 86, 88]

- Mass conservation or continuity equation where the net mass flow into a system must be zero.
- Momentum conservation which is based on the Navier-Stokes equation from Newton's second law. The net sum of forces acting on a system must be zero for momentum to be conserved.
- Energy balance from the first law of thermodynamics in which energy cannot be created nor destroyed but can be converted from one form to another.
- Species balance for chemical reactions where substances change but all atoms must be accounted for.

Detailed formulation and theoretical background of these equations can be found in Bird et al. [90]. The governing equations are partial differential non-linear equations which cannot be solved analytically. CFD codes therefore employ an iterative method by first linearizing these equations to form a system of algebraic equations using methods such as the finite-difference, the finite-volume, or the finite-element methods. It is important to note that the user-friendliness of CFD codes can deprive a user of the understanding of the fundamental physics of the problems being solved. This can lead to either over simplification or the incorporation of unnecessary details in the problem which can compromise the quality and accuracy of the results as well as the overall computational cost. Simplifying assumptions should therefore, be based on what changes may affect the primary flow characteristics being investigated. This judgment call can only come from a good understanding of the physical

system and a proper formulation of the fluid flow problem. Computational Fluid Dynamics (CFD) simulation process involves certain steps and these are discussed in the next section.

## **2. 5.1 CFD modelling steps**

### **Geometry creation/CAD model**

This step involves the definition of the internal fluid domain using a CAD program such as SolidWorks, Rhino, Siemens NX, SpaceClaim and DesignModeler. The dimension of the system geometry is used to defined the fluid domain. Higher accuracy is more likely to be achieved if the geometry defined accurately represents the real system [85, 88]. However, this can come at a high computational cost for very large or complex geometries. Depending on the type of problem being solved, it might be more realistic to perform some CFD simulations at a reduced scale of original system and eliminate geometry features that can cause meshing problems that lead to instability during the solution step.

### **Meshing/Grid generation**

This is the step where the internal fluid domain defined for the system is subdivided into a large number of fluid control volumes called cells. Several computer packages such as Gambit, ANSYS Meshing, and ICEM CFD can be used for this discretization. Solution of the equations that represents the fluid system are solved at the nodes, cell faces or centre of these cells. There are two types of grid generation methods: structured and unstructured grids [91, 92]. The unstructured grid is the common type of grid generation method because it uses different cell shapes e.g. tetrahedral, hexahedral, or prism layers so that the mesh adapts to features unique to complex geometries [85, 86]. Depending on the type of problems, similar cell sizes can be generated for the entire fluid domain or can be refined in a certain region (e.g. near the wall for pipes, at impeller blade tip) that is the focus of investigation or can affect the focus area significantly. Meshing can be very tedious but it depends on the complexity of the geometry. Increasing the number of grids generated can improve solution accuracy but at a high computational cost. Grid-independence techniques are often used to determine the number of cells that needs to be generated in order not to compromise the accuracy of the solution. Usually, a physical variable e.g. pressure drop, from the CFD solution is monitored starting with the smallest number of cells. The number of cells is increased, calculation

repeated, and the physical variable recorded. The refinement is continued until the physical variable does not change anymore with further refinement. There are also certain rule of thumb that can be used to estimate the size of cell or grid based on the characteristic length scale of the system geometry e.g. pipe diameter. A calculator developed in MATLAB for such estimation for incompressible single phase flow in horizontal pipes is presented in Appendix B.3.

### **Physics set-up and solution**

This is the step where equations are defined for the fluid system. In order to do this accurately, questions regarding the physical characteristics of the system need to be answered [91]. Examples of typical questions are [85, 93]:

- Is the fluid Newtonian or non-Newtonian?
- Is the flow laminar or turbulent?
- Is the system single phase or multiphase?
- Is there heat transfer?
- Is the system open or closed?
- Is there any interface diffusion or mass transfer?
- Is any reaction happening in the system?
- Is there any external force interacting with the system?
- Is a steady state or transient solution required?

Answering these questions will guide a user to properly define governing equations and models, fluid properties, and operating and boundary conditions. This step also involves setting the initial values for solution initialization, selecting the appropriate numerical scheme for the solution, setting convergence criteria, and implementing solution procedures. Based on the level of interactions in the system, a step-wise solution procedure may be used. For example, a first-order numerical scheme can first be used to solve for turbulence fields before switching to a second-order scheme [93]. For some multiphase flow problems, the

single phase system is first solved before activating the solution for the multiphase system. The main purpose of CFD codes like ANSYS Fluent, Star CCM+, or COMSOL Multiphysics is to implement this solution step.

### **Post-Processing**

This is the last step in CFD analysis of a system where results and data are collected from the simulation output and then translated into contours, animations, tables, and charts [85, 91, 92]. It also involves analysis of the results, reporting, and documentation of simulation outcomes. Most CFD codes have a built-in post-processor, however, there are other dedicated post-processing packages like Paraview and Tecplot. User-friendliness is one of the most important things engineers consider when choosing a CFD post-processor. Another important part of CFD post-processing analysis is the verification of the simulation results with analytical models or the validation with experimental data. At least one part of the CFD simulation process must involve a verification or validation step before results can be confidently used to make decisions or design changes in the real system.

## **2. 5.2 Turbulence modelling**

The motion of fluid in a system often determines the behaviour of the system e.g. the amount of energy lost due to friction or the rate of heat/species transfer. When the system's Reynolds number is high, the fluid domain is in chaos due to the high momentum [93, 94]. This generates many fluctuations in the velocity field, often referred to as turbulent eddies. Solving the Navier-Stokes equation using an exact numerical approach (Direct Numerical Simulation-DNS) is very costly computationally and impractical for most cases even with the advancement in computing capacity [85]. For DNS to be feasible, the size of the grid cells in the fluid domain must be smaller than the smallest eddy in the system. This will result in the generation of a large number of cells of the order of many millions for the fluid domain. Therefore, even DNS has been limited to relatively low Reynolds number applications [86]. The approach in CFD/numerical simulations is to use an approximate method to account for fluid turbulence. A common method is the statistics-based Reynolds-averaging method applied to the Navier-Stokes equation, hence, The Reynolds-Averaged Navier-Stokes-RANS equation [85, 86, 93, 94]. The Reynolds-averaging method is an ensemble-averaging method that decomposes the instantaneous velocity and other scalar quantities represented by the

transport equation into a mean part and a fluctuating part such that

$$u_i = \bar{u}_i + u'_i \quad (2.40)$$

where  $i = x, y, z$ ,  $u_i$  is the instantaneous velocity,  $\bar{u}_i$  is the mean velocity, and  $u'_i$  is the fluctuating velocity. The same decomposition is done for pressure and other scalar quantities like temperature and volume fraction. The Navier-Stokes equation for the three Cartesian coordinates is given by

$$\frac{\partial \rho}{\partial t} + \frac{\partial}{\partial x_i}(\rho u_i) = 0 \quad (2.41a)$$

$$\frac{\partial}{\partial t}(\rho u_i) + \frac{\partial}{\partial x_j}(\rho u_i u_j) = -\frac{\partial p}{\partial x_i} + \frac{\partial}{\partial x_j} \left[ \mu \left( \frac{\partial u_i}{\partial x_j} + \frac{\partial u_j}{\partial x_i} - \frac{2}{3} \delta_{ij} \frac{\partial u_k}{\partial x_k} \right) \right] \quad (2.41b)$$

After substituting the decomposed instantaneous velocity into the Navier-Stokes equation and then performing an ensemble (or time) averaging, the RANS equation derived in tensor notation is given by

$$\frac{\partial \bar{\rho}}{\partial t} + \frac{\partial}{\partial x_i}(\bar{\rho} \bar{u}_i) = 0 \quad (2.42a)$$

$$\frac{\partial}{\partial t}(\bar{\rho} \bar{u}_i) + \frac{\partial}{\partial x_j}(\bar{\rho} \bar{u}_i \bar{u}_j) = -\frac{\partial \bar{p}}{\partial x_i} + \frac{\partial}{\partial x_j} \left[ \mu \left( \frac{\partial \bar{u}_i}{\partial x_j} + \frac{\partial \bar{u}_j}{\partial x_i} - \frac{2}{3} \delta_{ij} \frac{\partial \bar{u}_k}{\partial x_k} \right) \right] + \frac{\partial}{\partial x_j}(-\bar{\rho} \overline{u'_i u'_j}) \quad (2.42b)$$

The equations have similar general form except that the instantaneous velocity has been replaced with the average velocity in Equation 2.41, and there is an extra term,  $-\bar{\rho} \overline{u'_i u'_j}$ , known as the Reynolds stresses in Equation 2.42. This extra term needs to be modelled in order for the equation to be closed i.e. the number of unknown variables equals the number of equations and the degree of freedom is zero. Modelling this term appropriately is the basis on which most turbulence equations are developed [85, 94]. There are two main approaches to modelling this fluctuation term. The first is the eddy/turbulent viscosity approach based on the work of Boussinesq in 1877 [85]. The Boussinesq theory assumes that turbulent flows are dominated by large energetic eddies responsible for mixing in the flow. Using this theory,

the fluctuation term in the RANS equation can be written as

$$-\overline{\rho u'_i u'_j} = \mu_t \left( \frac{\partial \bar{u}_i}{\partial x_j} + \frac{\partial \bar{u}_j}{\partial x_i} \right) - \frac{2}{3} \left( \bar{\rho} k \mu_t \frac{\partial \bar{u}_k}{\partial x_k} \right) \delta_{ij} \quad (2.43)$$

where  $\mu_t$  is the eddy or turbulent viscosity,  $\frac{\partial \bar{u}_i}{\partial x_j} + \frac{\partial \bar{u}_j}{\partial x_i} = \bar{S}_{ij}$  is the Reynolds averaged strain-rate tensor,  $\frac{\partial \bar{u}_k}{\partial x_k}$  is the divergence of velocity which disappears for incompressible flow,  $k$  is the turbulent kinetic energy given by  $k = (1/2)\overline{u'_i u'_i}$ . The Boussinesq assumption is the basis of first order and second order turbulence models. These models require low computational cost and are quite accurate for shear-dominated flows. However their performance reduces for highly rotating or stratified flows, swirls and other secondary flows. The second approach is the basis of the Reynolds Stress Transport Model. Exact equations are derived for the Reynolds stresses in the RANS equation fluctuation term by taking another time average of the RANS equation i.e. second-order moment. An equation is solved for each of the Reynolds stresses resulting in additional five equations for 2D problems and seven equations for 3D problems. The Reynolds stress model has more capability to give accurate predictions for complex flows but at a higher computational cost.

### Two equations model ( $k - \epsilon$ model)

The  $k - \epsilon$  model is a two equation turbulence model based on Boussinesq assumptions [94, 95]. Individual transport equations are solved for the turbulent kinetic energy,  $k$ , and the turbulent dissipation rate,  $\epsilon$ . The eddy viscosity is then computed as a function of turbulent kinetic energy and dissipation rate. There are three versions: the Standard, Realizable, and RNG  $k - \epsilon$  models. The differences in these three are the methods of calculating the eddy viscosity, the generation and dissipation terms in the turbulent dissipation transport equation, and the turbulent Prandtl number for the diffusion of  $k$  and  $\epsilon$  [93]. The transport equations for the Standard  $k - \epsilon$  model is given by

$$\frac{\partial}{\partial t}(\rho k) + \frac{\partial}{\partial x_i}(\rho k u_i) = \frac{\partial}{\partial x_j} \left[ \left( \mu + \frac{\mu_t}{\sigma_k} \right) \frac{\partial k}{\partial x_j} \right] + G_k + G_b - \rho \epsilon - Y_M + S_K \quad (2.44)$$

$$\frac{\partial}{\partial t}(\rho \epsilon) + \frac{\partial}{\partial x_i}(\rho \epsilon u_i) = \frac{\partial}{\partial x_j} \left[ \left( \mu + \frac{\mu_t}{\sigma_\epsilon} \right) \frac{\partial \epsilon}{\partial x_j} \right] + \frac{C_{1\epsilon}}{k} (G_k + C_{3\epsilon} G_b) - C_{2\epsilon} \rho \frac{\epsilon^2}{k} + S_\epsilon \quad (2.45)$$

where  $G_k = \mu_t(2S_{ij}S_{ij})$  is the generation of turbulent kinetic energy due to mean velocity strain,  $G_b$  is the generation of turbulent kinetic energy due to buoyancy,  $Y_M$  is the fluctuating dilation that contributes to the overall dissipation in compressible flow. The coefficients  $C_{1\epsilon} = 1.44$ ,  $C_{2\epsilon} = 1.92$ ,  $C_{3\epsilon} = 1.00$  are empirical constants,  $S_k$  and  $S_\epsilon$  are user-defined source terms, and  $\sigma_k = 1.0$  and  $\sigma_\epsilon = 1.3$  are the respective turbulent kinetic energy and turbulent dissipation rate Prandtl numbers. The turbulent viscosity is modelled as

$$\mu_t = \rho C_\mu \left( \frac{k^2}{\epsilon} \right) \quad (2.46)$$

where  $C_\mu = 0.09$  is a constant.

The  $k - \epsilon$  models are the most widely used turbulence models because of their ability to yield reasonable results for many industrial systems and because of their low computational cost [93]. Similar to the  $k - \epsilon$  model is the  $k - \omega$  model except that a transport equation is written for the specific dissipation rate  $\omega = k/\epsilon\beta^*$  instead of the turbulent dissipation rate  $\epsilon$ . For the  $k - \omega$  model, the eddy viscosity is written as a function of  $k$  and  $\omega$ . The standard  $k - \omega$  model accounts for low-Reynolds number effects, compressibility, and shear flow spreading.

### Reynolds stress model (RSM)

The two equations model from Boussinesq hypothesis assumes turbulence to be isotropic i.e. turbulence fluctuations are uniform throughout the fluid [95]. This assumption is an ideal one that cannot represent practical applications. The Reynolds stress model is a more sophisticated turbulence model that ignores the assumptions of isotropy [94]. The RSM is derived by averaging the product of the exact momentum equations of the fluctuations and the fluctuating velocities. The transport equation defining the Reynolds stress model is given by

$$\frac{\partial \tau_{ij}^R}{\partial t} + \frac{\partial \bar{u}_k \tau_{ij}^R}{\partial x_k} = P_{ij} - \Pi_{ij} - \epsilon_{ij} - D_{T,ijk} + D_{L,ijk} + \mu \nabla^2 \tau_{ij}^R \quad (2.47)$$

where,

$$\tau_{ij}^R = \overline{\rho u'_i u'_j} \quad (2.48a)$$

$$P_{ij} = -\left( \tau_{ik}^R \frac{\partial \bar{u}_j}{\partial x_k} + \tau_{jk}^R \frac{\partial \bar{u}_i}{\partial x_k} \right) \quad (2.48b)$$

$$\Pi_{ij} = p' \left( \frac{\partial \bar{u}'_j}{\partial x_i} + \frac{\partial \bar{u}'_i}{\partial x_j} \right) \quad (2.48c)$$

$$\epsilon_{ij} = 2\mu \frac{\partial \bar{u}_i}{\partial x_k} \frac{\partial \bar{u}'_j}{\partial x_k} \quad (2.48d)$$

$$D_{T,ijk} = \frac{\partial}{\partial x_k} (\overline{\rho u'_i u'_j u'_k} + \overline{p' u'_i} \delta_{jk} + \overline{p' u'_j} \delta_{ik}) \quad (2.48e)$$

$$D_{L,ijk} = \frac{\partial}{\partial x_k} \left[ \mu \frac{\partial}{\partial x_k} (\overline{u'_i u'_j}) \right] \quad (2.48f)$$

- $\tau_{ij}^R$  is the Reynolds stress
- $P_{ij}$  is the production of turbulent kinetic energy
- $\Pi_{ij}$  is the pressure-strain term
- $\epsilon_{ij}$  is the dissipation-rate term
- $D_{T,ijk}$  is the turbulent diffusion term
- $D_{L,ijk}$  is the molecular diffusion term
- $\frac{\partial \bar{u}_k \tau_{ij}^R}{\partial x_k}$  is the convection term

It can be seen that extra unknowns have been generated by taking the second-moment of the Reynolds stress i.e the turbulent diffusion, pressure-strain, and dissipation terms. These unknowns need to be modelled in order to close the equation. Models by Daly and Harlow [96][97], Gibson and Launder [98][99], and Sarkar and Balakrishnan [100] are examples of some adopted for the turbulent diffusion, pressure-strain, and dissipation terms respectively.

### 2. 5.3 Multiphase flow modelling

Multiphase flows contain more than one phase. These types of flows are common in minerals and oil sands processing. Typical multiphase flow can either be 2 phase i.e. gas-liquid,

liquid-liquid, liquid-solid, gas-solid, or 3 phase i.e. gas-liquid-solid, gas-liquid-liquid, liquid-liquid-solid [5, 8, 93, 101–103]. Usually, for multiphase flows, there is a carrier or continuous fluid phase (liquid or gas) and a discrete or dispersed phase (gas, liquid or solid). Multiphase flow presents several industrial challenges such as gas hydrate formation, sand blockage, and erosion wear. It is therefore, important to model these flows to be able to operate and design high-performance industrial system. Computational Fluid Dynamics (CFD) is a powerful tool for modelling multiphase flow systems. To apply CFD, the multiphase flow must first be identified e.g. slurry flow, free surface or pneumatic transport [36, 93, 103–108]. This is then followed by the selection of an appropriate model to represent the physics of the system. The three multiphase modelling methods employed for the studies in this thesis are described below.

### Volume-of-Fluid (VOF) model

The VOF model is most suited for solving two or more immiscible fluid phases e.g. free surface flow or flow with definite interface such as filling of a tank, draining of a vessel or the flow of liquid in an open channel [108]. A single set of momentum equations is solved for all the phases while the volume fraction of each phase is tracked throughout the entire fluid domain [8, 93, 101]. The volume fraction of all phases present in the fluid domain must sum to unity. Depending on the volume fraction, the properties and variables in a given control volume or cell can be representative of a phase or a mixture of the phases. This means for a given phase  $k$ , a volume fraction of  $\alpha_k = 1$  indicates that the variables and properties are representative of the phase  $k$ . If  $\alpha_k = 0$ , the properties have no contribution from the phase  $k$ . For  $0 < \alpha_k < 1$ , the properties are a blend of phase  $k$  and one or more of the other phases present in the cell. The VOF is often solved as a transient problem, however, a steady state solution can be performed for certain cases where the solution is independent of the initial conditions [93]. For the VOF, a continuity equation is solved for the volume fraction of each of the phases present except that of the primary phase. The continuity equation is given by

$$\frac{1}{\rho_i} \left[ \frac{\partial}{\partial t} (\alpha_i \rho_i) + \nabla \cdot (\alpha_i \rho_i \vec{v}_i) \right] = S_{\alpha_i} + \sum_{i=1}^n (\dot{m}_{ij} - \dot{m}_{ji}) \quad (2.49)$$

where  $\dot{m}_{ji}$  and  $\dot{m}_{ij}$  are the mass transfer rate between the phases and  $S_{\alpha_i}$  is a user-defined mass source term often set to zero. The volume fraction of the primary phase is obtained

from

$$\sum_{i=1}^n \alpha_i = 1 \quad (2.50)$$

The single momentum equation solved for the fluid domain is given by

$$\frac{\partial}{\partial t}(\rho \vec{u}) + \nabla \cdot (\rho \vec{u} \vec{u}) = -\nabla p + \nabla \cdot [\mu(\nabla \vec{u} + \nabla \vec{u}^T)] + \rho \vec{g} + \vec{F} \quad (2.51)$$

where the fluid properties

$$\rho = \sum_{i=1}^n \alpha_i \rho_i \quad (2.52)$$

and

$$\mu = \sum_{i=1}^n \alpha_i \mu_i \quad (2.53)$$

The terms  $\rho \vec{g}$  and  $\vec{F}$  represents gravity and external body forces respectively.

### Eulerian-Eulerian model

The Eulerian-Eulerian (E-E) model is a multiphase flow model that treats each phase in the fluid domain as interacting continua, whether solid, liquid, or gas. The E-E modelling method is very powerful and the number of phases that can be modelled is only limited by the computational capacity (memory) and the convergence stability [93]. Each Eulerian phase being modelled has a separate momentum (Navier-Stokes) equation and boundary condition [101, 109]. For phase  $i = 1 : n$ , the momentum equation is given by

$$\frac{\partial(\alpha_i \rho_i \vec{u}_i)}{\partial t} - \nabla \cdot (\alpha_i \rho_i \vec{u}_i \vec{u}_i) = -\alpha_i \nabla P + \alpha_i \rho_i \vec{g} + \nabla \cdot (\alpha_i \tau_i) + \vec{F}_{km} \quad (2.54)$$

where  $\vec{F}_{km}$  is the sum of all interphasial forces such as drag force, lift force, turbulent dispersion force, wall lubrication force, and virtual mass force [101].

The Eulerian approach has a special treatment for modelling particulate phase (Granular modelling) by calculating a granular temperature based on the solids fluctuating energy and a solid phase shear and bulk viscosity by applying the kinetic theory. This method was first proposed for gas-solid systems like the fluidized bed [110, 111] but has been applied to liquid-solids systems as well [89, 107]. Basically, the Eulerian-Granular approach extends

the Navier-Stokes equation to account for inter-particle collision and friction, while setting a maximum packing fraction limit for the particles. For a solid phase  $i = s$  interacting with a fluid phase  $i = l$ , the momentum equation for the granular phase can be written as

$$\frac{\partial(\alpha_s \rho_s \vec{u}_s)}{\partial t} - \nabla \cdot (\alpha_s \rho_s \vec{u}_s \vec{u}_s) = -\alpha_s \nabla P + \alpha_s \rho_s \vec{g} + \nabla \cdot (\alpha_s \tau_s) + \vec{F}_{km} \quad (2.55)$$

where the stress tensor,  $\tau_s$ , for the solids in the viscous force term has been modified to include a granular pressure and is defined by

$$\tau_s = (-P_s + \lambda_s \nabla \cdot \vec{u}_s) \mathbf{I} + \mu_s \{ [\nabla \vec{u}_s + (\nabla \vec{u}_s)^T] - \frac{2}{3} (\nabla \cdot \vec{u}_s) \mathbf{I} \} \quad (2.56)$$

where  $\lambda_s$  is the bulk solids viscosity. The granular pressure term introduced is defined by

$$P_s = \alpha_s \rho_s \Theta_s + 2\rho_s (1 + e_s) \alpha_s^2 g_o \Theta_s \quad (2.57)$$

The granular temperature  $\Theta_s$  is determined by an algebraic expression or by solving a transport equation given by

$$\frac{3}{2} \left[ \frac{\partial(\alpha_s \rho_s \Theta_s)}{\partial t} - \nabla \cdot (\alpha_s \rho_s \vec{u}_s \Theta_s) \right] = \tau_s \nabla \vec{u}_s + \nabla \cdot (k_s \nabla \Theta_s) - \gamma_s + \Omega_{fs} \quad (2.58)$$

where  $\gamma_s$  is the collisional dissipation energy and  $\Omega_{fs}$  is the transfer of kinetic energy from the fluctuation velocity of the solids to the fluid [89, 107, 112].

The Eulerian-Eulerian model cannot track individual particle motion in the flow but provides average values of local particle concentration and velocity. This limits the use of the Eulerian-Eulerian modelling for making calculations such as solid particle erosion. There are, however, recent methods developed to adapt the method for erosion modelling but is still subject to further development [113–115]. The E-E approach is also suitable for medium to high concentration solids systems, and where two-way fluid-particle or particle-surface coupling is important [101].

### Eulerian-Lagrangian model

The Eulerian-Lagrangian approach is a discrete phase modelling method particularly suitable for calculating individual particle, bubble, or droplet trajectories in a continuous fluid domain [93, 101]. The continuous phase is modelled via the Eulerian approach by solving the Navier-

Stokes momentum equation while the particle motion is modelled via a force balance based on Newton's second law. This is given by

$$\frac{d\vec{u}_p}{dt} = F_D(\vec{u} - \vec{u}_p) + \left(1 - \frac{\rho}{\rho_p}\right)\vec{g} + \vec{F} \quad (2.59)$$

$$\frac{d\vec{x}_p}{dt} = \vec{u}_p \quad (2.60)$$

where  $\vec{F}$  is an acceleration term that accounts for forces such as lift, virtual mass, and particle rotation [116–118]. The drag force per unit mass,  $F_D$ , is defined as

$$F_D = \left(\frac{18\mu}{\rho_p d_p^2}\right) \left(\frac{C_D Re}{24}\right) \quad (2.61)$$

where

$$Re = \frac{\rho d_p |\vec{u} - \vec{u}_p|}{\mu} \quad (2.62)$$

The drag coefficient  $C_D$  can be determined using correlations like that of Morsi and Alexander [119, 120]. The Eulerian-Lagrangian model can easily be applied when particle-particle interactions are negligible i.e. conditions where the particle phase concentration is very low and there is one-way coupling. This means that only the influence of the fluid turbulence on the particles is considered. Also, because details of position and velocity of individual particles can be obtained, the Eulerian-Lagrangian method is suitable for making solid particle erosion calculations.

## 2. 5.4 Implementation of erosion models in CFD

The erosion process is a local phenomenon, therefore, most solid particle erosion (SPE) models presented earlier in Section 2. 3 inputs local instantaneous particle impact velocity and particle impact angle as the primary wear-influencing variables. These models, when implemented in CFD analysis, provide detailed information such as the location of the erosion hot spots i.e. point of maximum wear, and the wear map or distribution. Fluid turbulence effects on the particles as well as the effects of a complex geometry can be modelled through CFD. The erosion models alone cannot provide such information. The Eulerian-Lagrangian modelling method is at the moment, the most suitable method for calculating erosion in

CFD [104, 105, 121]. The Eulerian treatment applied to the continuous carrier-fluid phase models the fluid turbulence and velocity distributions. The Lagrangian approach tracks discrete particles, and provides the inputs needed for the erosion models i.e. particle impact angle and impact velocity. There are a few recent numerical studies that have implemented Eulerian-Eulerian multi-fluid models for erosion prediction [113–115]. Messa et al. [113] used an approach in which the Lagrangian method is applied to the cell adjacent to the wall while the rest of the fluid domain is modelled using the Eulerian approach. Further improvement of the work through a repeated calculation of particle trajectories near the wall and a continuous update of the wear map was also carried out [114]. Yu et al. [115] also used the multi-fluid approach to model erosion in a gas solid elbow. The particle impact angle and impact velocity were defined based on the average particle velocity and the instantaneous particle velocity obtained from solving a particle turbulence kinetic energy equation. Having to model solid particle turbulence, especially when based on the Reynolds stress model, can introduce computational cost. The need to simplify these approaches so that they can be used with basic two equation models and also implementable in commercial CFD codes should be pursued. Also, the E-E methods have only been validated for low concentration slurry jet and pneumatic transport flows, neither of which has not fulfilled the need for an E-E erosion modelling approach i.e. erosion prediction for medium to high solids concentration systems. Hence, further validations for generality of these approaches is still required.

It should be noted that the advantage of the Lagrangian method is still being applied to these hybrid techniques for predicting erosion [113, 114]. Another thing to note is that implementing CFD for erosion calculation requires that hydrodynamics is accurately modelled and validated. Hydrodynamics has a strong influence on the behaviour of the particle phase, and in turn, the the rate of erosion. Validating hydrodynamics parameters like concentration, velocity gradients or vectors is essential [115, 122]. This also means that wear experiments should not only include measuring the wear rate/profile but also these hydrodynamics parameters for comprehensive validation. The interaction of particles with the wall must also be modelled accurately e.g. particle-wall rebound, and wall roughness. These parameters affect both the erosion rate and the erosion distribution [36, 123]. In the research conducted in this PhD thesis, the Eulerian-Lagrangian approach was used extensively, especially for the investigations in Part II. Under-Defined Functions (UDFs) were written to extract particle trajectory information (impact angle, impact velocity) from the Lagrangian scheme. Analysis of these particle impact variables revealed the aforementioned hydrodynamic effects on the

erosion wear predictions. More details about these investigations are in Chapters 6 and 7.

## References

- [1] R. G. Gillies, C. A. Shook, Modelling high concentration slurry flows, *Can. J. Chem. Eng.* 78 (2000) 709–716. doi:[10.1002/cjce.5450780413](https://doi.org/10.1002/cjce.5450780413).
- [2] B. Fotty, M. Krantz, J. Been, J. Wolodko, Development of a pilot-scale facility for evaluating wear in slurry pipeline systems, in: *Proc. Hydrotransp.* 18, September, Rio de Janeiro, Brazil, 2010, pp. 431–443.
- [3] R. J. K. Wood, The sand erosion performance of coatings, *Mater. Des.* 20 (1999) 179–191. URL: [http://dx.doi.org/10.1016/S0261-3069\(99\)00024-2](http://dx.doi.org/10.1016/S0261-3069(99)00024-2). doi:[10.1016/S0261-3069\(99\)00024-2](https://doi.org/10.1016/S0261-3069(99)00024-2).
- [4] A. Bartosik, Influence of coarse-dispersive solid phase on the particles-wall shear stress in turbulent slurry flow with high solid concentration, *Arch. Mech. Eng.* LVII (2010) 1–16. URL: <http://yadda.icm.edu.pl/baztech/element/bwmeta1.element.baztech-article-BOS5-0024-0071>. doi:[10.2478/v10180-010-0003-1](https://doi.org/10.2478/v10180-010-0003-1).
- [5] A. Bragg, Development of the PDF kinetic approach for modelling inertial particle dispersion in turbulent boundary layers, Phd thesis, University of Nottingham Upon Tyne, 2011.
- [6] M. Parsi, K. Najmi, F. Najafifard, S. Hassani, B. S. McLaury, S. A. Shirazi, A comprehensive review of solid particle erosion modeling for oil and gas wells and pipelines applications, *J. Nat. Gas Sci. Eng.* 21 (2014) 850–873. doi:[10.1016/j.jngse.2014.10.001](https://doi.org/10.1016/j.jngse.2014.10.001).
- [7] A. Sadighian, Investigating Key Parameters Affecting Slurry Pipeline Erosion, Ph.D. thesis, University of Alberta, 2016. doi:[10.1017/CB09781107415324.004](https://doi.org/10.1017/CB09781107415324.004). [arXiv:arXiv:1011.1669v3](https://arxiv.org/abs/1011.1669v3).
- [8] D. Besnard, F. Harlow, Turbulence in multiphase flow, *Int. J. Multiph. Flow* 14 (1988) 679–699. doi:[10.1016/0301-9322\(88\)90068-7](https://doi.org/10.1016/0301-9322(88)90068-7).

- [9] R. G. Gillies, C. A. Shook, K. C. Wilson, An improved two layer model for horizontal slurry pipeline flow, *Can. J. Chem. Eng.* 69 (1991) 173–178. URL: <http://doi.wiley.com/10.1002/cjce.5450690120>. doi:10.1002/cjce.5450690120.
- [10] R. G. Gillies, C. A. Shook, J. Xu, Modelling Heterogeneous Slurry Flows at High Velocities, *Can. J. Chem. Eng.* 82 (2004) 1060–1065. doi:10.1002/cjce.5450820523.
- [11] M. Rhodes, *Introduction to Particle Technology*, second ed., John Wiley & Sons, Ltd., West Sussex, England, 2008. URL: <https://books.google.ca/books?id=P9Qgvh7kMP8C>.
- [12] R. S. Sanders, *Fluid-Particle Systems and Application: Lecture notes*, Technical Report, University of Alberta, Edmonton, Alberta, Canada, 2015.
- [13] C. A. Shook, M. C. Roco, *Slurry flow: principles and practise*, Butterworth-Heinemann, Boston, USA, 1991. doi:<http://dx.doi.org/10.1016/B978-0-7506-9110-9.50007-4>.
- [14] R. B. Spelay, S. A. Hashemi, R. G. Gillies, R. Hegde, R. S. Sanders, D. G. Gillies, Governing Friction Loss Mechanisms and the Importance of Off-Line Characterisation Test in the Pipeline Transport of Dense Coarse-Particle Slurries, in: *ASME 2013 Fluids Eng. Div. Summer Meet.*, 2013, pp. V01CT20A013–V01CT20A013.
- [15] R. B. Spelay, R. G. Gillies, S. A. Hashemi, R. S. Sanders, Effect of pipe inclination on the deposition velocity of settling slurries, *Can. J. Chem. Eng.* 94 (2016) 1032–1039. doi:10.1002/cjce.22493.
- [16] R. G. Gillies, K. B. Hill, M. J. McKibben, C. A. Shook, Solids transport by laminar Newtonian flows, *Powder Technol.* 104 (1999) 269–277. doi:10.1016/S0032-5910(99)00104-7.
- [17] K. C. Wilson, R. R. Horsley, T. Kealy, Direct prediction of fall velocities in non-Newtonian materials, *Int. J. Miner. Process.* 71 (2003) 17–30. doi:10.1016/S0301-7516(03)00027-9.
- [18] K. C. Wilson, R. S. Sanders, R. G. Gillies, C. A. Shook, Verification of the near-wall model for slurry flow, *Powder Technol.* 197 (2010) 247–253. URL: <http://dx.doi.org/10.1016/j.powtec.2009.09.023>. doi:10.1016/j.powtec.2009.09.023.

- [19] J. Schaan, N. Cook, R. S. Sanders, On-line wear measurement for commercial-scale, coarse-particle slurry pipelines, in: 17th Int. Conf. Hydrotransp., Cape Town, South Africa, 2007, pp. 291–300.
- [20] P. Swamee, A. K. Jain, Explicit equations for pipe-flow problems, *ASCE J Hydraul Div* 102 (1976) 657–664.
- [21] S. W. Churchill, Friction factor equation spans all fluid flow regimes, *Chem. Eng. (New York)* 84 (1977) 91–92. URL: <https://www.scopus.com/inward/record.uri?eid=2-s2.0-0017769439{&}partnerID=40{&}md5=a878a518cf62db283094ff25416026fd>.
- [22] C. A. Shook, R. G. Gillies, R. S. Sanders, Pipeline hydrotransport: with applications in oil sand industry, SRC Pipe Flow Technology Centre, Saskatoon, Canada, 2002.
- [23] X. Song, Z. Xu, G. Li, Z. Pang, Z. Zhu, A new model for predicting drag coefficient and settling velocity of spherical and non-spherical particle in Newtonian fluid, *Powder Technol.* 321 (2017) 242–250. URL: <http://dx.doi.org/10.1016/j.powtec.2017.08.017>. doi:10.1016/j.powtec.2017.08.017.
- [24] A. Terfous, A. Hazzab, A. Ghenaim, Predicting the drag coefficient and settling velocity of spherical particles, *Powder Technol.* 239 (2013) 12–20. URL: <http://dx.doi.org/10.1016/j.powtec.2013.01.052>. doi:10.1016/j.powtec.2013.01.052.
- [25] R. G. Gillies, J. Schaan, R. J. Sumner, M. J. McKibben, C. A. Shook, Deposition velocities for newtonian slurries in turbulent flow, *Can. J. Chem. Eng.* 78 (2000) 704–708. URL: <http://doi.wiley.com/10.1002/cjce.5450780412>. doi:10.1002/cjce.5450780412.
- [26] G. Messa, S. Malavasi, Improvements in the numerical prediction of fully-suspended slurry flow in horizontal pipes, *Powder Technol.* 270 (2015) 358–367. URL: <http://dx.doi.org/10.1016/j.powtec.2014.10.027>. doi:10.1016/j.powtec.2014.10.027.
- [27] P. Doron, D. Barnea, Pressure drop and limit deposit velocity for solid-liquid flow in pipes, *Chem. Eng. Sci.* 50 (1995) 1595–1604. doi:10.1016/0009-2509(95)00024-Y.
- [28] A. D. Thomas, Predicting the deposit velocity for horizontal turbulent pipe flow of slurries, *Int. J. Multiph. Flow* 5 (1979) 113–129. doi:10.1016/0301-9322(79)90040-5.

- [29] R. S. Sanders, R. Sun, R. G. Gillies, M. J. McKibben, C. Litzberger, C. A. Shook, Deposition velocities for particles of intermediate size in turbulent flow, in: *Hydrotransport*, volume 16, 2004, pp. 429–442.
- [30] K. C. Wilson, G. R. Addie, A. Sellgren, R. Clift, *Slurry Transport Using Centrifugal Pumps*, Springer ebook collection / Chemistry and Materials Science 2005-2008, Springer US, 2008. URL: <https://books.google.ca/books?id=YNEMPnBt-M0C>.
- [31] B. Bbosa, E. DelleCase, M. Volk, E. Ozbayoglu, A comprehensive deposition velocity model for slurry transport in horizontal pipelines, *J. Pet. Explor. Prod. Technol.* (2016). URL: <http://link.springer.com/10.1007/s13202-016-0259-1>. doi:10.1007/s13202-016-0259-1.
- [32] K. C. Wilson, J. K. P. Tse, Deposition limit for coarse particle transport in inclined pipes, in: *Proc. 9th Int. Conf. Hydraul. Transp. Solids Pipes*, 1984, pp. 149–161.
- [33] H. Hashimoto, K. Noda, T. Masuyama, T. Kawashima, Influence of pipe inclination on deposit velocity, in: *Proc. 7th Int. Conf. Hydraul. Transp. Solids Pipes*, 1980, pp. 231–244.
- [34] R. Durand, *Basic Relationships of the Transportation of Solids in Pipes-Experimental Research*, Intern. Assoc. Hydr. Res., 5th Congr. Minneapolis, 1953 (1953).
- [35] R. G. Gillies, *Pipeline Flow of Coarse Particle Slurries*, Ph.D. thesis, University of Saskatchewan, 1993.
- [36] O. E. Adedeji, W. Yu, R. S. Sanders, Analysis of local wear variables for high-precision erosion modelling in complex geometries, *Wear* 426-427 (2019) 562–569. doi:10.1016/j.wear.2018.12.071.
- [37] D. R. Lester, L. A. Graham, J. Wu, High precision suspension erosion modeling, *Wear* 269 (2010) 449–457. doi:10.1016/j.wear.2010.04.032.
- [38] A. Gnanavelu, N. Kapur, A. Neville, J. F. Flores, N. Ghorbani, A numerical investigation of a geometry independent integrated method to predict erosion rates in slurry erosion, *Wear* 271 (2011) 712–719. URL: <http://dx.doi.org/10.1016/j.wear.2010.12.040>. doi:10.1016/j.wear.2010.12.040.

- [39] H. C. Meng, K. C. Ludema, Wear models and predictive equations: their form and content, *Wear* 181-183 (1995) 443–457. doi:[10.1016/0043-1648\(95\)90158-2](https://doi.org/10.1016/0043-1648(95)90158-2).
- [40] I. Finnie, Erosion of surfaces by solid particles, *Wear* 3 (1960) 87–103. doi:[10.1016/0043-1648\(60\)90055-7](https://doi.org/10.1016/0043-1648(60)90055-7). arXiv:[arXiv:1011.1669v3](https://arxiv.org/abs/1011.1669v3).
- [41] I. Finnie, Some Observations on the Erosion of Ductile Metals, *Wear* 19 (1972) 81–90.
- [42] I. Finnie, D. H. McFadden, On the velocity dependence of the erosion of ductile metals by solid particles at low angles of incidence, *Wear* 48 (1978) 181–190. URL: <http://www.sciencedirect.com/science/article/pii/0043164878901473>. doi:[10.1016/0043-1648\(78\)90147-3](https://doi.org/10.1016/0043-1648(78)90147-3).
- [43] Y. I. Oka, M. Nishimura, K. Nagahashi, M. Matsumura, Control and evaluation of particle impact conditions in a sand erosion test facility, *Wear* 250 (2001) 736–743.
- [44] Y. I. Oka, K. Okamura, T. Yoshida, Practical estimation of erosion damage caused by solid particle impact Part 1 : Effects of impact parameters on a predictive equation, *Wear* 259 (2005) 95–101. doi:[10.1016/j.wear.2005.01.039](https://doi.org/10.1016/j.wear.2005.01.039).
- [45] Y. I. Oka, H. Ohnogi, T. Hosokawa, M. Matsumura, The impact angle dependence of erosion damage caused by solid particle impact, *Wear* 203 (1997) 573–579.
- [46] Y. Zhang, E. P. Reuterfors, B. S. McLaury, S. a. Shirazi, E. F. Rybicki, Comparison of computed and measured particle velocities and erosion in water and air flows, *Wear* 263 (2007) 330–338. doi:[10.1016/j.wear.2006.12.048](https://doi.org/10.1016/j.wear.2006.12.048).
- [47] M. C. Powers, A new roundness scale for sedimentary particles, *J. Sediment. Res.* 23 (1953) 117–119.
- [48] M. Parsi, D. N. V. Gl, H. Arabnejad, E/CRC, A. Al-sarkhi, K. Fahd, A New Correlation for Predicting Solid Particle Erosion Caused by Gas-Sand Flow in Elbows, in: *Offshore Technol. Conf.*, 2018.
- [49] DNV, Recommended Practise RP O501: Erosive Wear in Piping Systems, 2011.
- [50] DNV GL, Managing sand production and erosion, Technical Report August, 2015.

- [51] N. R. Sarker, L. Zhang, D. Breakey, B. A. Fleck, R. S. Sanders, Laboratory-Scale Erosive Wear Measurements Conducted with a Toroid Wear Tester (TWT), in: 8th Int. Conf. Transp. Sediment. Solid Part., September, 2017, pp. 295–303.
- [52] C. Huang, P. Minev, J. Luo, K. Nandakumar, A phenomenological model for erosion of material in a horizontal slurry pipeline flow, *Wear* 269 (2010) 190–196. URL: <http://dx.doi.org/10.1016/j.wear.2010.03.002>. doi:10.1016/j.wear.2010.03.002.
- [53] C. Huang, S. Chiovelli, P. Minev, J. Luo, K. Nandakumar, A comprehensive phenomenological model for erosion of materials in jet flow, *Powder Technol.* 187 (2008) 273–279. URL: <http://dx.doi.org/10.1016/j.powtec.2008.03.003>. doi:10.1016/j.powtec.2008.03.003.
- [54] J. G. A. Bitter, A study of erosion phenomena part II, *Wear* 6 (1963) 169–190.
- [55] I. M. Hutchings, A model for the erosion of metals by spherical particles at normal incidence, *Wear* 70 (1981) 269–281.
- [56] R. Gupta, S. N. Singh, V. Sehadri, Prediction of uneven wear in a slurry pipeline on the basis of measurements in a pot tester, *Wear* 184 (1995) 169–178. doi:10.1016/0043-1648(94)06566-7.
- [57] P. Goosen, I. Malgas, An Experimental Investigation into Aspects of Wear in Boiler Ash Disposal Pipelines, in: Proc. Hydrotransp. 14, September, Maastricht, The Netherlands, 1999, pp. 8–10.
- [58] R. Jami, Investigation Using Polymer Additives to Mitigate Erosion in Multiphase Turbulent Pipe Flow, Master's thesis, University of Alberta, 2019.
- [59] M. Melissa J., Wall Erosion in Slurry Pipelines, Phd, University of Saskatchewan, 1992.
- [60] H. M. Clark, L. C. Burmeister, The influence of the squeeze film on particle impact velocities in erosion, *Int. J. Impact Eng.* 12 (1992) 415–426. doi:10.1016/0734-743X(92)90156-N.
- [61] N. R. Sarker, A Preliminary Study of Slurry Pipeline Erosion Using a Toroid Wear Tester, MSc thesis, University of Alberta, 2016.

- [62] L. Zhang, Relating slurry friction to erosion rate using a toroid wear tester, MSc thesis, University of Alberta, 2018.
- [63] R. Cooke, G. Johnson, P. Goosen, Laboratory Apparatus for Evaluating Slurry Pipeline Wear, Technical Report March, SAIT Seminar, Calgary, 2000.
- [64] A. Gnanavelu, N. Kapur, A. Neville, J. F. Flores, An integrated methodology for predicting material wear rates due to erosion, *Wear* 267 (2009) 1935–1944. URL: <http://linkinghub.elsevier.com/retrieve/pii/S0043164809003986>. doi:10.1016/j.wear.2009.05.001.
- [65] J. B. Zu, I. M. Ihtchings, G. T. Burstein, Design of a slurry erosion test rig, *Wear* 140 (1990) 331–344.
- [66] R. J. K. Wood, D. W. Wheeler, Design and performance of a high velocity air – sand jet impingement erosion facility, *Wear* 220 (1998) 95–112.
- [67] M. T. Benchaita, P. Griffith, E. Rabinowicz, Erosion of metallic plate by solid particles entrained in a liquid jet, *J. Eng. Ind.* 105 (1983) 215–222.
- [68] V. Javaheri, D. Porter, V.-t. Kuokkala, Slurry erosion of steel – Review of tests , mechanisms and materials, *Wear* 409 (2018) 248–273. doi:10.1016/j.wear.2018.05.010.
- [69] A. Mansouri, S. A. Shirazi, B. S. Mclaury, FEDSM2014-21613 (2014) 1–10.
- [70] A. Mansouri, H. Arabnejad, S. A. Shirazi, B. S. Mclaury, A combined CFD / experimental methodology for erosion prediction, *Wear* 333 (2015) 1090–1097. URL: <http://dx.doi.org/10.1016/j.wear.2014.11.025>. doi:10.1016/j.wear.2014.11.025.
- [71] A. Mansouri, A combined CFD-experimental method for developing an erosion equation for both gas-sand and liquid-sand flows, Phd thesis, University of Tulsa, 2016.
- [72] S. Karimi, A. Mansouri, B. S. Mclaury, S. A. Shirazi, Emperimental investigation oon the influence of particle size in a submerged slurry jet on erosion rates and pattermns, in: Proc. ASME 2017 Fluids Eng. Div. Summer Meet., Hawaii, USA, 2019, pp. 1–11.

- [73] S. Karimi, S. Shirazi, B. Mclaury, Effects of Fluid Viscosity and Impingement Angle on Submerged Jet Flowfields, in: Proc. ASME 2018 Fluids Eng. Div. Summer Meet., September, 2018, p. 83251. doi:[10.1115/FEDSM2018-83251](https://doi.org/10.1115/FEDSM2018-83251).
- [74] J. Owen, C. Ramsey, R. Barker, A. Neville, Erosion-corrosion interactions of X65 carbon steel in aqueous CO<sub>2</sub> environments, *Wear* 414-415 (2018) 376–389. URL: <https://doi.org/10.1016/j.wear.2018.09.004>. doi:[10.1016/j.wear.2018.09.004](https://doi.org/10.1016/j.wear.2018.09.004).
- [75] A. Neville, C. Wang, Erosion – corrosion mitigation by corrosion inhibitors — An assessment of mechanisms, *Wear* 267 (2009) 195–203. doi:[10.1016/j.wear.2009.01.038](https://doi.org/10.1016/j.wear.2009.01.038).
- [76] R. G. Gillies, R. Sun, M. Kosor, C. A. Shook, Laboratory Investigation of Inversion of Heavy Oil Emulsion, *Can. J. Chem. Eng.* 78 (2000) 757–763.
- [77] O. Urdahl, A. O. Fredheim, K. P. Loken, Viscosity measurements of water-in-crude-oil emulsions under flowing conditions: A theoretical and practical approach, *Colloids Surfaces A Physicochem. Eng. Asp.* 123-124 (1997) 623–634. doi:[10.1016/S0927-7757\(96\)03801-0](https://doi.org/10.1016/S0927-7757(96)03801-0).
- [78] E. E. Johnsen, H. Fordedal, O. Urdahl, A simplified experimental approach for measuring viscosity for water-in-crude-oil emulsions under flowing conditions, *J. Dispers. Sci. Technol.* 22 (2001) 33–39.
- [79] S. T. Johansen, S. Mo, E. Meese, J. E. S. Oliveira, J. F. R. Reyes, J. N. E. Carneiro, CFD Simulations of Multiphase Flows Containing Large Scale Interfaces and Dispersed Phases with Selected Production Technology Applications, OTC Bras. (2015). URL: <http://www.onepetro.org/doi/10.4043/26303-MS>. doi:[10.4043/26303-MS](https://doi.org/10.4043/26303-MS).
- [80] N. R. Sarker, M. A. Islam, R. S. Sanders, B. A. Fleck, CFD Analysis of the Hydrodynamics of an Air- Water Multiphase System in a Rotating Toroid Wheel, in: 23rd Annu. Conf. CFD Soc. Canada, April, Waterloo, ON, Canada, 2016.
- [81] R. C. Worster, D. F. Denny, Hydraulic transport of solid material in pipes, *Proc. Inst. Mech. Eng.* 169 (1955) 563–586.
- [82] V. V. Traynis, Parameters and flow regimes for hydraulic transport of coal by pipelines, Terraspace, Rockville. USA, 1977.

- [83] G. Henday, A comparison of commercial pipe materials intended for the hydraulic transport of solids, BHRA, 1988.
- [84] N. R. Sarker, D. E. S. Breakey, M. A. Islam, S. Sun, B. A. Fleck, R. S. Sanders, Performance and Hydrodynamics Analysis of a Toroid Wear Tester to Predict Erosion in Slurry Pipelines, *Wear* (2019) 203068. URL: <https://doi.org/10.1016/j.wear.2019.203068>. doi:10.1016/j.wear.2019.203068.
- [85] J. Blazek, Computational fluid dynamics: principles and applications, Elsevier publishing, 2001.
- [86] C. D. Rielly, J. Gimbut, Computational fluid mixing, in: *Food Mix.*, Blackwell Publishing Ltd., Oxford, UK, 2009, pp. 125–174.
- [87] O. E. Adedeji, Computational fluid dynamics modelling of a left ventricular assist device, Msc, Loughborough University, 2014.
- [88] C. A. J. Fletcher, Computational techniques for fluid dynamics 1 (1988).
- [89] A. Ekambara, R. S. Sanders, K. Nandakumar, J. H. Masliyah, Hydrodynamic simulation of horizontal slurry pipeline flow using ANSYS-CFX, *Ind. Eng. Chem. Res.* 48 (2009) 8159–8171. doi:10.1021/ie801505z.
- [90] R. B. Bird, W. E. Stewart, E. N. Lightfoot, *Transport phenomena*. 1960, Madison, USA (1960).
- [91] H. K. Versteeg, W. Malalasekera, *Computational fluid dynamics, finite Vol. method* (1995).
- [92] A. Sayma, *Computational Fluid Dynamics*, 2009.
- [93] ANSYS, ANSYS 17.0 Theory Guide, Technical Report, 2017. URL: <https://www.sharcnet.ca/Software/Ansys/17.0/en-us/help/flu{ }th/flu{ }th.html>.
- [94] S. B. Pope, *Turbulent Flows*, Cambridge University Press, 2000. URL: <https://books.google.ca/books?id=HZsTw9SMx-0C>.

- [95] D. Choudhury, Introduction to the Renormalization Group Method and Turbulence Modeling, Technical memorandum, Fluent Incorporated, 1973. URL: <https://books.google.ca/books?id=mKWEQwAACAAJ>.
- [96] B. J. Daly, F. H. Harlow, Transport equations in turbulence, *Phys. Fluids* 13 (1970) 2634–2649.
- [97] F.-S. Lien, M. A. Leschziner, Assessment of turbulence-transport models including non-linear RNG eddy-viscosity formulation and second-moment closure for flow over a backward-facing step, *Comput. Fluids* 23 (1994) 983–1004.
- [98] M. M. Gibson, B. E. Launder, Ground effects on pressure fluctuations in the atmospheric boundary layer, *J. Fluid Mech.* 86 (1978) 491–511.
- [99] B. E. Launder, Second-moment closure and its use in modelling turbulent industrial flows, *Int. J. Numer. Methods Fluids* 9 (1989) 963–985.
- [100] S. Sarkar, L. Balakrishnan, Application of a Reynolds stress turbulence model to the compressible shear layer, in: 21st Fluid Dyn. Plasma Dyn. Lasers Conf., 1990, p. 1465.
- [101] G. H. Yeoh, J. Tu, Computational techniques for multiphase flows, Elsevier, 2009.
- [102] F. N. Krampa, Two-Fluid Modelling of Heterogeneous Coarse Particles Slurry Flow, Ph.D. thesis, University of Saskatchewan, 2009. doi:10.1017/CB09781107415324.004. [arXiv:arXiv:1011.1669v3](https://arxiv.org/abs/1011.1669v3).
- [103] A. Abdulla, Estimating Erosion in Oil and Gas Pipeline due to Sand Presence, Msc, Blekinge Institute of Technology, Sweden, 2011.
- [104] R. Silva, F. A. P. Garcia, P. Faia, M. G. Rasteiro, Modelling Solid-Liquid Homogeneous Turbulent Flow of Neutrally Buoyant Particles using Mixture Model : A Study of Length scale and Closure Coefficients, *Multiph. Sci. Technol.* 26 (2014) 199–227.
- [105] G. J. Brown, Erosion prediction in slurry pipeline tee-junctions, *Appl. Math. Model.* 26 (2002) 155–170. URL: <http://www.sciencedirect.com/science/article/pii/S0307904X01000531>. doi:10.1016/S0307-904X(01)00053-1.

- [106] A. Vié, H. Pouransari, R. Zamansky, A. Mani, Particle-laden flows forced by the disperse phase: Comparison between Lagrangian and Eulerian simulations, *Int. J. Multiph. Flow* 79 (2016) 144–158. doi:[10.1016/j.ijmultiphaseflow.2015.10.010](https://doi.org/10.1016/j.ijmultiphaseflow.2015.10.010).
- [107] D. R. Kaushal, T. Thinglas, Y. Tomita, S. Kuchii, H. Tsukamoto, CFD modeling for pipeline flow of fine particles at high concentration, *Int. J. Multiph. Flow* 43 (2012) 85–100. URL: <http://dx.doi.org/10.1016/j.ijmultiphaseflow.2012.03.005>. doi:[10.1016/j.ijmultiphaseflow.2012.03.005](https://doi.org/10.1016/j.ijmultiphaseflow.2012.03.005).
- [108] C. M. Perez, *CFD Modelling of Laminar, Open-Channel Flows of Non-Newtonian Slurries*, Msc, University of Alberta, 2017.
- [109] F. Pourahmadi, J. A. C. Humphrey, Modelling solid-fluid turbulent flows with application to predicting erosive wear, *Math. Model.* 6 (1985) 82 –. URL: <http://www.sciencedirect.com/science/article/pii/0270025585900296>. doi:[http://dx.doi.org/10.1016/0270-0255\(85\)90029-6](http://dx.doi.org/10.1016/0270-0255(85)90029-6).
- [110] C. K. K. Lun, S. B. Savage, D. J. Jeffrey, N. Chepurnyi, Kinetic theories for granular flow: inelastic particles in Couette flow and slightly inelastic particles in a general flowfield, *J. Fluid Mech.* 140 (1984) 223–256.
- [111] D. Gidaspow, R. Bezburuah, J. Ding, Hydrodynamics of circulating fluidized beds: kinetic theory approach, in: *7th Int. Conf. Fluid.*, Illinois Inst. of Tech., Chicago, IL (United States). Dept. of Chemical Engineering, Gold Coast, Australia, 1991.
- [112] L. Chen, Y. Duan, W. Pu, C. Zhao, CFD simulation of coal-water slurry flowing in horizontal pipelines, *Korean J. Chem. Eng.* 26 (2009) 1144–1154. doi:[10.1007/s11814-009-0190-y](https://doi.org/10.1007/s11814-009-0190-y).
- [113] G. V. Messa, G. Ferrarese, S. Malavasi, A mixed Euler-Euler/Euler-Lagrange approach to erosion prediction, *Wear* 342-343 (2015) 138–153. URL: <http://dx.doi.org/10.1016/j.wear.2015.08.015>. doi:[10.1016/j.wear.2015.08.015](https://doi.org/10.1016/j.wear.2015.08.015).
- [114] G. V. Messa, S. Malavasi, A CFD-based method for slurry erosion prediction, *Wear* 398-399 (2018) 127–145. URL: <https://doi.org/10.1016/j.wear.2017.11.025>. doi:[10.1016/j.wear.2017.11.025](https://doi.org/10.1016/j.wear.2017.11.025).

- [115] W. Yu, P. Fede, E. Climent, S. Sanders, Multi-fluid approach for the numerical prediction of wall erosion in an elbow, *Powder Technol.* 354 (2019) 561–583. URL: <http://www.sciencedirect.com/science/article/pii/S0032591019304504>. doi:<https://doi.org/10.1016/j.powtec.2019.06.007>.
- [116] G. P. Saffman, The Lift on a Small Sphere in a Slow Shear, *J. Fluid Mech.* 22 (1965) 385–400.
- [117] A. Li, G. Ahmadi, Dispersion and Deposition of Spherical Particles from Point Sources in a Turbulent Channel Flow, *Aerosol Sci. Technol.* 16 (1992) 209–226.
- [118] B. Oesterlé, T. Bui Dinh, Experiments on the Lift of a Spinning Sphere in the Range of Intermediate Reynolds Numbers, *Exp. Fluids* 25 (1998) 16–22.
- [119] S. A. Morsi, A. J. Alexander, An Investigation of Particle Trajectories in Two-Phase Flow Systems, *J. Fluid Mech.* 55 (1972) 193–208.
- [120] E. K. Vakkilainen, M. Garcia Perez, T. Happanen, A brief overview of the drag laws used in the Lagrangian tracking of ash trajectories for boiler fouling CFD models, in: 26th Int. Conf. Impact Fuel Qual. Power Prod., September, Prague, 2016.
- [121] X. Chen, B. S. McLaury, S. A. Shirazi, Application and experimental validation of a computational fluid dynamics (CFD)-based erosion prediction model in elbows and plugged tees, *Comput. Fluids* 33 (2004) 1251–1272. doi:[10.1016/j.compfluid.2004.02.003](https://doi.org/10.1016/j.compfluid.2004.02.003).
- [122] C. A. R. Duarte, F. J. de Souza, R. V. Salvo, V. F. dos Santos, The role of inter-particle collisions on elbow erosion, *Int. J. Multiph. Flow* 89 (2017) 1–22. doi:[10.1016/j.ijmultiphaseflow.2016.10.001](https://doi.org/10.1016/j.ijmultiphaseflow.2016.10.001).
- [123] C. B. Solnordal, C. Y. Wong, J. Boulanger, An experimental and numerical analysis of erosion caused by sand pneumatically conveyed through a standard pipe elbow, *Wear* 336-337 (2015) 43–57. URL: <http://dx.doi.org/10.1016/j.wear.2015.04.017>. doi:[10.1016/j.wear.2015.04.017](https://doi.org/10.1016/j.wear.2015.04.017).

## **Part I**

# **Developing a bench-scale wear testing device known as the toroid wear tester (TWT) as a slurry pipeline prediction tool**

Chapter 3

# Characterization of the flow field in a Toroid Wear Tester

A part of this Chapter has been submitted as

*Oluwaseun E. Adedeji, Lisheng Zhang, Nitish R. Sarker, David E.S. Breakey, R.  
Sean Sanders, Characterization of the flow field in a Toroid Wear Tester*

to the Canadian Journal of Chemical Engineering. Some of this material was presented at the 67th Canadian Chemical Engineering Conference in Edmonton, AB, Canada, 23-25 October, 2017.

## **Abstract**

The Toroid Wear Tester (TWT) is a lab-scale device used for the assessment of slurry erosion in pipelines. Historically, its application has been limited to the relative ranking of material performance under different slurry flow conditions; however, recent studies have indicated that TWT tests could be predictive and directly applied to slurry pipeline design - with a better understanding of the flow inside the TWT. In the present study, air-liquid multiphase flow inside the TWT was investigated. Torque measurements were taken to characterize friction loss for different air-liquid combinations. A visualization experiment was also conducted to evaluate flow patterns within the TWT. In the experiment, the displacements of spherical glass beads were used to estimate velocity vector fields for different TWT rotational speeds. A Computational Fluid Dynamics (CFD) analysis was also conducted to complement the experimental measurements. A 3D transient analysis using the Volume of Fluid (VOF) approach was used to model the system. The simulation results agreed closely with the experimental findings. Furthermore, the simulations revealed that strong secondary flows (back flow, rotation) exist in the TWT. These type of flows do not occur in horizontal pipelines. Therefore, to use the TWT as a tool for slurry pipeline wear assessment, the differences in the flow field between the two systems must be properly quantified.

## List of Symbols

$D_h$	TWT channel hydraulic diameter, $m$
$f$	Fraction of liquid in the toroid wheel
$f_f$	Friction factor
$F_{EP}$	Equivalent pressure force, $N$
$g$	Gravity, $m/s^2$
$N$	Wheel rotational speed, $rpm$
$R$	TWT wheel outer radius, $m$
$Re$	Reynolds number
$r$	TWT wheel inner radius, $m$
$T$	Torque, $Nm$
$V$	Linear wheel speed, $rad/s$
$W$	Channel width, $m$
$\omega$	Wheel rotational speed, $rad/s$
$\tau_w$	Average wall shear stress, $Pa$
$\rho$	Liquid density, $kg/m^3$
$\rho_s$	Particle density, $kg/m^3$
$\mu_f$	Liquid viscosity, $Pa\cdot s$

## 3.1 Introduction

### 3.1.1 Background

The prediction of slurry pipeline erosion, which can be defined as the progressive removal of material from the pipe wall due to repeated impact of the dispersed particle phase, [1–7] is essential to successful pipeline design (materials selection, operating envelope specification) and safe, reliable operation (maintenance, shutdown planning). Industries that rely upon slurry transport (e.g. mining & mineral processing, dredging, oil and gas production) face severe implications of erosion-related pipe failures, including environmental pollution, loss of production, and increase in operating costs [8]. To bolster the performance of their systems against failure due to erosion, these industries need an effective erosion wear-prediction tool [3, 9]. Unfortunately, the complex multi-physics nature of the erosion process represents a major challenge to the development of a predictive model. For dense slurry pipeline systems, parameters like the bulk flow velocity, particle size and shape, carrier fluid viscosity, solids concentration, geometrical orientation, and the pipe material properties (such as hardness and ductility) all interact to dictate the extent of erosive wear [3, 10–15]. These parameters are difficult to monitor in industrial environments; hence, it is almost impossible to investigate how they affect erosion in slurry systems without a laboratory-scale experimental device. Moreover, wear data that can be scaled to properly design industrial slurry-handling equipment are much needed.

Over the last six decades, many laboratory-scale experimental devices have been developed to study slurry pipeline wear. The most popular ones include the Recirculating Pipe Loop (RPL) [2, 3, 9], Impingement Jet Tester (IJT) [14, 16, 17], Slurry Pot Tester (SPT) [10, 18, 19], and the Toroid Wear Tester (TWT) [4, 6–8, 13, 20]. Typically, experimental wear data generated from these devices are used to develop correlations and models which are compared to field data to interpret slurry pipeline wear at industrial scale. A limitation, however, is that most of these devices have significantly different hydrodynamics compared to a slurry pipeline [1–3, 11]. Clearly, the RPL does not suffer as much from this issue, but still comes with many drawbacks. For example, it requires a large amount of slurry and tests are very time-consuming which makes it expensive to operate [3, 7]. Slurry particles in the RPL also lose their abrasiveness with time due to repeated exposure to the pump and pipe walls during re-circulation. This is very different from the industrial-scale pipeline where

fresh slurry is constantly supplied. There is also an inherent scale-up problem due to the difference in pipe diameter, and the resulting challenges in comparing flow characteristics between the RPL and an industrial scale slurry pipeline [3].

The TWT is a device which overcomes many of these limitations, and is useful for testing the wear resistance of a variety of material types to dense slurry flow [4, 6, 8]. The design of the TWT was meant to mimic pipe flow to some extent so that wear data can be compared between the two systems. However, a preliminary investigation of the hydrodynamics of the TWT indicated that a direct comparison is not straightforward [5].

### 3. 1.2 Operation and development of the TWT

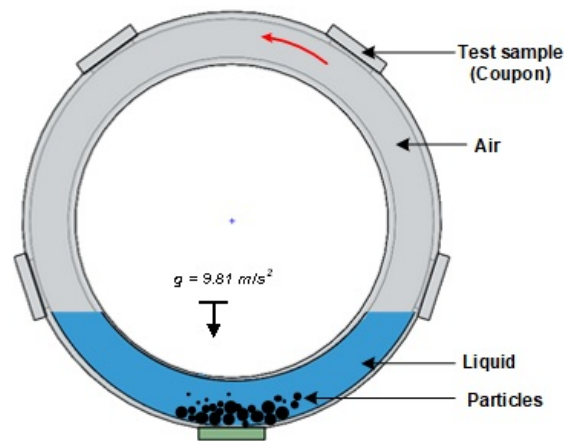


Figure 3.1: Illustration of the TWT operation [4].

The TWT is a hollow wheel which may be constructed from circular or rectangular channel pipe sections [5, 7, 21–23]. Figure 3.1 illustrates the operation of the TWT in this study [4]. The TWT is partially filled with slurry and then rotated in a vertical plane. Unlike the flow of slurry through a stationary pipe, the TWT forces a pipe to move around a relatively stationary slurry. In terms of type of multiphase systems, the slurry pipeline is a two phase (liquid-solid) system while the entire TWT is a three phase (air-liquid-solid) system. Depending on the rotational speed, fluid properties and particle size, the particles in the slurry can remain settled as a bed or can be fully suspended [5, 20]. Typical conditions that produce a settled bed include the presence of large and dense particles at low rotational speed. The attached test coupons (shown in Figure 3.1) are subjected to abrasive wear at

this settled bed condition as the wheel rotates. The slurry particles are also carried along the TWT wall up to the air-liquid interface where they "tumble" back into the bulk fluid because of gravity. Clearly, the TWT hydrodynamics differ in many regards to those of a slurry pipeline flow.

Despite these dissimilarities, the use of the TWT as an analogue for slurry pipe flow dates back to 1955 where Worster and Denny [24] investigated the degradation of coal slurry in a pipeline. They termed the TWT a "ring pipe" and reported the coal slurry to be approximately a stationary bed as the wheel rotates. Traynis [25] also studied slurry hydraulic drag, particle degradation, and erosive wear using these devices and concluded that they were suitable for simulating pipeline wear. The British Hydraulics Research Association (BHRA) also performed wear tests using a toroid with straight pipe sections [26]. They found that the toroid wheel produced wear patterns similar to those found in real pipes. Patterson & Cooke Consulting also performed wear tests using the TWT and reported good agreement with field scale data [7]. More recently, Sarker et al. [4, 8], Zhang [6], and Adedeji et al. [20] performed detailed investigations to study the ability of the TWT to reproduce slurry pipe flow conditions. Their results agreed qualitatively with pipeline wear data reported in the literature but only over a limited operating range. At conditions outside of this narrow range, they found that typical wear trends observed in slurry pipelines (e.g. wear rate dependence on solids concentration and particle size) do not hold in the TWT. This was partly accredited to the influence of secondary flows produced in the TWT and their effect on the interactions between the dispersed particles and the test coupons [4, 5, 8]. Therefore, it is apparent that if the TWT is to be used to assess wear performance of slurry pipelines, a fundamental understanding of its hydrodynamics is needed. Such an understanding must begin with an analysis of the behaviour of liquid-only flow within the TWT (actually, the two-phase air-liquid hydrodynamics: in the context of the TWT, any reference to "liquid flow" means a two-phase air-liquid multiphase system while "slurry flow" would mean a three-phase air-liquid-solid particle flow system, as shown in Figure 3.1).

### 3. 1.3 Scope and objectives

In a preliminary study of the TWT hydrodynamics [5], a Computational Fluid Dynamics (CFD) approach was used to predict velocity profiles, wall shear stress (WSS) distribution, and interfaces (volume fraction) for air-water flow. The simulation results showed a highly non-

uniform distribution of WSS on the TWT wall that suggests a very different hydrodynamics from pipe flow. Despite this insightful outcome from the CFD simulations, there are limited experimental investigations to support the findings [4–8].

In the present study, friction loss was characterized for liquid flow (i.e. air-liquid multi-phase flow) inside in the TWT through torque measurement experiments, and numerically via CFD simulations. Torque determines the degree of turbulent mixing [21] in the TWT which would affect particle behaviour in the slurry and consequently, the erosive wear mechanism. Also, to determine solids-related friction loss for a slurry in the TWT, accurate liquid-related torque values are required. Generally for slurry flows, the total friction loss is the sum of the contributions from its liquid and solid constituents [27–29]. In pipes, the friction loss due to the solid component of a slurry can be determined via established models [27]; however, no such model exists for the TWT. The present study provides a CFD model that accurately predicts the liquid-related torque (or friction loss) in the TWT.

Flow visualization experiments were also used to determine average velocity fields (or flow pattern) inside the TWT. A simple approach similar to Particle Tracking/Image Velocimetry (PTV/PIV) was adopted for the flow visualization experiments. Predicted average velocity fields obtained from the CFD simulations were then compared to those obtained from the experiments. Further analysis of the different types of secondary flows inside the TWT was also carried out using the simulation results. Flow observations in the TWT had suggested the presence of strong secondary flows that may influence fluid-particle-wall interactions very differently than in a horizontal slurry pipeline [4, 5].

In the present study, the following specific investigations were conducted:

1. The liquid-related torque was measured in the TWT for different operating speeds using fluids of different densities and viscosities. This allowed a relatively wide range of operating conditions to be investigated for the flow behaviour inside the TWT.
2. A visualization experiment was also conducted to determine average velocity fields (or flow patterns) within the TWT. A transparent acrylic toroid wheel was used in this experiment and two conditions (air-water flow at 30 and 45 *rpm*) were tested.
3. A Computational Fluid Dynamics (CFD) model implemented in ANSYS Fluent 17.2 was used to analyze the TWT air-liquid multiphase flow. The CFD simulations were first compared with the torque data from the torque experiments. The flow patterns

and profiles obtained from the visualization experiments also were compared to CFD predictions. The simulation results were further used to analyze the secondary flow (e.g back flow, rotation) at other TWT operating conditions.

## 3. 2 Experiment and method

### 3. 2.1 Details of the experimental rig

The TWT rig used in this study was built and installed at the Pipeline Transport Processes (PTP) Research Laboratory, University of Alberta [4, 6, 8]. The rig consists of four stainless steel wheels labelled A, B, C, and D as shown in Figure 3.2. The inner and outer diameters of the wheels are 0.488 *m* and 0.608 *m*, respectively. All the wheels have a rectangular cross-sectional area. The dimension of wheels A, B, and C is 60 × 65 *mm* while wheel D is 60 × 58 *mm*. Each of the wheels has five rectangular openings (the "Coupon windows") where coupons (i.e. test samples) are attached and held in place by a stainless steel coupon holder. To ensure a properly sealed wheel, a general-purpose lubricant by Rust Check and a 0.5 *mm* thick paper gasket by Dynoteq (Model: Tesnit BA-U) are placed between the coupons' edges and the coupon windows before they are secured. All the wheels are mounted on a central shaft of diameter 38.1 *mm*. The shaft is fitted into the two bearings on the supporting frame and is connected to a 2.237 *kW* motor through a timing belt pulley drive. The motor is connected to an alternating current (AC) power source through an electrical cable. The motor speed is remotely controlled and monitored by a variable frequency drive (VFD) through an in-house software installed on a computer. To prevent corrosion when running slurry wear experiments, all the wheels have a nitrogen ( $N_2$ ) charging port and an air discharge port to purge the wheels of oxygen.

To conduct torque measurement experiments, a torque sensor was installed on the central shaft. The capacity of the couplings and torque sensor are 80 *Nm* and 20 *Nm*, respectively [6]. All the components of the torque sensor system were purchased from FUTEK Advanced Sensor Technology Incorporated. This includes an analog amplifier powered by an electric source with constant voltage. The analog amplifier communicates the electrical signal from the torque sensor to a computer via a USB cable. The torque sensor consists of a strain gauge that changes resistance when the shaft deforms under a certain torque (due to the weight of the wheel plus the contents). The analog amplifier detects this change in resistance

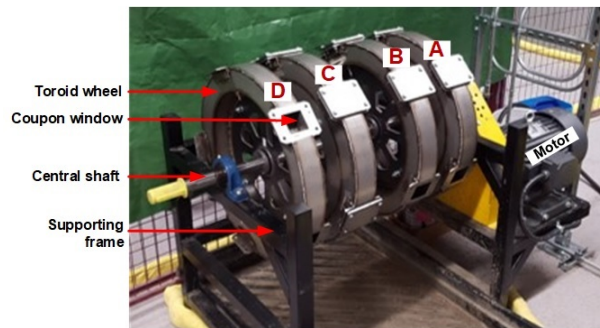


Figure 3.2: Photograph of the TWT rig at the PTP Research Laboratory.

and transmits the data which is collected and stored using an in-house MATLAB code that interacts with a DLL file provided by FUTEK.

To visualize the flow inside the TWT, a transparent acrylic toroid wheel (ATW) was fabricated. As shown in Figure 3.2, the TWT central shaft extends to allow attachment of the ATW. The ATW is not equipped with coupon windows, a nitrogen charging port, and an air discharge port like the stainless steel wheels. However, it contains two circular openings of diameter 20 mm on the side walls for liquid/slurry exchange. The dimension of the ATW is the same as that of wheels A, B, and C. To capture images and videos of flow inside the ATW, a High Speed Digital Camera (HSDC) by Canon (Model: T3i) is employed. An AC-to-DC adapter is used to supply power to the camera. The camera is connected to a computer via a USB and provides live observation of the flow, remote image capturing and recording. The live viewing option helps with proper alignment of the camera for visualization. A halogen light source is used to ensure proper illumination of the ATW contents.

### 3. 2.2 Torque measurement

The torque sensor installed on the TWT has already been calibrated by the manufacturer and was stated to be within 2% accuracy. However, another calibration test was conducted to verify the factory values based on comparison of measured and estimated moment of inertia. Similar accuracy as the manufacturer's was observed in the test. Complete details of the calibration test can be found in Zhang (2018) [6]. To begin with the liquid-related torque measurement, three liquid samples made from a mixture of corn syrup and water were prepared. Table 3.1 shows the viscosity and density of each of the three liquid samples, where the liquid sample on the first row on the table is water i.e. 0% corn syrup concentration.

The viscosities of the corn syrup-water mixtures were measured with a Discovery HR-2 Hybrid Rheometer (TA Instruments), using concentric cylinder geometry. The densities of the mixtures were calculated using a gravimetric method where the mass of a fixed volume of the liquid sample was measured. The various liquids tested represent the range of carrier fluid properties typical of slurry systems in many industries to be tested [3]. A maximum torque value twice that obtained when water is used was achieved with the 35% corn-syrup mixture.

Table 3.1: Viscosity and density of tested liquid samples

Corn syrup conc., (C, vol.%)	$\mu$ , <i>mPas</i>	$\rho$ , <i>kg/m<sup>3</sup></i>
0	1.00	998
20	2.75	1072
35	5.28	1128

To measure the torque, the TWT was first operated empty and the torque value recorded as  $T_0$ , (*Nm*). Afterwards, the wheel A (or B/C) shown in Figure 3.2 was then filled to one-third with one of the prepared liquid samples. The torque value was then measured and recorded as  $T_1$ . The liquid-related torque was calculated as  $T = T_1 - T_0$ . The torque measurements were taken at rotational speeds between 10-90 *rpm* with a 10 *rpm* increment. At each operating conditions tested, two to three measurements were taken and the average value recorded as the measured torque. The total torque required to rotate the TWT at a constant speed is the sum of the torques required to overcome internal and external friction [6, 21]. This is the measured torque  $T_1$  and is due to the mechanical parts and air drag (external), and the liquid contents of the TWT (internal). The measured torque  $T_0$ , is due to external friction alone (i.e. empty wheel rotated at the same speed).

The measured liquid-only torque and friction loss (or average wall shear stress,  $\tau_w$ ) are related by

$$T_1 - T_0 = \frac{\tau_{w,T} D_h \pi^2 (R + r)^2}{3} \quad (3.1)$$

where  $\tau_{w,T}$  is friction loss in the TWT,  $D_h$  is the hydraulic diameter of the toroid channel, and  $R$  and  $r$  are the outer and inner radius of the TWT wheel, respectively.

It is worth mentioning here again that the design of the TWT was to mimic pipe flow; hence, it would be interesting to see how shear stress or friction loss in the present TWT compares with pipe flow at an equivalent condition. Generally, one can show that friction loss

due to fluid flow inside a toroid ( $\tau_{w,T}$ ) may be correlated to that in a horizontal pipe ( $\tau_{w,P}$ ) by [21]

$$\tau_{w,T} = m\tau_{w,P} = 0.5f\rho V^2 \quad (3.2)$$

Here, the velocity  $V = R\omega$  is the TWT linear velocity,  $\omega$  is rotational speed in rad/s,  $\rho$  is the liquid density, and  $f$  the friction factor determined from established correlations [30, 31] and  $m$  is a constant. Clearly, if  $m = 1$ , then the friction losses in the two devices are equivalent. This method will also be used to further verify the torque measurements for all the liquid samples tested.

### 3. 2.3 Quantitative flow visualization

In this experiment, several video sequences of the ATW tests were recorded to estimate liquid flow patterns and velocity profiles inside the TWT for comparison with CFD simulations. The tests were also conducted to determine the suitability of Particle Tracking/Image Velocimetry (PTV/PIV) algorithms. To conduct the experiment, the transparent ATW was filled to one-third of its volume with water, and then seeded with glass bead particles at a very low concentration of 0.5 g/L. The glass beads are spherical, mono-dispersed and white in colour, with a density of  $2650 \text{ kg/m}^3$  and a diameter of  $250 \text{ }\mu\text{m}$ . For the experiments, the TWT was operated at 30 and 45 *rpm*. The Canon T3i digital camera was used to record the videos at a rate of 60 frames per second (FPS). This higher rate of recording is best if more details about the motion of the suspended particles is to be extracted to generate fluid velocity fields. The spatial resolution of the videos was set to  $1280 \times 720$  pixels such that  $4.6875 \times 10^{-4} \text{ m}$  is represented by 1 pixel. A black background was placed behind the acrylic wheel to provide good contrast for the recorded videos. To calculate the velocity vectors needed to show the fluid flow patterns, the FFmpeg multimedia conversion code was first used to generate \*.TIFF image files from the recorded videos. An in-house MATLAB code was then used to process the images which were limited to 1 second of video recording. The MATLAB code subtracts the background of the images to detail the particle location. It then tracks the displacement of particles between the image frames. The change in location and the time difference between the image frames were used to calculate vertical and horizontal velocity components ( $V_x, V_y$ ) which are then used to generate the average velocity vector field describing the fluid flow pattern.

## 3.3 Numerical Modelling

### 3.3.1 Model equations

A 3D transient analysis was carried out using the Volume of Fluid (VOF) modelling approach, in which a single set of momentum equations is solved for two or more immiscible fluids, tracking the volume fraction of each phase [32]. The solution of the continuity equation for the volume fraction of one phase is then used to track the interface between the phases. The VOF approach is suitable for the TWT system because the two phases (i.e. air, liquid) being modelled are immiscible, and there is a clear interface separating them. A transient analysis is also suitable because of the dynamic nature of the air-liquid interface. Also, no mass transfer is modelled for the TWT system; hence, no source term was implemented in the continuity equation for volume fraction which is given by

$$\frac{\partial}{\partial t}(\alpha_i \rho_i) + \nabla \cdot (\alpha_i \rho_i \vec{v}_i) = 0 \quad (3.3)$$

where  $\alpha$  is volume fraction,  $\rho$  is density, and  $v$  is velocity. For the TWT system,  $i = l$  for the liquid while the gas phase (air) volume fraction is obtained from

$$\alpha_g = 1 - \alpha_l \quad (3.4)$$

A single momentum equation is solved and is given by

$$\frac{\partial}{\partial t}(\rho \vec{v}) + \nabla \cdot (\rho \vec{v} \vec{v}) = -\nabla p + \nabla \cdot [\mu(\nabla \vec{v} + \nabla \vec{v}^T)] + \rho \vec{g} + \vec{F} \quad (3.5)$$

where  $\rho \vec{g}$  and  $\vec{F}$  are the gravitational body force and external body forces respectively. The properties  $\rho$  and  $\mu$  are volume-fraction averaged density and viscosity which makes the momentum equation volume fraction dependent.

To track the interface between the air and liquid phases, the modified High-Resolution Interface Capturing (HRIC) technique was implemented. The method solves the air-liquid interface as a "Sharp" interface which prevents excessive diffusion that leads to nonphysical results. The HRIC is, therefore, suitable for systems with a distinct interface between phases such as the TWT [32].

Surface tension is also modelled for the interface between the air and liquid phases. The Continuum Surface Stress (CSS) method was used for modelling the interfacial surface tension. The CSS is an iterative method of modelling surface tension without introducing any source term into the momentum equation [32]. In the CSS method, the surface tension force is defined by

$$F_{CSS} = \nabla \cdot \left[ \sigma (|\nabla \alpha| I - \frac{\nabla \alpha \otimes \nabla \alpha}{|\nabla \alpha|}) \right] \quad (3.6)$$

where  $\sigma = 0.072 N/m$  is the surface tension coefficient and  $I$  is the unit tensor.

For turbulence modelling, the Reynolds stress model (RSM) model with enhanced wall treatment was selected. The RSM is recommended when the effects of secondary flow like swirls and rotation are to be accounted for more rigorously [32–34].

### 3.3.2 Boundary conditions

The TWT is a closed system with no velocity inlet or pressure outlet boundary conditions. A no-slip wall shear boundary condition was specified for the entire domain. The wall was also assumed to be a smooth wall. A rotational wall motion was also defined in the absolute reference frame. It is important to ensure that the rotation-axis origin and direction align with the centre of the TWT. For every simulation, the corresponding rotational speed (in *rpm*) must be specified.

### 3.3.3 Geometry and meshing

A 3D model of the TWT was created in SpaceClaim<sup>®</sup>, one of the CAD tools available in the ANSYS Workbench Package. The dimension of the 3D model is the same as that used for the experiments i.e. outer diameter,  $OD = 0.608m$ ; inner diameter,  $ID = 0.488m$ ; and channel width,  $W = 0.065m$ . The ANSYS Meshing Tool was used to generate 545k hexahedral cells with 7 prism layers. The geometry created is shown in Figure 3.3a while Figure 3.3b shows the mesh generated with a close-up of the cross-section of the TWT channel. The prism layer cells generated are to resolve the boundary layer flow near the wall. This is important because it can significantly influence the accuracy of the predicted torque [5, 22]. The mesh quality analysis indicated a maximum aspect ratio of 16.6, which is a reasonable value for

these CFD simulations [32].

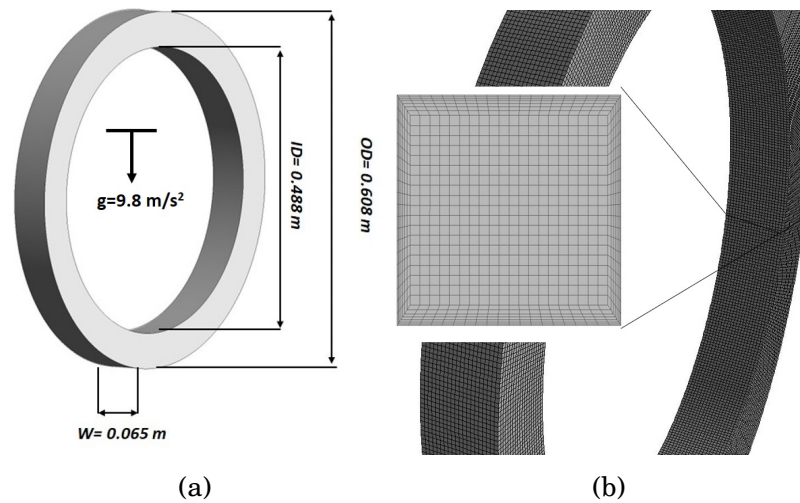


Figure 3.3: The toroid wheel (a) 3D geometry and (b) mesh generated.

In order to verify mesh independence, three additional mesh sizes (225k, 360k, and 880k) were created i.e two coarser meshes and one finer mesh. Air-water multiphase simulations were conducted for the TWT model at 60 *rpm* using each mesh size. The predicted torque ( $T$ ,  $Nm$ ), area-weighted average wall shear stress ( $\tau_w$ ,  $Pa$ ) and turbulent kinetic energy ( $k$ ,  $m^2/s^2$ ) are the physical quantities used to monitor the differences among the meshes. These quantities were identified to be of primary importance to the analysis conducted in this study. Figure 3.4 shows the percentage difference in these parameters using the finest mesh (880k) as a reference. At the 545k mesh size, a change of less than 1% was predicted. Considering the simulation cost, mesh quality, and this mesh independence analysis, the 545k mesh size was selected to complete the rest of the simulations.

### 3.3.4 Solution procedure

The first order implicit solution scheme was used for solving the TWT system model. This method requires the values of the volume fraction at the current time step; hence, a standard scalar transport equation is solved iteratively at each time step for the secondary phase volume fraction [32]. The Semi-Implicit Method for Pressure Linked Equations (SIMPLE) algorithm was used for pressure-velocity coupling. The second-order upwind method was used to solve the momentum equation while the first-order upwind method was used to solve

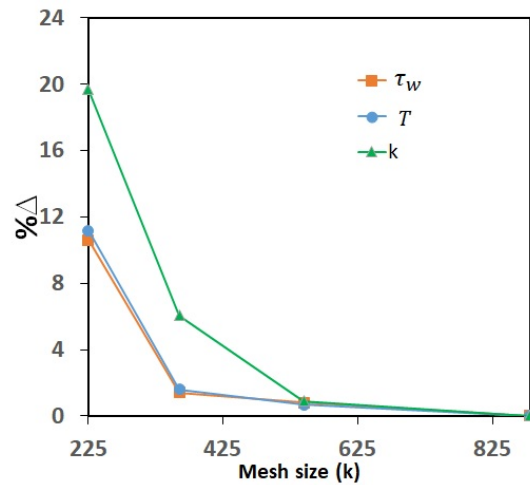


Figure 3.4: Mesh independence study using four mesh sizes (225k, 360k, 545k and 880k), testing three key parameters (Wall shear stress,  $\tau_w$ ; Torque,  $T$ ; Turbulent kinetic energy,  $k$ ).

the turbulence equations.

To run the simulation, an initialization process where 1/3 of the TWT model is filled with the liquid phase must first be carried out. The first step in the initialization process is to "mark" the region that will be occupied by the liquid phase at time  $t = 0$ . This was done using the "Adapt Cells" feature available in ANSYS Fluent where minimum and maximum  $x, y, z$  coordinate values are set to define the liquid phase region. The values specified are ( $x_{min} = -0.304$   $x_{max} = 0.304$ ), ( $y_{min} = -0.304$   $y_{max} = -0.128$ ), and ( $z_{min} = 0$   $z_{max} = 0.065$ ). The next step is to activate the "Patch" feature in ANSYS Fluent by initializing the solution. The hybrid initialization method is recommended. Once initialization is completed (10 iterations), one would be able to specify a volume fraction for liquid phase region that was previously defined (marked). A volume fraction of 1 was specified for the liquid phase (equals 0.33 for entire TWT domain) for all the simulations.

It is important to apply the smoothing option in the "Patch" feature at least twice to improve solution stability and convergence. For the simulations, fixed time steps ( $\Delta t$ ) were used and the total simulation time was set to allow at least six full revolutions (SFR) depending on the rotational speed simulated. To prevent solutions from diverging and to minimize simulation cost, large time step sizes were specified for lower rotational speeds and smaller sizes for higher ones. Table 3.2 shows the summary of the different time step sizes used in the simulations. A minimum of 5 iterations between simulation time steps was also

Table 3.2: Simulation time step sizes

$\omega$ (rpm)	Time for SFR (s)	$\Delta t$ (s)	Total No. of time steps
10	36.0	0.001	36000
20	18.0	0.0005	36000
30	12.0	0.0005	24000
40	9.0	0.00025	36000
50	7.2	0.00025	28800
60	6.0	0.00025	24000
80	4.5	0.000125	36000
90	4.0	0.000125	32000

specified. The convergence criterion was set to  $1 \times 10^{-4}$  for all residuals. Also, an additional convergence criterion based on the predicted torque value was used. To output the predicted torque value, a report of the moment ( $Nm$ ) about the TWT centre was created. The torque value from the report was then plotted against the simulation time. The simulations were only terminated after a steady torque value is predicted in addition to the criteria set for the residuals. Simulations were completed in an average of 48 hrs on an Intel Xeon (E5-2670), 2.6 GHz and 32 GB RAM computer with a dual processor.

## 3. 4 Results and discussion

### 3. 4.1 Measured and predicted torque data

The liquid-related torque data measured for the three liquid samples (see Table 3.1) at rotational speeds between 10-90 *rpm* with 10 *rpm* increments are reported. A measurement was not taken at 70 *rpm* because of excessive vibration of the entire TWT set-up which was ascribed to resonance effects [4]. The measured torque data are presented in Figure 3.5a and have been plotted against rotational speed. It is apparent from Figure 3.5a that the torque values recorded are greater for the liquid samples with higher viscosity (and density). The measured torque represents the total friction loss which includes the energy required by the rotating TWT wall to overcome frictional resistance and create momentum in the fluid. Since viscosity represents the resistance of fluid to flow while the density (or weight) determines the energy needed to produce inertia and accelerate the fluid, torque values should be greater for the liquid samples with higher viscosity and density [30].

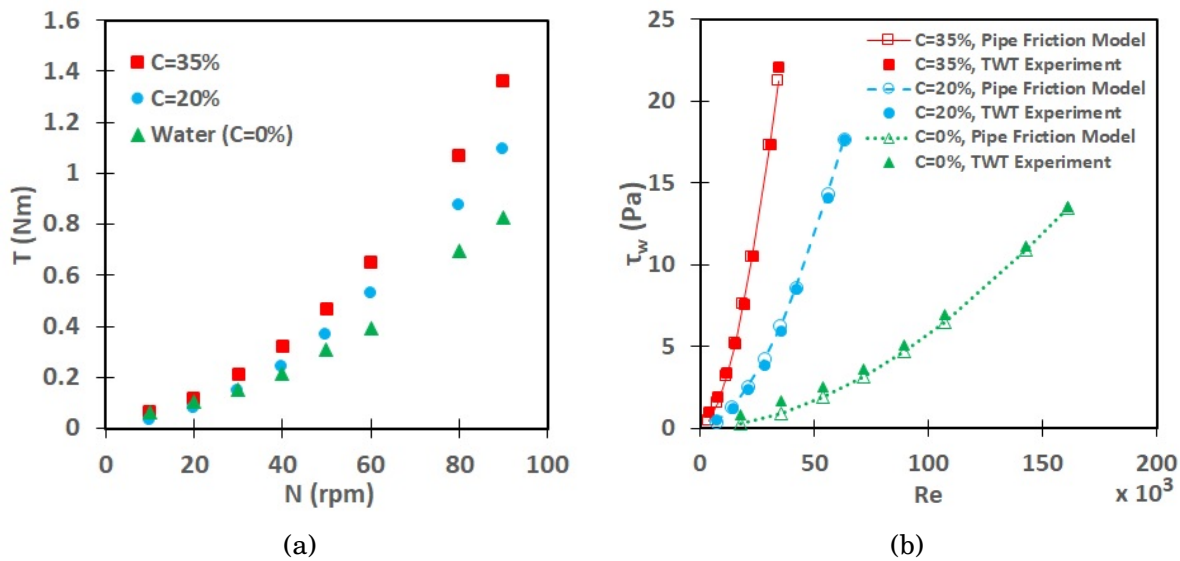


Figure 3.5: Experimental torque data for the liquid samples tested.

In Figure 3.5b, the torque data are reported as friction loss ( $\tau_w$ ) versus Reynolds number ( $Re$ ). The experimental friction losses were calculated from Equation 3.1 and have been compared to those obtained from the pipe friction loss model [30, 31] described in Equation 3.2 using the TWT operating conditions i.e. linear speed of the TWT ( $V = R\omega$ ) and the hydraulic diameter of the TWT channel ( $D_h = 2W(R - r)/(R - r + W)$ ). The calculated friction loss is equivalent of a single phase liquid flow in a horizontal pipe (with  $m = 1$  as in Equation 3.2). Reynolds number was defined as  $Re = \rho D_h R \omega / \mu$ . The Reynolds number as a reference for comparison is more appropriate than velocity alone since both density and viscosity changed for each liquid. As shown in Figure 3.5b, the pipe friction loss model (from Equation 3.2) predicted accurately the data obtained from direct torque measurement which confirms that torque measurements in a toroid can be used to simulate friction losses in pipes [21]. However, this does not mean flow in a TWT is the same as that in a pipe. For curved or rotating systems like the TWT, friction losses due to the existence of secondary flow can be very significant compared to a straight pipe where they essentially do not exist (at fully developed flow) [35, 36].

Figure 3.6 shows the comparison of torque data obtained from the CFD simulations and experiments. The Volume-of-Fluid (VOF) approach used in the CFD simulations predicted the measured liquid-related torque in the TWT to a reasonable level of accuracy.

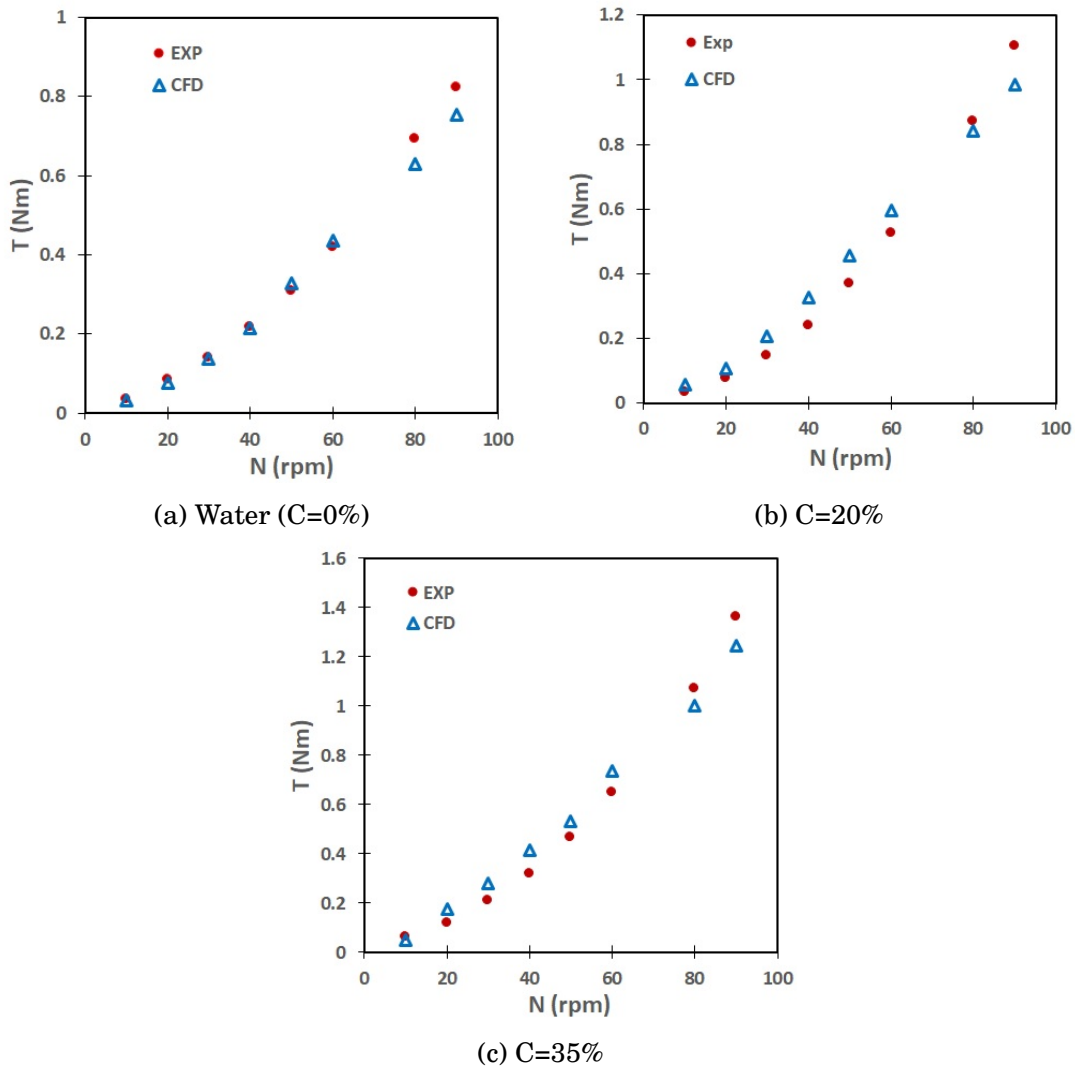


Figure 3.6: Comparisons of CFD-predicted and experimental torque.

The CFD predictions closely match the measured data for all three liquid cases within a maximum of 10% error. A greater difference between measured and predicted torque is seen at higher rotational speed (80 and 90  $rpm$ ). Overall, it is clear that the CFD simulations gave satisfactory predictions of torque - which can be used for future experimental design. However, the primary benefit of the CFD simulations is their ability to provide detailed flow visualization within the TWT that cannot be so readily obtained from experiments (these are presented in Section 3.4.2). Also, the close agreement between experiments and these simulations allows the extension of the CFD model to test design alternatives for the TWT.

For example, one can evaluate of the effect of wheel-to-channel diameter ratio on the TWT hydrodynamics.

### 3. 4.2 Fluid flow pattern and velocity profile

To visualize flow patterns (average velocity vectors) and also obtain velocity profiles for flow inside the TWT, several data planes have been defined as shown in Figure 3.7. The direction of rotation has also been indicated to define the upstream and downstream sides of the TWT.

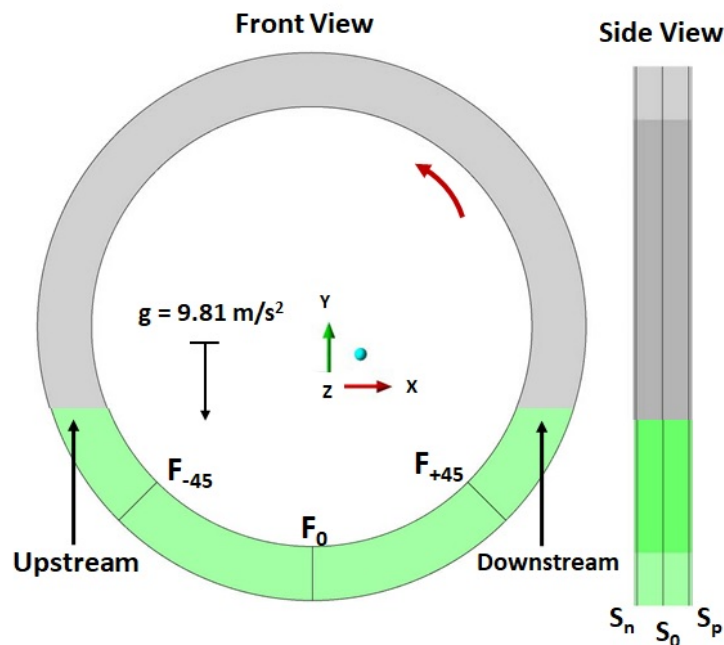


Figure 3.7: Data planes considered for flow pattern analysis.

The planes  $F_{-45}$ ,  $F_0$ , and  $F_{+45}$  are at positions  $-45^\circ$ ,  $0^\circ$ , and  $+45^\circ$  relative to the centre of the TWT, respectively. For the side view, the plane  $S_0$  divides the wheel into equal halves while both planes  $S_n$  and  $S_p$  are close to their respective walls i.e. each is at  $3.25\text{ mm}$  from the nearest wall, which is 5% of the TWT width. The fluid flow pattern and air-water interface obtained from an experiment are shown in Figure 3.8 while those from the mid-plane,  $S_0$ , of CFD simulations are shown in Figure 3.9. The flow direction is anti-clockwise and the downstream air-water interface has been presented.

The experimental flow patterns were approximated from the particle (glass beads) motion

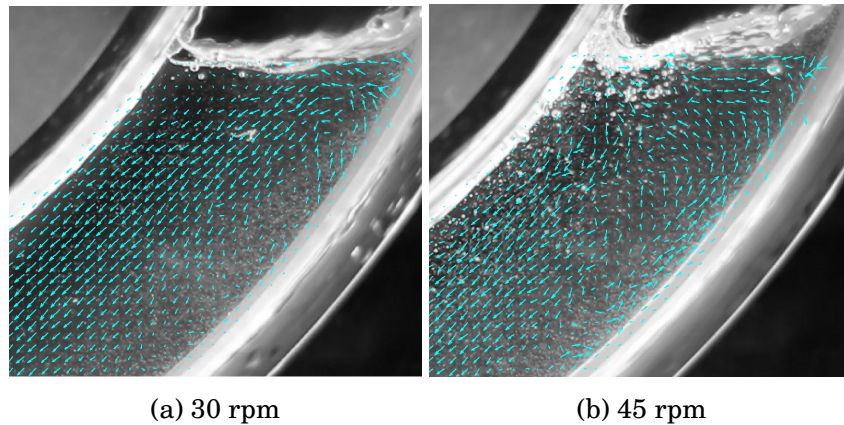


Figure 3.8: Flow patterns and water interface from visualization experiments: downstream.

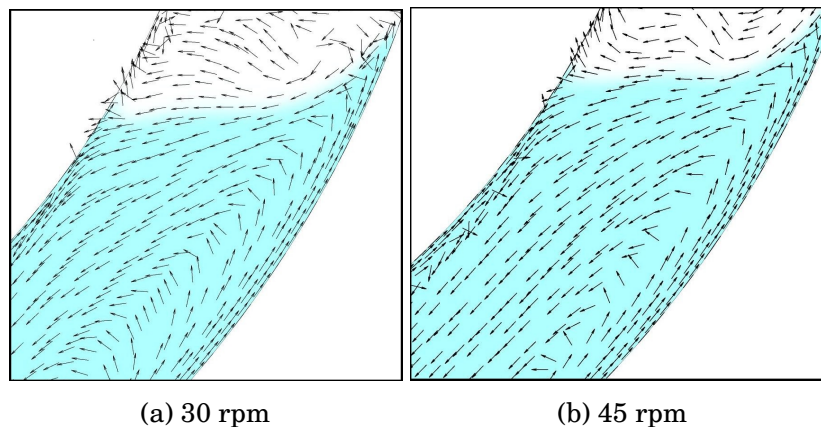


Figure 3.9: Flow patterns and water interface predicted by CFD: mid-plane  $S_0$ , downstream

throughout the entire depth of the TWT wheel instead of a specific plane (or light sheet) of the fluid flow such as in a complete PTV/PIV set up. For both 30 and 45 *rpm* cases, it can be observed that the CFD reasonably predicted the air-water interface and velocity vector fields obtained from the corresponding experiment. In Figures 3.8 and 3.9, three flow regions (forward, stagnation, and back flow) can be identified. The forward flow region is in contact with, and close to the rotating TWT wall. The flow in this region, as the name implies, is in the direction of the rotating TWT wheel which is indicated clearly by the vector arrows in Figure 3.9. The back flow region is at the centre or core of the TWT wheel channel. As shown in Figures 3.8 and 3.9, the flow direction in the back flow region is opposite to the direction of wheel rotation. The stagnation point is at the intersection of the forward and back flows where they cancel each other out i.e. in-between the forward and backward flow

regions where there seems to be no motion.

Axial flow velocity profiles (i.e. profiles for linear velocity in the  $x$ -direction,  $V_x$ ) from the experiments and CFD simulations are compared in Figure 3.10. The profiles were obtained from a line drawn at the centre of the TWT channel on plane  $F_{+45}$  (See Figure 3.7). The wheel channel height has been normalized as  $y/(R-r)$  and used as the ordinate. The case of 30 rpm is shown in Figure 3.10a and 45 rpm results are shown in Figure 3.10b.

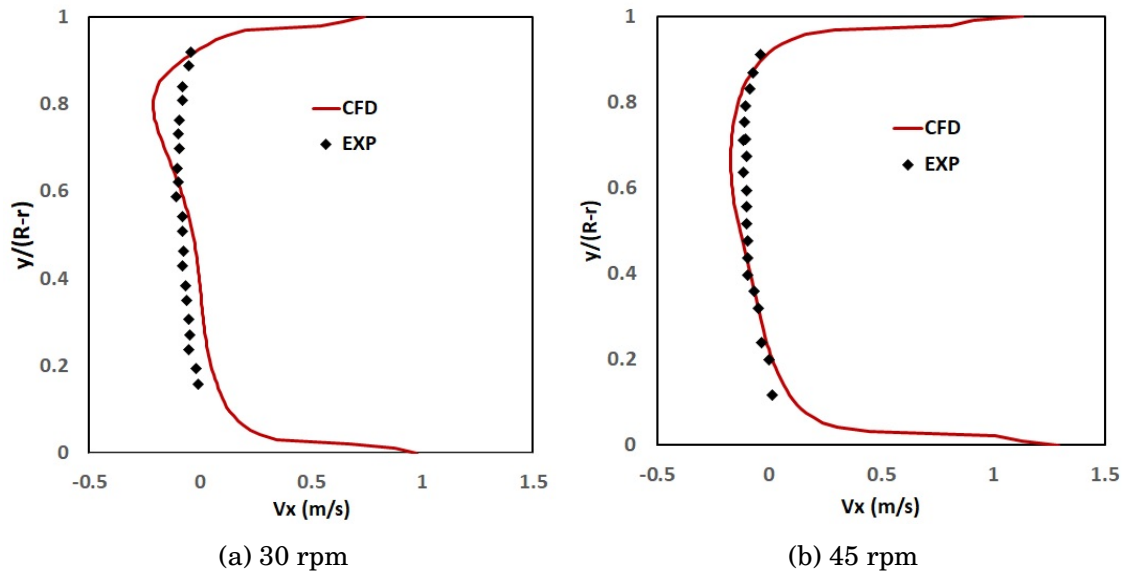


Figure 3.10: Comparison of experimental and predicted axial velocity profile at plane  $F_{+45}$ : air-water flow.

It is apparent that the CFD simulations and the experimental measurements agree within a reasonable level of accuracy. In the experiments, most of the glass beads used to estimate fluid velocities were found at the core of the TWT flow. The few particles near the wall impacted the rotating TWT wall with a high rebound, which means the estimated fluid velocities would include larger errors as they are not appropriately represented by the particle motion. This is why experimental measurements are not shown for the near-wall region. Figures 3.10a and 3.10b also show the regions with forward flow (positive velocity), backward flow (negative velocity), and the stagnation point (zero velocity). The forward flow region extends to about 25% of the TWT channel height at the bottom while it is only about 10% at the top.

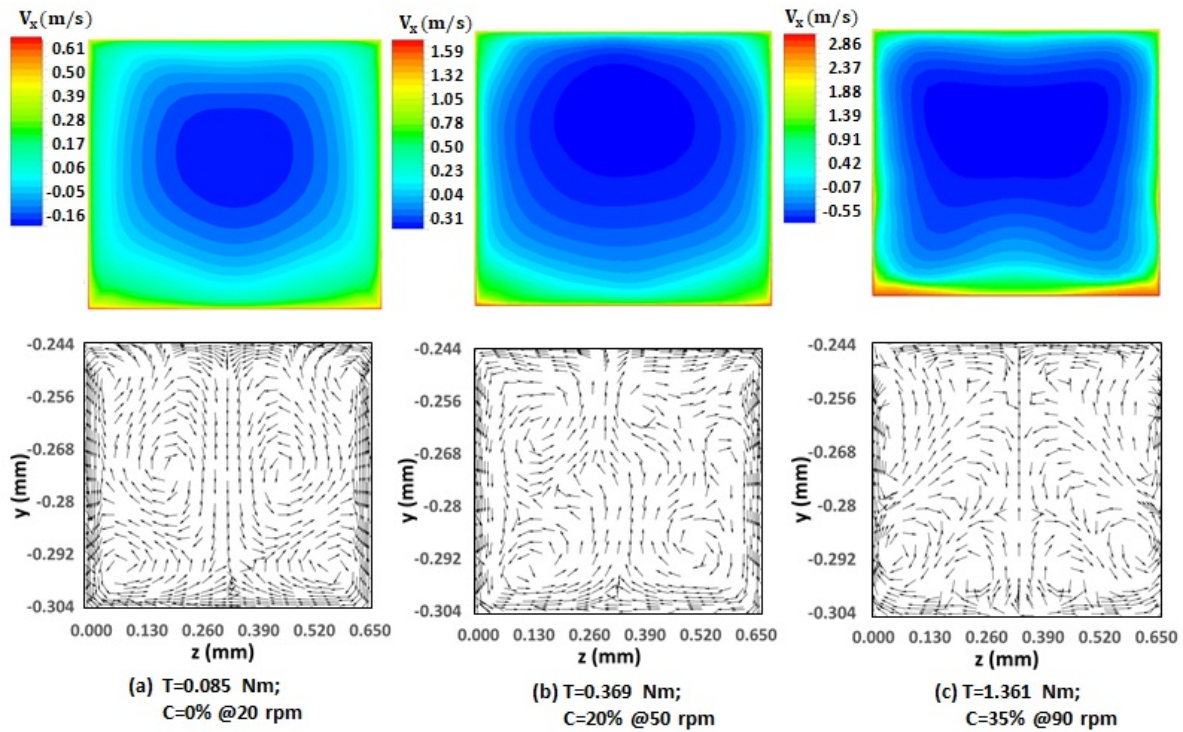


Figure 3.11: Comparison of velocity vector and colour plots for middle plane  $F_0$  at  $Re = 35000$  for the three liquid cases.

A comparison of predicted velocity colour plots (upper row) and vector plots (lower row) is provided in Figure 3.11 for  $Re \approx 35000$  for the three liquid samples (See Figure 3.5b). The operating condition of the TWT and the measured torque values have been indicated on the Figure. The global coordinates  $y$  and  $z$  have been used to depict the TWT channel height and width, respectively. It is apparent in Figure 3.11 that the back flow region is limited to the core of the TWT channel. Figure 3.11 also reveals that the magnitude of back flow (in velocity) increases with the measured torque in the TWT system. The colour plots also show that the forward flow region mostly occupies the corner walls of the TWT channel. Despite the similar Reynolds number, it is apparent that the torque value at each flow condition directly relates to the behaviour of back flow in the TWT system. For the velocity vector plots in Figure 3.11, fluid rotation can be seen to occur locally at several zones across the TWT channel. A much more defined flow pattern can be observed in the water case (i.e.  $C = 0\%$ ) with the low torque values. The fluid rotation becomes further disrupted with increase in torque such that a regular flow pattern cannot be identified.

Figures 3.12 and 3.13 show a comparison of the colour and velocity vector plots obtained for air-water flow from planes  $F_{-45}$ ,  $F_0$ , and  $F_{+45}$  (see Figure 3.7 for the locations identified by these descriptors). The colour plots show that the the back flow region is smallest at the

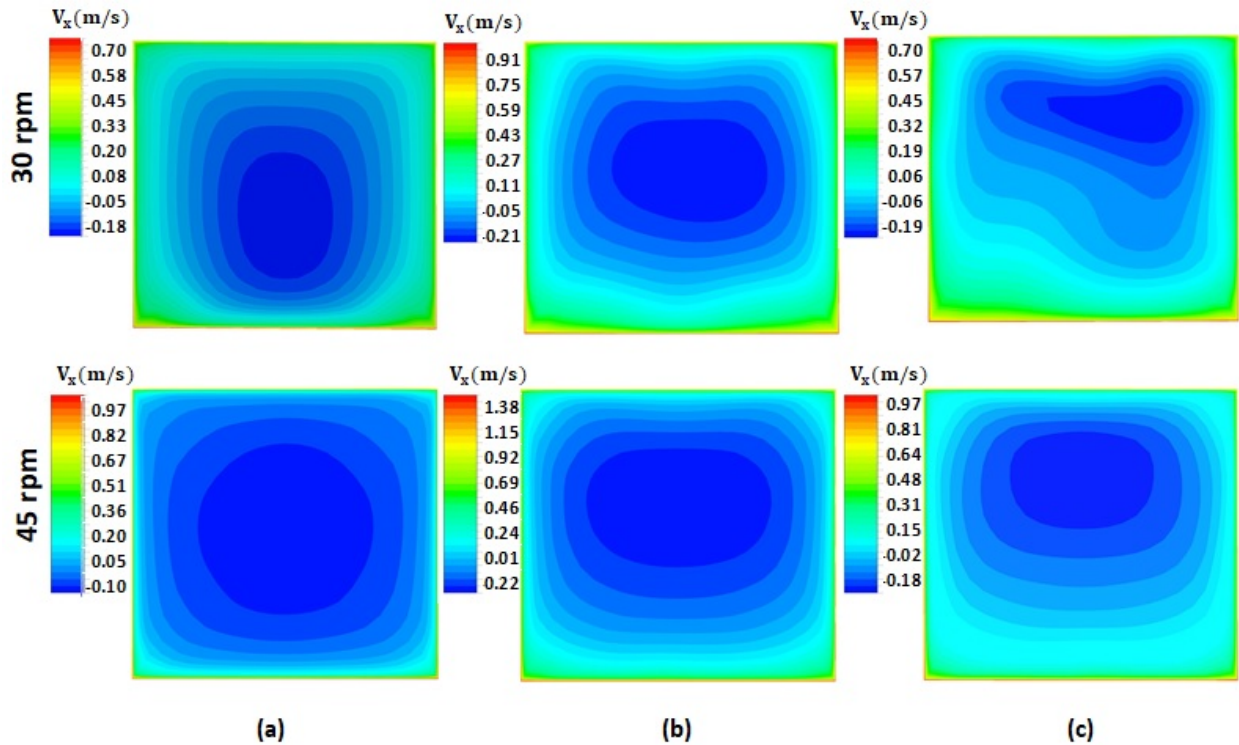


Figure 3.12: Velocity colour plots for planes (a)  $F_{-45}$ , (b)  $F_0$ , and (c)  $F_{+45}$ .

downstream side and largest at the upstream side. Also, comparing both cases of 30 and 45 *rpm* in Figure 3.12, it can be seen that the back flow region occupies a larger area at higher rotational speed (meaning higher torque), especially at the upstream side. The magnitude of forward flow is also greatest at the central (bottom) of the TWT as can be seen on the middle plane contour. In Figure 3.13, the pattern of fluid rotation inside the TWT can be inferred from the velocity vector plots. The rotation seems to originate from the centre of the TWT channel and moves both in the clockwise (to the right) and counter-clockwise (to the left) directions. For both 30 *rpm* and 45 *rpm*, this rotational flow pattern is persistent throughout the TWT channel i.e. it is similar at each of the upstream, midstream, and downstream planes (as with the colour plots in Figure 3.12).

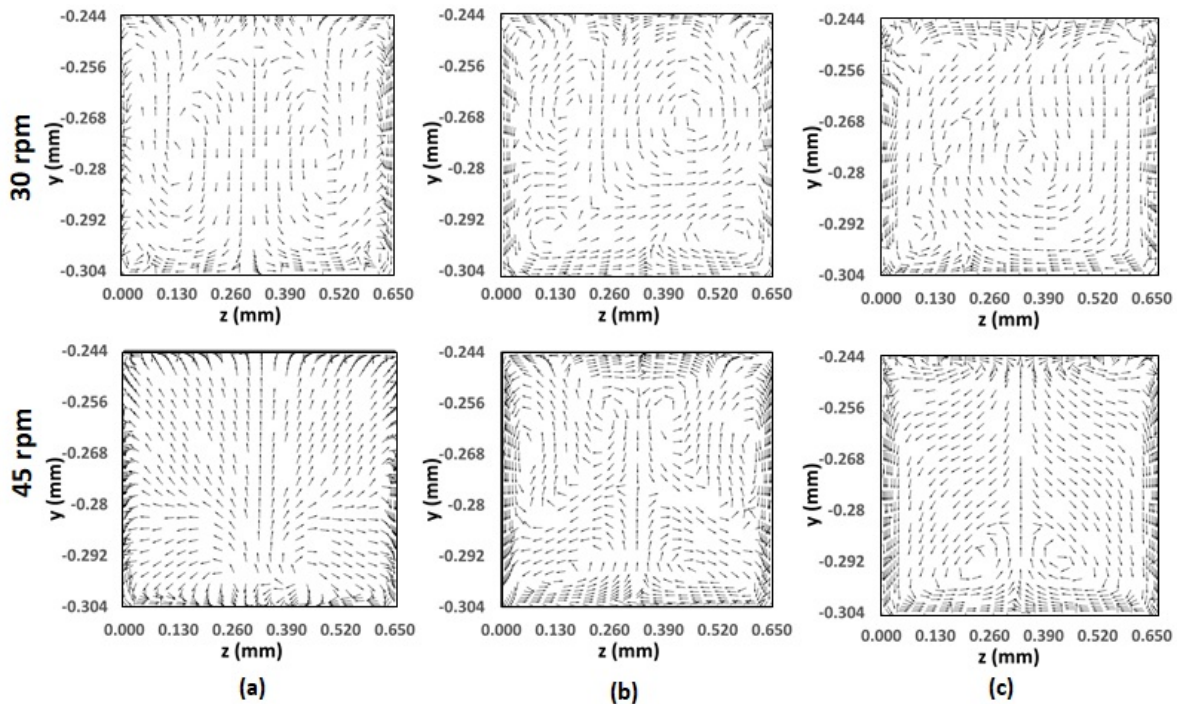


Figure 3.13: Velocity vector plots for planes (a)  $F_{-45}$ , (b)  $F_0$ , and (c)  $F_{+45}$ .

### 3.5 Implications for Wear Testing

The TWT is usually operated with concentrated, coarse particle slurries which allows a nearly stationary bed to form at the bottom of the wheel as shown in Figure 3.14. Test samples (coupons) are attached to the outer circumference of the wheel and are subjected to the abrasive action of the particles as the wheel rotates. The wheel is typically operated for about 96 hrs to allow significant and measurable wear damage of the test samples to occur. In Figure 3.14a, the 30 rpm case shows a fully settled particle bed while the 90 rpm case (Figure 3.14b) shows an expanded bed with some particles (in the bulk fluid) fully suspended by the fluid turbulence. Wear damage experienced by the test coupons would be entirely abrasive due to the weight of the particles in the 30 rpm case. However, the wear damage mechanism in the 90 rpm case would include both abrasion due to particle bed weight and some deformation due to impact of the suspended particles. Based on this observation, it appears the liquid-related torque in the TWT can be used to indicate the intensity of back flow that particles may be subjected to in the system, and thus it may be possible to infer the dominant wear mechanism.

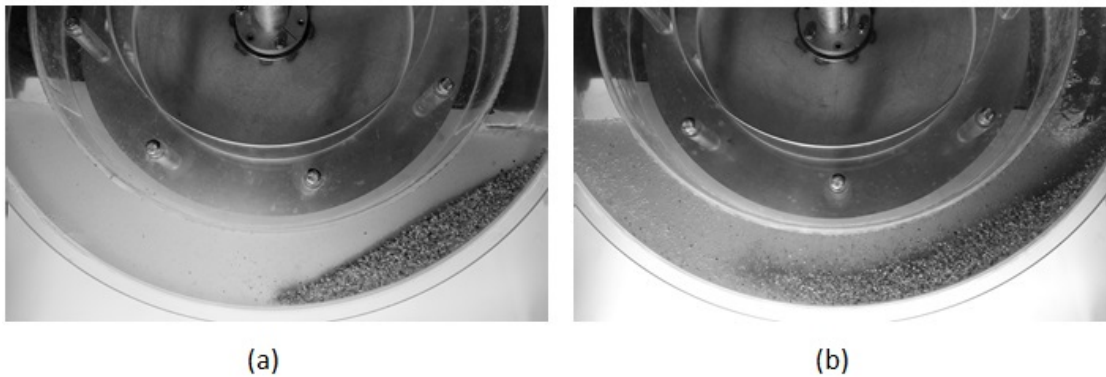


Figure 3.14: Particle response to the TWT hydrodynamics: Image shows 15 vol.% 1 mm gravel in water at (a) 30 rpm,  $T=0.14 Nm$ , and (b) 90 rpm,  $T=0.82 Nm$

The observation of slurry flow inside the TWT also revealed local rotational motion of particles in the bed, especially at higher TWT rotation speeds [4, 8]. The CFD simulations of Figure 3.13 showed that fluid rotation persists throughout the liquid phase which may be responsible for the observed local rotation of particles. The particles in the bed were also observed to follow a cyclic path i.e. particles near the wall are carried to the air-liquid interface and are tumbled back to the top of the bed and into the bulk flow [4, 8, 20]. This cyclic flow path is strongly influenced by the forward and back flow observed from the visualization experiments and CFD predictions. The bed of particles has also been assumed to be stationary, however, the forward flow region near the wall induced a relative motion between the particles and rotating wall. This means the linear velocity equivalent of the TWT rotational speed must be appropriately adjusted to a representative slurry mean flow velocity used in erosive wear correlations. In other words, proper scaling of variables that define the TWT operating conditions (e.g. using dimensionless numbers) is required for its application to industrial slurry pipelines.

## 3.6 Conclusions

In this study, experiments and CFD simulations have been used to characterize the toroid wear tester (TWT) hydrodynamics. The CFD simulations employed the Volume-of-Fluid (VOF) multiphase approach. The flow behaviour of three Newtonian liquid samples with different densities and viscosities was evaluated. Good agreement between CFD simulations

and the measured torque data was observed. Flow visualization experiments were also conducted to estimate fluid flow patterns in the TWT and three flow regions; namely, forward flow, back flow, and stagnation were identified. The results were compared to velocity profiles and velocity vector fields obtained from the CFD simulations. The conclusions made from analysis of the results in the present study are:

- The value of friction loss or torque in the TWT can be used to indicate the degree of secondary flows. It can also be used to indicate the type of wear mechanism occurring in the TWT. This study showed that it is possible to tell the current state of the particle bed from the measured (or predicted) friction loss, from which the predominant wear damage mechanism can be identified.
- Scaling procedures using dimensionless quantities to relate behaviour in two systems (e.g. pipe and TWT) must be applied with caution. For example, a similar Reynolds number (say between the TWT and a pipe) might mean a comparable degree of turbulence but an entirely different flow behaviour.

The results clearly show that flow behaviour within the TWT is highly dynamic with a characteristic reverse and rotational flow pattern. The TWT also has very different hydrodynamics when compared to horizontal pipelines which, for years, was presumed to be its analogue. Currently, a more detailed analysis of the flow patterns and particle motion inside the TWT is ongoing. A series of CFD simulations of a three-phase air-liquid-solid model with discrete element method (DEM) to provide details about the responsiveness of particles to the rotating wall and secondary flows is presently underway. Information about forces and energy transfer between a particle and the TWT wall can be obtained from these simulations to help better define wear mechanisms.

## References

- [1] C. A. Shook, M. McKibben, M. Small, Experimental investigation of some hydrodynamic factors affecting slurry pipeline wall erosion, *Can. J. Chem. Eng.* 68 (1990) 17–23. URL: <http://doi.wiley.com/10.1002/cjce.5450680102>. doi:10.1002/cjce.5450680102.
- [2] P. Goosen, I. Malgas, An Experimental Investigation into Aspects of Wear in Boiler Ash

- Disposal Pipelines, in: Proc. Hydrotransp. 14, September, Maastricht, The Netherlands, 1999, pp. 8–10.
- [3] A. Sadighian, Investigating Key Parameters Affecting Slurry Pipeline Erosion, Ph.D. thesis, University of Alberta, 2016. doi:[10.1017/CB09781107415324.004](https://doi.org/10.1017/CB09781107415324.004). arXiv:[arXiv:1011.1669v3](https://arxiv.org/abs/1011.1669v3).
- [4] N. R. Sarker, A Preliminary Study of Slurry Pipeline Erosion Using a Toroid Wear Tester, MSc thesis, University of Alberta, 2016.
- [5] N. R. Sarker, M. A. Islam, R. S. Sanders, B. A. Fleck, CFD Analysis of the Hydrodynamics of an Air- Water Multiphase System in a Rotating Toroid Wheel, in: 23rd Annu. Conf. CFD Soc. Canada, April, Waterloo, ON, Canada, 2016.
- [6] L. Zhang, Relating slurry friction to erosion rate using a toroid wear tester, MSc thesis, University of Alberta, 2018.
- [7] R. Cooke, G. Johnson, P. Goosen, Laboratory Apparatus for Evaluating Slurry Pipeline Wear, Technical Report March, SAIT Seminar, Calgary, 2000.
- [8] N. R. Sarker, D. E. S. Breakey, M. A. Islam, S. Sun, B. A. Fleck, R. S. Sanders, Performance and Hydrodynamics Analysis of a Toroid Wear Tester to Predict Erosion in Slurry Pipelines, *Wear* (2019) 203068. URL: <https://doi.org/10.1016/j.wear.2019.203068>. doi:[10.1016/j.wear.2019.203068](https://doi.org/10.1016/j.wear.2019.203068).
- [9] B. Fotty, M. Krantz, J. Been, J. Wolodko, Development of a pilot-scale facility for evaluating wear in slurry pipeline systems, in: Proc. Hydrotransp. 18, September, Rio de Janeiro, Brazil, 2010, pp. 431–443.
- [10] R. Gupta, S. N. Singh, V. Sehadri, Prediction of uneven wear in a slurry pipeline on the basis of measurements in a pot tester, *Wear* 184 (1995) 169–178. doi:[10.1016/0043-1648\(94\)06566-7](https://doi.org/10.1016/0043-1648(94)06566-7).
- [11] A. J. Karabelas, An Experimental Study of Pipe Erosion by Turbulent Slurry Flow, in: Proc. Hydrotransp. 5, May, Hannover, Germany, 1978, pp. 25–24.
- [12] O. E. Adedeji, W. Yu, R. S. Sanders, Analysis of local wear variables for high-precision erosion modelling in complex geometries, *Wear* 426-427 (2019) 562–569. doi:[10.1016/j.wear.2018.12.071](https://doi.org/10.1016/j.wear.2018.12.071).

- [13] N. R. Sarker, L. Zhang, D. Breakey, B. A. Fleck, R. S. Sanders, Laboratory-Scale Erosive Wear Measurements Conducted with a Toroid Wear Tester (TWT), in: 8th Int. Conf. Transp. Sediment. Solid Part., September, 2017, pp. 295–303.
- [14] A. Gnanavelu, N. Kapur, A. Neville, J. F. Flores, N. Ghorbani, A numerical investigation of a geometry independent integrated method to predict erosion rates in slurry erosion, *Wear* 271 (2011) 712–719. URL: <http://dx.doi.org/10.1016/j.wear.2010.12.040>. doi:10.1016/j.wear.2010.12.040.
- [15] Y. I. Oka, H. Ohnogi, T. Hosokawa, M. Matsumura, The impact angle dependence of erosion damage caused by solid particle impact, *Wear* 203 (1997) 573–579.
- [16] A. Mansouri, H. Arabnejad, S. A. Shirazi, B. S. Mclaury, A combined CFD / experimental methodology for erosion prediction, *Wear* 333 (2015) 1090–1097. URL: <http://dx.doi.org/10.1016/j.wear.2014.11.025>. doi:10.1016/j.wear.2014.11.025.
- [17] V. B. Nguyen, Q. B. Nguyen, Z. G. Liu, S. Wan, C. Y. H. Lim, Y. W. Zhang, A combined numerical – experimental study on the effect of surface evolution on the water – sand multiphase flow characteristics and the material erosion behavior, *Wear* 319 (2014) 96–109. URL: <http://dx.doi.org/10.1016/j.wear.2014.07.017>. doi:10.1016/j.wear.2014.07.017.
- [18] B. K. Gandhi, S. Singh, V. Seshadri, Study of the parametric dependence of erosion wear for the parallel flow of solid – liquid mixtures, *Tribol. Int.* 32 (1999) 275–282.
- [19] W. Tsai, J. A. Humphrey, I. Cornet, A. V. Levy, Experimental measurement of accelerated erosion in a slurry pot tester, *Wear* 68 (1981) 289–303. doi:10.1016/0043-1648(81)90178-2.
- [20] O. E. Adedeji, L. Zhang, D. Breakey, R. S. Sanders, Investigation of abrasive wear in contact load-dominated slurry flows using a Toroid Wear Tester, *Manuscr. Submitt. to Wear* (2020).
- [21] R. G. Gillies, C. A. Shook, Modelling high concentration slurry flows, *Can. J. Chem. Eng.* 78 (2000) 709–716. doi:10.1002/cjce.5450780413.
- [22] J. F. Roca, J. N. E. Carneiro, J. E. S. Oliveira, S. Mo, M. Fossen, S. T. Johansen, CFD Simulation of The Two-Phase Flow of Different Mixtures in a Closed System Flow

- Wheel, in: 10th Int. Conf. CFD Oil Gas, Metallurgical Process Ind., June, SINTEF, Trondheim, Norway, 2014, pp. 253–259.
- [23] O. Urdahl, A. O. Fredheim, K. P. Loken, Viscosity measurements of water-in-crude-oil emulsions under flowing conditions: A theoretical and practical approach, *Colloids Surfaces A Physicochem. Eng. Asp.* 123-124 (1997) 623–634. doi:[10.1016/S0927-7757\(96\)03801-0](https://doi.org/10.1016/S0927-7757(96)03801-0).
- [24] R. C. Worster, D. F. Denny, Hydraulic transport of solid material in pipes, *Proc. Inst. Mech. Eng.* 169 (1955) 563–586.
- [25] V. V. Traynis, Parameters and flow regimes for hydraulic transport of coal by pipelines, Terraspace, Rokcville. USA, 1977.
- [26] G. Henday, A comparison of commercial pipe materials intended for the hydraulic transport of solids, BHRA, 1988.
- [27] R. G. Gillies, C. A. Shook, K. C. Wilson, An improved two layer model for horizontal slurry pipeline flow, *Can. J. Chem. Eng.* 69 (1991) 173–178. URL: <http://doi.wiley.com/10.1002/cjce.5450690120>. doi:[10.1002/cjce.5450690120](https://doi.org/10.1002/cjce.5450690120).
- [28] R. G. Gillies, Pipeline Flow of Coarse Particle Slurries, Ph.D. thesis, University of Saskatchewan, 1993.
- [29] R. G. Gillies, C. A. Shook, J. Xu, Modelling Heterogeneous Slurry Flows at High Velocities, *Can. J. Chem. Eng.* 82 (2004) 1060–1065. doi:[10.1002/cjce.5450820523](https://doi.org/10.1002/cjce.5450820523).
- [30] B. R. Munson, A. P. Rothmayer, T. H. Okiishi, Fundamentals of Fluid Mechanics, 7th Edition, Wiley, 2012. URL: <https://books.google.ca/books?id=GQMcAAAAQBAJ>.
- [31] P. Swamee, A. K. Jain, Explicit equations for pipe-flow problems, *ASCE J Hydraul Div* 102 (1976) 657–664.
- [32] ANSYS, ANSYS 17.0 Theory Guide, Technical Report, 2017. URL: <https://www.sharcnet.ca/Software/Ansys/17.0/en-us/help/fluo{ }th/fluo{ }th.html>.
- [33] B. E. Launder, G. J. Reece, W. Rodi, Progress in the development of a Reynolds-stress turbulence closure, *J. Fluid Mech.* 68 (1975) 537–566. doi:[10.1017/S0022112075001814](https://doi.org/10.1017/S0022112075001814).

- [34] S. B. Pope, Turbulent Flows, Cambridge University Press, 2000. URL: <https://books.google.ca/books?id=HZsTw9SMx-0C>.
- [35] S. Jain, N. Singhal, S. N. Shah, Effect of Coiled Tubing Curvature on Friction Pressure Loss of Newtonian and Non-Newtonian Fluids - Experimental and Simulation Study, in: SPE Annu. Tech. Conf. Exhib., Society of Petroleum Engineers, Houston, Texas, 2004, p. 12. URL: <https://doi.org/10.2118/90558-MS>. doi:10.2118/90558-MS.
- [36] Y. Zhou, S. Shah, Fluid flow in coiled tubing: a literature review and experimental investigation, J. Can. Pet. Technol. 43 (2004).

Chapter **4**

# Investigation of abrasive wear in contact load-dominated slurry flow regime using a toroid wear tester

A part of this Chapter 4 has been submitted as

*"Oluwaseun E. Adedeji, Lisheng Zhang, David E.S. Breakey, R. Sean Sanders, Investigation of abrasive wear in contact load-dominated slurry flows using a toroid wear tester"*

to the 23rd International Conference of Wear of Materials, Banff, Canada, April 24-49 2021 and will be published in Wear Journal. The manuscript was submitted for peer review on September 07, 2020.

## Abstract

Friction loss in slurry pipelines transporting coarse (settling) particles are governed by two mechanisms: Coulombic and kinematic friction. The Coulombic (sliding bed) friction component produces a highly abrasive condition that results in significant wear at the pipe invert and produces asymmetric thinning of the pipe wall. In this paper, an experimental investigation was carried out to study abrasive wear under Coulombic friction-dominated slurry flow conditions. Experiments were conducted in a laboratory-scale apparatus known as the Toroid Wear Tester (TWT) using narrowly-sized coarse particles (0.125-4 mm) suspended in three different carrier fluids ( $\mu_f$ : 1-5.12 mPas,  $\rho_f$ : 998-1103 kg/m<sup>3</sup>). The friction loss attributable to the presence of the coarse particles was obtained from torque measurements made during each test. Visualization experiments were used to establish contact load-dominated (sliding bed) slurry flow conditions based on the ratio of flow velocity to the particle terminal settling velocity i.e.  $V/v_\infty$ . Abrasive wear experiments were then conducted with the TWT operating under full contact load conditions. It was found that the measured wear rates correlated with the magnitude of the Coulombic shear stress. The most important outcome of this study is the demonstrated potential to predict actual slurry pipeline wear rates from TWT experiments.

## List of Symbols

$T$	Torque, $Nm$
$N$	Rotational velocity, $RPM$
$W$	Toroid wear tester channel width, $m$
$\beta$	Angle subtended by bed of particles
$\theta$	Angle of rotation of bed of particles
$\rho_s$	Particle density, $kg/m^3$
$\rho_f$	Fluid density, $kg/m^3$
$g$	gravity, $m/s^2$
$\eta_s$	Coefficient of friction
$C_{max}$	Limiting solids volume concentration
$r$	Wheel radius, $m$
$r_{min}$	Wheel inner radius, $m$
$r_{max}$	Wheel outer radius, $m$
$D$	Wheel outer diameter, $m$
$V$	Wheel linear velocity, $m/s$
$v_\infty$	Particle terminal settling velocity, $m/s$
$\tau_c$	Coulombic stress, $Pa$
$n$	Velocity exponent in wear correlation

## 4.1 Introduction

### 4.1.1 Background

Most industrial slurry pipelines transporting coarse (settling) particles operate under heterogeneous flow conditions [1–7] that typically result in more abrasive conditions at the pipe invert [8–11]. This leads to an asymmetric wear damage distribution in the pipe where the pipe wall thickness loss is greater at pipe invert than at the top of the pipe [8, 12–14]. It has been reported that the degree of wear at the pipe invert can be 7 times that of the pipe soffit [8, 12–16]. This observed wear damage behaviour can be directly linked to the physical mechanisms that govern pressure drop (friction loss) in horizontal slurry pipelines.

One of the most widely used friction loss model for heterogeneous slurry flow, the Two-Layer model [1, 7, 17] includes two mechanisms through which the coarse (settling) particles contribute to the slurry friction loss: kinematic and Coulombic friction. The kinematic friction accounts for the impacts of the suspended particles with the pipe wall and with one another [1, 18]. This friction loss mechanism must be accounted for across the entire pipe cross-section (i.e. in both the upper and lower layers of the Two-Layer model). The Coulombic friction, on the other hand, is restricted to the lower portion of the pipe cross-section and is due to the immersed weight of particles which is partly transmitted to the pipe wall. The particles are, therefore, not completely suspended by the fluid turbulence and produce the Coulombic or "sliding bed" friction. This Coulombic friction is responsible for the additional wear damage typically found at the slurry pipe invert [8, 12].

Many researchers have studied the relationship between wear rate and Coulombic friction (and total friction loss) in slurry pipelines [8, 14, 15, 19, 20]. In the work of Shook et al. [8], slurry pipeline wear rate was shown to relate linearly to the immersed weight of particles and the particle flux (i.e solids concentration  $\times$  velocity). Other investigations like those of Yang et al. [20], Rizkalla and Fletcher [19], Sadighian [15], and Adane et al. [14] also showed a direct relationship between wear rate and the total friction loss due to the presence of the coarse particles i.e. the total of the kinematic and Coulombic friction minus the contribution from the carrier fluid. These studies did not, however, address the fact that wear mechanisms would differ depending on whether the slurry flow is dominated by kinematic or Coulombic friction loss. Wear in a slurry flow dominated by kinematic friction would mostly come from a high impact angle deformation damage mechanism while a

Coulombic friction-dominated slurry flow (with sliding bed) would experience highly abrasive action of particles with cutting damage mechanism [9–11, 21]. This means a single wear correlation can only be applied over a limited slurry operating condition and that different wear correlations are needed for different slurry flow regimes.

In this study, the focus is on abrasive wear damage produced under Coulombic friction-dominated slurry flow conditions. Experimental investigations were conducted using a laboratory-scale device known as the Toroid Wear Tester (TWT). The TWT has been used to simulate slurry pipeline flow and perform wear tests to rank pipeline construction materials [22–26], though, the ultimate goal is to develop a predictive tool for slurry pipeline wear. This means it must be possible to use wear correlations from the TWT to interpret wear data from industrial slurry pipelines. The inherent challenges are the differences between the TWT and slurry pipeline hydrodynamics (e.g. the presence of secondary flows in the TWT) which were investigated in previous studies [22–27]. These studies revealed wear trends (e.g. wear rate versus bulk flow velocity or particle size) similar to those in slurry pipelines but only for specific operating conditions; for example, when the TWT was operated at low rotational speeds and with coarse concentrated slurry. The objectives of this study are (1) to establish flow conditions dominated by Coulombic friction in the TWT and (2) to conduct abrasive wear tests under these conditions and study how wear rate correlates with Coulombic friction. The investigations conducted in this study are as follows:

- Friction losses in the TWT were characterized using torque measurements (described in Section 4. 2).
- Coulombic friction loss model for contact load (or sliding bed) slurry flow in the TWT was validated using the experimental torque data.
- Images from visualization experiments were used to study particle bed behaviour and further validate Coulombic friction-dominated flow conditions based on the ratio of slurry flow velocity to the particle terminal settling velocity (i.e.  $V/v_{\infty}$ ). Four slurry flow regimes- fully settled, partially settled, partially disperse, and fully dispersed - were identified in the TWT.
- Wear experiments were conducted to span over the entire slurry flow regimes identified in the TWT. The wear rates were correlated with the measured friction losses to establish a relationship in the Coulombic friction-dominated conditions.

## 4. 1.2 History and operation of the TWT

The TWT has been used as an analogue of slurry pipe flow to investigate flow characteristics and wear behaviour. The earliest record was in 1955 where Worster and Denny [28] investigated the degradation of coal particles during transport. They termed the TWT a "ring pipe" and reported the coal slurry to be approximately a stationary bed as the wheel rotates. Traynis [29] investigated the hydraulic drag of slurry, particle degradation, and erosive wear using the so called "ring pipes" and concluded that they were suitable for simulating pipeline wear. The British Hydraulics Research Association (BHRA) also performed wear tests using a toroid with straight pipe sections [30]. They found that the toroid wheel produced wear patterns similar to those found in pipes. Patterson & Cooke Consulting also performed wear tests using the TWT and reported good agreement with field scale data [22]. More recently, Sarker [23], Zhang [24], and Sarker et al. [25, 26] performed detailed investigations to study the performance of the toroid wheel as a wear tester. They concluded that it is possible to identify similar flow conditions in the TWT and pipe where the wear mechanisms are similar, which means that the TWT can be used to investigate slurry pipeline wear.

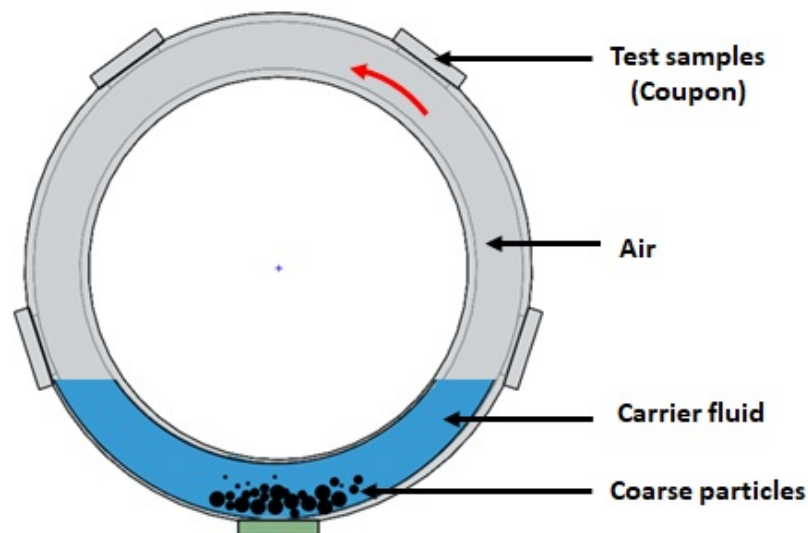


Figure 4.1: Illustration of the TWT operation. Adapted from Sarker [23].

Figure 4.1 shows a schematic that illustrates the basic operation of the TWT. The TWT described here is a hollow wheel fabricated from a section of a rectangular channel, bent to form a toroid shape. The TWT is partially filled to one-third capacity with concentrated

slurry and then rotated in a vertical plane. As the TWT rotates, the wall moves past a relatively stationary slurry so that the test coupons attached to the outer wall of the TWT (see Figure 4.1) are subjected to abrasive wear conditions. The characteristic velocity of the wear test is taken as the linear speed of the rotating wheel, and is assumed to be analogous to the bulk slurry velocity in a pipeline. Depending on the rotational speed, carrier fluid properties and particle size, the slurry particles may form a stationary settled bed or may be fully suspended. Again, slurry pipeline flows are characterized in a similar fashion.

## 4.2 Modelling Coulombic friction in the TWT

The total friction loss in the TWT is the torque required to rotate the wheel at a constant speed. This is the energy required to overcome internal and external friction [6, 24]. The external friction is a result of mechanical parts (e.g. bearings) and air drag while the internal friction is due to the contents of the TWT i.e. the liquid and solids that comprise the slurry. The friction loss due to the presence of the coarse (settling) particles can be determined from the torque measurements since

$$T_{solids} = T_{slurry + empty\ wheel} - T_{liquid + empty\ wheel} \quad (4.1)$$

where  $T$  is torque in  $Nm$ .

When the TWT system is operated under sliding bed conditions, the solids-only torque is purely due to Coulombic friction [1, 18, 24]. To model this Coulombic friction loss in the TWT, the pipe flow analysis of Gillies et al. [1] for slurry pipelines was adopted. Figure 4.2 shows the schematic illustrations of the TWT flow domain (Figure 4.2a) and the geometric descriptors of the bed (Figure 4.2b) from which the Coulombic friction model was developed for the TWT. As shown in Figure 4.2a, the particles are in contact with the two side walls and the bottom wall of the TWT channel. The arrows shown indicate the forces exerted by the particles on the bottom wall ( $F_1$ ) and side wall ( $F_2$ ) of the TWT channel. Also, as the TWT wheel rotates, the particle bed is inclined such that a perpendicular line at the centre of the bed is at an angle  $\theta$ . The bed also subtends an angle  $\beta$  at the centre of the wheel. These angles ( $\theta$ ,  $\beta$ ) change with the TWT rotational speed but are restricted to Coulombic friction-dominated conditions where particles are settled.

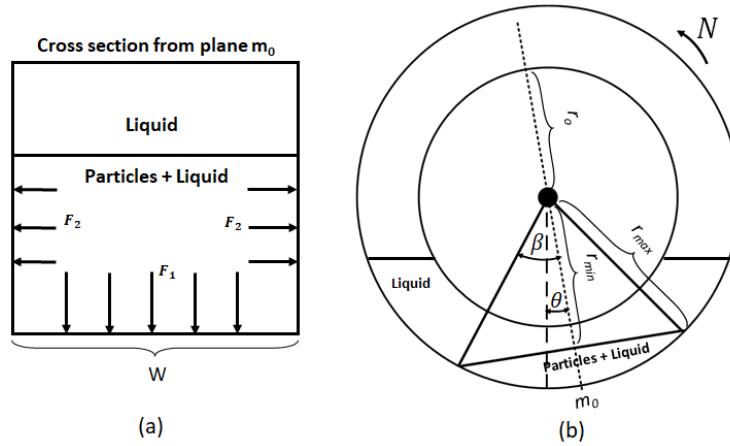


Figure 4.2: Schematic of Coulombic friction formulation for torque prediction in the TWT (a) cross section of wheel channel (b) wetted arc length.

The Coulombic friction model derived for the TWT is

$$\tau_c = \frac{12g\eta_s C_{max} \cos\theta (\rho_s - \rho_f)}{D_h \pi^2 (r_{max} + r_o)^2} \left[ \frac{W}{2} F_1 + F_2 \right] \quad (4.2)$$

where  $r_{min} = r_{max} \cos\beta$  and  $D_h$  is the hydraulic diameter of the TWT rectangular channel. The variable  $\eta_s$  is the coefficient of friction, which is typically taken as 0.5 for sand and gravel slurries in steel pipes [1, 17]. The limiting or maximum (settled bed) solids volume concentration is given by  $C_{max}$ . The limiting solids volume concentration differs for different particle size distributions and particle shapes, and must be measured at the respective operating condition where the model will be used to predict Coulombic in the TWT [24]. In this study, measured  $C_{max}$  was between 0.51-0.6. The variables  $\beta$  and  $\theta$  must also be measured from visualization experiments (Section 4.3.3).

The force  $F_1$  acting on the bottom wall of the TWT channel is given by

$$F_1 = (\sin\beta - \beta \cos\beta) r_{max}^3 \quad (4.3)$$

while the force  $F_2$  acting on the side walls of the TWT channel is

$$F_2 = \int_{r_{min}}^{r_{max}} r^3 \sqrt{1 - \frac{r_{min}^2}{r^2}} - r_{max} r^2 \cos\beta \cos^{-1} \left( \frac{r_{min}}{r} \right) \quad (4.4)$$

As mentioned, torque is the measured parameter during TWT operation. This torque (in  $Nm$ ) must be converted to Coulombic friction (in  $Pa$ ). A model for a circular channel toroid reported in the work of Gillies et al. [31] was adapted to convert torque and Coulombic friction, and is given by

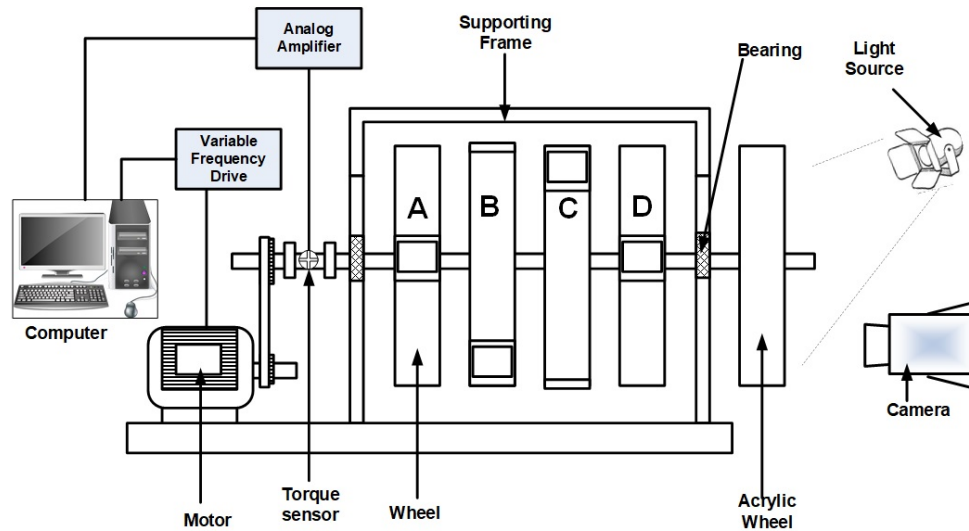
$$T = \frac{\tau_c D_h \pi^2 (r_{max} + r_o)^2}{3} \quad (4.5)$$

Details of the step-by-step development of the model can be found in Zhang [24]. The model in Equation 4.2 will be validated using that measured torque data for sand-water slurries.

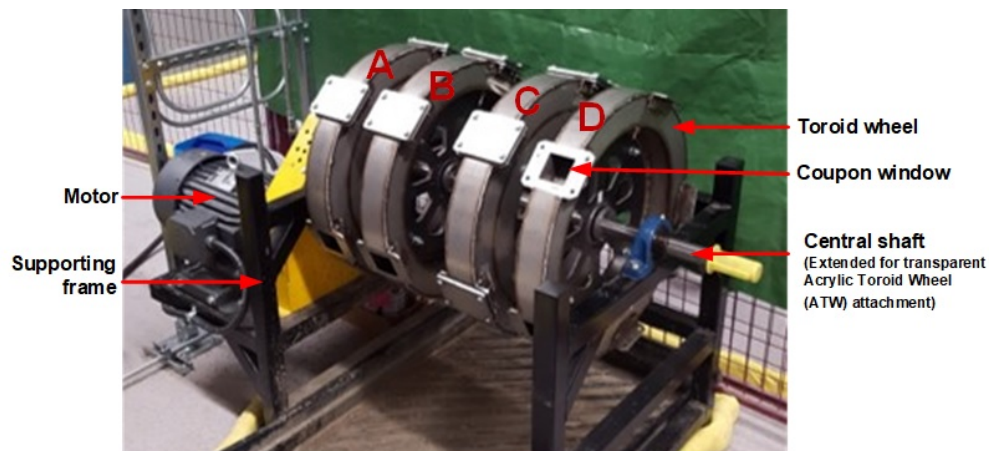
## 4.3 Experiments and Methods

### 4.3.1 Wear experiment

The TWT device in use in the Pipeline Transport Processes (PTP) Research Laboratory at the University of Alberta [23, 24, 26] is shown in Figure 4.3. The TWT rig consists of four stainless steel wheels labelled A, B, C, and D. The inner and outer diameters of the wheels are  $0.488\text{ m}$  and  $0.608\text{ m}$ , respectively. All the wheels were fabricated from a channel with a rectangular cross-sectional area. The dimension of the rectangular flow domain of wheels A, B, and C is  $60 \times 65\text{ mm}$  while that of wheel D is  $60 \times 58\text{ mm}$ . Each wheel has five rectangular openings (the "Coupon windows") where coupons (i.e. test samples) are attached and held in place by a stainless steel coupon holder. The wheels are mounted on a central shaft of diameter  $38.1\text{ mm}$ . The shaft is fitted into two bearings on the supporting frame and is connected to a  $2.24\text{ kW}$  ( $3\text{ hp}$ ) motor through a timing belt pulley drive. The motor is connected to an alternating current (AC) power source through an electrical cable. The motor speed is controlled by a variable frequency drive (VFD) through an in-house software installed on a computer. To prevent corrosion while running slurry wear experiments, all the wheels have a nitrogen ( $N_2$ ) charging port and an air discharge port to purge the wheels of oxygen. The test coupons for the wear measurement experiment were machined from ASTM A572 GR50 carbon steel plates purchased from US Steel Canada Inc. The coupons have dimensions of  $8\text{ mm} \times 100\text{ mm} \times 80\text{ mm}$  for wheels A, B, C, and  $8\text{ mm} \times 63.5\text{ mm} \times 63.5\text{ mm}$  for wheel D. The coupon sides that are not exposed to the flow during the experiment were coated with zinc oxide (ZnO) to eliminate corrosion on those surfaces.



(a)



(b)

Figure 4.3: The TWT device set up: schematic and photograph of the installation.

The wear experiments were conducted with slurries prepared from six different erodent particles with sizes that ranged from 0.125-4  $mm$ . Table 4.1 provides a summary of the different erodent particle types used. The carrier fluids used for the slurries were prepared from glycerin-water mixtures and have viscosity and density between 1-5.12  $mPas$  and 998-1103  $kg/m^3$ , respectively. Table 4.2 provides a summary of the carrier fluid properties. The particle-fluid combinations were selected to allow for collection of wear data over a wide range of slurry friction losses in the TWT.

Table 4.1: Properties of erodent particles used in the experiments of this study (All particles have a true density,  $\rho_s$ , of  $2650 \text{ kg/m}^3$ )

<b>Particle type</b>	<b><math>d_{50}</math> (mm)</b>
Gravel	4
Gravel	2
Gravel	1
Sil 4	0.425
Sil 1	0.25
LM 125	0.125

Table 4.2: Properties of carrier fluid used to prepare the slurries tested in this study

<b><math>C_L</math> (vol.% glycerin)</b>	<b>Viscosity, (<math>\mu_f, mPas</math>)</b>	<b>Density (<math>\rho_f, kg/m^3</math>)</b>
0	1	998
20	2.27	1050
40	5.12	1103

For each wear test, the wheels A, B, and C were filled to one-third capacity with 2.3 L of slurry. The solids volume concentrations ( $C_S$ ) tested were 10, 15, and 20% at rotational speeds of 30, 45, 60 and 90 *RPM*. Each experiment was conducted for 96 hours (4 days). Slurry was replaced every 24 hrs to minimize the effect of particle degradation on the measured wear loss. To eliminate corrosion effects, an oxygen scavenger (HYDROGUARD® from Angus Chemical Company) was used to reduce the level of dissolved oxygen (DO) in the slurry. Nitrogen ( $N_2$ ) at 5 *psig* was used to purge air out of the wheels. The initial mass of each test coupon was weighed (as  $m_i$ ) using an electronic balance (A & D Weighing, Model: Fx-3000i) before attachment to the wheel. To ensure a properly sealed wheel, a general-purpose lubricant by Rust Check and a 0.5 *mm* thick paper gasket by Dynoteq (Model: Tesnit BA-U) were placed between the coupons and coupon windows before they are secured by the holder. A DO probe (SPER Scientific, Model: 850048-i) was used to measure the DO level after purging to ensure it is less than 1.0 *ppm*. This purging procedure is repeated each time the slurry inside the TWT wheel was replaced. This usually took about 1 hour which means the actual run time of experiments is 92 hrs for the four days (i.e. 96 minus 4 hrs). At the end of each experiment, the coupons are detached from the wheel, cleaned, weighed and the final mass of each recorded as  $m_f$ . The mass difference ( $\Delta m(g) = m_i - m_f$ ) between initial and final weight of each coupon was used to calculate the erosion rate (mm/year) using

$$ER = \frac{\Delta m}{\rho_t A_t t} \times \frac{8760 \text{ hours}}{1 \text{ year}} \quad (4.6)$$

where  $\rho_t = 0.0078 \text{ g/mm}^3$  (the density of the coupon material),  $A_t(\text{mm}^2)$  is the area of coupon exposed to wear, and  $t(\text{hours})$  is the experimental run time.

Wear rate patterns on the exposed surfaces of the coupons were also measured using a surface profilometer (Mitutoyo, Model: Contracer CV-3100). The measurements were taken along  $140 \times 37$  lines on the coupon surface and were reported in  $x, y, z$  co-ordinates, where  $z$  is the depth or thickness loss in  $\text{mm}$ . An in-house MATLAB code was then used to process that data to display the erosion depth colour map. Wear rates for specific coupons were also determined from the surface profiles by calculating the total volume of material removed using a double trapezoidal integration implemented in MATLAB [23]. The accuracy of the wear rate for the coupons determined using the surface profile measurements was evaluated using the gravimetric method. The mean wear rates estimated from the surface profile measurements are within 20% of those obtained from the gravimetric method.

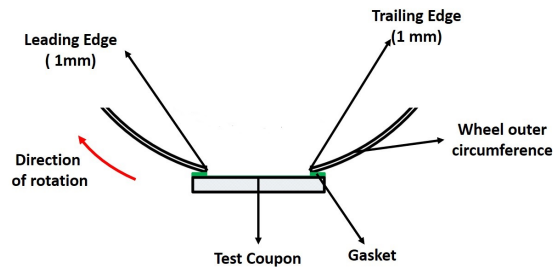


Figure 4.4: Coupon-wheel contact with edge clearance in the TWT.

In the design of the TWT, it was not possible to make the test coupons flush with the TWT wall, as shown in Figure 4.4. The thickness of the TWT wheel and the gasket between the test coupon and wheel introduced about 1  $\text{mm}$  clearance between the surface of the test coupons and the inner surface of the TWT wall. This clearance induces non-uniformity in the distribution of wear on the coupon surface, such that the leading edge experiences more than double the amount of wear at the trailing edge. In the development of the wear correlation in this study, the wear data were corrected to minimize the errors due to this leading-edge effect. Details about the correction procedure can be found in Sarker et al. [26].

### 4. 3.2 Torque measurement

To make torque measurements, a torque sensor was installed on the central shaft of the TWT. The torque sensor was already calibrated by the manufacturer to be within 2% accuracy. Further calibration tests were conducted to verify the stated factory accuracy margin [24]. An analog amplifier was used to communicate an electrical signal from the torque sensor to a computer via a USB cable. The torque sensor consists of a strain gauge that changes resistance when the shaft deforms due to the weight and rotation of the TWT wheel plus the contents. The transmitted data was collected and processed using an in-house MATLAB code which outputs the measured torque in  $Nm$ . The solids-related torque was determined from the torque measurements using the procedure summarized below:

1. The TWT was first operated empty at each rotational speed and the torque values recorded as  $T_0$ , ( $Nm$ ).
2. One of the wheels (A, B or C) shown in Figure 4.3 was then filled to one-third capacity with each of the prepared liquid samples. The torque values were measured and recorded as  $T_1$  for each of the liquid samples at the same rotational speeds tested in Step 1. The liquid-related torque values for each speed were calculated as  $T_L = T_1 - T_0$ .
3. One of the wheels (A, B or C) was then filled to one-third capacity with a prepared slurry. The torque values were measured and recorded as  $T_2$  for each of the liquid samples at all rotational speed tested. The slurry-related torque values were calculated as  $T_S = T_2 - T_0$ .
4. The solids-only torque is the difference between the torque measured for the slurry and that of the liquid used to prepare the slurry at the same rotational speed. The solids-only torque was, therefore, calculated as  $T = T_S - T_L = T_2 - T_1$ .

The solids-only torque values were obtained for the same liquid-particle combinations used in wear experiments. The experiments were run at rotational speeds between 10-90  $RPM$  with a 10  $RPM$  increment at solids volume concentrations ( $C_S$ ) of 10, 15, and 20%.

### 4. 3.3 Flow visualization

A transparent Acrylic toroid wheel (ATW) was used to conduct the flow visualization experiment. As shown in Figure 4.3, the TWT central shaft extends to allow attachment of the ATW. The ATW is not equipped with coupon windows, a Nitrogen charging port, or an air discharge port; however, it contains two circular openings of diameter 20 mm on the side walls for slurry charging and withdrawal. The dimensions of the ATW are the same as those of wheels A, B, and C. To conduct a visualization experiment, the ATW was filled to one-third of its volume with the respective slurry. The flow visualization experiments were conducted at identical TWT operating conditions to those under which the torque and erosion wear measurements were taken. A Canon T3i high speed digital camera was used to record videos at a rate of 60 frames per second (FPS) and capture images with a resolution of  $1280 \times 720$  pixels. The camera was connected to a computer via a USB cable which provides live observation of the flow inside the ATW. This helped with proper alignment of the camera for the visualization tests. A halogen light source was used to ensure proper illumination of the ATW contents. Also, according to the TWT Coulombic friction model (Equation 4.2), the variables  $\beta$  and  $\theta$  must be measured from captured images of the particle bed. The Java-based ImageJ image processing program was used to measure these angles. Details regarding this procedure can be found in Zhang [24].

## 4. 4 Results and discussion

### 4. 4.1 Identification of contact-load dominated flow in the TWT

The trend of the solids-related torque values can be used to deduce which friction loss mechanisms (Coulombic or kinematic) is dominant at specific operating conditions i.e. one can determine the degree of particle suspension to some extent. Figure 4.5 compares the behaviour of 0.250, 0.425, and 2 mm particles in the three different carrier fluids. Figure 4.5a presents the solids-related torque for slurries of the 2 mm gravel. Here, the torque values decrease on average, with increasing RPM for the entire rotational speeds. At the initial rotational speed (10 RPM), the particles are settled and friction loss is mostly produced by Coulombic forces. As the wheel speed increases, the particle bed begins to expand and the particles are gradually suspended by the fluid turbulence. This reduces the friction

(Coulombic) between the particle bed and TWT wall, thereby resulting in a decrease in the solids-related torque. How easily the particles become suspended is related to how rapidly the torque values decrease. This can be observed in Figure 4.5b that shows how the torque for suspension of Sil 1 (0.425 mm) particles in water and in the 20% glycerin-water mixture decreases with increasing rotational speed.

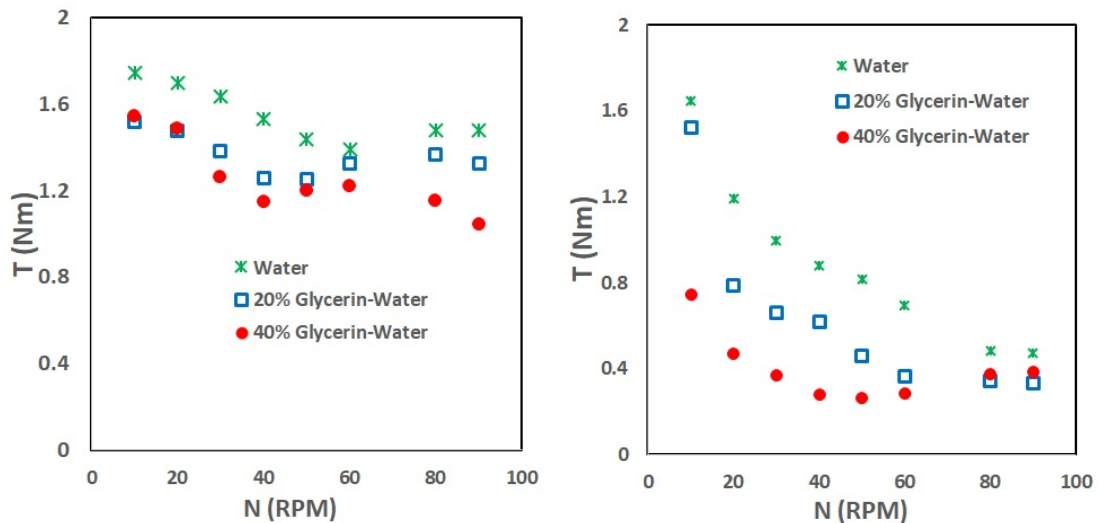
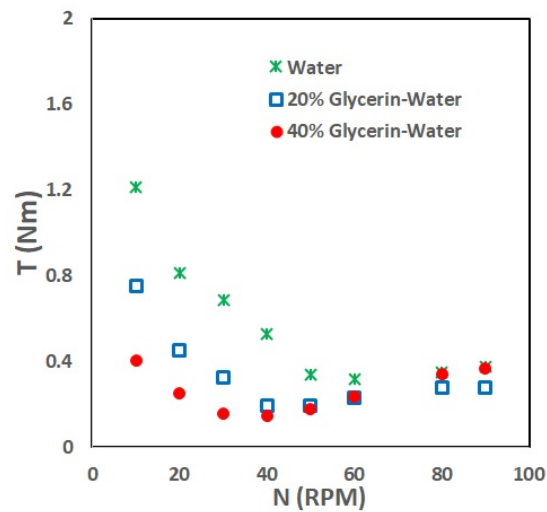
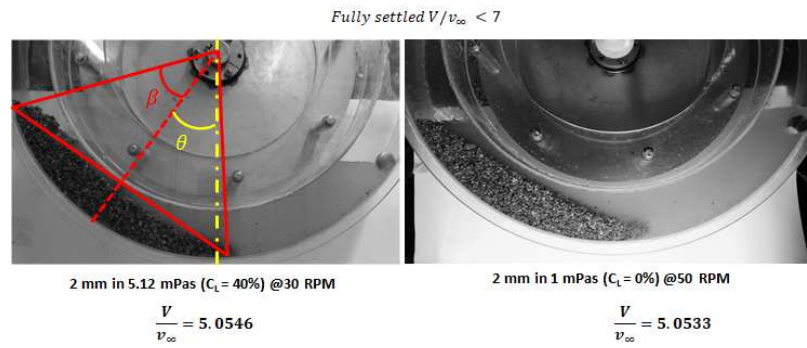
(a) Gravel (2 mm),  $C_S = 20\%$ (b) Sil 4 (0.425 mm),  $C_S = 20\%$ (c) Sil 1 (0.250 mm),  $C_S = 20\%$ 

Figure 4.5: Effect of fluid properties on the measured solids-related torque

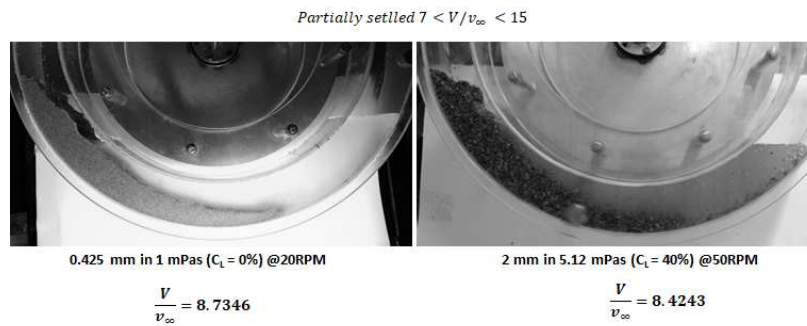
Furthermore in Figure 4.5b, when the particles are suspended in the 40% glycerin

mixture, the solids-related torque decreases to a minimum of  $0.264 \text{ Nm}$  at approximately  $50 \text{ RPM}$  and then begins to increase. This transition indicates the point where the settled bed of particles becomes mostly suspended and after which friction loss is mostly due to the random impact of the suspended particles on the TWT wall. In other words, the conditions changed from Coulombic to kinematic friction-dominated flow. In Figure 4.5c, the solids-related torque determined for mixtures containing Sil 1 ( $0.250 \text{ mm}$ ) particles exhibited similar behaviour. For each of the mixtures, the solids-related torque shows a trend similar to that of the larger ( $0.425\text{mm}$ ) particles suspended in the most viscous carrier fluid. Specifically, the solids-related torque decreases with increasing wheel speed until a minimum value is reached, at which point the torque increases with increasing RPM. The torque reaches a minimum value at successively lower wheel speeds as the carrier fluid's suspension properties increase (i.e., the density and viscosity increase). The behaviour of the particle bed was further evaluated through visualization experiments. The ratio of the flow velocity to the particle terminal settling velocity (i.e.  $V/v_\infty$ ) was used to characterize the flow behaviour. This dimensionless variable is used to calculate the magnitude of Coulombic friction in the slurry pipeline friction loss model [1], and was therefore selected for this reason. Figure 4.6 shows images of different particle beds at TWT operating conditions with similar  $V/v_\infty$ . All the images are at 20% solids volume concentration. It is apparent from the figure that when the  $V/v_\infty$  value is conserved, irrespective of the TWT operating conditions, the bed of particles exhibits similar behaviour. It was also observed that the fully settled condition dominated by contact load (Coulombic friction) occurs when  $V/v_\infty < 7$  (Figure 4.6a). Under this condition, the bed is entirely supported by the wall of the TWT wheel. As the system condition changes to higher  $V/v_\infty$  values, the particle bed is seen to expand continuously until the particles are fully dispersed at about  $V/v_\infty > 50$ . Different flow conditions termed as partially settled ( $7 < V/v_\infty < 15$ ), partially dispersed ( $15 < V/v_\infty < 50$ ), and fully dispersed ( $V/v_\infty > 50$ ) have been presented in Figures 4.6b, 4.6c and 4.6d, respectively.

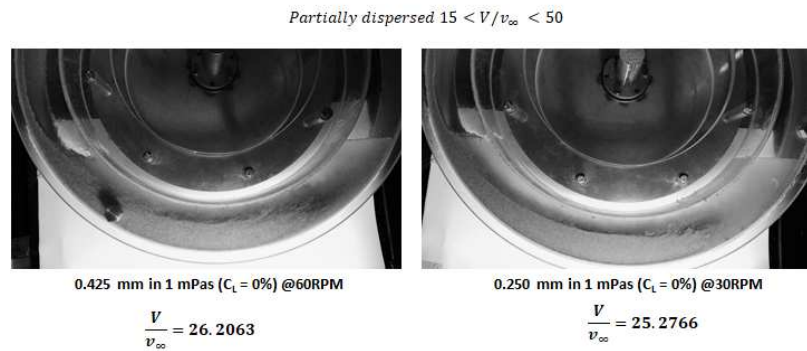
In physical terms, the variable  $V/v_\infty$  depicts how the energy of the fluid can resist the settling of particles or in other terms, and how easily the fluid can suspend particles in the bed. When  $V/v_\infty$  is low, the particles tend towards settling. On the other hand, when  $V/v_\infty$  is high, the system condition favours the suspension of particles.



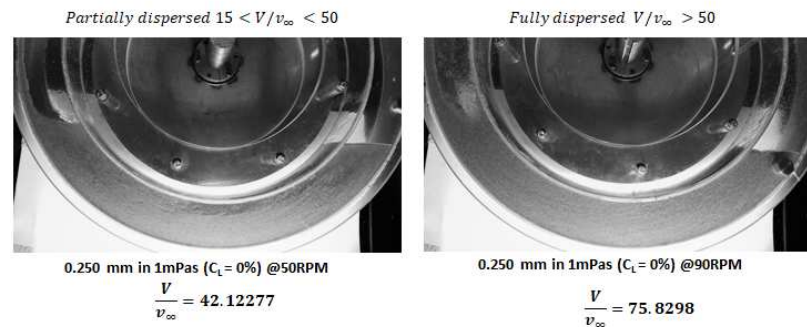
(a)



(b)



(c)



(d)

Figure 4.6: Visualization of slurry bed behavior under different system condition

Also shown in Figure 4.6a (image on the left) are lines drawn to measure the particle bed variables  $\beta$  and  $\theta$  used in the Coulombic friction model presented in Equation 4.2. The variables were measured only for sand-water slurry for the purpose of validating the model. It was only possible to measure these variables for 1 mm particles between 10-40 *RPM* and 2 mm particles between 10-60 *RPM*. These conditions are within  $V/v_\infty < 7$  identified previously. Also, beyond this point, the sliding bed expands and is much more dispersed. Hence, the measurement of  $\beta$  and  $\theta$  would not be accurate. Figure 4.7 shows comparison between measured and predicted Coulombic friction validated for the suspensions of 1 and 2 mm particles in water at solids volume concentrations of 10%, 15%, and 20% (differentiated by colours). The maximum error between the predicted and measured torque value is  $\pm 15\%$ . Increasing solids concentration also results in higher Coulombic friction because of the a greater weight of the particle bed. Also in Figure 4.7, it can be seen that the torque for 1 mm particles was slightly higher than those of the 2 mm particles especially at 20% solids volume concentration.

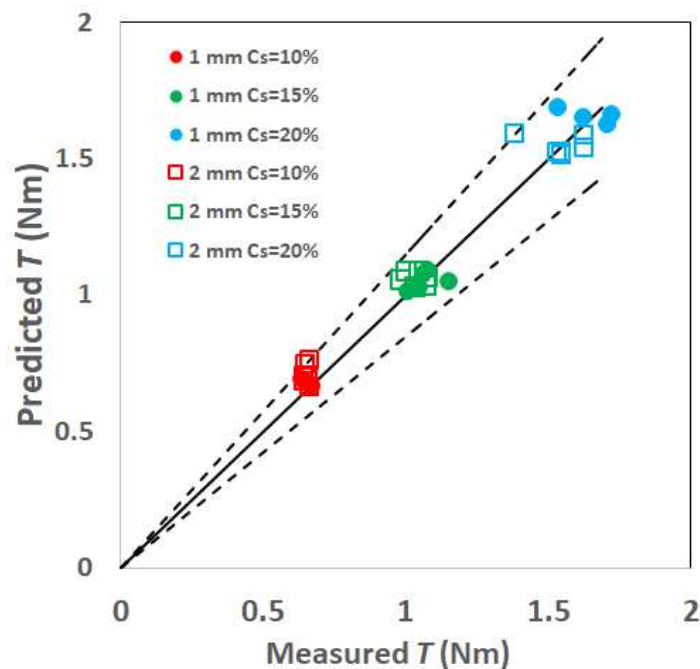


Figure 4.7: Parity plot for the measured and predicted Coulombic friction for sand-water slurry

This was only observed at the low rotational speeds that meet the fully settled bed

condition. One possible explanation for this observation was the presence of more fines in the 2 mm slurry which would slightly increase bulk fluid viscosity, hence, how easily the bed expands. Overall, for each slurry flow condition demonstrated in this section (i.e. from fully settled to fully dispersed), it is clear that the wear damage mechanisms would be different. This means more than one wear correlation may be needed to assess slurry systems depending on the prevailing operating condition. This study, however, focused on abrasive wear in the Coulombic friction-dominated slurry flow region ( $V/v_\infty \leq 7$ ). It is worth mentioning that  $V/v_\infty$  is specific to a given TWT geometrical length scale. For example,  $V/v_\infty$  can be the same in a slurry pipeline with different diameters. This means particles would be subjected to different degrees of turbulence (defined by Reynolds number) in each system. In other words, the bed conditions would look different in pipes of different diameter when at the same  $V/v_\infty$ . Therefore, each slurry system may require a specific analysis to identify slurry flow conditions to select the appropriate wear correlation.

## **4. 4.2 Wear in contact load-dominated slurry flow**

### **Wear pattern analysis and correction for edge effects**

Analysis of the wear map (contour) of test coupons used in the wear experiment suggests that the edge effect (previously described in Section 4. 3.1) is a major source of uncertainty in the gravimetric method used to calculate the wear rates. The surface profiles of some selected test coupons are shown in Figure 4.8. The effect of the TWT coupon-wall edge clearance is evident in the wear distribution.

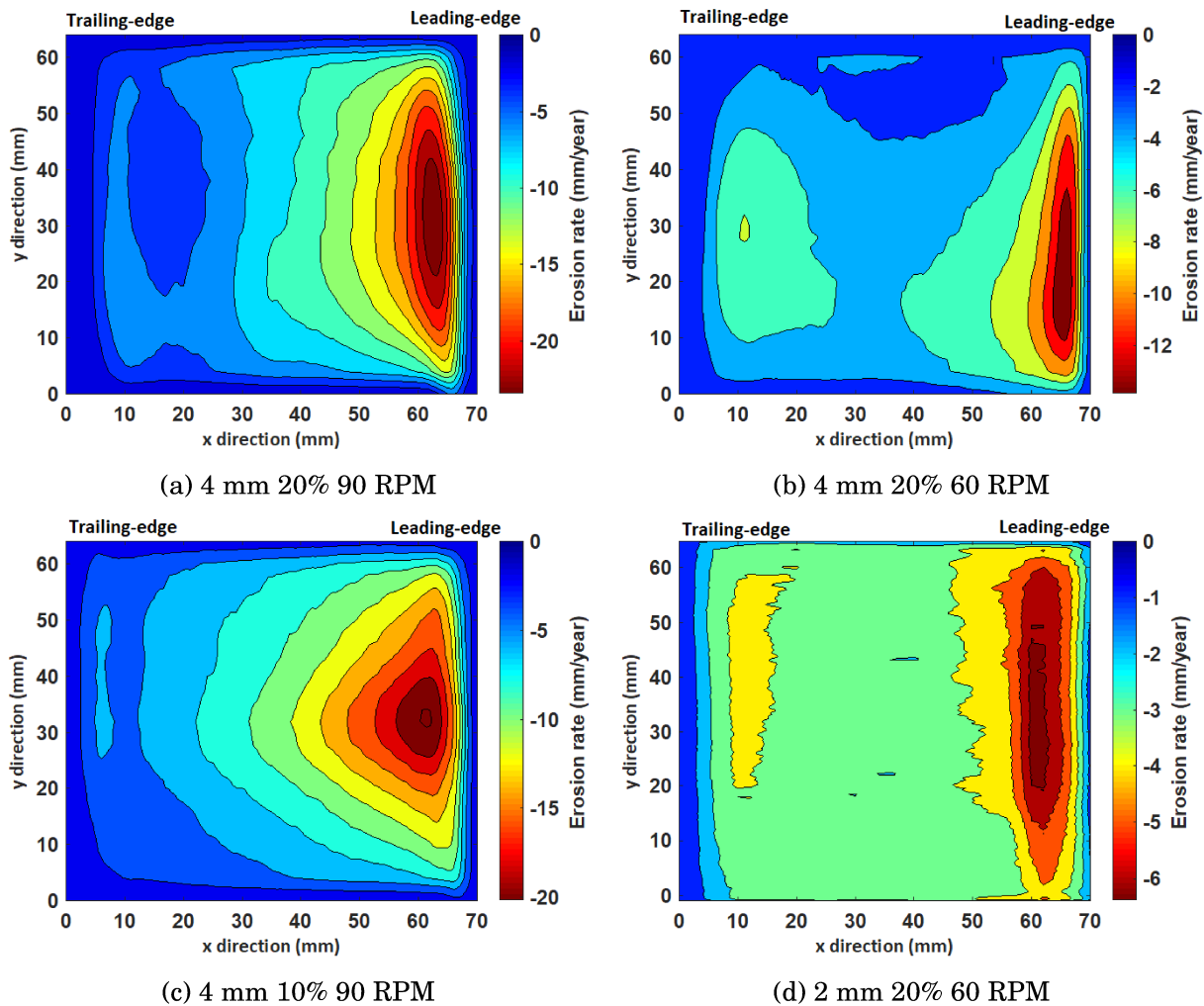


Figure 4.8: TWT test coupons wear map distribution.

The leading-edge side of the test coupons experienced significant wear compared to the trailing-edge where the distribution is more uniform. In fact, even without a surface profile measurement, the scar due to wear at the leading edge side of the coupons was visible to the naked eye. To account for the error due to this leading edge effect, wear rate was estimated for the trailing edge side of the coupon from the surface profile measurements. The mean wear rate from the surface profile was determined using double trapezoidal integration of the surface depth [23] which was implemented in MATLAB. This calculated the volume loss which was then converted to the average thickness loss per year using the material density and experimental run time. The corrected values of the wear rates were about by 40-60% less

than the initial measurements for 4 mm particles and 20-30% for 1 and 2 mm particles. The correction factors are higher for the 4 mm particles because they are much more abrasive. The effect of particle size can be observed by comparing Figure 4.8b with 4.8d. The maximum wear at the leading edge for the 4 mm particles is about 2 times that of the 2 mm particles. Therefore, eliminating the edge effects would result in higher values of the correction factors used for the 4 mm particles. The effect of wheel speed can also be seen to affect the leading edge effect. By comparing Figure 4.8a with 4.8b, it can be observed that maximum wear rate at the leading edge reduced by almost 50% going from 90 RPM to 60 RPM for the 4 mm particles at 20 vol.%. Also, comparing Figures 4.8a and 4.8c for the effect of solids volume concentration, the maximum wear rate at the leading edge was reduced by only 10% going from 20% to 10% solids concentration. Clearly, the severity of the damage at the leading edge side of the test coupons is more strongly dependent on particle size and wheel speed than on the solids volume concentration. The corrected wear rate values were used for analysis in the following section (Section 4.4.2).

### **Abrasive wear correlation**

Figure 4.9 presents the relationship between wear rate and Coulombic friction for suspensions of 4 mm, 2 mm and 1 mm particles at fully settled bed conditions in the TWT. The wear rates have been plotted against Coulombic friction alone in Figure 4.9a. In Figure 4.9b, the linear equivalent of the TWT rotational speed (30 RPM: 0.95 m/s, 45 RPM: 1.43 m/s, 60 RPM: 1.91 m/s, 90 RPM: 2.86 m/s) was multiplied by the Coulombic friction such that wear rate was plotted against  $\tau_c V^n$ . It is evident that the wear data show a linear relationship with Coulombic friction in Figure 4.9a for each slurry at the respective velocities. The severity of wear damage can also be seen to increase with particle size and rotational speed. Clearly, the 4 mm particles at 90 RPM (2.86 m/s linear velocity equivalent) are the most abrasive. The 2 and 1 mm particles at 30 RPM (0.95 m/s) are the least abrasive but with comparable wear rate values. Also, for each particle type shown in Figure 4.9a, the wear data that corresponds to each solids volume concentration have been indicated in the rectangular bars. It can be seen that higher solids volume concentration results in higher values of Coulombic friction and consequently, higher wear rates at the respective velocities and particle sizes. A linear relationship was also obtained in Figure 4.9b which presents the general form of abrasive wear in slurry pipelines [8, 14, 19, 20]. The value of  $x$  in the correlation on the plot represents

$\tau_c V^n$  where the velocity exponent  $n = 2$ . A good fit with  $R^2 = 0.9805$  was obtained for the wear data and the coefficient (i.e. 0.0266) represents the unique system characteristics e.g. geometry, material hardness and particle shape [32–37].

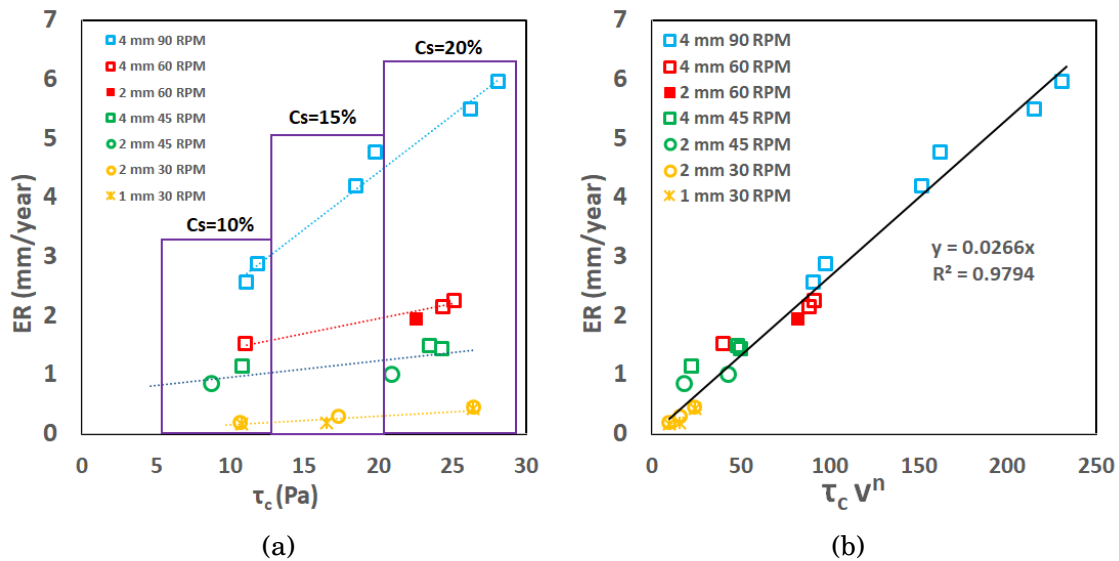


Figure 4.9: Correlation for abrasive wear at fully settled slurry condition in the TWT

On a general note, the wear rate relationship showed that both Coulombic friction and slurry flow velocity are the essential variables when estimating abrasive wear in slurries. The fact that the correlation follows the form of those obtained for slurry pipelines suggests there are definite similarities in wear damage mechanisms in the TWT and a pipeline. It also means there is increased potential to use the TWT as a tool to study and predict slurry pipeline wear. More investigations on the differences between the hydrodynamics and wear mechanisms inside the TWT and slurry pipeline are required for this correlation to be implemented. For example, how can one isolate the amount of wear due to only Coulombic friction in a pipe where both kinematic and Coulombic friction are equally dominant? How would one compare such wear rate to measurements taken in the TWT and also scale it to the overall wear loss in a pipe? However, since wear mechanisms on a local level are similar, the current wear correlation established here show how wear rate relates to slurry hydrodynamic variables in highly abrasive (sliding bed) conditions.

## 4.5 Conclusions

An investigation of abrasive wear in the sliding bed slurry flow regime was carried out using a bench-scale experimental device known as the Toroid Wear Tester (TWT). The behaviours of particle beds in the TWT were observed through visualization experiments. Coulombic friction-dominated slurry flow in the TWT was identified based on the ratio of the slurry flow velocity to the particle terminal settling velocity i.e.  $V/v_\infty$ . Analysis of the results revealed that the particle beds were fully settled when  $V/v_\infty \leq 7$  which means that Coulombic (sliding bed) friction dominates at this condition. The slurry bed behaviours were also validated with the images from the visualization experiments which confirmed that when  $V/v_\infty$  is constant, the particle bed behaves in a similar manner regardless of particle size and carrier fluid properties. A linear relationship was found to exist between wear rate and Coulombic friction when  $V/v_\infty \leq 7$ . The wear correlation obtained was identical to those reported for slurry pipeline systems in the literature. However, to use the TWT wear correlation for predicting slurry pipeline wear, one must isolate the contribution of Coulombic friction to the total wear loss in a slurry pipeline system. One option would be to completely eliminate (or account for) the intrinsic differences in the design and hydrodynamics between the TWT and a pipe. The latter would be the basis for translating wear data from the TWT to slurry pipelines or other systems where the local particle interactions with the target surface is similar to that in the abrasive conditions tested in the TWT.

## References

- [1] R. G. Gillies, C. A. Shook, K. C. Wilson, An improved two layer model for horizontal slurry pipeline flow, *Can. J. Chem. Eng.* 69 (1991) 173–178. URL: <http://doi.wiley.com/10.1002/cjce.5450690120>. doi:10.1002/cjce.5450690120.
- [2] A. D. Thomas, Predicting the deposit velocity for horizontal turbulent pipe flow of slurries, *Int. J. Multiph. Flow* 5 (1979) 113–129. doi:10.1016/0301-9322(79)90040-5.
- [3] K. C. Wilson, J. K. P. Tse, Deposition limit for coarse particle transport in inclined pipes, in: *Proc. 9th Int. Conf. Hydraul. Transp. Solids Pipes*, 1984, pp. 149–161.
- [4] R. Spelay, R. G. Gillies, S. A. Hashemi, R. S. Sanders, Effect of pipe inclination on

- the deposition velocity of settling slurries, *Can. J. Chem. Eng.* 94 (2016) 1032–1039. doi:[10.1002/cjce.22493](https://doi.org/10.1002/cjce.22493).
- [5] R. G. Gillies, J. Schaan, R. J. Sumner, M. J. McKibben, C. A. Shook, Deposition velocities for newtonian slurries in turbulent flow, *Can. J. Chem. Eng.* 78 (2000) 704–708. URL: <http://doi.wiley.com/10.1002/cjce.5450780412>. doi:[10.1002/cjce.5450780412](https://doi.org/10.1002/cjce.5450780412).
- [6] R. G. Gillies, C. A. Shook, Modelling high concentration slurry flows, *Can. J. Chem. Eng.* 78 (2000) 709–716. doi:[10.1002/cjce.5450780413](https://doi.org/10.1002/cjce.5450780413).
- [7] R. G. Gillies, C. A. Shook, J. Xu, Modelling Heterogeneous Slurry Flows at High Velocities, *Can. J. Chem. Eng.* 82 (2004) 1060–1065. doi:[10.1002/cjce.5450820523](https://doi.org/10.1002/cjce.5450820523).
- [8] C. A. Shook, M. McKibben, M. Small, Experimental investigation of some hydrodynamic factors affecting slurry pipeline wall erosion, *Can. J. Chem. Eng.* 68 (1990) 17–23. URL: <http://doi.wiley.com/10.1002/cjce.5450680102>. doi:[10.1002/cjce.5450680102](https://doi.org/10.1002/cjce.5450680102).
- [9] M. C. Roco, G. R. Addie, Erosion wear in slurry pumps and pipes, *Powder Technol.* 50 (1987) 35–46. doi:[10.1016/0032-5910\(87\)80081-5](https://doi.org/10.1016/0032-5910(87)80081-5).
- [10] M. C. Roco, Wear Mechanisms in Centrifugal Slurry Pumps, *Corros. Eng.* 46 (1990) 424–431.
- [11] N. Barkoula, J. Karker-Kocsis, Processes and influencing parameters of the solid particle erosion of polymers and their composites, *J. Mater. Sci.* 37 (2002) 3807–3820. doi:[10.1023/A.arXiv:0005074v1](https://doi.org/10.1023/A.arXiv:0005074v1).
- [12] J. Schaan, N. Cook, R. S. Sanders, On-line wear measurement for commercial-scale, coarse-particle slurry pipelines, in: 17th Int. Conf. Hydrotransp., Cape Town, South Africa, 2007, pp. 291–300.
- [13] B. Fotty, M. Krantz, J. Been, J. Wolodko, Development of a pilot-scale facility for evaluating wear in slurry pipeline systems, in: Proc. Hydrotransp. 18, September, Rio de Janeiro, Brazil, 2010, pp. 431–443.
- [14] K. F. Adane, M. Huard, A. Fuhr, Modeling Abrasion-Corrosion in Horizontal Pipeline Slurry Flows, 2019. URL: <https://doi.org/>.

- [15] A. Sadighian, Investigating Key Parameters Affecting Slurry Pipeline Erosion, Ph.D. thesis, University of Alberta, 2016. doi:[10.1017/CB09781107415324.004](https://doi.org/10.1017/CB09781107415324.004). arXiv:[arXiv:1011.1669v3](https://arxiv.org/abs/1011.1669v3).
- [16] A. J. Karabelas, An Experimental Study of Pipe Erosion by Turbulent Slurry Flow, in: Proc. Hydrotransp. 5, May, Hannover, Germany, 1978, pp. 25–24.
- [17] R. Spelay, S. A. Hashemi, R. G. Gillies, R. Hegde, R. S. Sanders, D. G. Gillies, Governing Friction Loss Mechanisms and the Importance of Off-Line Characterisation Test in the Pipeline Transport of Dense Coarse-Particle Slurries, in: ASME 2013 Fluids Eng. Div. Summer Meet., 2013, pp. V01CT20A013–V01CT20A013.
- [18] C. A. Shook, M. C. Roco, Slurry flow: principles and practise, Butterworth- Heinemann, Boston, USA, 1991. doi:<http://dx.doi.org/10.1016/B978-0-7506-9110-9.50007-4>.
- [19] P. Rizkalla, D. F. Fletcher, Development of a Slurry Abrasion Model Using an Eulerian-Eulerian ‘ Two-Fluid ’ Approach, in: Elev. Int. Conf. CFD Miner. Process Ind. CSIRO, December, Melbourne, Australia, 2015, pp. 1–8.
- [20] G. Yang, D. Serate, K. Tsai, M. Wu, Wear Modeling of Dense Slurry Flow in Oil Sands Coarse Tailings (CT) Pipelines, 2018. URL: <https://doi.org/>.
- [21] C. Huang, P. Mineev, J. Luo, K. Nandakumar, A phenomenological model for erosion of material in a horizontal slurry pipeline flow, Wear 269 (2010) 190–196. URL: <http://dx.doi.org/10.1016/j.wear.2010.03.002>. doi:[10.1016/j.wear.2010.03.002](https://doi.org/10.1016/j.wear.2010.03.002).
- [22] R. Cooke, G. Johnson, P. Goosen, Laboratory Apparatus for Evaluating Slurry Pipeline Wear, Technical Report March, SAIT Seminar, Calgary, 2000.
- [23] N. R. Sarker, A Preliminary Study of Slurry Pipeline Erosion Using a Toroid Wear Tester, MSc thesis, University of Alberta, 2016.
- [24] L. Zhang, Relating slurry friction to erosion rate using a toroid wear tester, MSc thesis, University of Alberta, 2018.
- [25] N. R. Sarker, L. Zhang, D. Breakey, B. A. Fleck, R. S. Sanders, Laboratory-Scale Erosive Wear Measurements Conducted with a Toroid Wear Tester (TWT), in: 8th Int. Conf. Transp. Sediment. Solid Part., September, 2017, pp. 295–303.

- [26] N. R. Sarker, D. E. S. Breakey, M. A. Islam, S. Sun, B. A. Fleck, R. S. Sanders, Performance and Hydrodynamics Analysis of a Toroid Wear Tester to Predict Erosion in Slurry Pipelines, *Wear* (2019) 203068. URL: <https://doi.org/10.1016/j.wear.2019.203068>. doi:10.1016/j.wear.2019.203068.
- [27] N. R. Sarker, M. A. Islam, R. S. Sanders, B. A. Fleck, CFD Analysis of the Hydrodynamics of an Air- Water Multiphase System in a Rotating Toroid Wheel, in: 23rd Annu. Conf. CFD Soc. Canada, April, Waterloo, ON, Canada, 2016.
- [28] R. C. Worster, D. F. Denny, Hydraulic transport of solid material in pipes, *Proc. Inst. Mech. Eng.* 169 (1955) 563–586.
- [29] V. V. Traynis, Parameters and flow regimes for hydraulic transport of coal by pipelines, Terraspace, Rockville. USA, 1977.
- [30] G. Henday, A comparison of commercial pipe materials intended for the hydraulic transport of solids, BHRA, 1988.
- [31] R. G. Gillies, R. Sun, M. Kosor, C. A. Shook, Laboratory Investigation of Inversion of Heavy Oil Emulsion, *Can. J. Chem. Eng.* 78 (2000) 757–763.
- [32] O. E. Adedeji, W. Yu, R. S. Sanders, Analysis of local wear variables for high-precision erosion modelling in complex geometries, *Wear* 426-427 (2019) 562–569. doi:10.1016/j.wear.2018.12.071.
- [33] D. R. Lester, L. A. Graham, J. Wu, High precision suspension erosion modeling, *Wear* 269 (2010) 449–457. doi:10.1016/j.wear.2010.04.032.
- [34] Y. I. Oka, T. Yoshida, Practical estimation of erosion damage caused by solid particle impact Part 2 : Mechanical properties of materials directly associated with erosion damage, *Wear* 259 (2005) 102–109. doi:10.1016/j.wear.2005.01.040.
- [35] Y. Zhang, E. P. Reuterfors, B. S. McLaury, S. a. Shirazi, E. F. Rybicki, Comparison of computed and measured particle velocities and erosion in water and air flows, *Wear* 263 (2007) 330–338. doi:10.1016/j.wear.2006.12.048.
- [36] A. Mansouri, A combined CFD-experimental method for developing an erosion equation for both gas-sand and liquid-sand flows, Phd thesis, University of Tulsa, 2016.

- [37] A. Gnanavelu, N. Kapur, A. Neville, J. F. Flores, N. Ghorbani, A numerical investigation of a geometry independent integrated method to predict erosion rates in slurry erosion, *Wear* 271 (2011) 712–719. URL: <http://dx.doi.org/10.1016/j.wear.2010.12.040>. doi:10.1016/j.wear.2010.12.040.

# Estimation of wear loss related to Coulombic and kinematic stress in dense slurry flow

A part of this Chapter has been accepted for presentation at the Hydrotransport Conference 2021 as

*Oluwaseun E. Adedeji, R. Sean Sanders, Estimation of wear loss related to Coulombic and kinematic friction in dense slurry flow in horizontal pipelines.*

The complete manuscript is ready for submission to Particle Science and Technology journal.

## Abstract

In a slurry pipeline, the total wear loss is the sum of the contributions from erosive and abrasive mechanisms. The erosive component is due to the random impact of particles while the abrasive component is due to the sliding action of particles. These mechanisms also correspond to kinematic and Coulombic friction loss in slurry flow respectively. Typically, the total wear loss in a slurry pipe can easily be quantified, however, the wear contribution due to each of these mechanisms is often not known. Quantifying the wear contributions due to each of these mechanisms will allow the selection of appropriate models for wear prediction as well as the design of an experimental wear-testing facility with hydrodynamics that is representative of the slurry system. In this study, the wear rates due to erosion and abrasion are quantified using a method of analysis that combined both numerical and semi-mechanistic slurry modelling techniques, namely Computational Fluid Dynamics (CFD) simulations and the Saskatchewan Research Council (SRC) Two-Layer Pipe-Flow Model<sup>TM</sup>. Experimental wear data obtained from high concentration slurry (20 Vol % and 30 Vol %) in a recirculating pipe-loop tester were used for the analysis. The wear data covered a wide range of operating regimes with slurry mean flow velocity between 2.28-8.22 m/s and two particle sizes of 250 $\mu$ m and 425 $\mu$ m. The results obtained gave a strong indication which wear mechanism will be dominant based on the contact load fraction or the ratio of kinematic to Coulombic friction loss in a slurry pipeline system.

## List of Symbols

$A$	Pipe cross sectional area, $m^2$
$A_1$	Top layer cross sectional area, $m^2$
$A_2$	Bottom layer cross sectional area, $m^2$
$c$	Instantaneous solids concentration
$C_1$	Top layer solids volume concentration
$C_2$	Bottom layer solids volume concentration
$C_v$	Delivered solids volume concentration
$C_r$	<i>in-situ</i> solids volume concentration
$C_c/C_r$	Contact load fraction
$D$	Pipe diameter, $m$
$E_{A_1}$	Top layer mass loss
$E_{A_2}$	Bottom layer mass loss
$E_T$	Total Wear loss
$E^o$	Specific erosion rate, $mm/Kg$
$E_C$	Wear loss due to Coulombic stress
$E_K$	Wear loss due to kinematic stress
$E_C$	Wear loss due to Coulombic stress
$ER$	Erosion rate, $mm/yr$
$F$	Normal force, $N$
$f_s$	Solids friction factor
$f_f$	Fanning friction factor
$g$	gravity, $m/s^2$
$h$	Height to interface, $m$
$d_p$	Particle diameter, $m$
$dP/dz$	Pressure gradient, $Pa/m$
$R$	Pipe radius, $m$
$Re_D$	Flow Reynolds number
$Re_p$	Particle Reynolds number
$S_1$	Top layer wetted perimeter, $m$
$S_2$	Bottom layer wetted perimeter, $m$
$S_{12}$	interface between top and bottom layer, $m$
$V$	Slurry mean velocity, $m/s$
$v$	Instantaneous particle velocity, $m/s$
$V_1$	Top layer slurry flow velocity, $m/s$
$V_2$	Bottom layer slurry flow velocity, $m/s$
$n, k, b, m$	Haung model fitting constants

$\rho_s$	Particle density, $kg/m^3$
$\rho_f$	Fluid density, $kg/m^3$
$\eta_s$	Coefficient of friction
$\mu_f$	fluid viscosity, $Pa\cdot s$
$\beta$	Angle subtended by lower layer
$\tau_{k1}$	Top layer kinematic stress, $Pa$
$\tau_{k2}$	Bottom layer kinematic stress, $Pa$
$\tau_k$	Kinematic stress, $Pa$
$\tau_c$	Coulombic stress, $Pa$
$\tau_w$	Wall shear stress, $Pa$
$\alpha$	Circumferential pipe angle

## 5.1 Background

In the design of slurry-transporting pipelines, many operational requirements must be met. For example, friction loss calculations for pump power requirement, a minimum operating velocity to avoid the deposition and accumulation of particles which can lead to blockage, and an optimal operating velocity to minimize failures due to wear damage must all be determined. The interaction of particles (in the slurry) with the pipe wall causes the wear damage that results in these failures [1]. Also, typical descriptions of friction loss mechanisms in slurry flows [2–4] are based on interaction of particles with the pipe wall; in fact, it has been shown that particle-impact wear can be correlated to these friction losses [1, 5, 6]. Depending on the operating and system condition of the slurry pipeline e.g. flow velocity, particle size, pipe diameter, the particles can either be fully suspended (homogeneous flow) or partially suspended (heterogeneous flow) by the fluid turbulence [7, 8]. The wear and friction mechanisms differ for these slurry flow conditions. It is suggested that kinematic friction will be associated with high impact angle *erosive wear* dominated by deformation damage while Coulombic friction will correlate with low impact angle *abrasive wear* dominated by cutting damage [9–11]. Fig. 5.1 shows an illustration of the difference between the erosive and abrasive wear mechanisms based on the slurry flow condition.

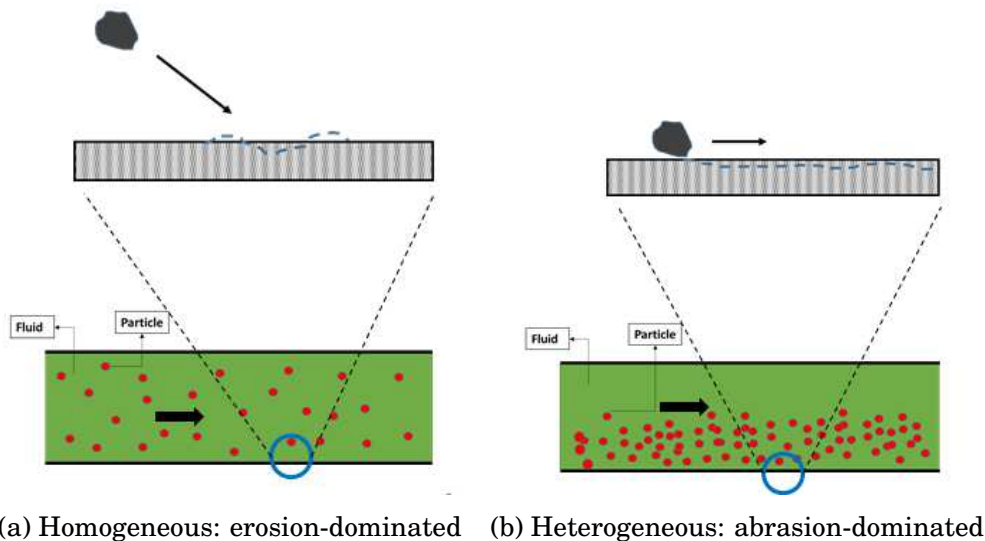


Figure 5.1: Types of slurry flow condition and the related wear mechanism

High velocity flows transporting small to medium size particles will likely result in erosive wear as shown in Fig. 5.1a, while flows transporting very large particles will result in cutting/abrasive wear as shown in Fig. 5.1b. A typical slurry pipeline system will have both erosive and abrasive wear occurring simultaneously. The total material loss or wear in a slurry pipeline is the sum of these erosive and abrasive wear mechanisms. Also, this total material loss is often the parameter known or measured when evaluating the wear performance for operating slurry pipelines. It is of great value to be able to determine the contributions of each of these two mechanisms to the total wear loss for the following reasons:

- Depending on the operating conditions of a slurry pipeline, the flow can be dominated by kinematic or Coulombic friction loss (or, more typically, a combination of the two). Knowledge of which wear mechanism is dominant allows one to select the appropriate wear model for performance evaluation. This is because wear models are system-specific. This means wear models developed at hydrodynamic conditions similar to those in the system being evaluated will give more accurate predictions because of the similarity in the dominating mechanism.
- To understand wear damage in an industrial pipeline, experimental investigations are usually carried out using bench-scale devices. Knowledge of the dominant damage mechanism will inform the choice of suitable wear-testing experimental device(s) within the appropriate operating envelope. For example, a jet impingement or slurry pot tester [12, 13] might be more suitable for wear studies of a kinematic friction-dominated slurry system than a toroid wear tester [14–17], which would be selected for Coulombic-friction dominated systems. None of these devices has comparable hydrodynamics to that in a slurry pipeline; however, at a local level, they can provide useful information about the specific wear mechanisms that they represent in a slurry pipeline i.e. erosion or abrasion.
- The interpretation of wear from one scale to another for slurry pipelines or from one geometry to another e.g. experimental device to industrial system, will yield more reasonable results if the knowledge of the dominant wear mechanisms in each of the scales or geometry are known.

In the present study, for the first time based on the knowledge of the authors, a method is developed to estimate the proportion of the total wear loss in slurry pipelines due to

each of the wear damage mechanisms described previously. This method combines the capability of Computational Fluid Dynamics (CFD) in predicting particle flux, and the underlying principles of the Saskatchewan Research Council (SRC) two-layer model that allows the calculation of kinematic and Coulombic friction loss for heterogeneous slurry flow. Experimental wear data obtained from concentrated slurry flow ( $C = 20\text{-}30\%$  solids by volume) in a recirculating pipe-loop wear tester were used for the analysis [5, 18]. The wear data covered a wide range of operating regimes with the slurry mean flow velocity between 2.28 and 8.22 m/s and with particle sizes of 250 and 450  $\mu\text{m}$ . The experiments were carried out by researchers at the Pipeline Transport Processes (PTP) Research Group using the facility at the Saskatchewan Research Council (SRC) Pipe Flow Technology Centre<sup>TM</sup> in Saskatoon. The SRC two-layer model helped to identify an interface for which the kinematic and Coulombic friction mechanisms can be separated and then mapped unto the related wear mechanisms i.e. kinematic friction to erosive wear and Coulombic friction to abrasive wear. Details of the methodology is provided in Section 5.3 while a background of the formulation of the SRC two-layer model is presented in the next section.

## 5.2 The SRC two-layer model

The SRC two-layer model is a semi-mechanistic model used to calculate friction loss for heterogeneous slurry pipeline flows. The model consists of a series of materials balances, force balances, and the solution of the coarse particle concentration distribution [2–4, 8, 19, 20]. The schematic of the theoretical and hypothetical two layers, which forms the basis of the model, is shown in Fig. 5.2. As shown in Fig. 5.2, the model consists of a fast moving, low concentration upper layer and a slow moving, high concentration lower layer. Because of this there is a step change in the velocity and concentration distribution, allowing an interface to be defined between an upper and lower layer. The two types of friction loss mechanisms which constitutes the SRC two-layer model are kinematic and Coulombic friction. The upper layer only consists of kinematic friction i.e.  $\tau_{k1}$ . This mechanism consists of the total friction losses due to carrier fluid and the the suspended solid particles. The particles impact one another and the wall of the pipe randomly, resulting in the solids friction loss. The lower layer includes both kinematic and Coulombic friction i.e.  $\tau_{k2}$  and  $\tau_c$ . The Coulombic friction comes from the normal stress imposed by the immersed weight of the particles acting on the pipe wall in the lower layer. The fraction of coarse solids contributing this Coulombic friction

is known as contact load fraction.

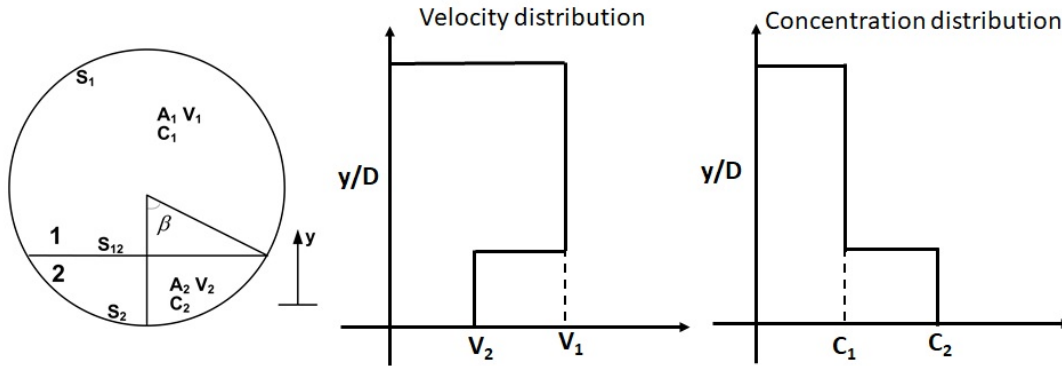


Figure 5.2: Schematic representation of the SRC two layer model

The pressure gradient calculated based on these friction loss mechanisms for layer 1 for horizontal pipe flows is given by

$$\frac{dP}{dz} = \frac{\tau_{k1}S_1 + \tau_{12}S_{12}}{A_1} \quad (5.1)$$

and for layer 2

$$\frac{dP}{dz} = \frac{\tau_{k2}S_2 - \tau_{12}S_{12} + \tau_c S_2}{A_2} \quad (5.2)$$

where  $\tau_k$  is the kinematic friction contribution,  $\tau_{12}$  is the interfacial stress (which retards flow in the upper layer and impels flow in the lower layer),  $\tau_c$  is the Coulombic friction contribution,  $S$  is the wetted perimeter, and  $A$  is the cross-sectional area. The subscripts 1, 2 represents the upper and lower layer respectively. The kinematic friction loss consists of a fluid-related and a particle-related component and is defined by

$$\tau_k = \frac{1}{2} (f_f \rho_f + f_s \rho_s) V^2 \quad (5.3)$$

where  $f_f$  is the Fanning friction factor and  $f_s$  is the solids friction factor. Correlations such as that of Swamee-Jain [21, 22] or Churchill [23] can be used to determine the fluid friction

factor while that for the solids friction factor can be determined from a correlation based on the dimensionless particle diameter and the limiting solids volume concentration [4]. The Coulombic friction part of the model,  $\tau_c$ , is defined as

$$2 \int_0^\beta \tau_c dS_2 = 0.5gD^2\eta_s(\rho_s - \rho_f)(C_2 - C_1)(\sin\beta - \beta\cos\beta) \quad (5.4)$$

where  $\eta_s$  is the coefficient of sliding friction between the particles and the pipe wall, which is usually taken as 0.5 for sand and gravel on steel pipe [8]. The variable  $\beta$  sets the interface between the upper and lower layers as shown in the SRC two-layer model formulation. As will be discussed in Section 5.3, this variable is an important part of the methodology to isolate the kinematic and Coulombic friction components. For this study, the SRC two-layer model has been programmed into MATLAB<sup>®</sup>. The algorithm for solving the model equations can be found in Gillies et al. [2]. Implementing the model in MATLAB<sup>®</sup> has allowed for extraction of the variables needed for analysis in this study i.e.  $\tau_k$ ,  $\tau_c$ , and  $\beta$ . Also based on this work, the assumption is that only erosive wear is occurring in the upper layer because it only has kinematic friction while both erosive and abrasive wear occur in the lower layer.

## 5.3 Methodology

### 5.3.1 Development of method

Several investigations have been carried out to study abrasive wear and its relationship to slurry hydrodynamics variables [1, 5, 6, 13, 24–28]. In most of the studies, a correlation has been established between wear rate and slurry friction loss. Particularly, the work by Shook et al. [1] showed a direct linear relationship between wear rate and the product of particle flux and normal (Coulombic) load imposed by the particles transported in a horizontal pipeline. The particle flux is the product of local particle velocity and solids volume concentration. The abrasive wear equation presented in their work was developed from the proportionality expression given by

$$E^o \propto cvF \quad (5.5)$$

where  $c$  is the local solids concentration,  $v$  is the local particle velocity, and  $F$  is the sum of the gravitational and particle-particle interaction forces which is used to determine the normal stress acting on the pipe wall. The term  $E^o$  is defined as a specific wear rate in which the wear rate is divided by the mass throughput of the slurry flow. The mass throughput is the product of the mean particle flux ( $C_v V$ ), the particle density ( $\rho_s$ ), and the pipe cross-section area ( $A = \pi D^2/4$ ). Attention is directed towards the local particle flux i.e.  $cv$  in the expression that Shook et al. [1] plotted against the local wear rate values at o'clock positions around the pipe. One of the figures they reported is shown in Fig. 5.3 for experimental data in a 50 mm acrylic pipe transporting 180  $\mu\text{m}$  particles at 20% solids volume concentration and at a slurry mean velocity of 3 m/s.

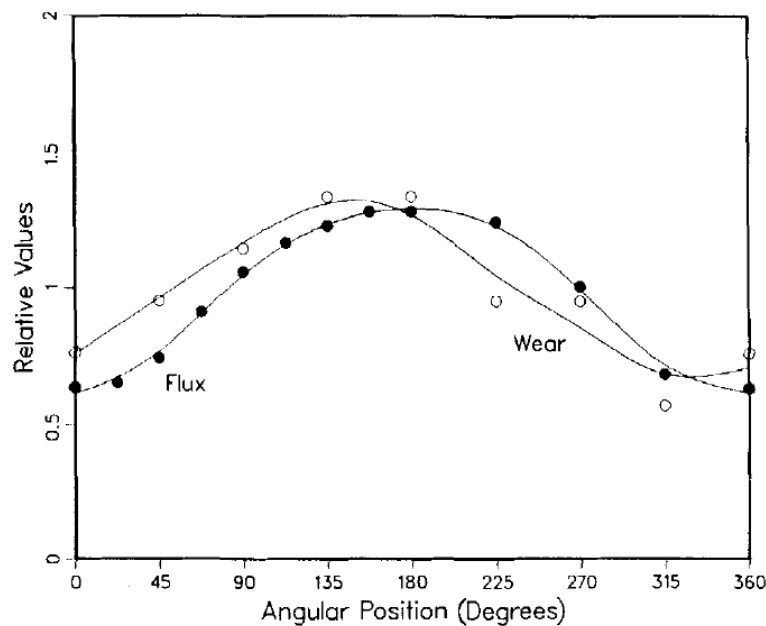


Figure 5.3: Wear rate vs particle flux for 180  $\mu\text{m}$  particles at slurry flow velocity of  $V = 3$  m/s, solids volume concentration of  $C = 20\%$  in a 50 mm horizontal acrylic pipe [1]

Relative values i.e. local values divided by the mean values, of both the wear rate and the particle flux have been plotted. The mean values for the wear rate or particle flux for the whole pipe were determined using trapezoidal integration. It can be seen from the figure that a Gaussian distribution can be used to represent the local distribution of both the wear

rate and the particle flux. The trends for both plots are also similar moving around the pipe circumference thus indicating that the wear rate changes linearly with the particle flux.

To develop the method of analysis used in this work, consider a situation where the total mass loss due to wear in the pipe specimen is the only available data. If the pipe cross-section is divided into an upper and a lower layer as shown in Fig. 5.4a, the mean particle flux can be calculated for each layer. Simulations will be used to predict this particle flux and a trapezoidal integration will be used to calculate the mean value. The trapezoidal integration is implemented using MATLAB.

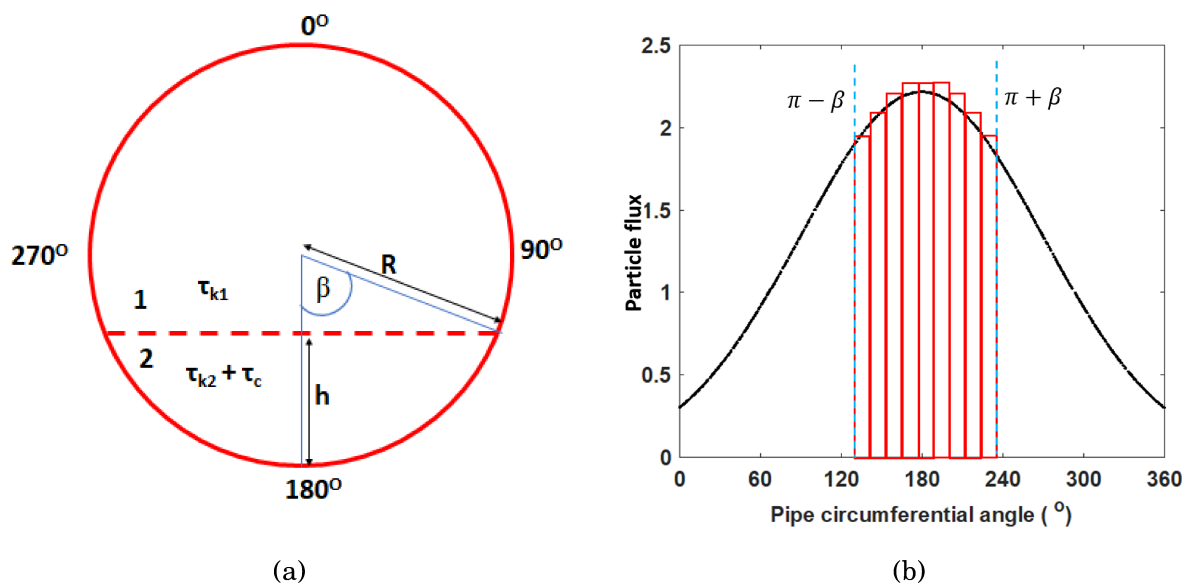


Figure 5.4: Schematic for estimating mean local wear rate

As shown in Fig. 5.4, the SRC two-layer model can be used to determine the boundary that separates the upper and lower layer. The interface height  $h$  is given by the expression

$$\frac{h}{D} = \frac{1}{2}[1 - \cos(\beta)] \quad (5.6)$$

Also, as shown in Equation 5.5, there is a linear relationship between wear loss and particle flux. This also means the total mass loss in the lower layer of the pipe as defined by the interface  $h$  will be proportional to the mean particle flux calculated for the layer. Using linear proportion, the mass loss in the lower layer can be calculated from

$$\frac{E_{A_2}}{E_T} = \frac{\int_0^{y=h} cvdy}{\int_0^{y=D} cvdy} \quad (5.7)$$

where the particle flux  $cv$  is obtained from CFD and  $E_T$  is the total mass loss in the pipe obtained from experimental measurement. The expression on the RHS of Equation 5.7 will be termed the *particle flux ratio* in this study. It should be noted that the estimated wear rate  $E_{A_2}$  for the lower layer of the pipe accounts for both abrasive and erosive wear since it contains both kinematic and Coulombic friction components. To separate the individual wear rates, the following algebraic steps are taken:

The total mass loss for the upper layer of the pipe is given by

$$E_{A_1} = E_T - E_{A_2} \quad (5.8)$$

The wear loss  $E_{A_1}$  is due to kinematic friction only. This means the amount of material loss due to Coulombic stress alone i.e. abrasion can be defined by

$$E_c = \frac{E_T - E_{A_2}}{(\tau_{k1}S_1/\tau_cS_2)} \quad (5.9)$$

while that based only on kinematic friction (erosion) is given by

$$E_k = E_T - E_c \quad (5.10)$$

By comparing the ratio of  $E_k$  to that of  $E_c$ , the dominant wear mechanism for slurry flows in horizontal pipelines at different operating conditions can be determined.

### 5. 3.2 Preliminary analysis

The discussion in this section focuses on how material loss in the upper and lower layers of the pipe changes with flow condition. A schematic illustrating this transition is shown in Fig. 5.5. Firstly, the wetted (or cross-sectional) surface area of the lower layer becomes smaller as the particles become more efficiently suspended i.e. as  $C_c/C_r$ , the contact load fraction, decreases. Secondly, the thickness loss gradually moves from being asymmetric to a more uniform distribution. This means that for high contact-load fraction i.e. Case A in Fig. 5.5,

the thickness loss ratio (TLR) of the bottom 6 o'clock to the top 12 o'clock position will be greater than 1.

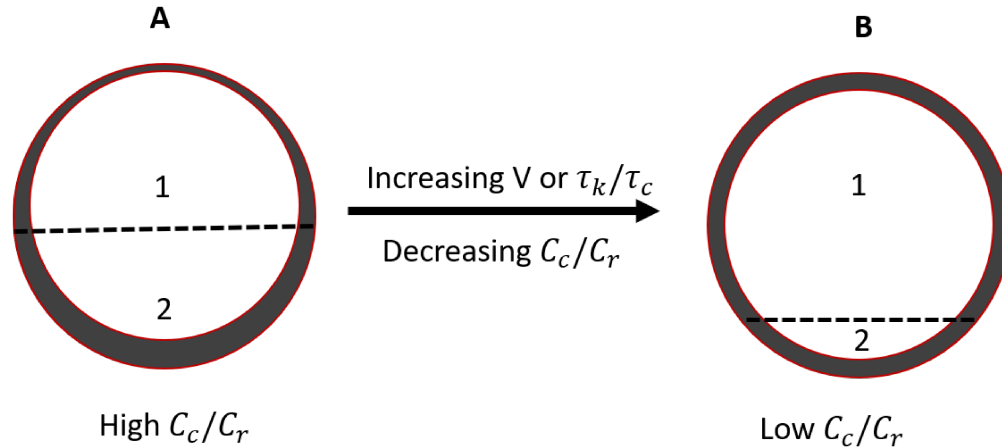


Figure 5.5: Visual representation of variation of the two layers (SRC model) and pipe wall thickness loss with velocity

For Case B where velocity has been increased and the system can be approximately treated as homogeneous, the thickness loss ratio tends towards 1 i.e. as  $C_c/C_r \rightarrow 0$ ,  $TLR (mm/mm) \rightarrow 1$ . However, if the total mass losses that pertain to layers 1 and 2 are determined, the mass loss ratio (MLR-kg/kg) of the bottom layer to the top layer will range from a value greater than 1, and tend towards 0 as  $C_c/C_r$  also approaches 0. This is because at fully homogeneous conditions, the second layer will disappear because  $C_c/C_r$  will be equal to zero. At very high abrasive conditions i.e. an *ideal and theoretical* condition where no particle exists in layer 1 and all particles form a sliding bed in layer 2, the wear (mass) loss will be restricted to layer 2. The MLR of the bottom layer to the top layer under this condition will tend towards infinity because there is zero mass loss in the top layer. The methodology in this study found the mass loss ratio (MLR) as the most suitable metric for comparing wear between the top and bottom layers based on the available data. In the Results and Discussion section, the predictions obtained using this approach will be evaluated to determine if they seem reasonable, as expected in a slurry pipeline.

## 5.4 Experimental Details

Experimental slurry pipeline wear data from research studies conducted by the Pipeline Transport Processes (PTP) research group at the University of Alberta have been used in this study [5, 18]. The experiments were carried out using the recirculating pipe loop (RPL) wear-testing facility at the Saskatchewan Research Council (SRC) Pipe Flow Technology Centre in Saskatoon, SK. The RPL tester is designed to hold two test spools of different diameters simultaneously, thus allowing two different flow velocities for each test spool in one experimental run. For the experimental data in this study, the test spools have an internal diameter of 70.92 and 86.79 mm. The length of all pipe test spools used is 0.61 m. Two solids volume concentration of 20% and 30% were tested while the slurry mean flow velocity was varied from 2.28 to 8.22 m/s. A more detailed description of RPL wear tester can be found in Sadighian [5] and Jami [18]. For this study, simulations were carried out for the operating condition of each experimental run. Table 5.1 presents a summary of all the experimental conditions that will be simulated as well as the corresponding measured wear data.

Table 5.1: Experimental wear data and conditions simulated in CFD

Run	$d_p$ (mm)	D (m)	$C_v$	V (m/s)	ER (mm/yr)
1	0.425	0.08679	0.2	3.42	0.161
2	0.425	0.08679	0.2	3.04	0.109
3	0.425	0.08679	0.2	2.66	0.075
4	0.425	0.08679	0.2	2.29	0.060
5	0.250	0.08679	0.2	2.31	0.153
6	0.250	0.08679	0.3	4.16	0.269
7	0.250	0.08679	0.3	5.30	0.688
8	0.425	0.07092	0.2	3.43	0.201
9	0.425	0.07092	0.2	3.98	0.401
10	0.425	0.07092	0.2	4.55	0.433
11	0.425	0.07092	0.2	5.13	0.501
12	0.250	0.07092	0.2	3.54	0.230
13	0.250	0.07092	0.3	6.38	0.780
14	0.250	0.07092	0.3	8.22	1.576

The wear rate data will be converted to total mass loss for the analysis using a uniform time basis, the experimental spool length of 0.61 m, and the density of the test material which is A106 commercial carbon steel. It is important to note here that there is limited

slurry pipeline wear data available in the literature that is relevant to this study. This stems from the difficulty and the cost-implications of obtaining such data; for example, the charging of fresh slurry into the recirculating pipe-loop is not feasible and will require enormous volume capacity of the testing facility as well as cost, especially with one data point taking about 3 to 6 weeks run time. Therefore, the slurry charged into the pipe loop is usually replaced at intervals in which particle degradation by the slurry pump is minimal i.e. at a time where the loss of particle sharpness due to the shearing action of the slurry pump impeller is considered not to be significant.

## 5.5 Computational Fluid Dynamics (CFD) Modelling

### 5.5.1 Model description and equations

In this study, a 3D transient analysis was carried out for all simulation cases. The Eulerian-Eulerian multi-fluid approach based on the Kinetic Theory of Granular Flow (KTGF) was implemented to model the slurry pipeline system [29, 30]. This method accounts for the interaction between particles and is suitable for high-concentration systems like the one considered in this study. The CFD code ANSYS Fluent 19.0<sup>®</sup> was used and a summary of the models selected has been provided in Table 5.2. A User-Defined Function (UDF) was written to specify a fully-developed velocity profile for the inlet boundary condition. For the solution method, the SIMPLE algorithm was used in all the simulations. The solver calculation was done using a time step of 0.001s and run time of 10s. A second-order solution scheme was used for the momentum equation while a first-order solution scheme was adopted for solving the turbulence equation and volume fraction. To address convergence problems, the momentum under-relaxation factor was set to 0.2 while the default values were used for the other parameters. A convergence criterion of  $1 \times 10^{-4}$  was set for all residuals. Also, mesh generation was carried out in ICEM CFD 17.0<sup>®</sup> using the O-grid blocking method. High quality unstructured grids were generated such that the maximum aspect ratio is less than 10.

Table 5.2: Models selected for CFD simulations

<b>Interaction</b>	
Turbulence	Realizable k- $\epsilon$ , dispersed
Wall function	Enhanced wall treatment
Virtual mass	None
Drag	Gidaspow[31]
Lift	none
Turbulent dispersion	Burns et al.[32]
Restitution coefficient	0.9
<b>Granular Phase</b>	
Granular temperature	Algebraic
Granular viscosity	Gidaspow[31]
Granular bulk viscosity	Lun et al.[33]
Frictional viscosity	None
Solid pressure	Lun et al.[33]
Radial distribution	Lun et al.[33]
Packing limit	0.63
Elastic modulus	Derived
<b>Boundary conditions</b>	
Wall (Continuous phase)	No slip
Wall (Dispersed phase)	Slip (zero shear)
Velocity inlet	Specified fully-developed profile

## 5. 5.2 CFD model validation

In order to use the CFD model confidently for this study, a validation step is essential. Experimental data from the work of Gillies et al. [3] were used for this validation step. The selected data are the measured concentration distributions for 270  $\mu\text{m}$  particles in a 103 mm ID pipe. The slurry mean flow velocity is 5.4 m/s. Three cases of 10%, 20%, and 30% solids volume concentration were simulated. The simulation results are shown in Fig. 5.6. It can be seen from the figure that the predicted particle concentration distributions closely match the experimental data.

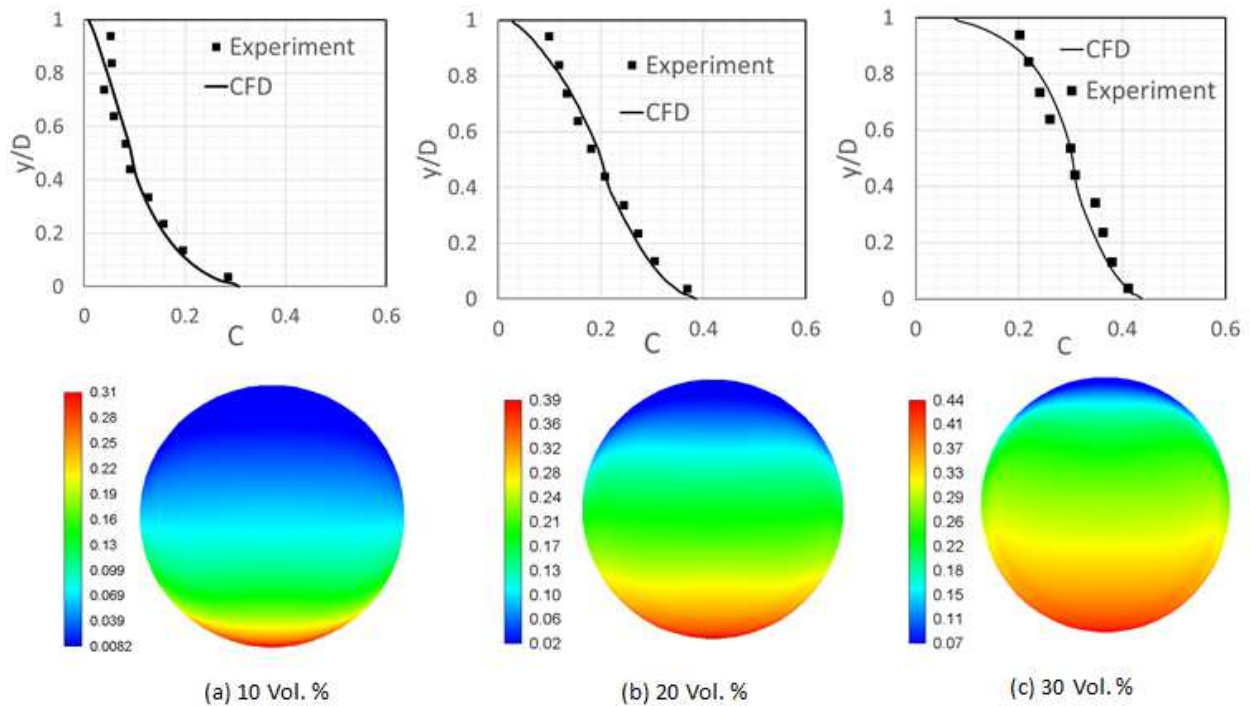


Figure 5.6: Predicted concentration distribution for Gillies et al. [3] experimental data

As expected in a heterogeneous slurry flow, the solids volume concentration at the lower half of the pipe is higher than that in the upper half due to gravitational stratification. This means the particles tend to settle because of their weight, however, the presence of fluid turbulence partly suspends the particles, thus leading to the concentration gradient observed. It is important to note that the slurry conditions used for this validation are representative of those of under which the experimental wear data used in this study were collected.

## 5.6 Results and discussion

### 5.6.1 Predicted slurry hydrodynamics

In this section, simulation results for slurry hydrodynamics for some of the experimental runs in Table 5.1 are presented. The selected simulation results are shown in Fig. 5.7. The effect of particle size is examined by comparing Runs 4 and 5 while the effect of slurry mean velocity is examined by comparing Runs 5 and 7.

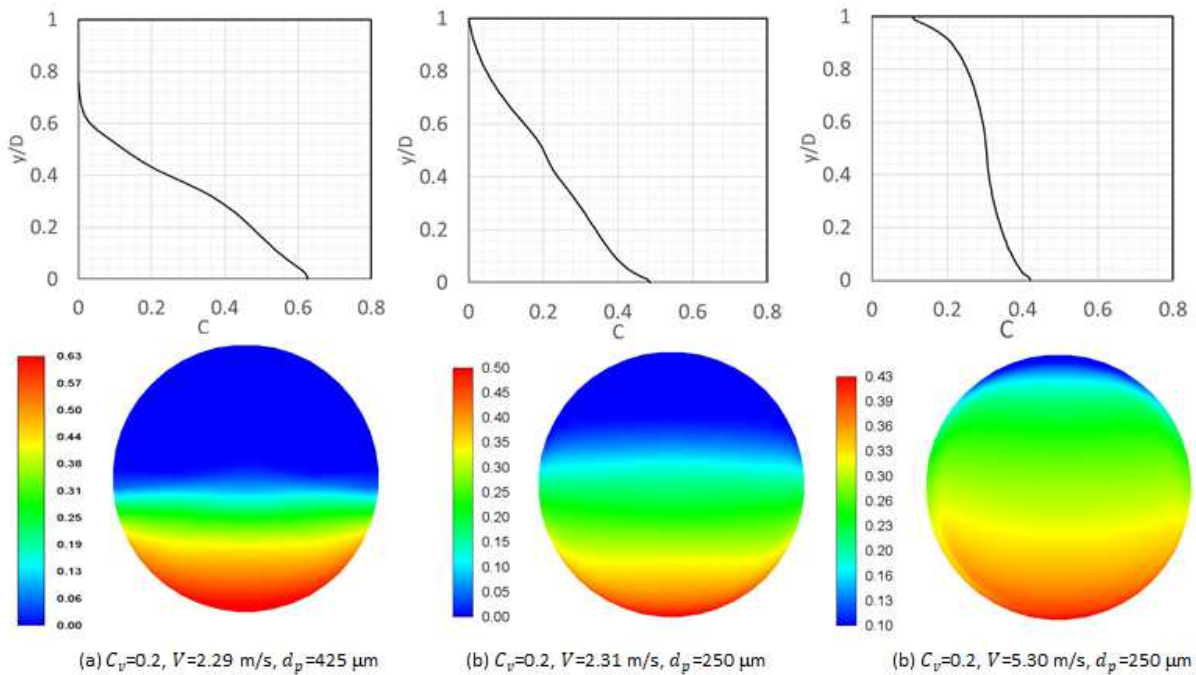


Figure 5.7: Predicted concentration distribution for (a) Run 4 (b) Run 5 and (c) Run 7 in Table 5.1

It can be seen in Fig 5.7 that for the larger particle size i.e. 425  $\mu\text{m}$ , the particles are more concentrated in the lower half of the pipe when compared to the 250  $\mu\text{m}$  particles. The 250  $\mu\text{m}$  particles are more efficiently suspended by the fluid turbulence, thus forming a less skewed concentration profile. Further increase in slurry mean velocity results in more uniform distribution of particles across the pipe cross-section. Increasing the velocity results in higher degree of turbulence, hence, the fluid has more energy to suspend and transport the particles against gravity. These predictions are expected, and are typical of slurry hydrodynamics behaviour [29].

## 5. 6.2 Analysis of experimental data

The measured wear rate from the pipe loop experiments is plotted against velocity in Fig. 5.8a while in Fig. 5.8b, it is plotted against the slurry friction loss (or wall shear stress), which includes the kinematic and Coulombic components used for the analysis in this study.

The friction loss was calculated from the SRC two-layer model that was programmed into MATLAB.

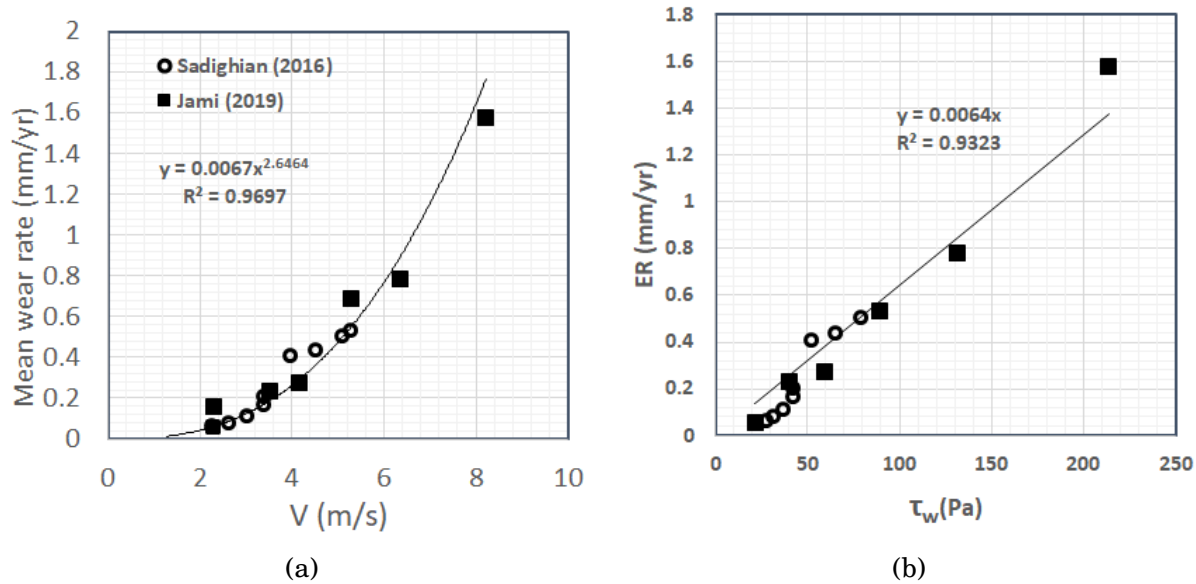


Figure 5.8: Measured average wear rate against (a) mean slurry velocity (b) slurry friction loss

In Fig. 5.8a, the typical power-law relationship between wear rate and velocity can be seen in the fitted trend. The numerical value of velocity exponent is also similar to those reported in literature [12, 26]. In Fig. 5.8b, a linear relationship exists between the wear rate and the slurry friction loss. Many authors have reported a similar relationship between slurry pipeline wear and friction loss (or wall shear stress) [1, 5, 6, 27, 28]. It is worth mentioning here that the wall shear stress indicated in Figure 5.8b consists of those contributed by the liquid (in the kinematic friction) and solids (in the kinematic and Coulombic friction). An ideal situation would be to use only the solids-related component of the kinematic friction loss for wear correlations; however, the present shortcomings of the model would not allow such a choice for the analysis conducted in this study. In the SRC two-layer model, the kinematic friction formulation includes a near-wall lift [34, 35] which is a tempering effect for the solids-related contribution. As velocity increases, this solids-related part of the kinematic friction also increases until it reaches a certain point where it begins to diminish, eventually becoming zero. However, the total friction loss continues to increase with velocity. If a wear model is correlated to only solids-related friction loss, the model predictions will also tend

towards zero at high flow velocities where the near-wall lift effect is very active. This is contradictory to what is expected in a wear correlation that should predict a wear rate that increases continuously with velocity in a power-law relationship.

### 5. 6.3 Validation of method

The calculation of the particle flux ratio i.e. the integral on the right-hand side of Equation 5.7 is important in estimating the amount of wear in the lower and upper sections of the pipe. In this section, the objective is to determine the wear loss that can be ascribed to these two layers and then compare the predictions with those obtained from the Huang et al. [36] model and an ultrasound thickness loss (UTL) measurement [5]. The needed particle flux ratio as presented in Equation 5.7 is calculated from CFD predictions, and then plotted against the contact load fraction calculated from the SRC two-layer model. This is shown in Fig. 5.9. The contact-load fraction relates the difference in the upper and lower layer solids concentrations in Equation 5.4 by an expression given by

$$\frac{C_c}{C_r} = \frac{(C_2 - C_1)A_2}{C_r A} \quad (5.11)$$

where  $C_c$  is the contact-load solids volume concentration and  $C_r$  is the *in-situ* solids volume concentration. Generally, as seen in Fig. 5.9, the particle flux ratio increases with increase in the contact load fraction. This is expected since a larger contact load fraction means most of the particles are in the lower layer of the pipe. This also translates to conditions of low slurry mean velocity and/or large particle sizes. Now using Equation 5.7 and the total mass loss from the experimental data, the particle flux ratio was used to determine the amount of wear that occurs in the lower layer of the pipe. It is important to point out that in the lower layer, both abrasive and erosive wear are occurring simultaneously. Before going further to isolate these two components, the total wear estimated for the lower section of the pipe was verified using the Huang et al. [36] wear model. The Huang et al. [36] wear model is a phenomenological wear model based on cutting and deformation mechanisms for horizontal slurry pipelines as described in Chapter 2. The model is able to predict wear rate at o'clock positions around the pipe circumference. The Huang et al. [36] model is defined as

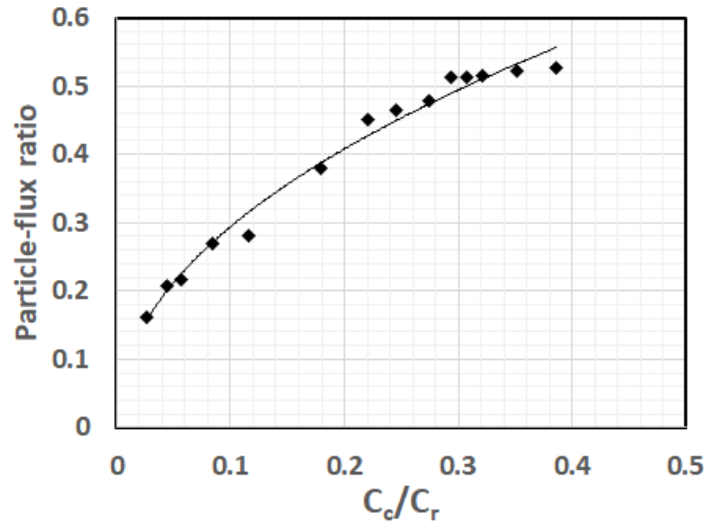


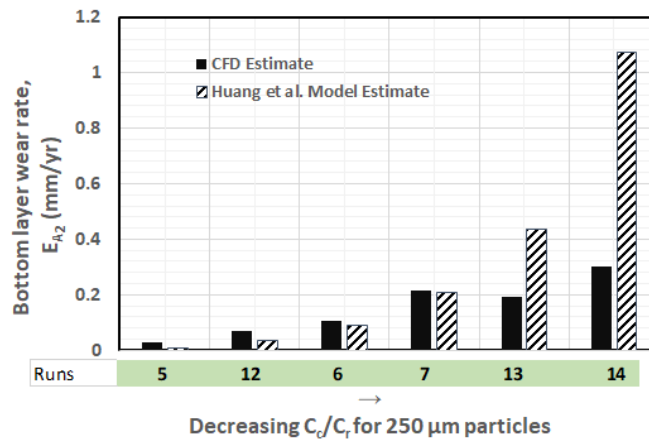
Figure 5.9: Particle flux ratio versus contact load fraction

$$ER = k \rho_s^{1+3(1-n)/4} d_p^{2(1-n)} V^2 C_v^t \left[ \frac{bV}{Re_D^{m/2}} + \frac{d_p^2(1-C_v)(\rho_s - \rho_f) \cos \alpha}{18\mu_f(1+0.1Re_p^{0.75})} \right]^{(5-3n)/2} \quad (5.12)$$

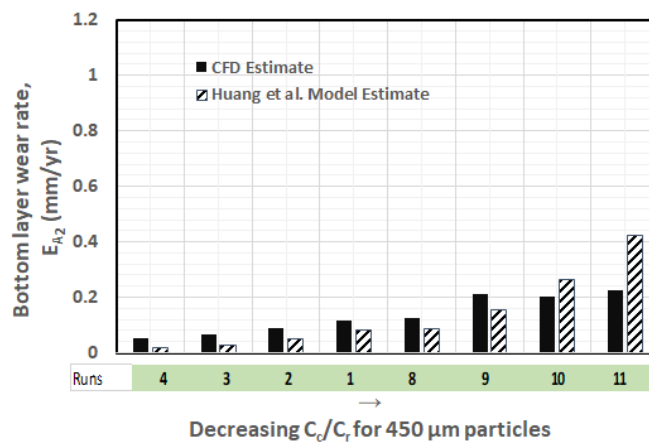
Where  $n, k, b$  are constants fitted from the experimental data,  $m = 0.2$ , and  $Re_D = \rho_f V D / \mu_f$  is the Reynolds number,  $D$  is pipe diameter,  $V$  is the mean slurry velocity, and  $\alpha$  is o'clock position angle on the circumference of the pipe. The mean erosion rate for the lower section of the pipe can be calculated from the Huang et al. [36] model by performing an integration given by

$$ER = \sum_i ER_i = \frac{1}{\pi} \int_{\pi-\beta}^{\pi} ER(\alpha) d\alpha \quad (5.13)$$

The estimated wear rates for the bottom layer of the pipe from the CFD method and the Huang model are shown in Fig. 5.10. Generally, the wear rate increases as the contact load fraction decreases. This is because it corresponds to increase in slurry flow velocity, therefore, the particles possess more energy to cause the wear damage.



(a)



(b)

Figure 5.10: Total wear rate for the bottom layer of the pipe: CFD estimate versus Huang's model estimate

Also, it can be seen that there is close agreement between the estimated bottom-layer wear rate from the CFD method and the Huang wear model except for the high slurry flow velocity condition. The Huang wear model over-predicted the wear rate in the high velocity condition, especially for the smaller 250  $\mu\text{m}$  particles. The Huang model includes both cutting and deformation damage mechanisms, with each strongly depending on the slurry mean velocity through a power law relationship (exponent approaching a value of 4). This strong dependency will be pronounced at high flow velocity conditions which may lead to over-prediction of wear. The Huang model should be further validated for these high velocity conditions in order to identify the best operating region for its application. Also, to compare

the bottom layer wear rate estimate between  $250\ \mu\text{m}$  and  $450\ \mu\text{m}$ , predictions from the CFD method for similar operating conditions were plotted as shown in Fig. 5.11. As expected, the model predicted a higher estimate for the larger particle size ( $450\ \mu\text{m}$ ). At these conditions, the larger particle size will have greater contact load and impose more stress on the target material which will result in greater wear damage.

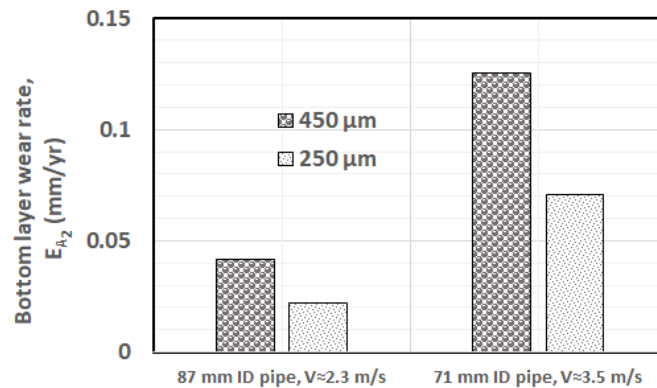


Figure 5.11: Comparison of bottom layer wear rate for  $450\ \mu\text{m}$  and  $250\ \mu\text{m}$

The results from the CFD method have captured the basic physics of erosion modelling. To further validate the predictions from this method, the bottom-to-top layer wear ratio is compared to that obtained from ultrasound thickness loss (UTL) measurements. Sadighian [5] made UTL measurements at o'clock positions around the pipe circumference. Measurement was taken at regular intervals for the first 100 hrs, then at 300 hrs, and then at 1100 hrs of experimental run time. The UTL measurements for the case of 20% solids concentration at a slurry flow velocity of 2.28 m/s are shown in Fig. 5.12. As can be seen, the measurement done in real-time is noisy and also recorded some increase in thickness, a phenomenon that Sadighian [5] attributed to the presence of deposits on the pipe wall. A final thickness loss measurement at the 6 o'clock and 12 o'clock positions was made and presented as a thickness loss ratio (TLR). The data showed the bottom position (6 o'clock) thickness loss were higher than that at the top by 5-20%, with the lowest velocity having the largest percentage difference. In this study, these measurements have been converted to a mass loss ratio (MLR) and compared to that estimated from the CFD method in this work.

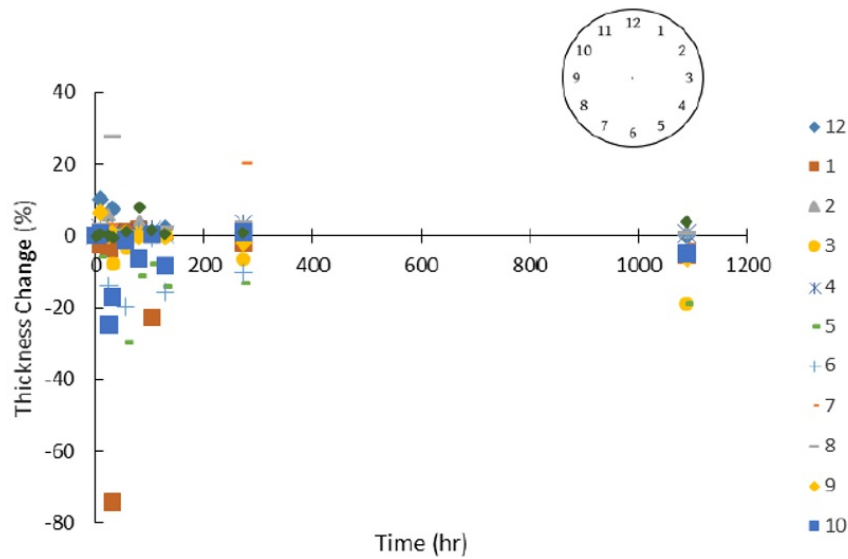


Figure 5.12: Ultrasound thickness measurement - 450  $\mu\text{m}$ , 2.28 m/s, 20% v/v, ID = 87 mm [5]

The relative wear rate estimated for the bottom and top layer of the pipe is plotted against the contact load fraction,  $C_c/C_r$  and presented in Fig. 5.13. Looking at Fig. 5.13a, there is good agreement between the CFD method and that calculated from experimental measurement.

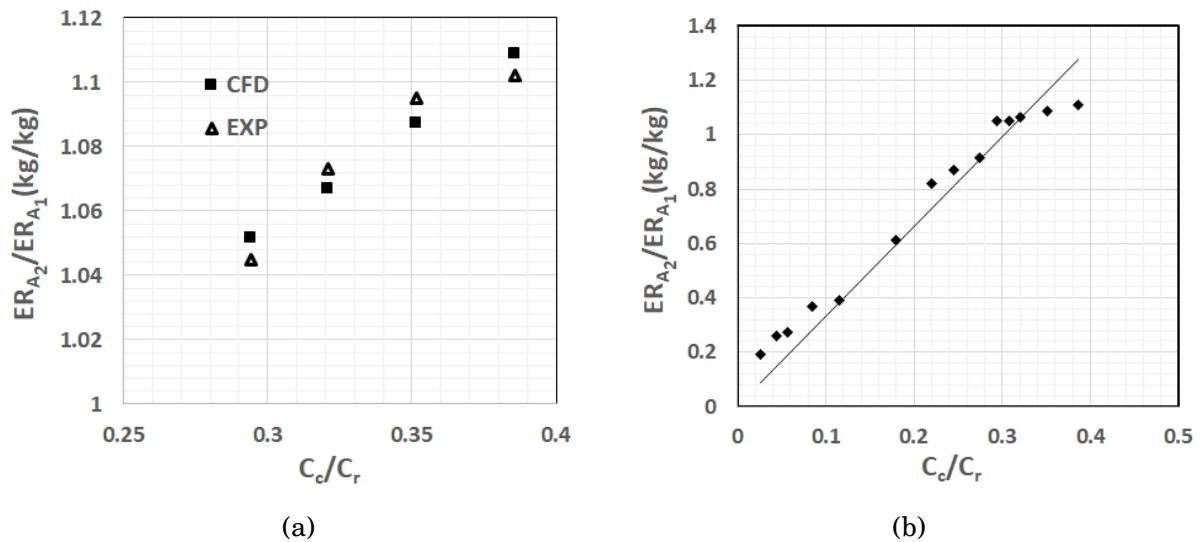


Figure 5.13: Relative wear rate: mass loss ratio for bottom-to-top layer (a) Comparison with experiment (b) All estimates from CFD method

The estimated mass loss at the bottom layer is greater than that at the top layer and it ranges from 4-12%. Generally, as the contact-load fraction increases i.e. at lower slurry flow velocity, the bottom layer of the pipe experiences higher load and more severe abrasive damage while the frequency of particle impact in the top layer is reduced. Similar trend shown in Fig. 5.13a can also be seen in Fig. 5.13b for all the predicted data from the CFD method. Since there is good agreement between the predicted estimates and experimental data, further calculation was done to estimate the contribution to each of kinematic and Coulombic friction losses to the total wear rate. The results are presented in the next section.

## 5. 6.4 Wear-Friction loss relationship

### Abrasion-to-erosion wear ratio

The ratio of total mass loss due to Coulombic friction (abrasion) to that due to kinematic friction (erosion) is plotted against the ratio of the kinematic friction loss to the Coulombic friction loss i.e.  $\tau_k/\tau_c$ . The ratio  $\tau_k/\tau_c$  is calculated as

$$\frac{\tau_k}{\tau_c} = \frac{\tau_{k1}S_1 + \tau_{k2}S_2}{\tau_c S_2} \quad (5.14)$$

The plot is shown in Fig. 5.14a. In Fig. 5.14b, however, the wear loss due to the individual slurry friction loss mechanisms has been divided by the total wear loss recorded for the pipes. The axis of  $\tau_k/\tau_c$  is displayed using log-scale to allow the data to spread across the plot. For a given slurry pipeline system, increasing velocity increases the total friction loss, however, the contribution due to the Coulombic part diminishes while that of the kinematic friction increases and dominates. The abrasion-to-erosion ratio, therefore, is expected to decrease with increase in  $\tau_k/\tau_c$ . This is the behaviour shown in the plots presented in Fig 5.14a and 5.14b. Also, it can be seen from the figures that the pipeline system used in the experiment is still dominated by kinematic friction, hence, by the erosive wear i.e. all  $ER_c/ER_k$  values are less than 1. For example, in Fig 5.14a, when  $\tau_k/\tau_c = 2$ , the contribution to total wear loss of the abrasive wear component is about 60% that of the erosive contribution.

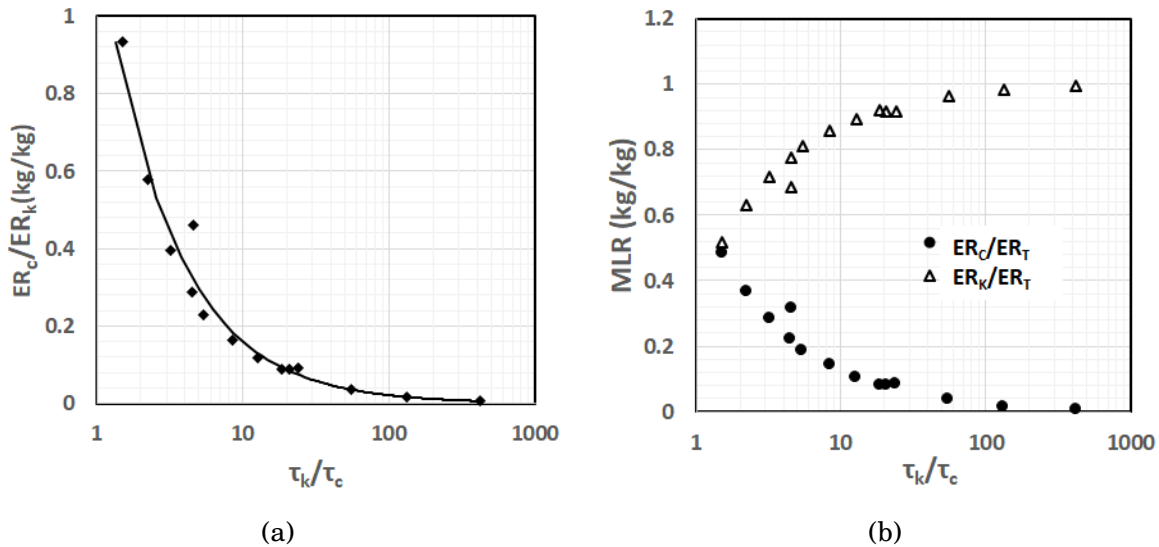


Figure 5.14: Wear ratio (a) Abrasion-to-erosion (b) Erosion-to-total wear and Abrasion-to-total wear

This is about 40% contribution to the total wear loss as shown in Fig. 5.14b. A 50-50 contribution from erosion and abrasion can be seen when  $\tau_k/\tau_c = 1.5$ . Note that the sum of every complementary erosion and abrasion data point in Fig. 5.14b must equal to 1. At high values of  $\tau_k/\tau_c$ , the erosive component tends to 1 in Fig. 5.14b. This is because the flow is dominated by kinematic friction, hence, the entire mass loss experienced by the pipe is due to high-energy impact of particles. The abrasive wear component however, tends to 0 under this condition. The distribution of wear (wall thickness) around the pipe circumference will be uniform under this condition since the flow is almost homogeneous, and particles are impacting randomly and equally in all directions.

### Erosion/Abrasion-Velocity relationship

The wear rate-velocity relationship is usually a power law type with the velocity exponent ranging from 2 to 4 [12, 16, 26, 36, 37]. A similar relationship is observed when the estimated wear rate due to kinematic friction alone is plotted against the slurry mean flow velocity. Recall that a power law correlation was also derived when the total wear rate was plotted against velocity in Fig. 5.8 but with a slight difference in the fitting coefficient and exponent. The similarity is because the erosive wear was dominating already and the difference in fitting constants is due to the additional contribution from abrasive wear which is not large

enough to alter the power-law relationship trend. It is reasonable to say that the conditions in the recirculating pipe-loop wear tester are dominated by kinematic friction, and therefore, erosive wear.

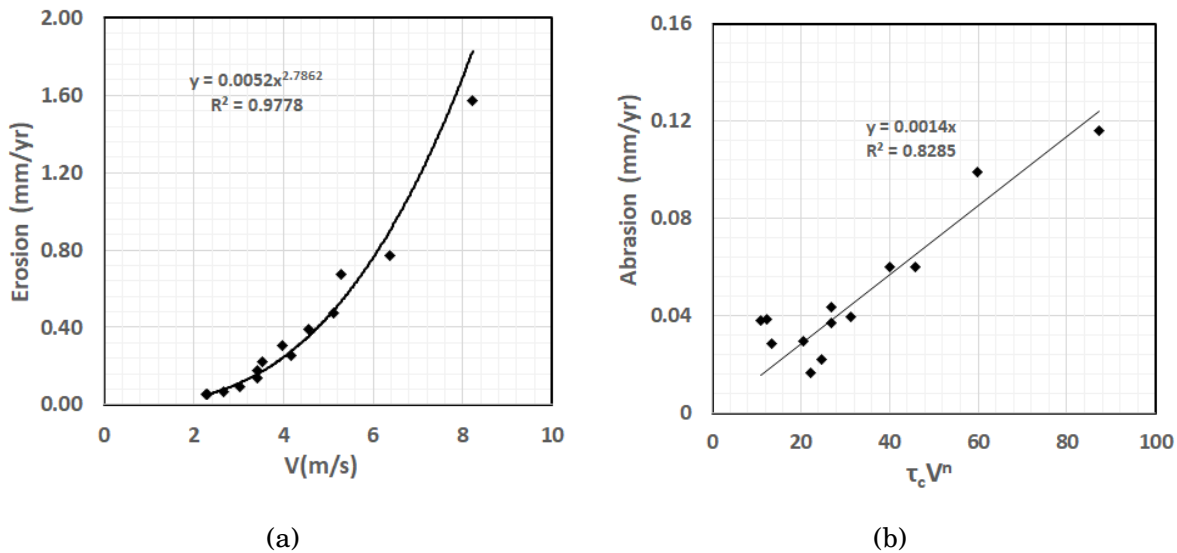


Figure 5.15: Wear relationships versus velocity (a) Erosion (b) Abrasion

Wear rate due to abrasion alone plotted against slurry flow velocity did not yield any specific trend. However, based on abrasive wear relationships defined in the literature [1, 6, 27, 28], the product of Coulombic stress and  $V^n$  was correlated to the estimated abrasive wear. The plot obtained is shown in Fig. 5.15b with  $n = 2$ . The load imposed by the weight of the particles on the pipe wall is crucial when accounting for abrasion. The load also needs to be dragged along the pipe length at a particular velocity for the cutting action that results in abrasion. It is reasonable that a trend exists for the relationship between the abrasive wear and the product of the Coulombic stress and slurry mean velocity. A similar relationship was obtained for the abrasive wear correlation obtained for the toroid wear tester (TWT) presented in Chapter 4. This observation can provide the foundation for interpreting slurry wear between the TWT and the pipe geometry.

Generally, a barrier to the methodology in this study that needs further investigation is the determination of the specific boundary/regime for which one assumes erosion-dominated wear or abrasion-dominated wear in the slurry system. Particularly, based on the analysis in this work, experimental evidence is needed to determine the  $\tau_k/\tau_c$  ratio that will result in

uniform thickness loss around the pipe circumference and in which regime uneven wear is expected. This means one should be able to relate the degree of non-uniform distribution of wear to  $\tau_k/\tau_c$  e.g. say 20% more wear at the pipe invert at certain values of  $\tau_k/\tau_c$  and 50% at other values. It is also important to note that this will differ for different erodent-target material combinations and one will also have account for the particle shape and size distribution. The analysis in this study is specifically for experimental data for sand-steel materials combination.

## 5.7 Conclusions

In this study, a CFD method was developed to isolate the individual contributions of abrasive and erosive wear to the total wear loss in a slurry pipeline system. The method combined CFD predictions of particle flux distributions, the slurry wear theory of Shook et al. [1], and the physics of the SRC two-layer pipe flow model to perform the isolation. Pipe wall thickness data from an ultrasound thickness loss measurement and the Huang et al. [36] model were used for validation. Erosive wear was defined such that it pertains only to kinematic friction loss while abrasive wear to Coulombic friction loss according the SRC model prediction. Several erosion/abrasion-friction loss relationships were derived to analyze the possible wear mechanisms that dominate at certain operating conditions in a slurry pipeline system. The erosive wear correlation still follows the power law relationship with velocity, however, abrasive wear includes the normal load due to the particles by multiplying  $V^2$  with the Coulombic stress. The abrasive wear correlation is similar to the one obtained from a previous study of abrasive wear loss in a toroid wear tester (TWT). The wear-friction loss relationships developed here will find application in the interpretation of wear between different pipe scales or from an experimental device such as the TWT to the slurry pipeline. There is, however, a need to further investigate and validate the methodology using other experimental and simulation studies.

## References

- [1] C. A. Shook, M. McKibben, M. Small, Experimental investigation of some hydrodynamic factors affecting slurry pipeline wall erosion, *Can. J. Chem. Eng.* 68 (1990) 17–23. URL:

- <http://doi.wiley.com/10.1002/cjce.5450680102>. doi:10.1002/cjce.5450680102.
- [2] R. G. Gillies, C. A. Shook, K. C. Wilson, An improved two layer model for horizontal slurry pipeline flow, *Can. J. Chem. Eng.* 69 (1991) 173–178. URL: <http://doi.wiley.com/10.1002/cjce.5450690120>. doi:10.1002/cjce.5450690120.
- [3] R. G. Gillies, C. A. Shook, J. Xu, Modelling Heterogeneous Slurry Flows at High Velocities, *Can. J. Chem. Eng.* 82 (2004) 1060–1065. doi:10.1002/cjce.5450820523.
- [4] R. B. Spelay, S. A. Hashemi, R. G. Gillies, R. Hegde, R. S. Sanders, D. G. Gillies, Governing Friction Loss Mechanisms and the Importance of Off-Line Characterisation Test in the Pipeline Transport of Dense Coarse-Particle Slurries, in: *ASME 2013 Fluids Eng. Div. Summer Meet.*, 2013, pp. V01CT20A013–V01CT20A013.
- [5] A. Sadighian, Investigating Key Parameters Affecting Slurry Pipeline Erosion, Ph.D. thesis, University of Alberta, 2016. doi:10.1017/CB09781107415324.004. arXiv:arXiv:1011.1669v3.
- [6] K. F. Adane, M. Huard, A. Fuhr, Modeling Abrasion-Corrosion in Horizontal Pipeline Slurry Flows, 2019. URL: <https://doi.org/>.
- [7] R. G. Gillies, Pipeline Flow of Coarse Particle Slurries, Ph.D. thesis, University of Saskatchewan, 1993.
- [8] R. G. Gillies, C. A. Shook, Modelling high concentration slurry flows, *Can. J. Chem. Eng.* 78 (2000) 709–716. doi:10.1002/cjce.5450780413.
- [9] M. C. Roco, G. R. Addie, Erosion wear in slurry pumps and pipes, *Powder Technol.* 50 (1987) 35–46. doi:10.1016/0032-5910(87)80081-5.
- [10] M. C. Roco, Wear Mechanisms in Centrifugal Slurry Pumps, *Corros. Eng.* 46 (1990) 424–431.
- [11] N. Barkoula, J. Karker-Kocsis, Processes and influencing parameters of the solid particle erosion of polymers and their composites, *J. Mater. Sci.* 37 (2002) 3807–3820. doi:10.1023/A.arXiv:0005074v1.

- [12] R. Gupta, S. N. Singh, V. Sehadri, Prediction of uneven wear in a slurry pipeline on the basis of measurements in a pot tester, *Wear* 184 (1995) 169–178. doi:[10.1016/0043-1648\(94\)06566-7](https://doi.org/10.1016/0043-1648(94)06566-7).
- [13] H. Arabnejad, A. Mansouri, S. A. Shirazi, B. S. McLaury, Development of mechanistic erosion equation for solid particles, *Wear* 332-333 (2015) 1044–1050. doi:[10.1016/j.wear.2015.01.031](https://doi.org/10.1016/j.wear.2015.01.031).
- [14] R. Cooke, G. Johnson, P. Goosen, Laboratory Apparatus for Evaluating Slurry Pipeline Wear, Technical Report March, SAIT Seminar, Calgary, 2000.
- [15] N. R. Sarker, A Preliminary Study of Slurry Pipeline Erosion Using a Toroid Wear Tester, MSc thesis, University of Alberta, 2016.
- [16] N. R. Sarker, L. Zhang, D. Breakey, B. A. Fleck, R. S. Sanders, Laboratory-Scale Erosive Wear Measurements Conducted with a Toroid Wear Tester (TWT), in: 8th Int. Conf. Transp. Sediment. Solid Part., September, 2017, pp. 295–303.
- [17] L. Zhang, Relating slurry friction to erosion rate using a toroid wear tester, MSc thesis, University of Alberta, 2018.
- [18] R. Jami, Investigation Using Polymer Additives to Mitigate Erosion in Multiphase Turbulent Pipe Flow, Master's thesis, University of Alberta, 2019.
- [19] C. A. Shook, M. C. Roco, *Slurry flow: principles and practise*, Butterworth- Heinemann, Boston, USA, 1991. doi:<http://dx.doi.org/10.1016/B978-0-7506-9110-9.50007-4>.
- [20] C. A. Shook, R. G. Gillies, R. S. Sanders, *Pipeline hydrotransport: with applications in oil sand industry*, SRC Pipe Flow Technology Centre, Saskatoon, Canada, 2002.
- [21] R. S. Sanders, *Fluid-Particle Systems and Application: Lecture notes*, Technical Report, University of Alberta, Edmonton, Alberta, Canada, 2015.
- [22] P. Swamee, A. K. Jain, Explicit equations for pipe-flow problems, *ASCE J Hydraul Div* 102 (1976) 657–664.
- [23] S. W. Churchill, Friction factor equation spans all fluid flow regimes, *Chem. Eng. (New York)* 84 (1977) 91–92. URL: <https://www.scopus.com/inward/record.uri?eid=2-s2.0-0017769439&partnerID=40&md5=a878a518cf62db283094ff25416026fd>.

- [24] B. Fotty, M. Krantz, J. Been, J. Wolodko, Development of a pilot-scale facility for evaluating wear in slurry pipeline systems, in: Proc. Hydrotransp. 18, September, Rio de Janeiro, Brazil, 2010, pp. 431–443.
- [25] J. Schaan, N. Cook, R. S. Sanders, On-line wear measurement for commercial-scale, coarse-particle slurry pipelines, in: 17th Int. Conf. Hydrotransp., Cape Town, South Africa, 2007, pp. 291–300.
- [26] A. J. Karabelas, An Experimental Study of Pipe Erosion by Turbulent Slurry Flow, in: Proc. Hydrotransp. 5, May, Hannover, Germany, 1978, pp. 25–24.
- [27] G. Yang, D. Serate, K. Tsai, M. Wu, Wear Modeling of Dense Slurry Flow in Oil Sands Coarse Tailings (CT) Pipelines, 2018. URL: <https://doi.org/>.
- [28] P. Rizkalla, D. F. Fletcher, Development of a Slurry Abrasion Model Using an Eulerian-Eulerian ‘Two-Fluid’ Approach, in: Elev. Int. Conf. CFD Miner. Process Ind. CSIRO, December, Melbourne, Australia, 2015, pp. 1–8.
- [29] A. Ekambara, R. S. Sanders, K. Nandakumar, J. H. Masliyah, Hydrodynamic simulation of horizontal slurry pipeline flow using ANSYS-CFX, Ind. Eng. Chem. Res. 48 (2009) 8159–8171. doi:10.1021/ie801505z.
- [30] D. R. Kaushal, T. Thinglas, Y. Tomita, S. Kuchii, H. Tsukamoto, CFD modeling for pipeline flow of fine particles at high concentration, Int. J. Multiph. Flow 43 (2012) 85–100. URL: <http://dx.doi.org/10.1016/j.ijmultiphaseflow.2012.03.005>. doi:10.1016/j.ijmultiphaseflow.2012.03.005.
- [31] D. Gidaspow, R. Bezburuah, J. Ding, Hydrodynamics of circulating fluidized beds: kinetic theory approach, in: 7th Int. Conf. Fluid., Illinois Inst. of Tech., Chicago, IL (United States). Dept. of Chemical Engineering, Gold Coast, Australia, 1991.
- [32] A. D. Burns, T. Frank, I. Hamill, J. M. Shi, The Favre averaged drag model for turbulent dispersion in Eulerian multi-phase flows, in: 5th Int. Conf. Multiph. Flow, 392, Yokohama, Japan, 2004, pp. 1–17. URL: [http://www.drthfrank.de/publications/2004/Burns\\_{\\_}Frank\\_{\\_}ICMF\\_{\\_}2004\\_{\\_}final.pdf](http://www.drthfrank.de/publications/2004/Burns_{_}Frank_{_}ICMF_{_}2004_{_}final.pdf).

- [33] C. K. K. Lun, S. B. Savage, D. J. Jeffrey, N. Chepuruiy, Kinetic theories for granular flow: inelastic particles in Couette flow and slightly inelastic particles in a general flowfield, *J. Fluid Mech.* 140 (1984) 223–256.
- [34] K. C. Wilson, A. Sellgren, Interaction of Particles and Near-Wall Lift in Slurry Pipelines (2003) 73–77.
- [35] K. C. Wilson, R. S. Sanders, R. G. Gillies, C. A. Shook, Verification of the near-wall model for slurry flow, *Powder Technol.* 197 (2010) 247–253. URL: <http://dx.doi.org/10.1016/j.powtec.2009.09.023>. doi:10.1016/j.powtec.2009.09.023.
- [36] C. Huang, P. Miney, J. Luo, K. Nandakumar, A phenomenological model for erosion of material in a horizontal slurry pipeline flow, *Wear* 269 (2010) 190–196. URL: <http://dx.doi.org/10.1016/j.wear.2010.03.002>. doi:10.1016/j.wear.2010.03.002.
- [37] B. K. Gandhi, S. Singh, V. Seshadri, Study of the parametric dependence of erosion wear for the parallel flow of solid – liquid mixtures, *Tribol. Int.* 32 (1999) 275–282.

## **Part II**

# **Improving the performance of erosion models for wear prediction in complex geometries and for operational decision making**

# Analysis of local wear variables for high-precision erosion modelling in complex geometries

A part of this Chapter has been published as

*"Adedeji O.E., Yu W., Sanders R.S., Analysis of local wear variables for high-precision erosion modelling in complex geometries. Wear. 2019;426-427:562-569. doi:<https://doi.org/10.1016/j.wear.2018.12.071>".*

The paper was also presented at the 22rd International Conference of Wear of Materials, Miami, USA, April 13-19th, 2019

## **Abstract**

Particle-laden flows in complex geometries often require a more robust performance from erosion models in order to obtain accurate prediction of wear. Most erosion models developed over the last six decades have not been able to achieve the desired accuracy needed for these complex systems, primarily because they are based on single particle-wear material interactions, experimental correlations, and often do not capture the full physics of the erosion process. Recently, the capability of computational fluid dynamics (CFD) in resolving fluid-particle-wall interactions more realistically has been shown to have great potential in the development of high-performance erosion models, especially when combined with experimental data analysis. This paper adopts this combined CFD-experimental methodology to improve the prediction performance of some selected erosion models. Experimental data for the wear of an elbow in gas-solid flow from a previous study was combined with new CFD predictions of local wear variables such as particle impact angle, particle impact velocity, and particle mass rate. A geometry correction factor function (GCFF) is developed which can adapt locally to erosion wear prediction in a standard elbow. The combination of the GCFF with an erosion model significantly improved the predicted rate for the gas-solid elbow.

## List of Symbols

$E_{rate}$	Erosion rate
$E_{ratio}$	Dimensionless erosion ratio, $kg/kg$
$E_{exp-data}$	Experimental erosion rate
$\dot{m}_p$	Local particle mass flow rate, $kg/m^2s$
$d_p$	Particle diameter, $m$
$V_p$	Particle impact velocity, $m/s$
$\alpha$	Particle impact angle
$C$	Erosion model constant
$C_{pt}$	Property-dependent erosion model coefficient
$C_{GCF}$	Geometry-dependent erosion model coefficient
$G$	Geometry correction factor function
$\beta_1$	Angle along bend radius
$\beta_2$	Angle defining pipe circumference
$r$	Elbow radius, $m$
$D$	Pipe diameter, $m$
$\rho_t$	Target material density, $kg/m^3$
$\rho_f$	fluid density, $kg/m^3$
$\mu_f$	fluid viscosity, $Pa\cdot s$
$H_v$	Vickers hardness, $GPa$
$V_{ref}$	Oka model reference particle impact velocity, $m/s$
$d_{ref}$	Oka model reference particle diameter, $m$
$n$	Oka model velocity exponent
$n_1$	Cutting damage exponent
$n_2$	Deformation damage exponent
$k_1$	Target material property exponent
$k_3$	Particle diameter exponent
$K$	Oka model coefficient
$Re_g$	Reynolds number
$I$	Turbulence intensity
$e_n$	Normal restitution coefficient
$e_t$	Tangential restitution coefficient
$\Delta\gamma$	Wall roughness parameter
$R_q$	Standard deviation of roughness structure
$R_a$	Mean height of roughness structure
$RS_m$	Characteristics length between roughness structure

## 6.1 Introduction

Many particle-handling industries face erosion wear problems and would benefit from reliable erosion models that can predict where and when a failure is likely to occur [1]. Many erosion models have been developed and well-used by industries [2–8], however, the complete physics of fluid-particle-wall dynamics of the erosion process have not previously been fully captured by any of these models. This means that (i) experimental data for the particular geometry or flow system under consideration are required and (ii) accurate predictions at one scale or in a specific geometry rarely translates to good predictions at a different scale or after a change in geometry. These challenges are particularly apparent in complex geometries such as elbows, tees, and cyclones or when one wishes to use small-scale laboratory tests to predict wear performance of a large-scale industrial process. Consider wear in an elbow, for example: both bend diameter and curvature significantly affect both the location and extent of the wear as well as the wear profile [9–11]. Existing erosion models, being system-specific are not able to capture these changes in geometry characteristics, hence there is a need to include a geometry correction factor. This means the overall erosion wear rate should be a product of a geometry-related factor/function and the particle-impact related function. The objective of this study is to conduct a combined CFD-experimental analysis of CFD-predicted local wear variables and experimental wear data, to develop a geometry correction factor function (GCFF) for a vertical-to-horizontal elbow which can be used with some common erosion models. For this work, CFD software ANSYS Fluent 19.0<sup>®</sup> is used to generate the local wear variables (impact velocity, impact angle, mass rate) for a gas-solid flow through an elbow system. The experimental data from the elbow system of Solnordal et al. [12] are used in this analysis. The methodology adopted in this study shows how to analyze local wear variables to improve wear prediction in complex geometries, which will be necessary if results are to be scalable and/or transferable from one geometry to another, e.g. conducting impinging jet tests to study wear in an elbow.

## 6.2 Background

Many erosion models often include a geometry correction factor especially when they are used for wear prediction in an elbow with gas-solid flows [7, 9–11, 13–15]. One of the previous

studies on the development of a geometry correction factor for gas-solid flow in elbow systems was by McLaury et al. [10]. In their work, an elbow radius factor was defined as

$$ERF_{r/D} = \exp\left[-\left(\frac{0.215\rho_f^{0.4}\mu_f^{0.65}}{d_p^{0.3}} + 0.03\rho_f^{0.25} + 0.12\right)\left(\frac{r}{D} - 1.5\right)\right] \quad (6.1)$$

where  $\rho_f$  is the fluid density,  $\mu_f$  is the fluid viscosity,  $d_p$  is the particle diameter, and  $r/D$  is the elbow curvature. Based on the definition of this elbow radius geometric factor in Equation 6.1, the expression will always yield a constant value at a given flow condition for any elbow with  $r/D \neq 1.5$ . This constant value will be multiplied with an erosion model to account for the characteristic effect of the elbow geometry being considered. The limitation of this geometry correction factor by McLaury et al. [10] however, is that it cannot adapt locally to the wear prediction in the elbow i.e. it cannot capture the local changes in wear rate produced by local changes in particle-fluid or particle-wall interactions due to fluid turbulence. This is also the major drawback in the geometry correction factors which has been included in many erosion models [7, 9–11, 13–15]. Since the erosion process is a local phenomenon, it is important that a geometry correction factor that can capture local changes of wear variables be developed. This is the major contribution of this study. Computational fluid dynamics (CFD) is employed in this study because of its capability in resolving local fluid-particle-wall interactions [11, 12, 16–21]. In addition to the geometry correction factor function adapting locally to wear prediction, it was also defined to be flexible and easily used for other similar elbow geometries at other larger scales.

### 6.3 Methodology

The methodology applied in this study for the development of the geometry correction factor function (GCFF) consists of three main part as shown in Fig. 6.1. From the figure, it is clear that experimental data, accurate flow modelling via CFD, an erosion model, and a definition for the GCFF for localized prediction of correction factors is needed. The experimental case [12] from which data is obtained for both model development and validation will be described in Section 6.4. The details of CFD modelling and simulation will also be discussed in Section 6.5 and also in the preceding parts of the results section. In this section, the rationale for the development of GCFF based on erosion models (See proof of GCFF in Appendix D.1) is

presented.

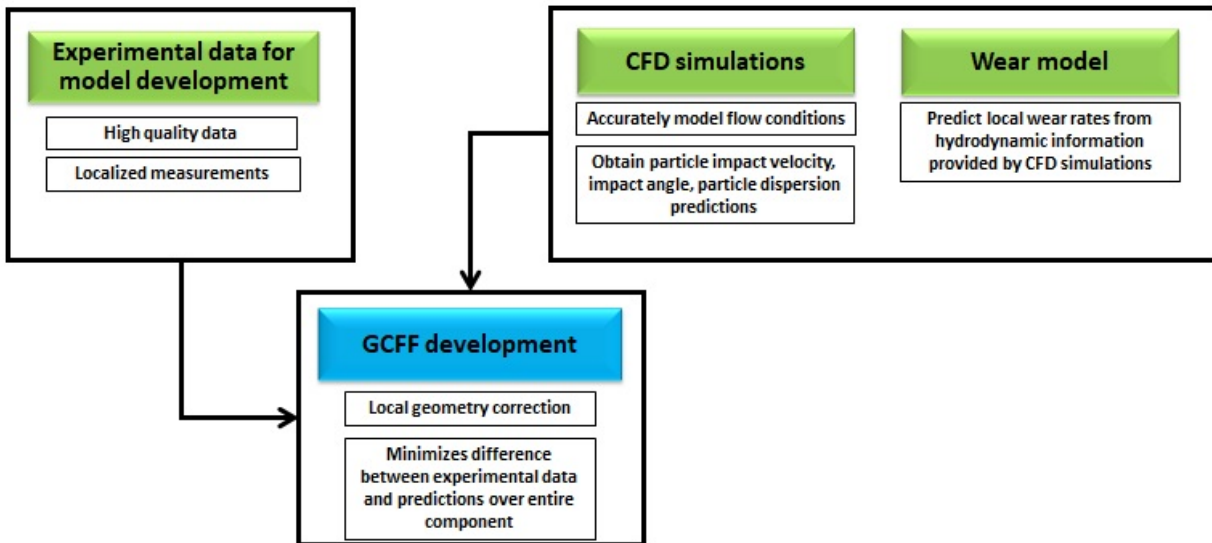


Figure 6.1: Geometry correction factor function (GCFF) development methodology

Erosion wear rate, which is the rate of material loss from a surface impacted by solid particles, depends on both fluid-particle dynamics and interactions, and erodent-target properties. These properties include particle impact velocity, particle impact angle, particle mass rate, particle size and density, particle shape and roughness, particle hardness, target material roughness, and target material hardness [16]. Many erosion models take the general form given by [18]

$$E_{rate} = \dot{m}_p [CV_p^n f(\alpha)] \quad (6.2)$$

where,  $\dot{m}_p$  is the particle mass rate,  $V_p$  and  $\alpha$  are the particle impact velocity and angle respectively,  $f(\alpha)$  is an impact angle function and  $n$ , the particle impact velocity exponent. In addition,  $C$  is a constant that may depend on erodent properties, target material properties, and/or geometry characteristics. The dimensionless erosion ratio is given by the bracketed expression i.e.

$$E_{ratio} = CV_p^n f(\alpha) \quad (6.3)$$

Essentially, Equation 6.3 can be represented by any of the traditional erosion models such as those of Oka *et al.* [5, 6], Det Norske Veritas (DNV) [7], the Tulsa model [22], and

Finnie [2–4]. The Oka model is one of the most commonly used erosion models because of its performance and flexibility. It considers the target material hardness property, making it useful for different erodent-target material combinations. For this study, the Oka model will be used in all analysis and model performance testing. The Oka model is defined as

$$C_{pt} = (1 \times 10^{-9} \rho_t) K (H_v)^{k_1} (V_{ref}^{-n}) \left( \frac{d_p}{d_{ref}} \right)^{k_3} \quad (6.4a)$$

$$n = 2.3(H_v)^{0.038} \quad (6.4b)$$

where,  $\rho_t$  is the density of the target material,  $d_p$  is the erodent particle diameter,  $d_{ref}$  is the reference particle diameter with a value of 326  $\mu\text{m}$ ,  $V_{ref}$  is the reference velocity with a value of 104 m/s, and  $H_v$  is the Vickers hardness of the target material in GPa. The exponent  $n$  is the particle impact velocity exponent which depends on the particle properties and the target material hardness. The coefficient  $K$  and exponents  $k_1$  and  $k_3$  are constants which strongly depend on the particle properties and target material hardness, and may vary for different erodent-target materials combination.

The impact angle function  $f(\alpha)$  is also defined by

$$f(\alpha) = (\sin \alpha)^{n_1} (1 + H_v(1 - \sin \alpha))^{n_2} \quad (6.5a)$$

$$n_1 = 0.71(H_v)^{0.14} \quad (6.5b)$$

$$n_2 = 2.4(H_v)^{-0.94} \quad (6.5c)$$

where the exponents as shown, also depends on the target material hardness as well as other particle properties such as shape. These exponents are also an indication of the cutting and deformation damage by the eroding particles.

The Oka erosion model, like other popular erosion models were developed from a direct sand-blast test or dry impingement jet test. The hydrodynamics in these experimental facilities is ideal for erosion model development, however, the fitting coefficients calculated from the experiments conducted in these systems will not account for secondary flows that may be present in some complex geometries like elbows and tees. Therefore, to use an erosion model like the Oka model for wear prediction in such complex geometries, an additional coefficient is needed to account for the peculiar hydrodynamics of the complex geometries. Therefore,

the erosion model coefficient becomes  $C = C_{pt}C_{GCF}$ , where  $C_{GCF}$  represents a geometry correction factor. The coefficient  $C_{GCF}$  can either be a constant or in a functional form. For simple systems and geometries,  $C_{GCF} = 1$  can be a reasonable assumption, especially when one is predicting erosion rate for a system that is hydrodynamically similar to the one for which the erosion model was developed. This is because the effect of the unaccounted physics of the erosion process has been absorbed into the empirical constants of the erosion model. For complex geometries, DNV [7] recommended a value of  $C_{GCF} = 2.5$  for pipe bends and provided estimation procedures for other complex geometries such as a blinded tee and a flow reducer. McLaury et al. [10] work presented in Section 6.2 shows a correlation for  $C_{GCF}$  as a function of the carrier fluid viscosity, density, particle diameter, and the bend curvature for a pipe elbow.

In this study,  $C_{GCF}$  is defined such that local value for the geometry correction factor can be obtained for the elbow geometry. The schematic in Fig. 6.2 shows how the elbow is characterized using two angles,  $\beta_1$  and  $\beta_2$  instead of the radius of curvature  $r/D$ .

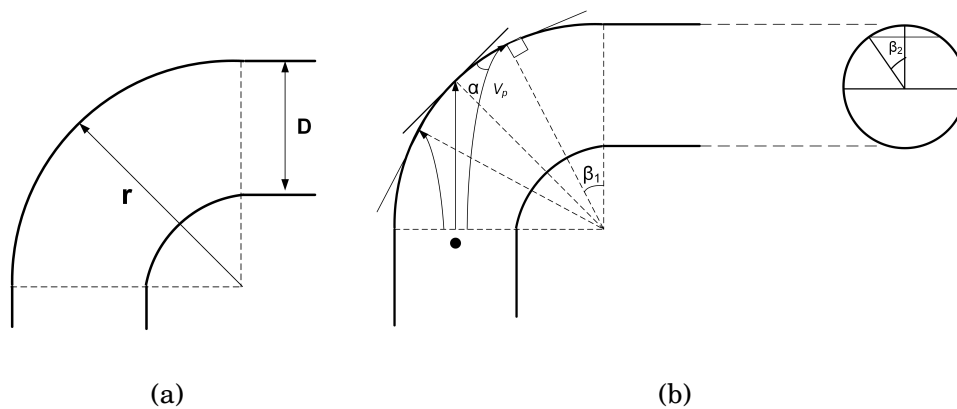


Figure 6.2: Elbow definition using (a) radius of curvature (b) characteristic angles  $\beta_1$  and  $\beta_2$

The angle  $\beta_1$  is the angle along the elbow curvature from vertical to horizontal, while  $\beta_2$  is the angle that defines the circumference of the pipe diameter from the 12 o'clock position. Based on the schematic in Fig. 6.2b, the geometry correction factor function (GCFF) can be defined as

$$C_{GCF} = G(\beta_1, \beta_2) \quad (6.6)$$

Data to fit a GCFF function needs to be generated from both experimental data and CFD-

simulations. As shown in Fig. 6.1, the GCFF model objective is to minimize the difference between experimental data and erosion model predictions on the geometry surface. This means that the data required can be obtained from an expression given by

$$\frac{E_{exp-data}}{\dot{m}_p \times E_{ratio-Oka-model}(\alpha, v_p)} = G(\beta_1, \beta_2) \quad (6.7)$$

The functional form of the GCFF will be determined based on the best fit obtained from the generated data. Two data sets, one for model development and one for validation (presented in Section 6.4) will be used in the analysis. The equation derived for Equation 6.7 in this study is presented in Section 6.6. Although  $C_{GCF}$  is shown here to be a function of geometry parameters alone, it represents the complex nature of the hydrodynamics generated by the geometry or its deviation from a seemingly simple and well parameterized geometry for which a typical erosion model was derived.

## 6.4 Description of experimental case

The experimental data considered in this work were published by Solnordal et al. [12]. They studied a standard 90° vertical-to-horizontal (V-H) elbow which has a diameter of 102.5 mm with an in-flow of particles at the rate of 0.03 kg/s. The summary of the conditions for which the experiments were performed is given in Table 6.1.

Table 6.1: Experimental conditions [12]

Test elbow diameter	102.5 mm
Particle mass flowrate	0.03 kg/s
Particle mass mean diameter	184 μm
Particle density	2650 kg/m <sup>3</sup>
Air mass flow rate	0.78 kg/s
Air inlet velocity to elbow	80 m/s
Air pressure	101.3 kPa
Air temperature	25°C
Air density	1.18 kg/m <sup>3</sup>
Air viscosity	1.8e-5 Pa·s

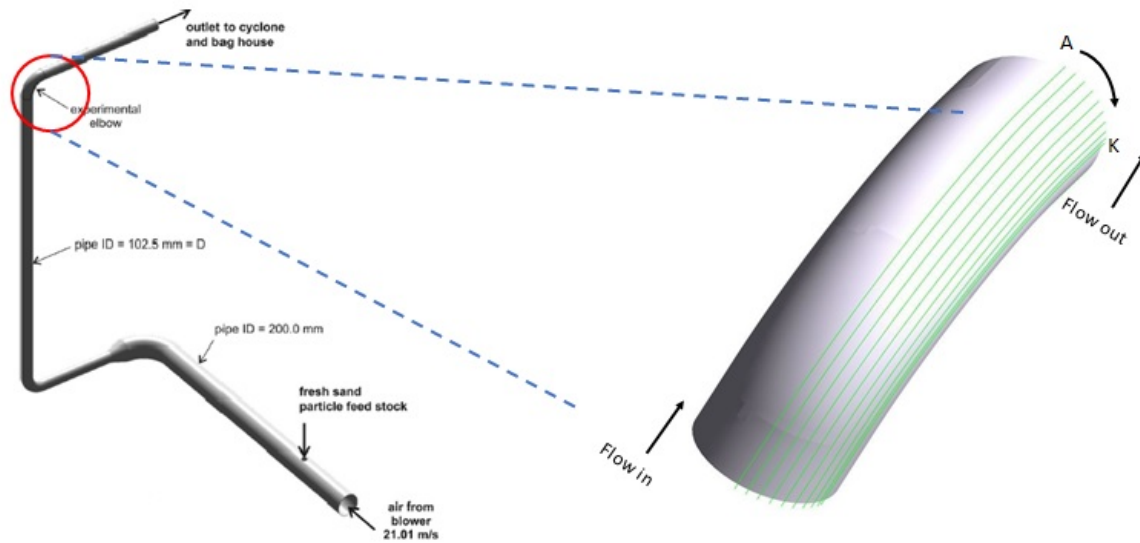


Figure 6.3: Geometry of experimental facility showing test elbow [12]

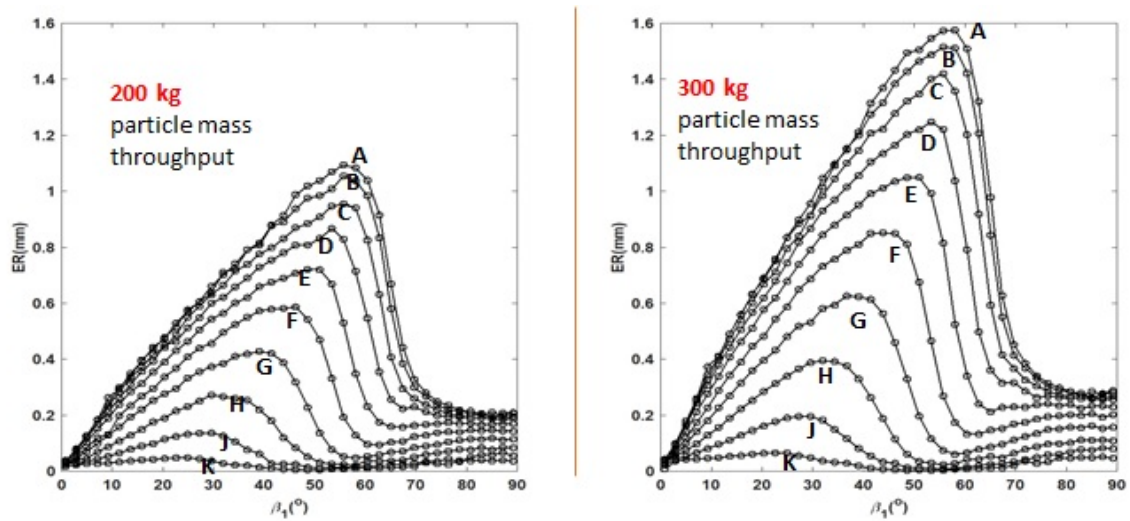


Figure 6.4: Erosion depth profile from experimental measurement [12]

The experimental facility with a zoomed-in view of the test elbow is also shown in Fig. 6.3. The authors used a profilometer, the Sheffield Discovery II D-8 co-ordinate measurement machine (CMM) to map out the surface profiles along the specific lines labelled A to K depicted in Fig. 6.3. Measured wear rate data for 10 profiles labelled A to K were then

used by the authors to generate a 2D wear map of the elbow surface. Two sets of data were collected: at 200 kg and at 300 kg sand mass throughput. These two sets of data are presented in Fig. 6.4. The 200 kg data will be used for the geometry correction factor function model development while model testing and validation will be carried out using the 300 kg data. Complete details of the experimental procedures can be found in Solnordal et al. [12].

## 6.5 Numerical formulation

In this study, a three-dimensional analysis using the Eulerian-Lagrangian method was implemented. The CFD code ANSYS Fluent 19.0<sup>®</sup> was used for the analysis. For erosion modelling, three steps are involved in the analysis which are (1) flow modelling (2) particle tracking (3) erosion calculation.

### 6.5.1 Model equations

#### Gas phase

The gas phase momentum and mass conservation was modelled using the Reynolds-Averaged Navier-Stokes equation [20, 21]. The equations are given by

$$\frac{\partial(\rho u_i)}{\partial x_i} = 0 \quad (6.8)$$

$$\frac{\partial(\rho u_i u_j)}{\partial x_i} = -\frac{\partial p}{\partial x_i} + \frac{\partial}{\partial x_j} \left[ (\mu + \mu_t) \left( \frac{\partial u_i}{\partial x_j} + \frac{\partial u_j}{\partial x_i} \right) \right] + \rho g_i \quad (6.9)$$

The RNG  $k - \epsilon$  model was used for turbulence modelling [23]. The turbulence kinetic energy and the turbulence dissipation rate are solve by transport equations which are given by

$$\frac{\partial(\rho k u_i)}{\partial x_i} = \frac{\partial}{\partial x_j} \left[ \alpha_k \mu_{eff} \frac{\partial k}{\partial x_j} \right] + G_k + \rho \epsilon \quad (6.10)$$

$$\frac{\partial(\rho \epsilon u_i)}{\partial x_i} = \frac{\partial}{\partial x_j} \left[ \alpha_\epsilon \mu_{eff} \frac{\partial \epsilon}{\partial x_j} \right] + \frac{C_{1\epsilon}}{k} G_k - C_{2\epsilon} \rho \frac{\epsilon^2}{k} \quad (6.11)$$

where

$\mu_{eff} = \mu + \mu_t$	is the effective viscosity
$\mu_t = \rho C_\mu \left(\frac{k^2}{\epsilon}\right)$	is the turbulence viscosity
$\alpha_k = \alpha_\epsilon = 1.393$	are the inverse Prandtl number
$G_k = \mu_t (2S_{ij}S_{ij})$	is the production of turbulence energy
$C_\mu$	= 0.0845
$C_{1\epsilon}$	= 1.42
$C_{2\epsilon}$	= 1.68

### Particle phase

The particle or discrete phase was modelled using the Lagrangian method that uses the Newton's second law to track individual particle [20, 21]. For rigid spherical particles, the particle trajectory, linear momentum, and angular momentum equations are given by

$$\frac{dx_i}{dt} = u_{pi} \quad (6.12)$$

$$m_p \frac{du_{pi}}{dt} = m_p \frac{3\rho C_D}{4\rho_p d_p} |u_i - u_{pi}| (u_i - u_{pi}) + F_{si} + F_{ri} + \left(1 - \frac{\rho}{\rho_p}\right) m_p g_i \quad (6.13)$$

$$(0.1 m_p d_p^2) \frac{d\omega_{pi}}{dt} = \frac{\rho d_p^5 C_\omega}{60} |\vec{\Omega}| |\vec{\Omega}| = T_i \quad (6.14)$$

The spherical drag law by Morsi and Alexander [24, 25] was used to calculate the drag coefficient and is given by

$$C_D = a_1 + \frac{a_2}{Re_p} + \frac{a_3}{Re_p^2} \quad (6.15)$$

The value of constants  $a_1, a_2$ , and  $a_3$  depends on the particle Reynolds number and are given in Table 6.2

Table 6.2: Morsi and Alexander drag law constants

Range	$a_1$	$a_2$	$a_3$
$Re_p < 0.1$	0	24	0
$0.1 < Re_p < 1$	3.690	22.73	0.0903
$1 < Re_p < 10$	1.222	29.1667	-3.8889
$10 < Re_p < 100$	0.6167	46.50	-116.67
$100 < Re_p < 1000$	0.3644	98.33	-2778

The rotational drag coefficient  $C_\omega$  is Defined according to the correlation by Dennis et al. [26] and is given by

$$C_\omega = \frac{6.45}{\sqrt{Re_\omega}} + \frac{32.1}{Re_\omega} \quad (6.16)$$

where,

$$Re_\omega = \frac{\rho |\vec{\Omega}| d_p^2}{4\mu} \quad (6.17)$$

$$\vec{\Omega} = 0.5 \vec{\nabla} \times \mathbf{u}_i - \omega_{pi} \quad (6.18)$$

The term  $F_{si}$  is the Saffman's lift force [27, 28] which is defined by

$$\vec{F}_{si} = \frac{2K v^{1/2} \rho d_{ij}}{\rho_p d_p (d_{lk} d_{kl})^{1/4}} (\vec{u} - \vec{u}_p) \quad (6.19)$$

where  $K = 2.594$  and  $d_{ij}$  is the deformation tensor. The rotational or Magnus lift force is based on the formulation of Oesterlé and Bui Dinh [29] and is defined by

$$F_{ri} = \frac{1}{2} A_p C_{RL} \rho \frac{|\vec{V}|}{|\vec{\Omega}|} (\vec{V} \times \vec{\Omega}) \quad (6.20)$$

where,

- $A_p$  is the projected particle surface area
- $\vec{V}$  is the relative fluid-particle velocity
- $\vec{\Omega}$  is the relative fluid-particle angular velocity

The rotational lift coefficient,  $C_{RL}$  is defined by

$$C_{RL} = 0.45 + \left( \frac{Re_\omega}{Re_p} - 0.45 \right) \exp(-0.05684 Re_\omega^{0.4} Re_p^{0.3}) \quad (6.21)$$

For wall rebound, the model by Grant and Tabakoff [30, 31] was used for particle-wall restitution coefficient. The normal and tangential components of the restitution coefficient are given by

$$e_n = 0.993 - 1.76\alpha + 1.56\alpha^2 - 0.49\alpha^3 \quad (6.22a)$$

$$e_t = 0.998 - 1.55\alpha + 2.11\alpha^2 - 0.67\alpha^3 \quad (6.22b)$$

The rough wall model available in ANSYS Fluent 19.0<sup>®</sup> which is based on the work of Sommerfeld and Huber [32] was implemented to model wall roughness. If  $R_a$  is the mean height of the roughness structure,  $R_q$  is the standard deviation of the roughness structure, and  $RS_m$  is the characteristic length between roughness structure, then the wall roughness parameter  $\Delta\gamma$  is given by

$$\Delta\gamma = \begin{cases} \tan^{-1} \frac{2R_q}{RS_m}, & \text{if } d_p < \frac{RS_m}{\sin(\tan^{-1} \frac{2R_q}{RS_m})} \\ \tan^{-1} \frac{2R_a}{RS_m}, & \text{otherwise} \end{cases} \quad (6.23)$$

In this study, the a one-way coupling was implemented as the degree of interaction, therefore, particle-particle collision interaction was not considered. This is a reasonable assumption for dilute systems such as the test case considered in this study which has a particle volume fraction of  $1.75 \times 10^{-5}$  [20]. The turbulent dispersion of particles was modelled using the Discrete Random Walk (DRW) [33]. This is a stochastic tracking technique that integrates the trajectory of each particle using the instantaneous fluid velocity. By increasing the number of tries of the DRW, a sufficient number of representative particles are accounted for in the integration.

## 6. 5.2 CFD set-up and solution

### Geometry and mesh

The complete 3D model of the geometry as published by Solnordal et al. [12] was created using SpaceClaim<sup>®</sup> available in the ANSYS Workbench Package<sup>®</sup>. A 3D unstructured hexahedral mesh was generated for the geometry using O-grid meshing method in ICEM CFD 17.0<sup>®</sup>. The grid generated for the test elbow and the geometry inlet is shown in Fig. 6.5.

As depicted in Fig. 6.5a,  $11 \times 11 \times 19$  surface elements were generated for the air inlet while as in Fig. 6.5b, 45 cells were generated across the elbow inlet to the elbow outlet. The total number of cells generated is approximately 750,000. Before deciding to use this number of cells, a mesh independence analysis was carried out on the model using single phase airflow simulation. This is shown in Fig. 6.6 where the turbulence intensity predicted at the elbow extrados is monitored. It can be seen from the figure that further grid refinement after

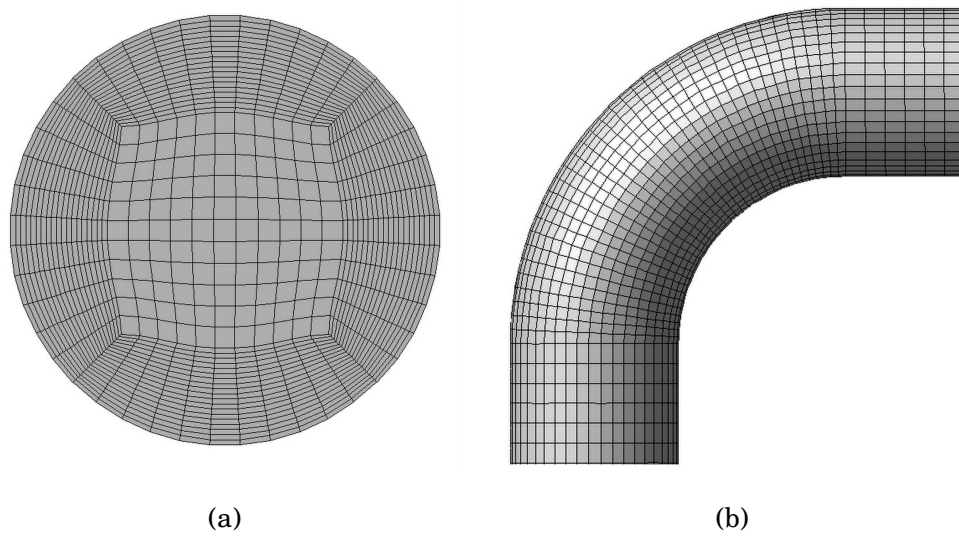


Figure 6.5: Mesh grid for (a) geometry inlet (b) test elbow

750,000 cells did not result in any change in the variable being monitored .i.e. the turbulence intensity profile. Also, 750,000 number of cells was found to be optimal for solution accuracy, convergence, time, and mesh quality.

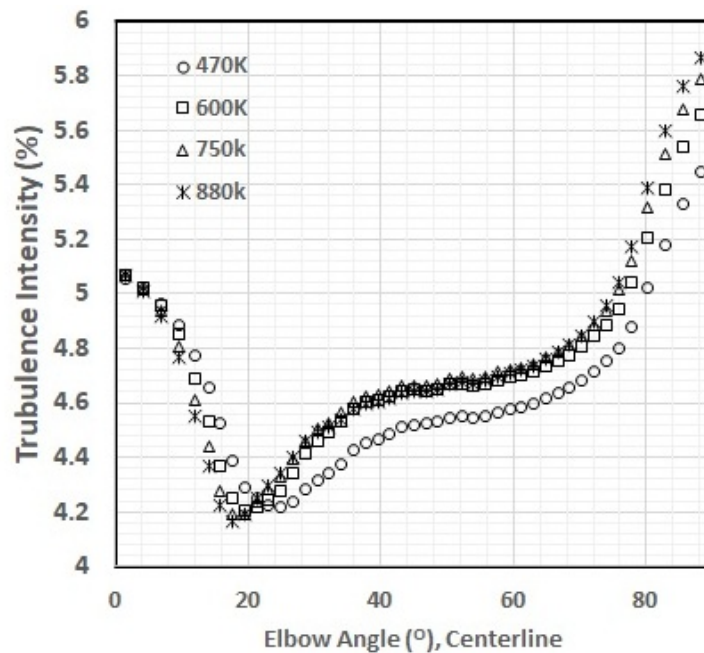


Figure 6.6: Mesh independence analysis- Turbulence intensity predicted at elbow extrados

## Boundary conditions

For boundary conditions, a velocity inlet and pressure outlet were specified for the test geometry for air flow. A uniform velocity magnitude of  $21.01 \text{ m/s}$  and hydraulic diameter of  $0.2 \text{ m}$  was specified at the air inlet. Turbulence intensity for the air inlet was also calculated using [34]

$$I = 0.16(Re_g)^{-0.125} \quad (6.24)$$

The inlet surface for particles was set to  $0.5 \text{ m}$  downstream of the air inlet to replicate conditions of the experimental set-up. Escape boundary condition was used for the discrete particle phase inlet and outlet flow. A mass flow rate of  $0.03 \text{ kg/s}$  was specified for the particle inlet with a face normal inlet velocity of  $1 \text{ m/s}$ . For simplicity and because the sand tested had a narrow particle size distribution [12], the particles were assumed to be inert, spherical and uniform with a mass mean diameter of  $184 \mu\text{m}$ . For the wall boundary condition, a no-slip wall was specified for shear condition and zero for wall roughness for the air phase. A reflect boundary condition was specified for the discrete phase using restitution (or reflection) coefficient models by Grant and Tabakoff [30] as presented in Equation 6.22. Particle phase wall roughness parameters according to Equation 6.23 were specified. The values specified for the mean height, standard deviation, and length of the roughness structure are  $8 \mu\text{m}$ ,  $2 \mu\text{m}$ , and  $8 \mu\text{m}$  respectively. Several wall roughness parameters were tested and these values gave the optimal distribution of wear around the elbow when compared to experimental results. Also, similar values were used by Solnordal et al. [12] and they reported a reasonable prediction of the wear map. These values also will result in a roughness parameter value of approximately  $\Delta\gamma = 10$  which was used in the work of Duarte et al. [20] and Sommerfeld and Lain [35]. A value of 0.2 was used for the particle-wall friction coefficient which is the default value.

## Solution procedure

A steady state solution was carried out using the SIMPLE algorithm for pressure-velocity coupling for the air phase. The absolute reference frame was used for velocity formulation and a second-order solution method was used for pressure, momentum, and turbulence equation. The under-relaxation factors and solution limits for the solvers were left at their default

values. The hybrid method of solution was used for the particle phase with trapezoidal and implicit methods for higher order and lower order tracking scheme respectively. A User-Defined Function (UDF) was written to track the particles and collect the necessary particle impact data needed for analysis. Since a one-way coupling was considered, the air phase was first solved. A maximum number of iteration of 1000 was specified in which convergence of all residual parameters reached a value less than  $1 \times 10^{-8}$ . The discrete phase scheme was then turned on for particle tracking. About 390,000 particles were released and tracked in the fluid domain. An independent study for statistical relevance of the particle tracking scheme was done and this number of particles was selected as the optimal choice.

## 6.6 Results and discussion

### 6.6.1 Flow validation

Flow validation is often the first step in CFD modelling before proceeding with the analysis of subject in focus. In this study, an independent hydrodynamics study was conducted using the adopted modelling methods. The work of Huber and Sommerfield [32, 36] was selected as the case for flow validation. In their work, glass beads of diameter of  $40 \mu m$  was transported by air through a horizontal stainless steel pipe of diameter  $150 mm$ . The air superficial velocity was  $27 m/s$  and the particle mass loading was  $0.7 kg$  particles/kg air. The length of the horizontal pipe section is about  $10 m$ . Measurements of particle velocity profiles were taken at a point  $8 m$  downstream of the inlet. The comparison between CFD predictions and experimental data for normalized root mean square (RMS) and mean particle velocities are shown in Fig. 6.7. It can be seen from the figure that a good agreement was obtained between experiment and simulation using the modelling method adopted in the study. This step is essential, particularly because of the lack of hydrodynamics data available for the elbow being studied.

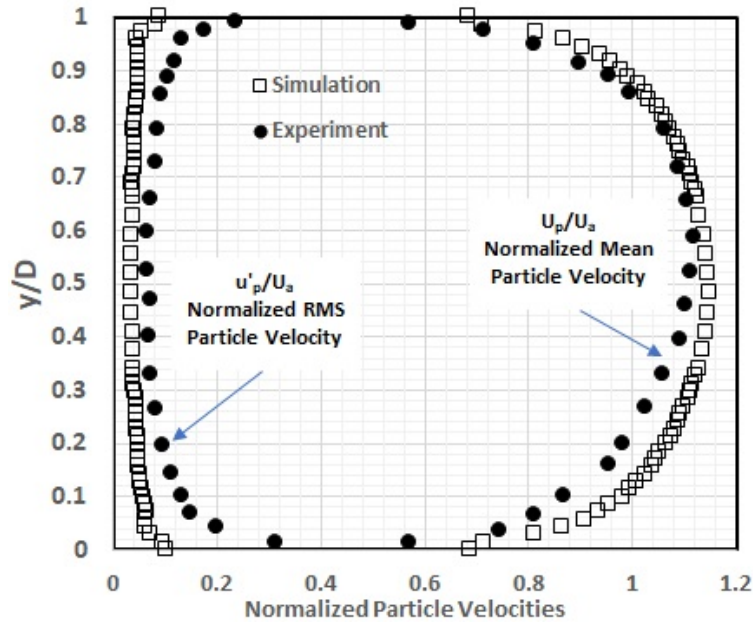


Figure 6.7: Comparison of CFD prediction and experimental data for normalized particle velocities [32, 36]

## 6. 6.2 Wear rate and local wear variables predictions

Highly accurate CFD simulations is one of the essential components in the development of the GCFF model as presented earlier in Fig. 6.1 and Equation 6.7. In these section, results are obtained for three particle-wall interaction cases; smooth wall, rough wall, and rough wall with particle rotation as shown in Fig. 6.8.

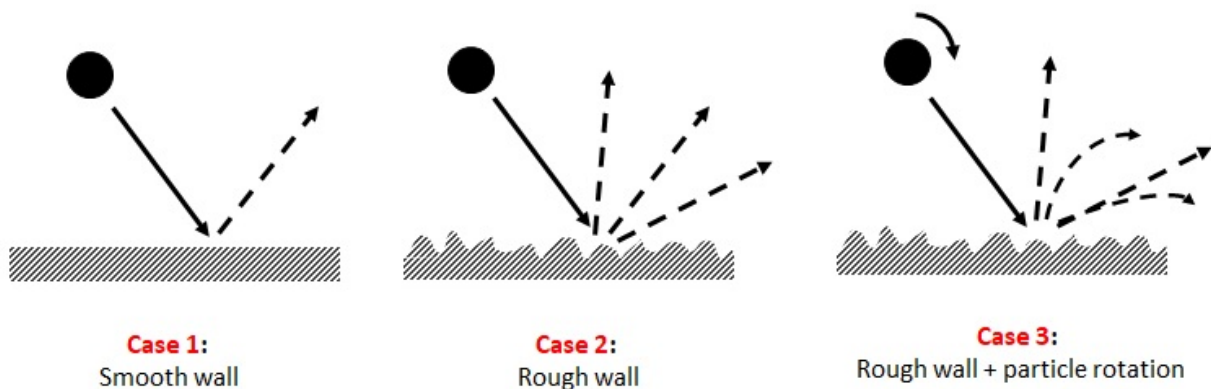


Figure 6.8: Particle-wall interaction simulation cases

In the figure, the solid arrows is the path of the particles before impact while the dotted arrows represents the possible path(s) of the particle after rebound. The smooth wall case is the ideal and most simplistic case of particle-wall interaction in which the path of particle after rebound can almost always be predetermined. In ANSYS Fluent<sup>®</sup> for the rough wall case, a virtual wall is used to replace the real one at the point of particle-wall contact [33]. The inclination angle of the virtual wall which determines the path of the particle after rebound is computed as a function of statistical surface roughness parameters and the current particle diameter. For the case of rough wall with particle rotation, additional modelling is considered in which angular velocity is calculated for the particles based on the equilibrium between particle inertia and drag.

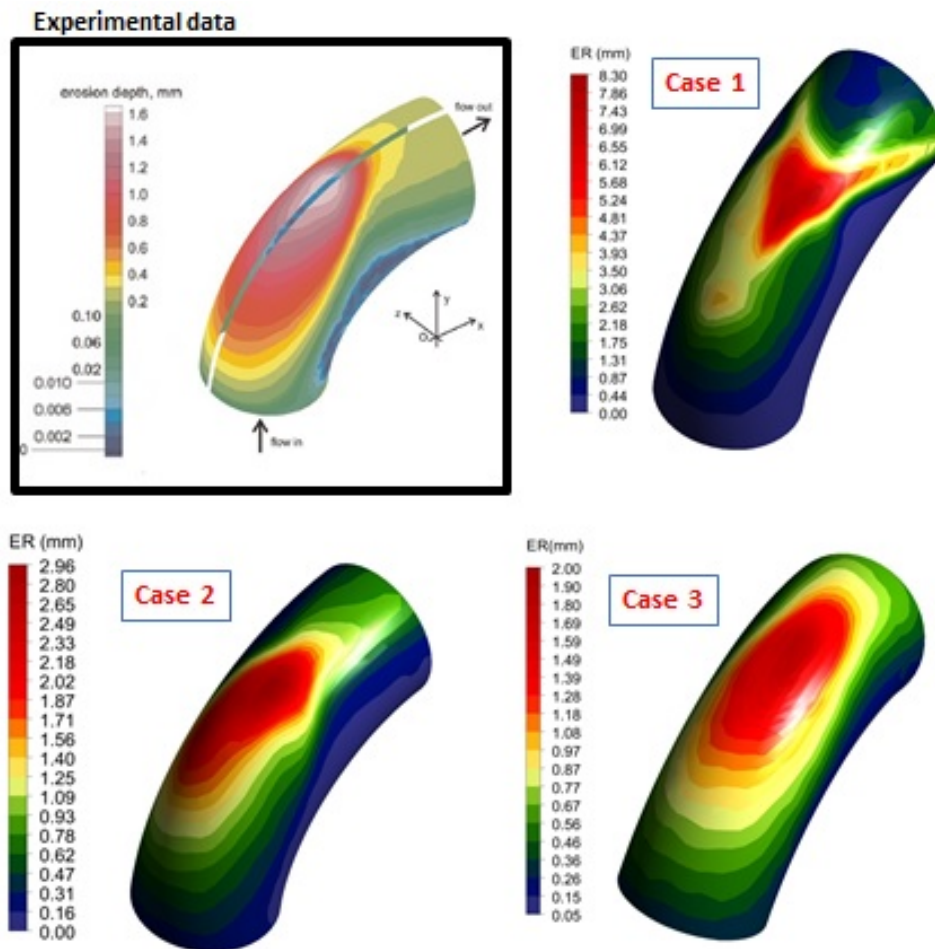


Figure 6.9: Contour plots of erosion depth calculated for smooth wall (Case 1), rough wall (Case 2), and rough wall with particle rotation (Case 3) versus experimental data

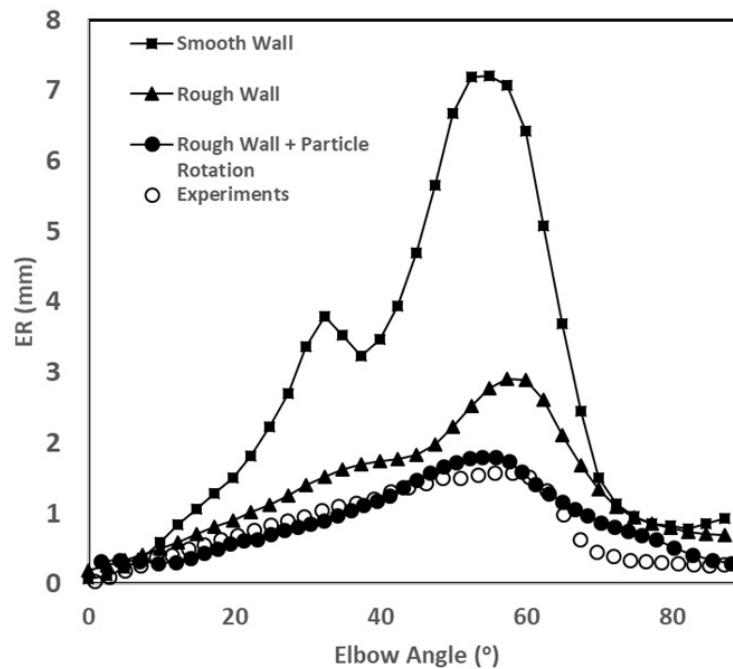


Figure 6.10: Elbow centre line profiles of erosion depth calculated for smooth wall (Case 1), rough wall (Case 2), and rough wall with particle rotation (Case 3) versus experimental data

Erosion depth calculations made using the Oka model for these three cases are shown in Fig. 6.9 for the elbow extrados (outer side). The elbow centre line erosion depth profile for these three cases are also shown in Fig. 6.10. The experimental data used for comparison is the centre line profile (profile A, see Fig. 6.3 and Fig. 6.4) for the 300 kg particle mass throughput. It is apparent from the figures that the erosion depth predictions for the case of rough wall plus particle rotation closely match the experimental data with the smooth wall case showing the characteristics “rabbit-ears” observed in many other numerical studies of erosion rate [37–40]. Also, from Fig. 6.10, the simulation prediction matches the erosion data more closely at the elbow entrance region i.e. elbow angle between  $0^\circ$  to  $45^\circ$ , compared to the exit region i.e. elbow angle between  $45^\circ$  to  $90^\circ$ . The conditions at the elbow entrance region resembles that of a direct impact/impingement from which the erosion model was developed, hence, the better performance of the erosion model seen. However, towards the elbow exit, the impact of particles is not direct and could results from secondary flows patterns. This is not captured by the erosion model and has resulted in the reduced prediction performance in this region. The wall roughness and particle rotation on the local wear variables i.e. particle impact velocity, impact angle, and mass rate was also examined as shown in Fig. 6.11.

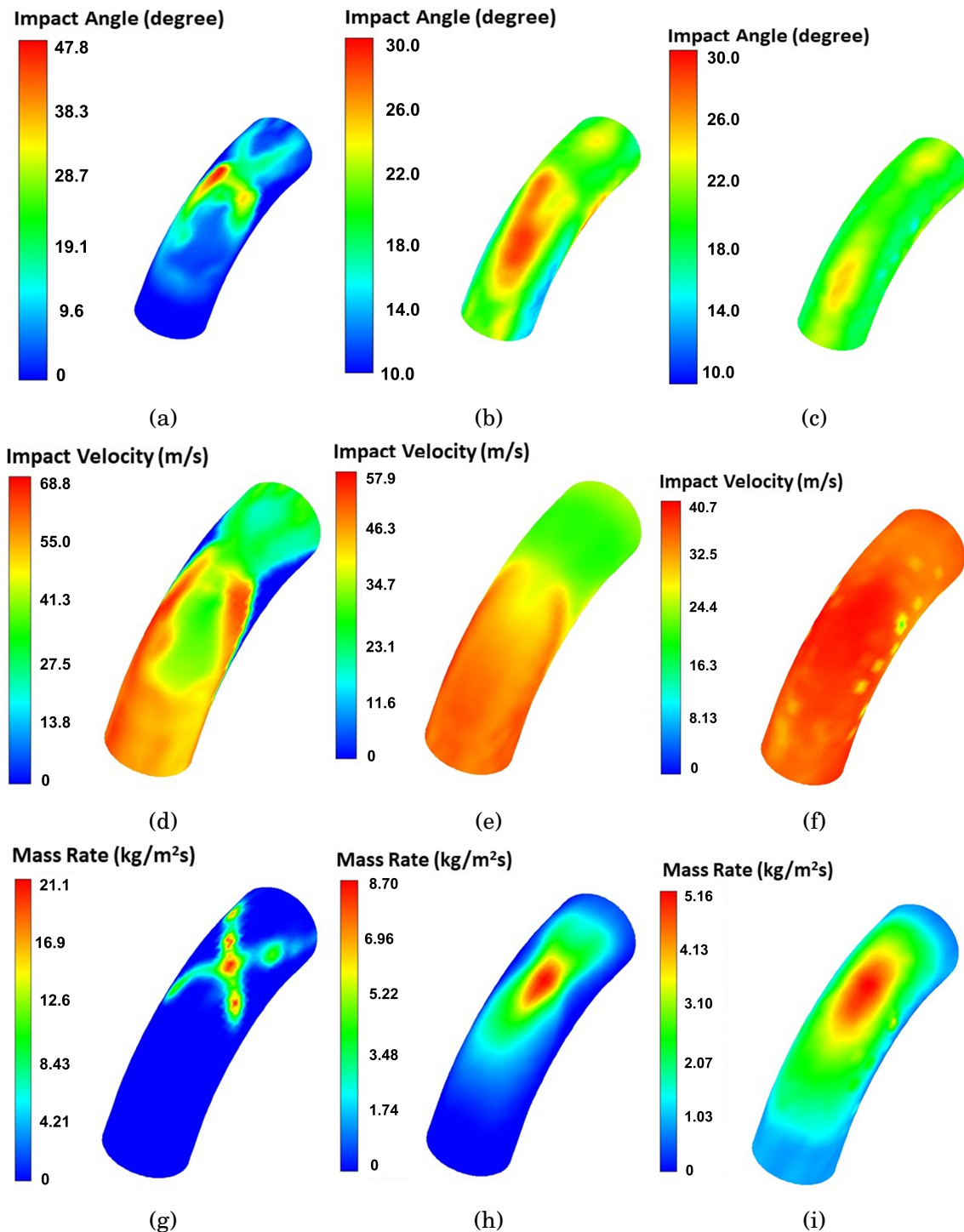


Figure 6.11: Comparison of particle impact variables (a)-(c) particle impact angle for smooth wall, rough wall, and rough wall with particle rotation respectively (d)-(f) particle impact velocity for smooth wall, rough wall, and rough wall with particle rotation respectively (g)-(i) particle mass rate for smooth wall, rough wall, and rough wall with particle rotation respectively

As can be observed in the contour plots in Fig. 6.11, there is notable difference in the simulation results going from smooth wall to rough wall with particle rotation. For the smooth wall case, the particle impact variables are more concentrated around the centre spot on the outer wall of the elbow. This is also visible in the particle trajectories for the smooth wall, rough wall, and rough wall with particle rotation cases shown in Fig. 6.12.

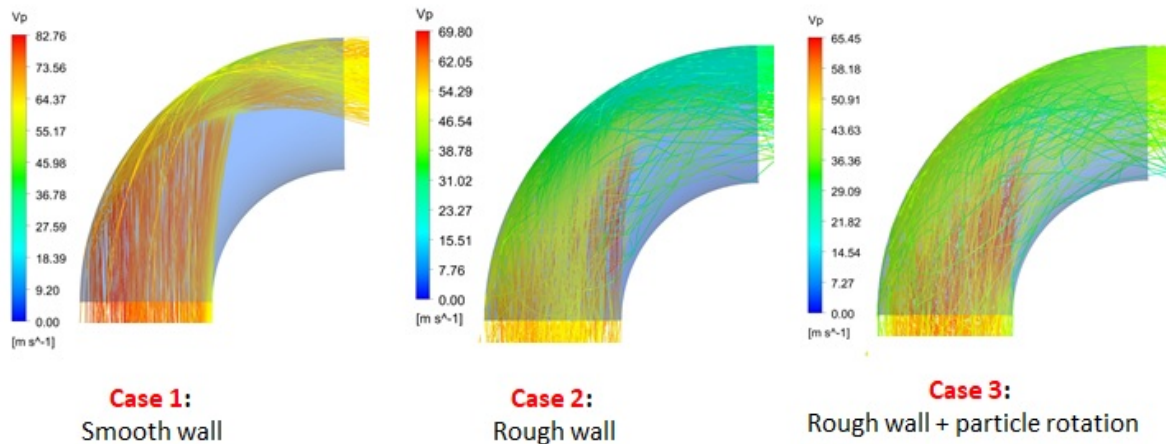


Figure 6.12: Particle tracks for smooth wall (Case 1), rough wall (Case 2), and rough wall with particle rotation (Case 3)

Also for this smooth wall case, particle rebound is low and there is less shadowing effect, hence, the particle impact is focused locally on a point because most of the particles are directed to the core of the elbow and away from the wall. This observation has been shown to result in a wear map totally different from that observed in recent experimental findings [12, 20, 35]. Accounting for target material wall roughness decreased the focusing effect and increased dispersion of particles in the core of the flow inside the elbow. This led to the particles impacting over a larger surface area of the elbow wall, resulting in the more even distribution of the local wear variables. This distribution may be considered more realistic than the case of smooth walls since the wear map distribution begins to resemble that observed experimentally [12]. Accounting for the effect of particle rotation further increased the dispersion of particles in the flow. With particle rotation, rotational lift force comes into effect and the particles impact even over a larger surface area of the elbow wall [21]. Particle impact angle can be seen to be between  $10^\circ - 25^\circ$  for the case of a rough wall

with particle rotation,  $10^\circ - 30^\circ$  for rough wall only case and  $0^\circ - 50^\circ$  for the smooth wall case. Particle impact velocities ranged from 0-70 m/s for the smooth wall case, 20-60 m/s for rough wall case, and 20-40 m/s when both a rough wall and particle rotation were considered. The decrease in the range of values was also shown in the particle mass rate with the smooth wall having a maximum of  $21.1 \text{ kg/m}^2\text{s}$ . The rough wall case has a maximum value of  $8.7 \text{ kg/m}^2\text{s}$  and the case with rough wall and particle rotation has a maximum value of  $5.16 \text{ kg/m}^2\text{s}$ .

From the discussion in this section, it is clear that the case of rough wall with particle rotation best represents the condition for particle-wall interaction in the elbow system. Therefore, the predicted local wear variables for the case will be implemented for the development of the GCFF model in the following section.

### 6. 6.3 GCFF development and validation

#### Data analysis and model development

Based on the discussion in Section 6. 6.2, predicted particle impact velocities, particle impact angles, and particle mass flow rates were extracted from the simulation results. A User-Defined Function (UDF) code based on recommendations from ANSYS [41] and Mansouri [42] was written to track and collect these local wear variables data. As discussed in Section 6. 3, the calculated particle impact data are supplied into the Oka erosion model [5, 6] to predict the erosion ratio. The erosion model prediction is then combined with combined with the 200 kg sand throughput wear data in the work of Solnordal et al. [12] according to Equation 6.7. Data was calculated for fitting the geometry correction factor function this equation. The Oka model constants and coefficients for a sand-aluminum erodent-material combination were used in the erosion ratio model equation [20]. The set of data generated was fitted into a model using the MATLAB 2016b<sup>®</sup> Curve Fitting Tool. The form of the model for the geometry correction factor function (GCFF) is given by

$$G(\beta_1, \beta_2) = A \left( \sum_{n=1}^3 \sin^n(B_n \beta_1 + C_n) \right)$$

$$\text{Where, } A = (1 + a_1 \beta_2 + a_2 \beta_2^2)$$

$$B_n = (1 + \sin \beta_2)^{k_n} \left( \frac{\pi}{2} + b_{1n} \beta_1 + b_{2n} \beta_1^2 \right)$$

$$C_n = \text{constant}$$
(6.25)

where  $a_1, a_2, b_{1n}, b_{2n}, k_n$  are fitting constants. The numerical values of these constants are given in Table 6.3.

Table 6.3: Numerical values of GCFF model constants

Index	$a$	$b_1$	$b_2$	$C$	$k$
1	-0.04457	4.518	-1.821	-0.4231	0.3993
2	-0.3699	2.672	-0.971	1.322	0.1079
3	-	0.2502	-0.1889	-0.7606	1.099

In the approach adopted to develop the GCFF, the calculated data were fitted in a step-wise manner to different standard model forms, which was a learning process that informed our choice of model selection and ultimately led to the sinusoidal form of the model - with the coefficients having a polynomial form – as described here.

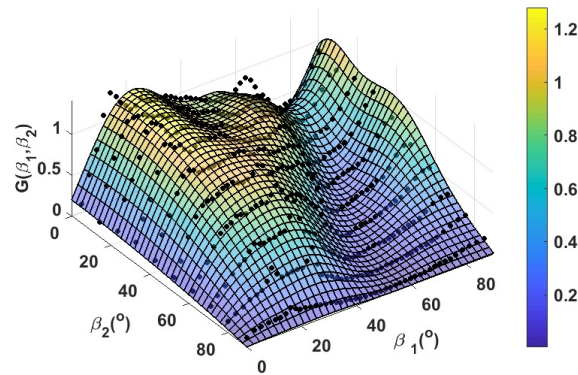


Figure 6.13: Surface plot of the fitted geometry correction factor function,  $G(\beta_1, \beta_2)$

The Least Absolute Residual (LAR) robust method and the Levenberg-Marquardt algorithm were adopted for the fitting of the final model. The surface plot for the fitted model is shown in Fig. 6.13, and as can be seen from the figure, it is evident that there is a good fit between the derived function and the generated data. The R-squared value for the fitted GCFF model is 0.967. Fig. 6.14 also shows the contour plot of the GCFF and the values of correction factors that will be calculated locally for wear rate adjustment. It is evident from the plot that the GCFF can adapt to local positions on the elbow surface to correct wear rate predictions by calculating correction factors unique to these positions. It is important to note that the value of the model's fitting constants may vary for a different erodent-material

combination. The system considered is also a gas-solid system and some changes are expected when considering liquid-solid systems.

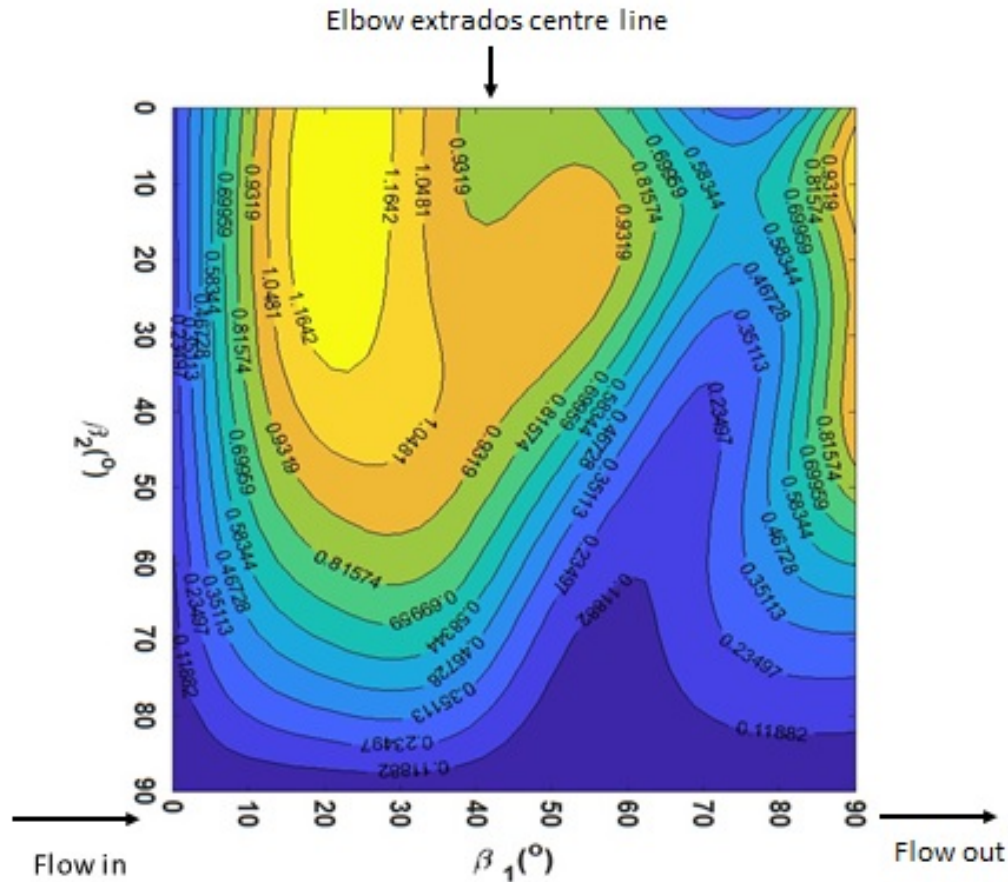


Figure 6.14: Contour plot of the fitted geometry correction factor function,  $G(\beta_1, \beta_2)$

### Model testing for erosion prediction

For model performance testing, the 300 kg sand mass throughput data in the work of Solnordal et al. [12] was used. The Oka erosion model was still used for the validation. Four profile data for the test elbow (A, D, G, and K) were selected for model validation. The comparison of the predictions for cases with and without the inclusion of the geometry correction factor function (GCFF) model is presented in Fig. 6.15. All the figures on the left show the prediction without the use of the GCFF model while the figures on the right have the GCFF model included.

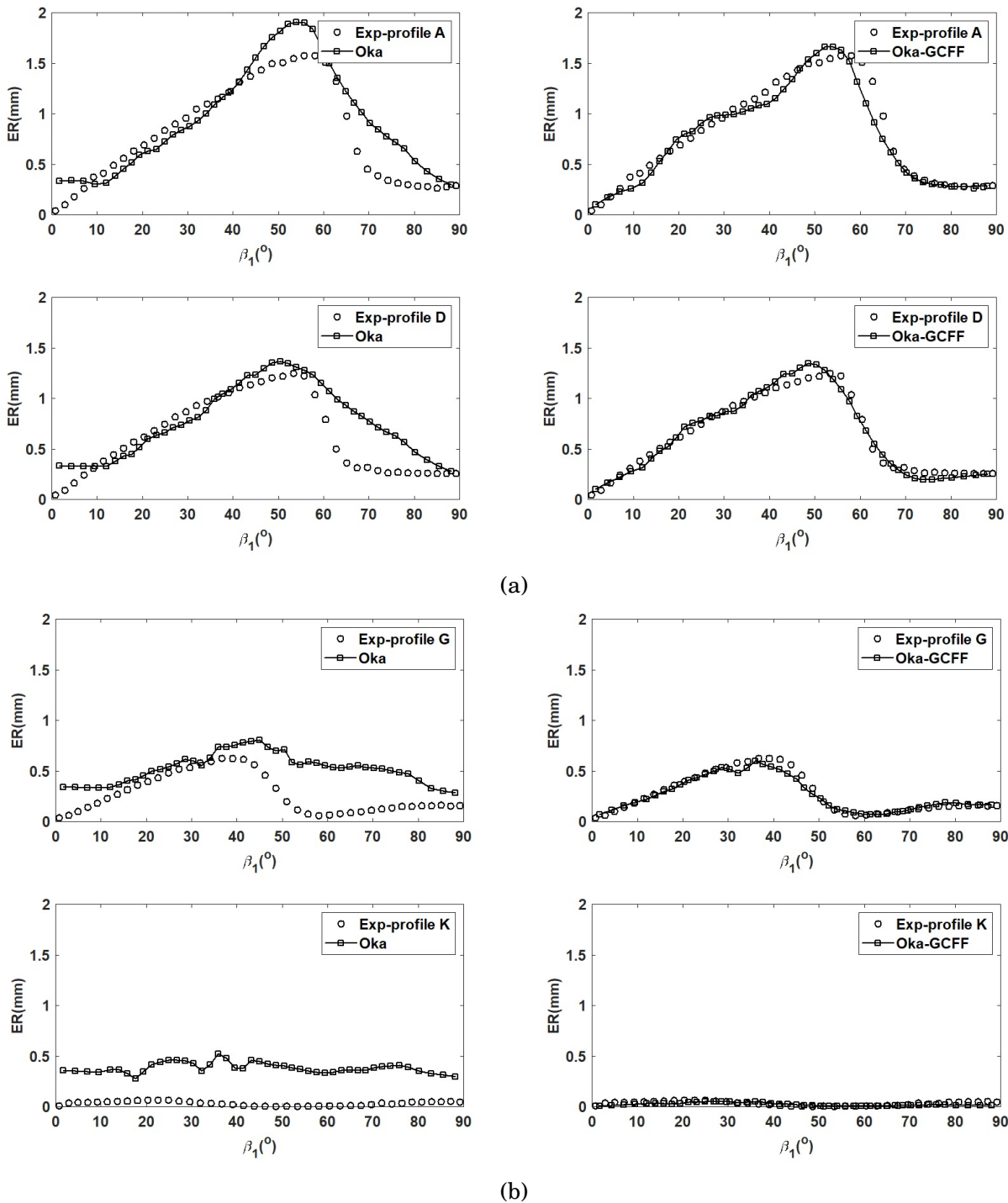


Figure 6.15: Performance of Oka model versus Oka model with the developed GCFF model

It is clear from Fig. 6.15 that there is significant improvement in the prediction accuracy of the Oka erosion model when the geometry correction factor model is included. For the centre line profile A and for profile D which is within  $30^\circ$  to the elbow centre line, the Oka model predictions was particularly improved for the experimental wear data at the elbow outlet region. For profiles closer to the elbow intrados i.e. profiles G and K, the improvement in wear prediction is more pronounced, especially for profile K where the use of Oka model alone predicted wear rates which differ significantly from the measured data. Previous works have mostly compared the elbow centre line wear rate profile (profile A) with CFD predictions and have often neglected the intrados (inner side of elbow) region wear data for this case. The result from this work has been able to show hoe improved wear prediction can be obtained in this region in an elbow system. The findings from this study also made it clear that the GCFF affords some flexibility because of its use with an existing erosion model, making it a more robust geometry correction factor which is suitable for gas-solid elbow systems.

## 6.7 Conclusions and future works

This study presents a new approach to combining CFD simulations and experimental measurements to improve the prediction of wear in complex geometries. First, the effects of wall roughness and particle rotation on the accuracy of predicted wear rate was investigated via CFD simulations. The results also showed that erosion models are more accurate under conditions and/or in geometries similar to the ones for which they were developed. Complex geometries therefore require a correction factor to improve the prediction performance of these erosion models. The geometry correction factor function (GCFF) developed in this work has proven to be useful, in this case with the Oka erosion model for the vertical-to-horizontal standard elbow considered in this study. The inclusion of the geometry correction factor improved considerably the accuracy of the erosion model in predicting the experimental wear data. Additionally, the developed GCF as well as the method of analysis in this study have made the following significant contributions:

1. The geometry correction factor was defined as  $G(\beta_1, \beta_2)$  i.e. it is entirely dependent on elbow dimensions and not on the flow itself. It should therefore be possible to apply the geometry correction factor model developed here to larger (but geometrically similar) elbows with no additional experimental wear data required. Additionally, the approach

taken here allows one to apply the GCFF to other elbow orientations since they can also be defined by  $\beta_1, \beta_2$ . Any effects due to a change in system conditions such as particle diameter and flow velocity should have no impact on the performance of the GCF since such effects will be captured in the erosion model itself. It is important to note that further tests and simulation studies are needed to show the generality of the GCFF model described above.

2. Many complex geometries such as tees and cyclones can also have a geometry correction factor using the method employed in this study. To implement this, one will first of all run a series of CFD simulations for the system to determine (a) conditions for which a pilot plant can be run if one is needed, and (b) the region of critical wear in the system. A 3D wear map for a test section in such pilot plant can further be obtained. Following the method of analysis applied in this work, a GCFF can be developed for the system, which depends only on the geometry characteristics of the system. This custom GCFF can then be confidently taken from the pilot plant to the industrial scale system to predict their wear rates at that scale more accurately. The rationale here is that if operating conditions such as Reynolds number and Stokes number are matched between the pilot plant and the industrial scale system, no fluid-particle physics will be lost in the empirical coefficients that defines the developed GCFF when it is taken from pilot scale to industrial scale.

## References

- [1] M. C. Roco, G. R. Addie, Erosion wear in slurry pumps and pipes, *Powder Technol.* 50 (1987) 35–46. doi:10.1016/0032-5910(87)80081-5.
- [2] I. Finnie, Erosion of surfaces by solid particles, *Wear* 3 (1960) 87–103. doi:10.1016/0043-1648(60)90055-7. arXiv:arXiv:1011.1669v3.
- [3] I. Finnie, Some Observations on the Erosion of Ductile Metals, *Wear* 19 (1972) 81–90.
- [4] I. Finnie, D. H. McFadden, On the velocity dependence of the erosion of ductile metals by solid particles at low angles of incidence, *Wear* 48 (1978) 181–190. URL: <http://www.sciencedirect.com/science/article/pii/0043164878901473>. doi:10.1016/0043-1648(78)90147-3.

- [5] Y. I. Oka, H. Ohnogi, T. Hosokawa, M. Matsumura, The impact angle dependence of erosion damage caused by solid particle impact, *Wear* 203 (1997) 573–579.
- [6] Y. I. Oka, K. Okamura, T. Yoshida, Practical estimation of erosion damage caused by solid particle impact Part 1 : Effects of impact parameters on a predictive equation, *Wear* 259 (2005) 95–101. doi:[10.1016/j.wear.2005.01.039](https://doi.org/10.1016/j.wear.2005.01.039).
- [7] DNV, Recommended Practise RP O501: Erosive Wear in Piping Systems, 2011.
- [8] H. C. Meng, K. C. Ludema, Wear models and predictive equations: their form and content, *Wear* 181-183 (1995) 443–457. doi:[10.1016/0043-1648\(95\)90158-2](https://doi.org/10.1016/0043-1648(95)90158-2).
- [9] F. A. Bikbaev, V. I. Krasnov, M. Z. Maksimenko, V. L. Berezin, I. B. Zhilinski, N. T. Otroshko, Main factors affecting gas abrasive wear of elbows in pneumatic conveying pipes, *Chem. Pet. Eng.* 9 (1973) 73–75. URL: <https://doi.org/10.1007/BF01139742>. doi:[10.1007/BF01139742](https://doi.org/10.1007/BF01139742).
- [10] B. S. McLaury, J. Wang, S. A. Shirazi, SPE, J. R. Shadley, E. F. Rybicki, Solid Particle Erosion in Long Radius Elbows and Straight Pipes, *Annu. Spe Tech. Conf.* (San Antonio, 10/5-8/97) *Proc. [Production Oper. Eng.* (1997) 977–986.
- [11] X. Song, P. Luo, S. Luo, S. Huang, Numerical simulation study on the influence of incident position on erosion characteristics of gas-particle two-phase flow in 90 degree elbow, *Adv. Mech. Eng.* 9 (2017) 1–18. doi:[10.1177/1687814017733249](https://doi.org/10.1177/1687814017733249).
- [12] C. B. Solnordal, C. Y. Wong, J. Boulanger, An experimental and numerical analysis of erosion caused by sand pneumatically conveyed through a standard pipe elbow, *Wear* 336-337 (2015) 43–57. URL: <http://dx.doi.org/10.1016/j.wear.2015.04.017>. doi:[10.1016/j.wear.2015.04.017](https://doi.org/10.1016/j.wear.2015.04.017).
- [13] A. T. Bourgoyne, Experimental Study of Erosion in Diverter Systems Due to Sand Production, *Soc. Pet. Eng.* (1989). doi:[doi:10.2118/18716-MS](https://doi.org/10.2118/18716-MS).
- [14] K. Jordan, Erosion in Multiphase Production of Oil & Gas, in: *Corrosion, NACE International*, 1998.
- [15] M. Parsi, D. N. V. Gl, H. Arabnejad, E/CRC, A. Al-sarkhi, K. Fahd, A New Correlation for Predicting Solid Particle Erosion Caused by Gas-Sand Flow in Elbows, in: *Offshore Technol. Conf.*, 2018.

- [16] D. R. Lester, L. A. Graham, J. Wu, High precision suspension erosion modeling, *Wear* 269 (2010) 449–457. doi:[10.1016/j.wear.2010.04.032](https://doi.org/10.1016/j.wear.2010.04.032).
- [17] Z. Johar, M. Jadid, P. Carigali, S. N. A. Shaffee, M. S. A. Zamberi, Experimental and CFD Erosion Modelling of Large Radius Pipe Elbows in, in: *Int. Pet. Technol. Conf.*, Kuala Lumpur, Malaysia, 2014, pp. 1–13.
- [18] A. Gnanavelu, N. Kapur, A. Neville, J. F. Flores, N. Ghorbani, A numerical investigation of a geometry independent integrated method to predict erosion rates in slurry erosion, *Wear* 271 (2011) 712–719. URL: <http://dx.doi.org/10.1016/j.wear.2010.12.040>. doi:[10.1016/j.wear.2010.12.040](https://doi.org/10.1016/j.wear.2010.12.040).
- [19] A. Mansouri, H. Arabnejad, S. A. Shirazi, B. S. Mclaury, A combined CFD / experimental methodology for erosion prediction, *Wear* 333 (2015) 1090–1097. URL: <http://dx.doi.org/10.1016/j.wear.2014.11.025>. doi:[10.1016/j.wear.2014.11.025](https://doi.org/10.1016/j.wear.2014.11.025).
- [20] C. A. R. Duarte, F. J. de Souza, R. V. Salvo, V. F. dos Santos, The role of inter-particle collisions on elbow erosion, *Int. J. Multiph. Flow* 89 (2017) 1–22. doi:[10.1016/j.ijmultiphaseflow.2016.10.001](https://doi.org/10.1016/j.ijmultiphaseflow.2016.10.001).
- [21] M. Zamani, S. Seddighi, H. R. Nazif, Erosion of natural gas elbows due to rotating particles in turbulent gas-solid flow, *J. Nat. Gas Sci. Eng.* 40 (2017) 91–113. URL: <http://dx.doi.org/10.1016/j.jngse.2017.01.034>. doi:[10.1016/j.jngse.2017.01.034](https://doi.org/10.1016/j.jngse.2017.01.034).
- [22] Y. Zhang, E. P. Reuterfors, B. S. McLaury, S. a. Shirazi, E. F. Rybicki, Comparison of computed and measured particle velocities and erosion in water and air flows, *Wear* 263 (2007) 330–338. doi:[10.1016/j.wear.2006.12.048](https://doi.org/10.1016/j.wear.2006.12.048).
- [23] D. Choudhury, Introduction to the Renormalization Group Method and Turbulence Modeling, Technical memorandum, Fluent Incorporated, 1973. URL: <https://books.google.ca/books?id=mKWEQwAACA AJ>.
- [24] S. A. Morsi, A. J. Alexander, An Investigation of Particle Trajectories in Two-Phase Flow Systems, *J. Fluid Mech.* 55 (1972) 193–208.
- [25] E. K. Vakkilainen, M. Garcia Perez, T. Happanen, A brief overview of the drag laws used in the Lagrangian tracking of ash trajectories for boiler fouling CFD models, in: *26th Int. Conf. Impact Fuel Qual. Power Prod.*, September, Prague, 2016.

- [26] S. C. R. Dennis, S. N. Singh, D. B. Ingham, The Steady Flow Due to Rotating Sphere at Low and Moderate Reynolds Numbers, *J. Fluid Mech.* 101 (1980) 257–279.
- [27] A. Li, G. Ahmadi, Dispersion and Deposition of Spherical Particles from Point Sources in a Turbulent Channel Flow, *Aerosol Sci. Technol.* 16 (1992) 209–226.
- [28] G. P. Saffman, The Lift on a Small Sphere in a Slow Shear, *J. Fluid Mech.* 22 (1965) 385–400.
- [29] B. Oesterlé, T. Bui Dinh, Experiments on the Lift of a Spinning Sphere in the Range of Intermediate Reynolds Numbers, *Exp. Fluids* 25 (1998) 16–22.
- [30] G. Grant, W. Tabakoff, Erosion Prediction in Turbomachinery Resulting from Environmental Solid Particles, *J. Aircr. - J Aircr.* 12 (1975) 471–478.
- [31] G. Haider, H. Arabnejad, S. A. Shirazi, B. S. Mclaury, A mechanistic model for stochastic rebound of solid particles with application to erosion predictions, *Wear* 376-377 (2017) 615–624. URL: <http://dx.doi.org/10.1016/j.wear.2017.02.015>. doi:10.1016/j.wear.2017.02.015.
- [32] M. Sommerfeld, N. Huber, Experimental analysis of modelling of particle-wall collisions, *Int. J. Multiph. Flow* 25 (1999) 1457–1489.
- [33] ANSYS, ANSYS 17.0 Theory Guide, Technical Report, 2017. URL: <https://www.sharcnet.ca/Software/Ansys/17.0/en-us/help/fluo{ }th/fluo{ }th.html>.
- [34] P. Patro, S. K. Dash, Prediction of acceleration length in turbulent gas – solid flows, *Adv. Powder Technol.* 25 (2014) 1643–1652. URL: <http://dx.doi.org/10.1016/j.apt.2014.05.019>. doi:10.1016/j.apt.2014.05.019.
- [35] M. Sommerfeld, S. Lain, Parameters Influencing Dilute - Phase Pneumatic Conveying Through Pipe Systems: A Computational Study by the Euler/Lagrange Approach, *Can. J. Chem. Eng.* 93 (2015) 1–17. doi:10.1002/cjce.22105.
- [36] N. Huber, M. Sommerfeld, Characterization of the cross-sectional particle concentration distribution in pneumatic conveying systems, *Powder Technol.* 79 (1994) 191–210.

- [37] C. A. R. Duarte, F. J. de Souza, V. F. dos Santos, Numerical investigation of mass loading effects on elbow erosion, *Powder Technol.* 283 (2015) 593–606. URL: <http://dx.doi.org/10.1016/j.powtec.2015.06.021>. doi:10.1016/j.powtec.2015.06.021.
- [38] G. C. Pereira, F. J. de Souza, D. A. de Moro Martins, Numerical prediction of the erosion due to particles in elbows, *Powder Technol.* 261 (2014) 105–117. URL: <http://dx.doi.org/10.1016/j.powtec.2014.04.033>. doi:10.1016/j.powtec.2014.04.033.
- [39] A. Uzi, Y. Ben Ami, A. Levy, Erosion prediction of industrial conveying pipelines, *Powder Technol.* 309 (2017) 49–60. URL: <http://dx.doi.org/10.1016/j.powtec.2016.12.087>. doi:10.1016/j.powtec.2016.12.087.
- [40] L. Xu, Q. Zhang, J. Zheng, Y. Zhao, Numerical prediction of erosion in elbow based on CFD-DEM simulation, *Powder Technol.* 302 (2016) 236–246. URL: <http://dx.doi.org/10.1016/j.powtec.2016.08.050>. doi:10.1016/j.powtec.2016.08.050.
- [41] ANSYS, ANSYS Fluent UDF Manual, Technical Report, 2013.
- [42] A. Mansouri, A combined CFD-experimental method for developing an erosion equation for both gas-sand and liquid-sand flows, Phd thesis, University of Tulsa, 2016.

# Investigation of erosion damage and the limitations of API RP 14E guideline in SAGD OTSG operations

A part of this chapter will be submitted as

*"Oluwaseun E. Adedeji, Anupam Kumar, Perdikcakis Basil, R. Sean Sanders, Investigation of erosion-related failure in SAGD OTSG boiler tubes and the limitations of API RP 14E"*

to the Journal of Engineering Failure Analysis.

## Abstract

Steam Assisted Gravity Drainage (SAGD) is an *in-situ* oil sands extraction method that requires the injection of high pressure steam underground to facilitate the recovery of oil. The required steam is generated in a Once-Through-Steam-Generator (OTSG) system that is usually fed with a low quality water. Industries have reported possible erosion damage in the OTSG boiler tubes because of the transport of dense inorganic particles formed in the upstream section of the tubes. However, the masking evidence of other damage mechanisms such as flow accelerated corrosion, as well as the low concentration and small sizes of the inorganic eroding particles have seemingly suggested that the contribution of erosion to failure of the OTSG is not significant. Also, industries use the API RP 14E guideline to set the threshold (limiting) velocity in the OTSG. However, the API RP 14E does not provide quantitative erosion rates to determine the true operating envelope for the OTSG system. In this study, Computational Fluid Dynamics is employed to study erosion damage in an OTSG tube. Analysis of the results revealed that the API RP 14E is not an effective decision-making tool for operating the OTSG, especially because it cannot capture the effects of particle size and fluid turbulence. An increase of 75% in erosion damage was predicted when particle size changes from 10  $\mu\text{m}$  to 30  $\mu\text{m}$  at any given flow rate. Also, a 10% increase in flow velocity, even below the API RP 14E suggested limit, predicted a decrease in the failure time for the boiler tubes by 40-50%.

## List of Symbols

$C$	API RP 14E correlation constants
$C_k$	Erosion model coefficient
$D$	Pipe diameter, $m$
$d_p$	Particle diameter, $m$
$d_{ref}$	Oka model reference particle diameter, $m$
$d_{p,ref}$	Parsi model reference particle diameter, $m$
$e_n$	Normal restitution coefficient
$e_t$	Tangential restitution coefficient
$ER$	Erosion rate
$F_s$	Particle shape factor
$H_v$	Vickers hardness, $GPa$
$k_1$	Target material property exponent
$k_3$	Particle diameter exponent
$K$	Oka model coefficient
$n$	Oka model velocity exponent
$n_1$	Cutting damage exponent
$n_2$	Deformation damage exponent
$Pnr$	Penetration ratio
$Re$	Reynolds number
$V_e$	API RP 14E erosion limit velocity, $m/s$
$V_f$	Superficial fluid velocity, $m/s$
$V_p$	Particle impact velocity, $m/s$
$V_{ref}$	Oka model reference particle impact velocity, $m/s$
$VHN$	Vickers hardness number
$W_p$	Particle mass flow rate, $kg/s$
$x$	Steam mass fraction
$v_g$	Saturated steam specific volume, $m^3/kg$
$v_l$	Saturated water specific volume, $m^3/kg$
$\rho_m$	API RP 14E mixture density, $kg/m^3$
$\rho_t$	Target material density, $kg/m^3$
$\alpha$	Particle impact angle
$\rho_p$	Particle density, $kg/m^3$
$\rho_f$	Fluid density, $kg/m^3$

## 7.1 Introduction

Once-Through-Steam-Generators (OTSGs) are often used to generate large amounts of steam for bitumen production in Steam-Assisted Gravity Drainage (SAGD) oil production operations [1, 2]. It is a complex system that involves heat, mass, mechanical energy, and species transfer in a high temperature and pressure environment. These phenomena make the OTSG a multiphase flow system affected by the formation of deposits, the presence of particles, and the mechanical properties of the materials for its construction. A schematic of a typical OTSG system used in SAGD oil recovery operations is shown in Fig. 7.1. A mixture of boiler feed water (BFW) and recycle water is pressurized to about 12 MPa and sent to the economizer. The economizer is heated by convection and designed to ensure that water entering the radiant zone is at least boiling at the supply pressure. The saturated high pressure water is evaporated in the radiant section (combustion zone). The outlet stream from the radiant section which is about 80% steam is sent to a high pressure (HP) separator [2].

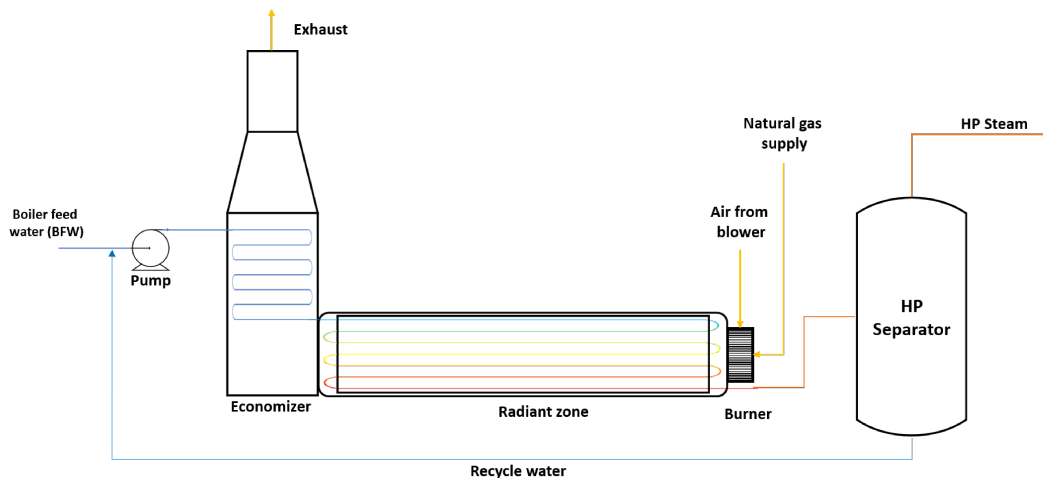
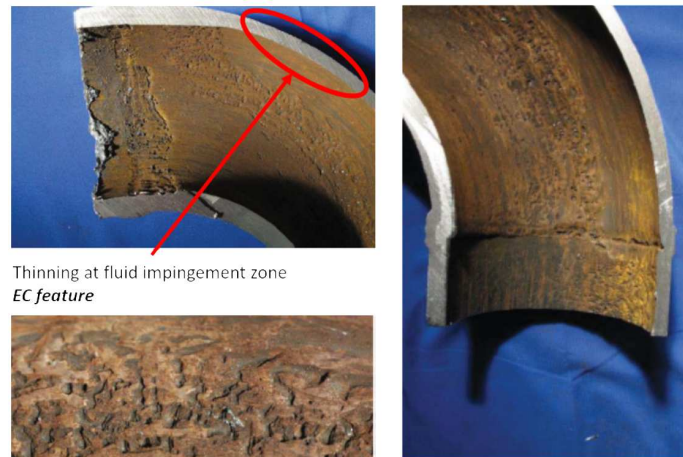


Figure 7.1: Schematic of an OTSG system for SAGD bitumen recovery (based on Gwak and Bae [2])

Generally, the operating conditions of OTSGs allow several forms of wear damage to occur in the system. In SAGD operations, the BFW is of low quality and contains many impurities which causes fouling in the boiler tubes as well as the presence of other soluble organic and inorganic substances in the process stream. For example, when the BFW enters an elevated

temperature region, scales and precipitates start to form, mostly in the economizer section. This formation of scales can lead to failures such as thermal fatigue in the economizer [3]. Also, dense inorganic particles such as Aegirine ( $NaFe(SiO_3)_2$ ) with particle size range between 10-120  $\mu\text{m}$  are also transported into the radiant section [4]. The flow velocity in the radiant section is about 20-25 m/s, thus, the entrained particles possess sufficient kinetic energy to cause erosion damage in the boiler tubes [4]. It is apparent that in the OTSG system, there is a complex interaction of various mechanisms such as thermal stress (from overheating due to fouling), erosion, erosion-corrosion (EC), and flow-accelerated corrosion (FAC) contributing to the total wear damage in the OTSG [4, 5].

Erosion is the mechanical removal of materials from equipment surfaces and is driven by solid particle impacts. Flow accelerated corrosion (FAC) is a process where the protective oxide layer of the metal is continuously dissolved in the flowing fluid stream [5]. In other words, FAC is an enhanced corrosion driven by electrochemical dissolution and mass transfer of metal ions. Erosion corrosion (EC) is a coupled interaction of mechanical removal, dissolution and mass transfer of metal ions and oxide layer [6–8]. In the industry, the challenge that integrity engineers face is determining which damage mechanisms are mainly responsible for failure whenever it occurs. So far, evidence of pure erosion in the OTSG is not available. However, there is evidence of flow-accelerated corrosion (FAC) and erosion-corrosion (EC) damage that have been reported in literature. Images of some OTSG tube sections from the work of Godfrey et al. [4] are shown in Fig. 7.2a. Images of recently obtained OTSG tube samples in our laboratory are also shown in Fig. 7.2b. It can be seen from the figures that (i) many damage mechanisms could be happening simultaneously, (ii) different damage mechanism(s) could dominate under different operating conditions, and (iii) the damage mechanisms are likely to interact and influence each other. For example, the flow velocity is a parameter that affects erosion, EC and FAC. At high flow velocity, transported particles have higher kinetic energy which will lead to higher wear rates upon impact on the tube wall. Similarly, if FAC is predominant, high velocity means a higher concentration gradient for dissolved iron species between the bulk flow and the material surface, leading to higher FAC rate [5]. Note that factors like the material composition (e.g. Chromium content) also determines material hardness and the dissolution rate of iron species, thus affecting both erosion and FAC rates [5]. Also, going from the inlet stream to the outlet of the OTSG boiler tubes, a transition occurs from liquid flow to a multiphase flow that includes a mixture of gas, liquid droplets/film, and precipitated/entrained particles.



Thinning at fluid impingement zone  
*EC feature*



Irregular rounded depressions  
*FAC feature*

Lack of, or the presence of depleted black (protective) layer that dissolves quickly in the presence of acid  
*EC Feature*

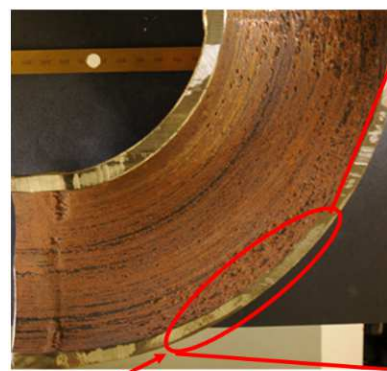
(a)



Longitudinal banding in bends and straight section - *EC feature*



Flash rust from atmospheric corrosion  
*EC previously occurred to expose metal surface through removal of protective layer*



Thinning at fluid impingement zone  
*EC feature*



Irregular elongated depressions  
*Combined FAC-EC feature*

(b) Recent Images

Figure 7.2: Wear damage mechanisms observed in tube samples from OTSGs used in SAGD oil sands extraction (a) From Godfrey et al. [4] (b) Recent Images

Wear mechanisms under these different flow regimes are likely to differ considerably i.e. erosion-corrosion may dominate in a certain region of the tube while flow accelerated corrosion may be dominant in another region. The presence of a liquid film, if any, may also affect the damage rate in that region [9, 10]. It is apparent that the complex nature of wear damage in the OTSG makes it very unlikely, almost impossible, to have evidence of pure erosion occurring, since it would have been masked by the presence of other dominating wear damage mechanisms. Because of this lack of visible evidence, the contributions of erosion to damage in OTSG tubes have often been downplayed. There are other reasonable assumptions that make industries consider erosion to be a less significant contributor to damage in OTSGs:

1. Fouling materials which are entrained by the fluid material are not strong enough to cause significant penetration on tube material. This may be true for the tube materials; however, they might be strong enough to compromise the integrity of the protective layer, thus, making erosion-corrosion more severe.
2. The dense inorganic solids such as Aegirine ( $3550 \text{ kg/m}^3$ ) present in the OTSG system are in very low concentrations (3-7 PPM) and are mostly in small particle sizes (10-30  $\mu\text{m}$ ), hence, the erosion damage is assumed to be negligible. However, the higher density, the needle-like shape, and the higher hardness of Aegerine relative to steel, make it a highly abrasive particle [4].
3. The assumption in (2) above is also supported by many industries because they use the API RP 14E guideline [11] to predict "erosion limit" velocity. As will be shown in this study, the API RP 14E correlation does not include the effects of particle size and shape, and cannot capture the effect of solids concentration at very low concentrations such as those found in OTSGs.

The above list is comprised mostly of assumptions and so far, there is no work done to determine whether erosion damage is significant or not in the OTSG system, or if the API RP 14E guideline is a viable tool for defining the operating envelope to limit erosion damage.

In this study, a numerical investigation using Computational Fluid Dynamics (CFD) simulations is carried out to quantify the contribution of pure solid particle erosion (SPE) to wear damage in the U-bend section of a boiler tube in a SAGD OTSG system. Furthermore, CFD analysis will be used to show that the API RP 14E guideline is not suitable for making

operational decisions for the OTSG e.g. increasing steam production to increase productivity based on its suggested erosion limit velocity.

It is important to note that this work does not attempt to identify erosion as the dominant mechanism but rather, the goal is to illustrate the wear rates that could occur for pure erosion only. Also, CFD has been adopted as a tool to conduct this investigation because of its capability to resolve local fluid-particle-wall interactions, thus making it a very useful tool in analyzing erosion wear. It has been extensively used and validated for solid particle erosion prediction for pneumatic and slurry flows [12–19]. Also, to identify the prevailing wear mechanism in a complex system such as the OTSG, one must design an appropriate method to isolate and study the contribution of each possible wear mechanism as well as determine operating region(s) where they persist (see Appendix D.2). This work is one of the steps that needs to be taken to accomplish this task. It is recognized that more complex multiphase flow regimes e.g. the presence of liquid film may exist in the OTSG system, however, this study will focus on two-phase gas-solid flow. Finally, the use of CFD to solve such complex multiphase systems for wear prediction is still developing, and some targeted experimental investigations which currently are not available will be required to validate the simulations when both gas and liquid phases are present.

## 7.2 Background

### 7.2.1 Review of API RP 14E industrial guideline

The American Petroleum Institute proposed a recommended practice guideline to estimate erosion limit velocity known as the API RP 14E [11]. The guideline is an empirical correlation that relates the mixture fluid density and the limit velocity through

$$V_e = \frac{C}{\sqrt{\rho_m}} \quad (7.1)$$

where  $V_e$  is the erosion limit velocity,  $\rho_m$  is the mixture density and  $C$  is an empirical constant that depends on the type of system as well as the conditions inside the system. The recommended value of  $C$  is 100 for continuous service and 125 for intermittent service [20]. A much lower value than 100 is suggested for systems that contain solid particles, however,

no specific value was set. The API RP 14E was originally proposed for the design of piping systems carrying single phase gas or multiphase gas-liquid mixtures in offshore oil and gas platforms [21–24]. This initially proposed application questions the use of the guideline for predicting erosion limit velocity. In fact, the origin of the equation is unclear and there is no experimental evidence to support the logic for its application [24]. However, the simplicity of the API RP 14E has allowed it to find extensive use in industry, and particularly, for the operation of OTSGs used in SAGD operations. The conservative nature of the API RP 14E has been said to sometimes limit production capacity and overestimate pipe sizes during design [22, 24]. This is because the operational envelope defined by the API RP 14E for industrial systems is arbitrary and superficial. Therefore, industries that want to increase production rate are unable to assess the implications of such a decision using the API RP 14E guideline.

Some other concerns about the applicability of the API RP 14E come from the fact that the erosion limit velocity is inversely proportional to the mixture density. In other words, API RP 14E suggests that for otherwise identical conditions (e.g. pipe material, erodent properties), erosion limit velocity should increase with decreasing fluid density which is in opposition to the hundreds of peer-reviewed publications that reported a higher erosion rate in gas phase than in a liquid phase. Several authors have worked to generalize or improve the application of API RP 14E correlation through extensive theoretical and experimental research [20, 23, 25–27]. However, more complexities were introduced which does not justify the use of the guideline as a simple correlation. Many industries therefore, still find semi-mechanistic solid particle erosion (SPE) wear models such as the Oka et al. model [28–30], the DNV RP O501 [31], or the E/CRC (Tulsa) model [19, 32] to be more useful. These models account for important wear-influencing factors such as material hardness, particle size and shape unlike the API RP 14E where the constant  $C$  is the only tuning parameter to account for these effects. The implementation of SPE models in CFD simulations further strengthens their capacity by accounting for particle-wall interactions through wall rebound and wall roughness models as well as the effects of fluid turbulence [33–36]. For a complex system like the OTSG, it is apparent that a more detailed analysis of the boiler tube damage is needed than what the API RP 14E can provide. The CFD simulations in this work provide such detailed analysis, specifically for solid particle erosion due to steam-solid flow in the U-bends of the boiler tubes in radiant section of the OTSG.

## 7. 2.2 OTSG case study

This section provides the details about the operating conditions and dimensions of the OTSG boiler tube that will be analyzed. As mentioned earlier, The OTSGs used in SAGD bitumen recovery are usually fed with poor quality boiler feed water (BFW) compared to their counterpart in the nuclear/power industry [2]. This has made it possible for dense particles like Aegirine ( $NaFe(SiO_3)_2$ ) to form and be transported in the boiler tubes, which then causes erosion. The particle sizes mostly range from  $10 \mu m$  to about  $30 \mu m$ , while in extreme cases, large particles up to  $60-120 \mu m$  can be recovered. The solids concentration of particles in the system is about  $3 mg/L$  or  $PPM$  which is equivalent to a solids volume fraction of  $8.45 \times 10^{-7}$  for Aegerine. The carrier fluid is saturated steam with quality of  $80\%$  at a pressure of  $11 MPa$  i.e at a temperature of about  $318^\circ C$ . Because of the steam quality, it is possible to want to consider other multiphase phenomenon such as liquid droplet impingement (LDI) or the present of an annular liquid film. However, the flow velocity of averagely  $20 m/s$  at which the OTSG is operated does not support phenomenon like the LDI [6] while it is very unlikely for the tube wall at the operating temperature to have a liquid film thick enough to affect particle impingement. Also, the type of analysis considered in this study does not require the complexity of this kind of coupled multiphase interactions. Therefore, the carrier fluid will be taken as a single gas (steam) phase with its properties calculated based on the steam tables. For example, the steam density is calculated using

$$\rho = \frac{1}{[xv_g + (1-x)v_l]} \quad (7.2)$$

where  $x$  is the steam quality as mass fraction, and  $v_g$  &  $v_l$  are the specific volume ( $m^3/kg$ ) of saturated steam and saturated water at the system condition. A summary of the specifications and operating conditions considered for the CFD simulations are provided in Table 7.1. From the Table, it will be seen that a velocity of  $40 m/s$ , which is very high and unrealistic for the industrial system will also be simulated. The actual OTSG system operates between  $20-25 m/s$  hence the velocities selected for simulations are for parametric study, while still covering the system's operating envelope. The length of the straight pipe section in the industrial OTSG system is  $\approx 20 m$ . The dimensions of the geometry and the direction of flow used for the CFD simulations are shown in Fig. 7.3.

Table 7.1: OTSG system specifications and conditions

Pipe diameter ( $m$ )	0.0737
Particle diameters ( $\mu m$ )	10,30,60,120
Bend radius ( $m$ )	0.2286
Pipe length ( $m$ )	19.8
Particle density ( $kg/m^3$ )	3550
Steam quality	0.8
Steam density, saturated at 11 MPa ( $kg/m^3$ )	77.26
Steam viscosity ( $Pa\cdot s$ )	2.08E-05
Steam velocities ( $m/s$ )	20, 30, 40
Solids volume fraction	8.45E-07

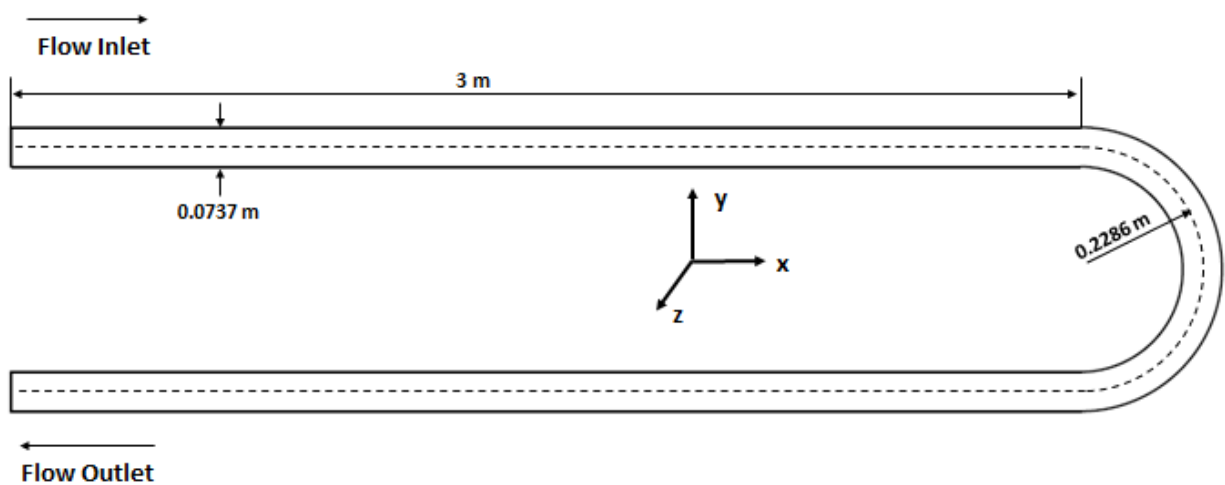


Figure 7.3: Single U-bend system geometry for CFD simulation

The pipe length shown in Figure 7.3 is such that it is long enough to ensure a fully-developed flow before the U-bend entrance, hence, there is no need to simulate the entire 20 m length. Gravity acts in the negative  $y$ -direction, hence the flow is horizontal in the straight pipe section and vertical in the U-bend section. Two different target materials used for the construction of the OTSG tubes are considered in the simulations. They are Carbon Steel (A106C) and Alloy Steel (P22), the P22 being the harder of the two based on Vickers hardness scale (ASTM E92-17). Also, the constant  $C$  in the API RP 14E equation (Equation 7.1) is such that  $C^2 = 38950 \text{ kg}/m\cdot s^2$  for A106C and  $C^2 = 49430 \text{ kg}/m\cdot s^2$  for P22. It will be seen in Table 7.1 that flow conditions below and above the API RP 14E limit velocities for each target material (see Table 7.2) will be used to study the extent of damage due to wear.

Table 7.2: Target materials properties with API RP 14E constants and velocity limits

Material	$H_v$ (GPa)	$\rho_t$ (kg/m <sup>3</sup> )	$C^2$ (kg/ms <sup>2</sup> )	$V_e$ (m/s)
A106C	1.285	7850	38,950	22.5
P22	1.628	7835	49,430	25.3

## 7.3 CFD Model Development

### 7.3.1 Model equations

The CFD simulations were implemented in the commercial CFD code ANSYS Fluent®. A 3D steady state analysis was carried using the Eulerian-Lagrangian modelling approach. The Eulerian treatment was applied to the carrier fluid phase to calculate the flow field by solving the Reynolds-Averaged Navier-Stokes (RANS) equation [37, 38] given by

$$\frac{\partial(\rho u_i)}{\partial x_i} = 0 \quad (7.3)$$

$$\frac{\partial(\rho u_i u_j)}{\partial x_i} = -\frac{\partial p}{\partial x_i} + \frac{\partial}{\partial x_j} \left[ (\mu + \mu_t) \left( \frac{\partial u_i}{\partial x_j} + \frac{\partial u_j}{\partial x_i} \right) \right] + \rho g_i \quad (7.4)$$

The re-normalized group (RNG)  $k - \epsilon$  turbulence model was used to calculate the turbulence kinetic energy and dissipation rate for the carrier fluid [39]. The Lagrangian approach was applied to the discrete/dispersed phase to solve for the particle motion and calculate the trajectory of the particles in the fluid domain. This was modelled via a force balance based on Newton's second law which is given by

$$m_p \frac{du_{pi}}{dt} = m_p \frac{3\rho C_D}{4\rho_p d_p} |u_i - u_{pi}| (u_i - u_{pi}) + F_{si} + F_{ri} + \left(1 - \frac{\rho}{\rho_p}\right) m_p g_i \quad (7.5)$$

$$\frac{dx_{pi}}{dt} = u_{pi} \quad (7.6)$$

$$(0.1 m_p d_p^2) \frac{d\omega_{pi}}{dt} = \frac{\rho d_p^5 C_\omega}{60} |\vec{\Omega}| |\vec{\Omega}| = T_i \quad (7.7)$$

where  $C_D$ , the drag coefficient is from the correlation of Morsi and Alexander [40] which is

given by

$$C_D = a_1 + \frac{a_2}{Re_p} + \frac{a_3}{Re_p^2} \quad (7.8)$$

The value of constants  $a_1, a_2$ , and  $a_3$  depends on the particle Reynolds number and are given in Table 6.2

Table 7.3: Morsi and Alexander drag law constants

Range	$a_1$	$a_2$	$a_3$
$Re_p < 0.1$	0	24	0
$0.1 < Re_p < 1$	3.690	22.73	0.0903
$1 < Re_p < 10$	1.222	29.1667	-3.8889
$10 < Re_p < 100$	0.6167	46.50	-116.67
$100 < Re_p < 1000$	0.3644	98.33	-2778

The rotational drag coefficient  $C_\omega$  is Defined according to the correlation by Dennis et al. [41] and is given by

$$C_\omega = \frac{6.45}{\sqrt{Re_\omega}} + \frac{32.1}{Re_\omega} \quad (7.9)$$

where,

$$Re_\omega = \frac{\rho |\vec{\Omega}| d_p^2}{4\mu} \quad (7.10)$$

$$\vec{\Omega} = 0.5 \vec{\nabla} \times \mathbf{u}_i - \omega_{pi} \quad (7.11)$$

The term  $F_{si}$  is the Saffman's lift force [42, 43] which is defined by

$$\vec{F}_{si} = \frac{2Kv^{1/2}\rho d_{ij}}{\rho_p d_p (d_{lk} d_{kl})^{1/4}} (\vec{u} - \vec{u}_p) \quad (7.12)$$

where  $K = 2.594$  and  $d_{ij}$  is the deformation tensor. The rotational or Magnus lift force is based on the formulation of Oesterlé and Bui Dinh [44] and is defined by

$$F_{ri} = \frac{1}{2} A_p C_{RL} \rho \frac{|\vec{V}|}{|\vec{\Omega}|} (\vec{V} \times \vec{\Omega}) \quad (7.13)$$

where,

- $A_p$  is the projected particle surface area  
 $\vec{V}$  is the relative fluid-particle velocity  
 $\vec{\Omega}$  is the relative fluid-particle angular velocity

The rotational lift coefficient,  $C_{RL}$  is defined by

$$C_{RL} = 0.45 + \left( \frac{Re_\omega}{Re_p} - 0.45 \right) \exp(-0.05684 Re_\omega^{0.4} Re_p^{0.3}) \quad (7.14)$$

The Discrete Random Walk (DRW) method was used to model the turbulent dispersion of the particles [45]. The model by Grant and Tabakoff [35] was used to calculate particle-wall restitution coefficient. The normal and tangential components of the model are given by

$$e_n = 0.993 - 1.76\alpha + 1.56\alpha^2 - 0.49\alpha^3 \quad (7.15a)$$

$$e_t = 0.998 - 1.55\alpha + 2.11\alpha^2 - 0.67\alpha^3 \quad (7.15b)$$

The default value of 0.2 was used for the particle-wall friction coefficient. The rough wall model by Sommerfeld and Huber [34] available in ANSYS Fluent<sup>®</sup> was implemented to model wall roughness. The wall roughness parameter  $\Delta\gamma$  is defined based on the mean height of the roughness structure  $R_a$ , the standard deviation of the roughness structure  $R_q$ , and the characteristic length between roughness structure  $RS_m$  is , and is given by

$$\Delta\gamma = \begin{cases} \tan^{-1} \frac{2R_q}{RS_m}, & \text{if } d_p < \frac{RS_m}{\sin(\tan^{-1} \frac{2R_q}{RS_m})} \\ \tan^{-1} \frac{2R_a}{RS_m}, & \text{otherwise} \end{cases} \quad (7.16)$$

Similar wall roughness parameters ( $R_a = 8\mu m$ ,  $R_q = 2\mu m$ ,  $RS_m = 8\mu m$ ) used in the work of Adedeji et al. [13] was applied to all particle sizes except for the 10  $\mu m$  particles in which a smooth wall was applied. The higher ratio of particle diameter to the mean roughness height in the case of the 10  $\mu m$  particle gives erroneous and nonphysical results, hence, the choice of the smooth wall.

### 7.3.2 Erosion model

The erosion model selected for this study is the Oka et al. erosion model [28–30]. The Oka model has been used extensively in industry and academia and has shown good performance

for wear prediction in many applications. The general form of the Oka erosion model is given by

$$ER = C_k V_p^n f(\alpha) \quad (7.17)$$

where the empirical coefficient  $C_k$  is given by

$$C_k = (1 \times 10^{-9} \rho_t) K (H_v)^{k_1} (V_{ref}^{-n}) \left( \frac{d_p}{d_{ref}} \right)^{k_3} \quad (7.18)$$

where,  $\rho_t$  is the density of the target material,  $d_p$  is the erodent particle diameter,  $d_{ref}$  is the reference particle diameter with a value of 326  $\mu\text{m}$ ,  $V_{ref}$  is the reference velocity with a value of 104 m/s, and  $H_v$  is the Vickers hardness of the target material in GPa. The impact angle function  $f(\alpha)$  is also defined by

$$f(\alpha) = (\sin \alpha)^{n_1} (1 + H_v (1 - \sin \alpha))^{n_2} \quad (7.19)$$

The coefficient  $K$  and exponents  $k_1$  and  $k_3$  are constants which strongly depend on particle properties and target material hardness, and may vary for different erodent-target materials combinations. The exponents  $n$ ,  $n_1$ , and  $n_2$  all depend on the particle properties and the target material hardness, and are given by.

$$n = 2.3(H_v)^{0.038} \quad (7.20a)$$

$$n_1 = 0.71(H_v)^{0.14} \quad (7.20b)$$

$$n_2 = 2.4(H_v)^{-0.94} \quad (7.20c)$$

The exponent  $n$  is the particle impact velocity exponent which is an indication of the energy of the particles that is transferred to cause the wear damage. The exponents  $n_1$  and  $n_2$  also are an indication of the cutting and deformation damage by the eroding particles.

### 7. 3.3 CFD code validation case

It is important to validate the erosion model and CFD code with reliable experimental data [37] before proceeding with a numerical investigation. Without validation, CFD results

may be biased on a number of independent parameters used in the physical erosion models. Because the OTSG system is modelled as a gas-solid system, the validation case selected is also a gas-solid system published in the work of Solnordal et al. [12]. In their work, they provided the experimental data used to generate a 2D wear map for a standard 90° vertical-to-horizontal elbow system. The gas phase is air at a mass flow rate of 0.78 kg/s while the particle phase is sand ( $\rho_p = 2650 \text{ kg/m}^3$ ,  $d_p = 184 \mu\text{m}$ ) at a mass flow rate of 0.03 kg/s. The test elbow pipe diameter is 102.5 mm, which makes the flow velocity entering the elbow to be  $\approx 80 \text{ m/s}$ . The experimental and CFD predicted wear map are shown in Fig. 7.4.

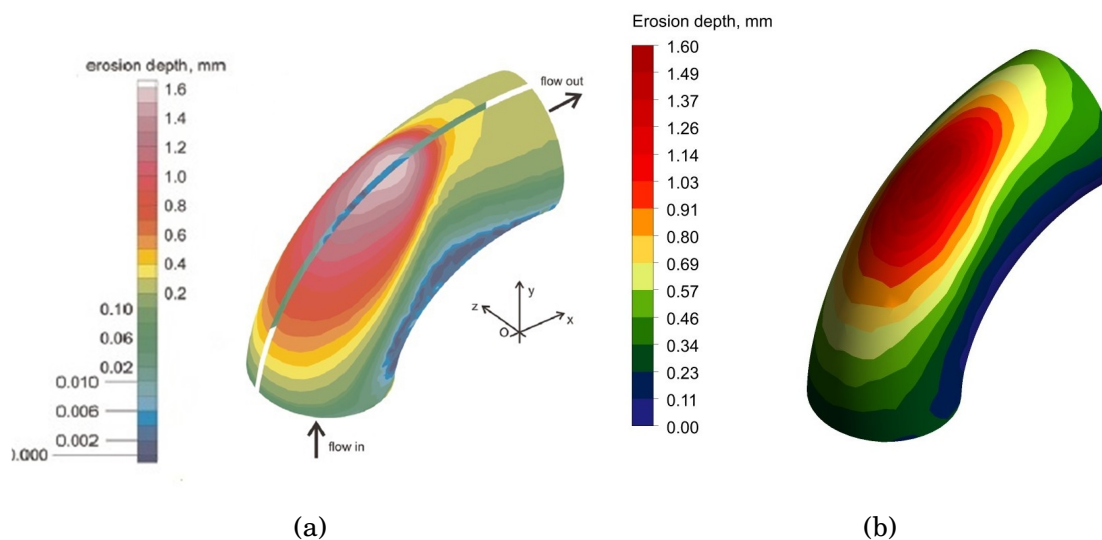


Figure 7.4: Comparison between (a) experimental wear map [12] and (b) CFD predictions for the particle-impact related wear of an elbow in a gas-solid flow

The Solnordal et al. [12] wear map in Fig. 7.4a and the CFD simulation results in Fig. 7.4b show good agreement. A maximum erosion depth of about 1.6 mm observed experimentally was also predicted using CFD simulations. The trajectory of the particles as they enter and leave the elbow is also shown in Fig 7.5. It can be seen from the predicted particle tracks that particles at the core of the flow through the elbow have the highest velocities, which means that they possess the highest impact energy. This also means that the central region of the elbow will experience the greatest amount of wear, which is depicted in the contour plot in Fig. 7.4. More details about the experimental system and other numerical simulations of the system can be found in the literature [12, 13, 37].

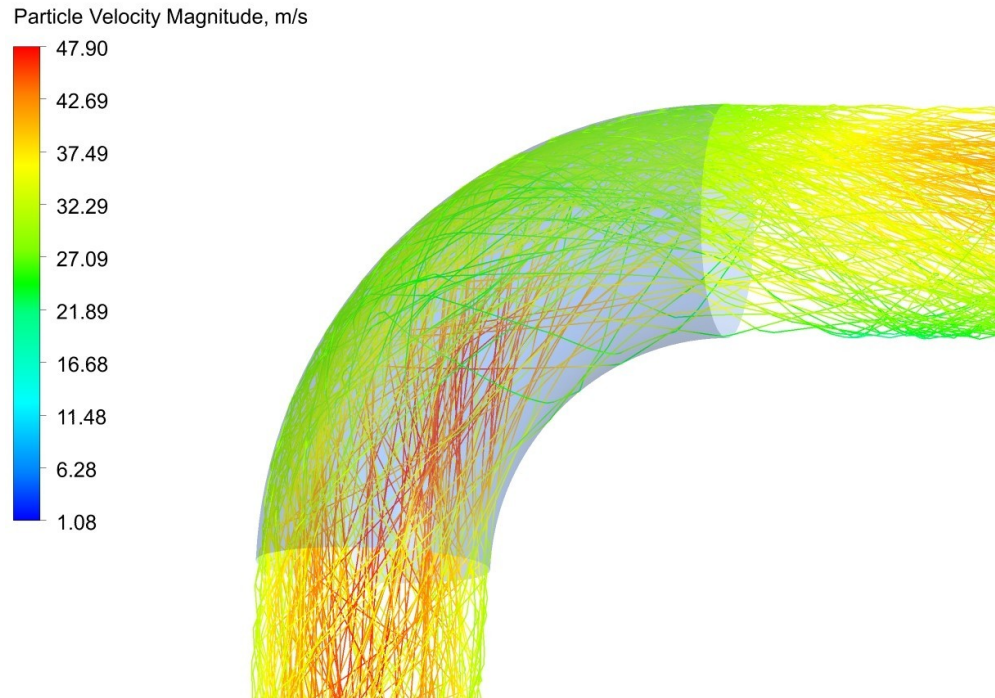


Figure 7.5: Trajectory of particles through the gas-solid elbow

### 7.3.4 OTSG model set-up and solution

The 3D CAD model for OTSG U-tube system as shown in Fig. 7.3 was created using SolidWorks<sup>®</sup>. An unstructured grid with hexahedral cells was used to discretize the fluid flow domain using ANSYS Meshing<sup>®</sup>. The mesh generated for the geometry model is shown in Fig. 7.6. Eight prism layer cells were applied to the wall so the wall boundary layer is captured adequately. About 1.15 million cells were generated for the system.

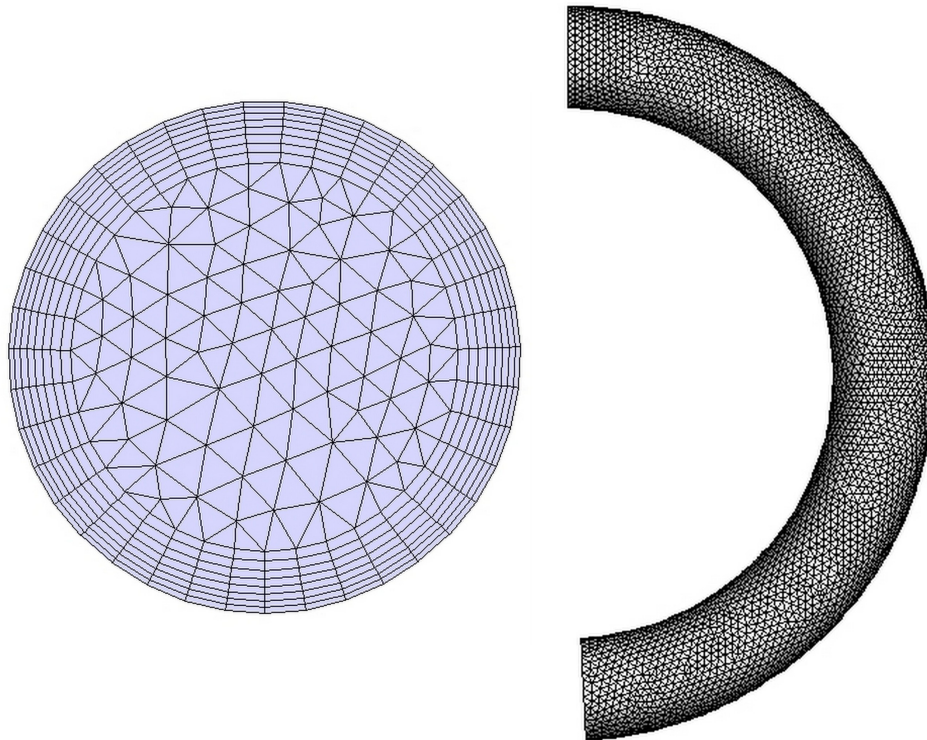


Figure 7.6: Unstructured grid for the OTSG U-bend: *left* (inlet surface), *right* (U-bend wall)

For CFD modelling of the fluid-particle multiphase system, a steady state solution was first obtained for the fluid phase, and the particle phase was then solved as a post-processing step. A velocity inlet, pressure outlet, and no-slip wall were set as boundary conditions for the model. The fluid phase solution converged with all residuals being less than  $10^{-8}$ . Also, because of the low solids volume fraction of  $8.45 \times 10^{-7}$ , one-way coupling was used to account for the fluid-particle interaction i.e. only the effect of the fluid turbulence on the particles is considered. For the particle phase, about 300,000 particles were tracked to ensure statistical relevance.

Erosion calculations were made after the particle tracking step. The Lagrangian model provides information such as the particle impact velocity and impact angle which are inputs for erosion wear calculation. The Oka et al. [28–30] erosion model presented earlier in Section 7. 3.2 was used for the erosion calculation. The model is already integrated into ANSYS Fluent<sup>®</sup>, however, appropriate values for parameters such as material hardness must be supplied into the model in order to obtain accurate predictions.

## 7.4 Results and Discussion

### 7.4.1 Effect of target material hardness

Both particle and target material hardness are important in determining the severity of erosion experienced in a system [30]. This section compares the erosion wear rate for A106C and P22. The Vickers hardness ( $H_v$ ) for A106C and P22 in  $GP\alpha$  are 1.285 and 1.628 respectively as shown in Table 7.2. They were each used as inputs for the Oka et al. erosion model. The relative erosion rate between A106 and P22 is shown in Fig 7.7. The amount in percentage by which erosion wear in A106C is greater than that in P22 is shown in Fig. 7.7a for all particle sizes and flow velocity considered.

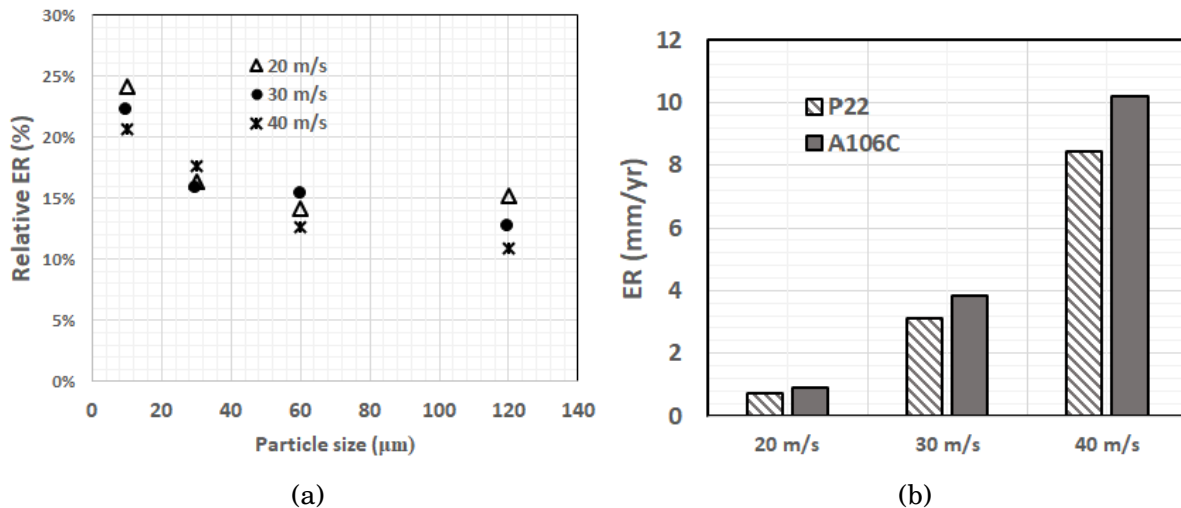


Figure 7.7: Erosion rate for A106C vs P22 for (a) all simulation conditions (b) 10 μm particles

The case of 10 μm particles which is assumed to be the dominant particle size in the OTSG system is also shown in Fig. 7.7b. All the predictions in the figures are the maximum wear rate (hot spots) obtained for the OTSG boiler tubes. The relative erosion rate in Fig 7.7a is calculated using

$$Relative\ ER(\%) = \left( \frac{ER_{A106C} - ER_{P22}}{ER_{P22}} \right) \times 100\% \quad (7.21)$$

It can be seen from Fig 7.7a that A106C experiences between 10-25% more wear than P22 at similar operating conditions. Generally, the difference in the erosion rate between the two

target materials is highest for the 10  $\mu\text{m}$  particles compared to the other larger particle sizes. This trend is similar for all the velocity conditions simulated. This behaviour observed is expected since the hardness of A106C is 20% less than that of P22. Another way to look at the difference between the target materials is to compare their predicted failure times based on the pipe specifications which is a 3" schedule XXS pipe (ASME B36.10/19) with thickness of 15.6 mm. The failure time in months is calculated using

$$\text{Failure time (months)} = \left( \frac{\text{Pipe Thickness (mm)}}{\text{ER (mm/year)}} \right) \times \frac{12 \text{ months}}{\text{year}} \quad (7.22)$$

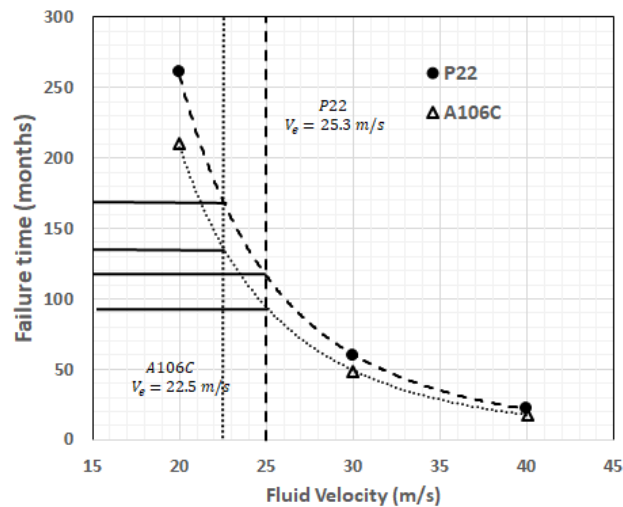


Figure 7.8: CFD Predicted failure time for A106C and P22 for 10  $\mu\text{m}$  particles

The predictions obtained for 10  $\mu\text{m}$  particles are presented in Fig. 7.8. At a typical OTSG operating velocity i.e. 25 m/s, there is about 25% difference in failure times for both materials, with P22 lasting longer. As expected, the failure time for both materials reduces with increasing fluid velocity i.e. failure occurs sooner at higher velocities. There is about 300-500 % decrease in the failure time as the fluid velocity is increased from 20 m/s to 30 m/s for both materials. Assuming that the predictions exactly represents the OTSG response to solid particle erosion, an increase of 2 m/s added to the operating velocity can reduce the failure time by approximately 1 year (12 months). It is also observed that at a higher velocity, the difference in failure time between the target materials becomes smaller. This is because, the erosion rate is predominantly driven by velocity at this condition and the effect

of other variables have been recessed. It is important to note that these failure times are only predictions meant for comparison basis and will need to be validated before they can represent what could happen under actual plant conditions. For example, operating OTSG made from A106C based on this analysis will be expected to fail after 20 years. This is not true when compared to what the actual plant system experiences. This prediction could mean that (1) both erosion-corrosion and/or FAC corrosion are contributing significantly to the wear in the boiler tubes which will speed up the damage process especially if the synergistic effect is active; (2) the mean size of particles might be greater than reported or fluctuates at different times; and (3) the average concentration of the solid particles is higher than reported. If corrosion is considered alongside erosion, the failure time between the material types will diverge to an even greater extent. It has been reported that the composition, particularly the Chromium content of the target material, will affect the rate at which it will be susceptible to corrosion, particularly, FAC [5]. For P22, the Chromium content is about 1.9-2.6% while that of A106C is less than 0.4%, meaning that if there is erosion-corrosion, the failure time will differ largely than for the erosion-only case presented here, with the A106C failing first.

## 7. 4.2 Effect of particle size

The main advantages of erosion prediction using CFD over the use of an industrial guideline like the API RP 14E are the ability to (1) output erosion rate in mm/year; (2) obtain a local wear distribution; and (3) study the effects of particle trajectory which is reflective of the particle size and density, fluid density and viscosity, and the fluid turbulence. This section will present and discuss results obtained for different particle sizes between 10-120  $\mu\text{m}$  simulated at a velocity of 20 m/s for the U-bend geometry. The predicted erosion rate contours for A106C are shown in Fig. 7.9. It is apparent from the contour plots that the hot spot i.e the maximum erosion rate is located on the U-bend of the tube. It can also be seen (Fig. 7.9) that the maximum erosion rate increases with increasing particle diameter.

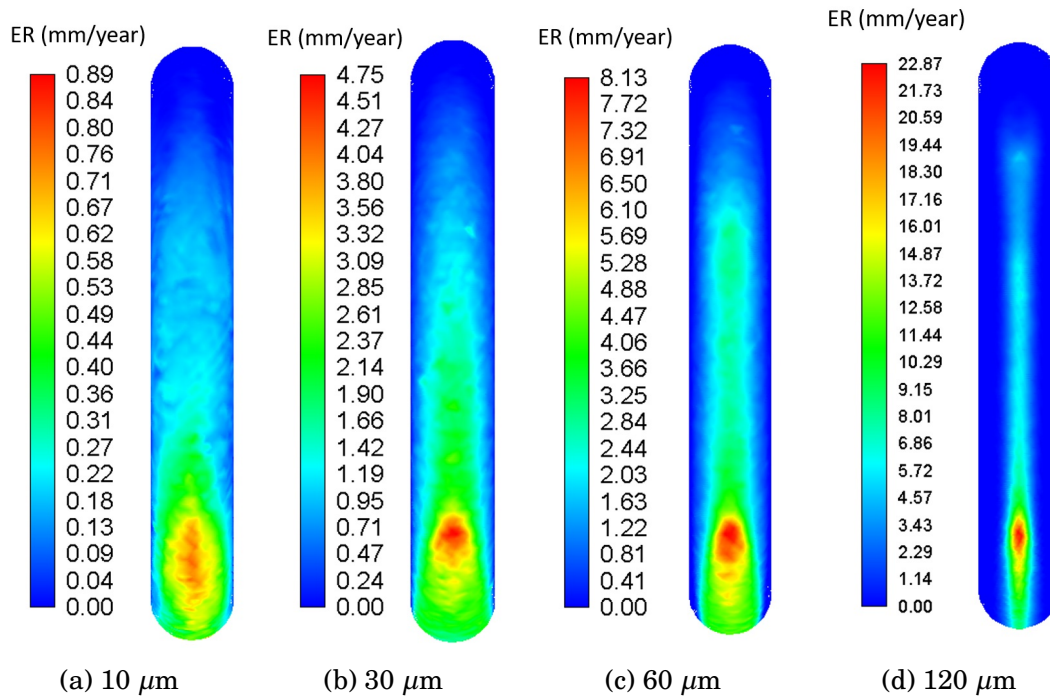


Figure 7.9: Predicted erosion rate for different particle diameters at  $V=20$  m/s for A106C

The heatmaps show that a larger surface area on the outlet side of the U-bend will be experiencing wear for the small particles with the erosion hot spot also covering a wider surface area. For larger particle diameters, the hotspot becomes narrower on the outlet side of the tube and begins to appear on the inlet side of the tube as well. In all the cases, a further increase in particle diameter (say above  $120 \mu\text{m}$ ) and a decrease in fluid density (e.g. low pressure steam) will shift the erosion hot spot from outlet side to the inlet side of the tube. To demonstrate this, a parametric study was carried out in which dry steam at atmospheric pressure (density of  $0.556 \text{ kg/m}^3$ ) was simulated at a velocity of 20 m/s and particle diameter of  $60 \mu\text{m}$ . Fig. 7.10 shows the particle trajectory and heatmap contour plots obtained for the cases i.e. dry steam at atmospheric pressure and one at the OTSG condition. As shown in Fig. 7.10a, the particles do not follow the fluid path as much as they do in the case of Fig. 7.10b, thus, causing more impact on the U-bend at the inlet side.

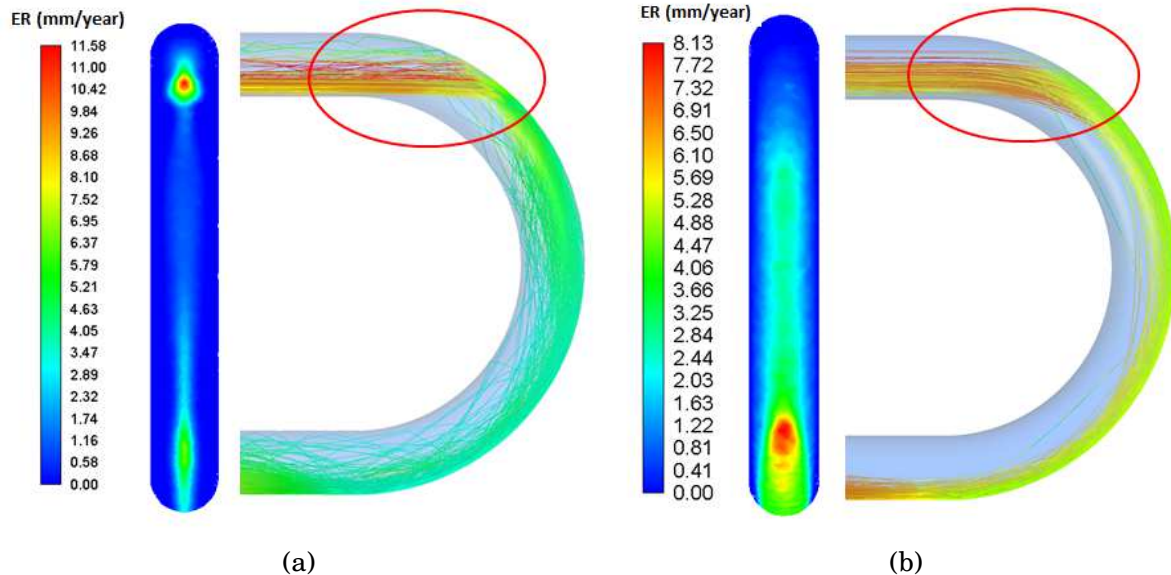


Figure 7.10: Erosion rate heatmaps for 60  $\mu\text{m}$  particles at 20m/s for A106C (a) saturated steam at 0.1 MPa (b) saturated steam at 11 MPa

This apparently resulted in the maximum wear rate hot spot location being at the inlet side of the bend. The trajectory also shows the particles dispersed randomly after the impact as they are transported through the bend. In Fig. 7.10b, the particles tend to impact the U-tube bend more at the outlet side, although, most of them also tend to be dragged along the wall. This also explains why more surface area on the outlet side of the bend has more wear compared to Fig. 7.10a. Also, the predictions are a result of the effects of fluid turbulence and the responsiveness of the particles to the fluid motion - often measured by the particle Stokes number [46–48].

A more realistic approach to study the effect of particle size is to account for particle size distribution instead of assuming all particles are of identical sizes in the multiphase gas-solid flow. It was assumed for the CFD simulations that (1) each particle size contributes to the damage without being hindered by other particle sizes; (2) there is no enhancement or attenuation of damage by one particle size based on interaction with another particle size; and (3) all particle sizes have the same volume fraction in the flow. With these assumptions, independent simulations can be conducted for each particle size, and the individual contribution to total wear loss determined with simple proportions. Fig. 7.11 was generated to illustrate the contribution of four different particle sizes.

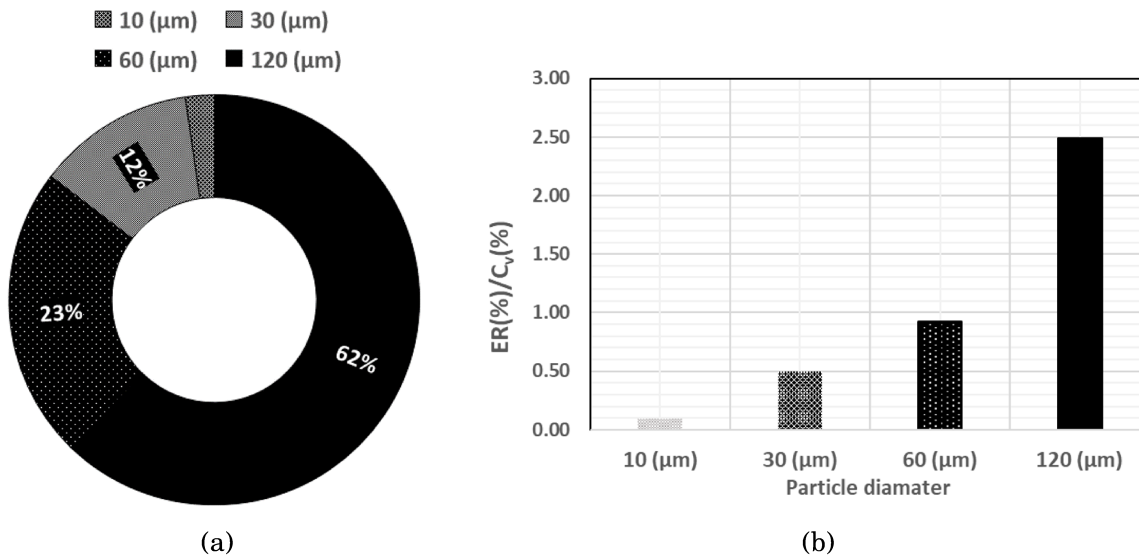


Figure 7.11: Extent of wear damage caused by individual particle size

The bar chart (Fig. 7.11b) shows the ratio of the percentage of the erosion damage (ER-%) caused by one of the particle sizes to the volume fraction percentage of that particle size in the entire solids content i.e. ( $C_v = 25\%$ ). For example, the 120  $\mu\text{m}$  particles which is 25% of the entire solids content (by volume), will contribute 62% to the entire damage, hence, the ER/ $C_v$  ratio ( $62\%/25\%$ ) is greater than 1. The opposite is the case for 10 to 60  $\mu\text{m}$  particles where the ER/ $C_v$  is less than 1. In a multi-particle system, this metric can be used to estimate more accurately when a failure is likely to happen instead of basing the prediction on a single particle diameter. It should be noted that the result presented is based on the assumption that particles are non-interacting; in reality, however, there may be attenuation in wear damages.

### 7. 4.3 Effect of superficial flow velocity

The results in this section show the predicted erosion wear rate for the two target materials (A106C and P22) for flow velocities bracketing the API RP 14E threshold velocities for each of the materials. The implications of the findings are discussed in terms of the predicted failure times for each target material. The erosion rates reported are the maximum values at the damage hot spot. Fig. 7.12a and 7.12b show the erosion damage for particle sizes 30 $\mu\text{m}$ , 60 $\mu\text{m}$ , and 120 $\mu\text{m}$  for A106C and P22 respectively. The API RP 14E limit velocity

has been indicated on both figures. It can be seen from the predictions that for both target materials, erosion rate was less than 250 mm/year for  $8.45E-7$  solids volume concentration for all particle sizes at 20 m/s. However, there is an exponential increase in the erosion rate at flow velocities above the API RP 14E predicted limits especially for the large particle sizes.

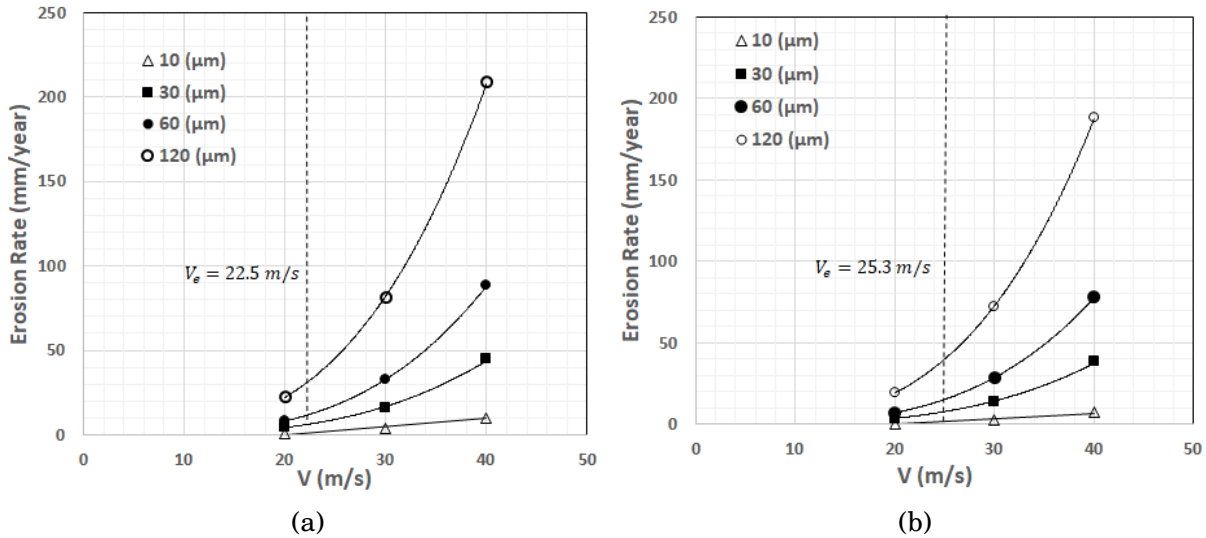


Figure 7.12: Erosion rate predictions for (a) P22 and (b) A106C, with the vertical dashed line representing the API RP 14E limit velocity

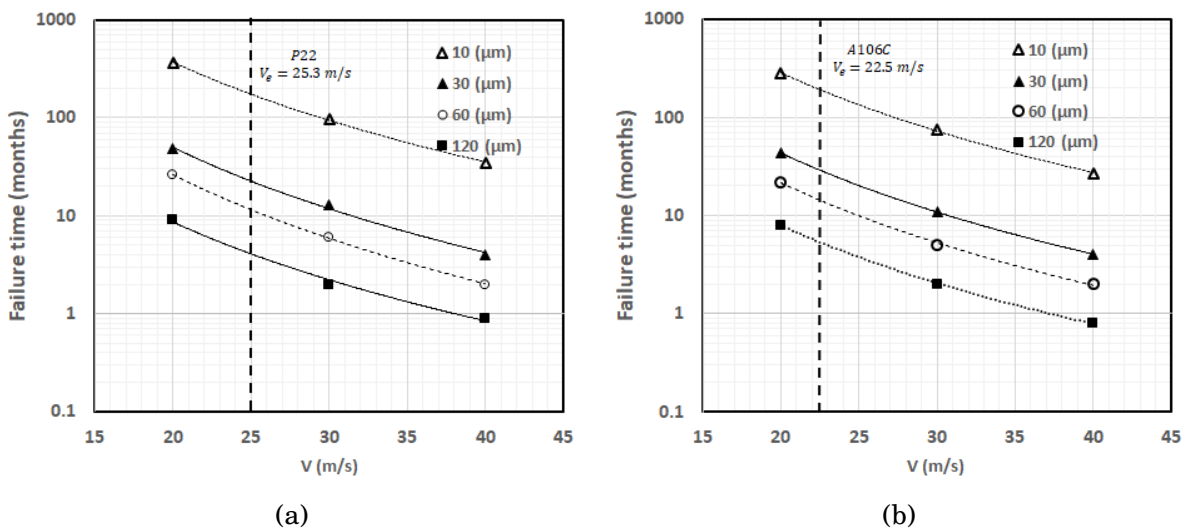


Figure 7.13: Predicted failure times for (a) P22 and (b) A106C alloys, with the vertical dashed line representing the API RP 14E limit velocity

Such an exponential increase in the erosion rate due to flow velocity and change in particle diameter cannot be explained by the API RP 14E guideline. For the 3" nominal pipe size with thickness 15.6 mm, failure time is presented in Fig. 7.13a and 7.13b for A106C and P22 respectively. The figures show a decrease in predicted failure time from 43 months to about 10 months for A106C and 48 months to 11 months for P22 when flow velocity is increased from 20 m/s to 30 m/s for 30 $\mu$ m particles i.e. below and above the API predicted velocity limits. In fact, a slight increase in velocity say from 20 m/s to 22 m/s (10% increase) will change the predicted failure time by approximately 30 %. It is important to note that the velocity increase indicated here is still below the API RP 14E limits for both target materials. This example indicates what could possibly happen when decisions are made to increase steam production in the OTSG. Another notable outcome of the predictions presented in Fig.7.13 is the failure time predicted for the different particle sizes. A change of particle size from 30 $\mu$ m to 60 $\mu$ m at 20 m/s would decrease the predicted failure time from almost 43 months to 22 months for A106C and from around 48 months to 24 months for P22. This is approximately a 50% decrease in predicted failure time for doubling particle size. Such strong dependency on particle size is not captured by the API RP 14E correlation.

#### 7. 4.4 Effect of solids volume concentration

The solids concentration is usually given in parts per million (PPM) or mg/L or in terms of volume fraction. The reported solids concentration in the OTSG boiler tubes was 3 g/L which is equivalent to a volume fraction of 8.45E-7 for Aegerine particles. The results presented so far are based on this solids volume concentration. The effect of increasing the particle concentration in the system to more than double i.e. 2E-6 which is about 7 mg/L is shown in Fig. 7.14 for A106C carbon steel at flow velocity of 20 m/s. Similar trend is observed for the P22 alloy steel as well as for other operating velocity. It can be seen from the figure that increasing the particle concentration from 3 mg/L to 7 mg/L resulted in at least 200% increase in the predicted maximum erosion wear in the tube for all the particle sizes except for the 10  $\mu$ m particle where the increase is about 100%. This means the failure times will decrease by a factor of three. Clearly, this behaviour cannot be predicted by the API RP 14E. The mixture density in the API RP 14E correlation will not change significantly if the solids concentration changes as illustrated in this analysis. This means that the same limit velocity will be predicted for both concentrations. This is very risky if operational decisions are being

made using the API RP 14E without detailed investigation of the different parameters that can affect the wear rate. Without proper investigation, one might want to say the the particle concentration is very low and should not be a huge concern, however, a predicted failure time going from say 5 years to about 1.5 years is not to be taken lightly.

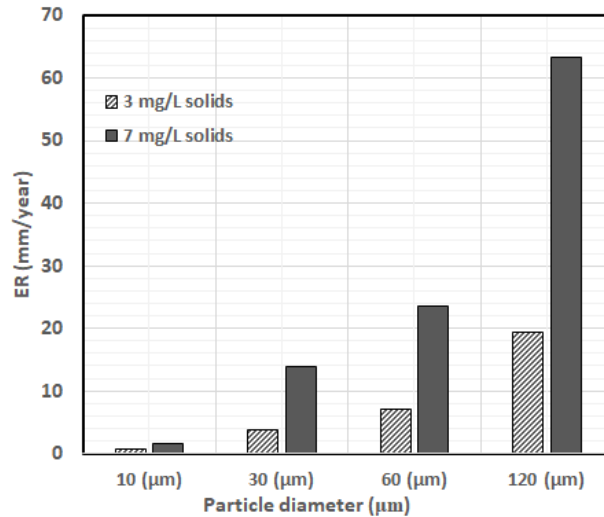


Figure 7.14: Predicted maximum wear rate for different particle sizes at two different concentrations- target material: A106C, operating velocity: 20 m/s

### 7. 4.5 Performance of 2D CFD erosion models

There are some other wear correlations that may be useful in evaluating erosion rate in the OTSG tube without the need to implement them in a CFD code. In this section, the Parsi et al. [49] wear correlation is used to predict the erosion rate in the OTSG boiler tubes. The Parsi et al. [49] wear correlation was developed based on dimensionless analysis of gas-solid elbow systems. Two dimensional (2D) CFD simulations were used to generate erosion data for a wide range of particle and flow conditions. The wear correlation is given by

$$ER(mm/yr) = 6.0183 \times 10^{-2} V_f F_s W_p \left( \frac{VHN}{VHN_{ref}} \right)^{-0.5} (Pnr)^{1.0584} \quad (7.23)$$

where  $V_f$  is fluid superficial velocity in m/s,  $W_p$  is the particle mass flow rate in kg/s,  $F_s$  is the particle shape factor that range from 0.25 to 1 for well-rounded and very angular particles respectively. The parameter  $VHN$  is the Vickers hardness number which is 166 for P22 alloy steel and 131 for A106C carbon steel. The reference Vickers hardness number  $VHN_{ref} = 305$

which corresponds to that of stainless steel SS2205. The variable  $Pnr$  is the dimensionless penetration number which is defined by

$$Pnr = Re^{1.372} \left( \frac{d_p}{D} \right)^{3.41} \left( \frac{\rho_p}{\rho_f} \right)^{1.45} \left( \frac{d_{p,ref}}{d_p} \right)^{3.1} \quad (7.24)$$

where  $Re$  is the Reynolds number,  $D$  is the pipe diameter,  $\rho_p$  and  $\rho_f$  are the particle and fluid density respectively,  $d_p$  is the particle diameter and  $d_{p,ref}$  is the reference particle diameter with a value of  $400\mu\text{m}$ . The equation above clearly accounts for flow and particle conditions that is not considered in the API RP 14E. However, because it is based on 2D CFD simulations, the performance is also checked against that from the 3D CFD simulations presented earlier in this study. A comparison made for A106C is shown in Fig. 7.15. A shape factor of 0.55 i.e. sub-rounded particles was used for the Parsi et al. [49] model calculations.

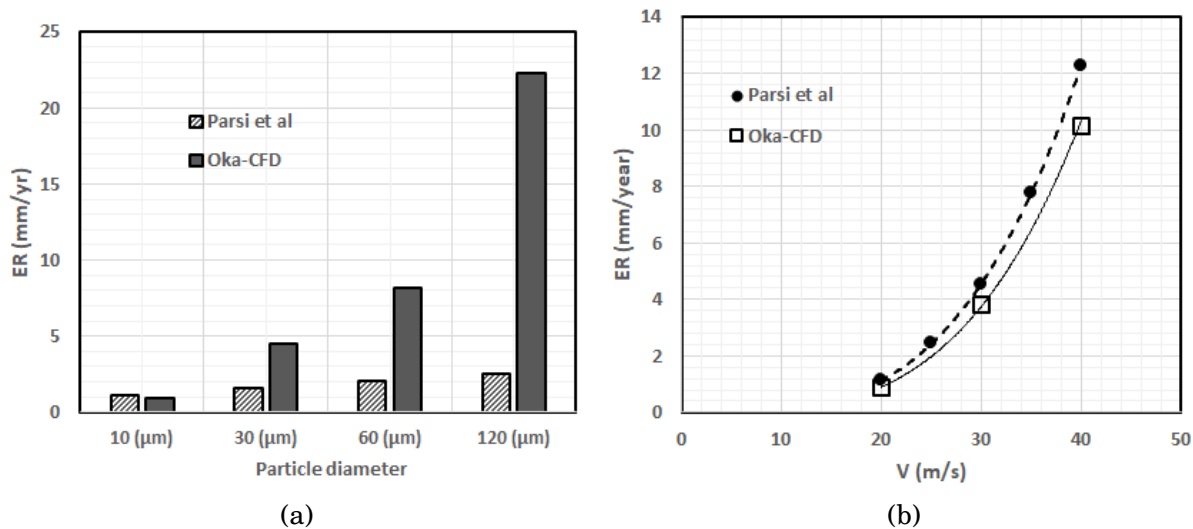


Figure 7.15: Comparison between 3D CFD-Oka model calculations and 2D-CFD Parsi model calculations for (a) different particle sizes at 20 m/s, and (b) different flow velocities for 10  $\mu\text{m}$  particles

It can be seen from Fig. 7.15a that the Parsi et al. [49] model under-predicted the erosion rate for the larger particle sizes (30-120  $\mu\text{m}$ ) i.e. it did not capture the effect of particle size as strongly as the 3D model using Oka et al. [30] erosion model. This may be because the model being 2D-based, did not account strongly for the effects of fluid turbulence and secondary flows that exist in the bend, which affect the trajectory of the particles. For conditions inside the OTSG which predominantly consists of 10  $\mu\text{m}$  particles, the Parsi model

will find significant use for assessing wear performance of the system. In Fig. 7.15b, the predictions for both Parsi model and Oka model implemented in 3D CFD simulations are within reasonable agreement for the 10  $\mu\text{m}$  particles. Since the OTSG system predominantly contains this range of particle sizes, the Parsi model can also be used for estimation of erosion wear rate in the system before a full 3D CFD analysis is conducted. The model also clearly has superior capability compared to the API RP 14E since it outputs erosion wear rate and takes into account wear-influencing variables other than the flow velocity. The model also uses macro-variables e.g. superficial velocity, mass flow rate, thus making it an easy-to-use tool for industries for quick assessment of the effects of changing operating conditions in the OTSG system.

## 7.5 Conclusions

In this work, a CFD investigation of solid particle erosion (SPE) in the U-bend of an OTSG boiler tube used in SAGD oil sands extraction was carried out. The Oka erosion model which was validated with experimental work done by Solnordal et al. [12] was implemented in the CFD code. Two main findings from this study are as follows:

1. The contribution of erosion to the total wear damage/failure in the OTSG boiler tubes should not be ignored
2. The API RP 14E guideline is not a suitable tool for determining the operating envelope for the SAGD OTSG as well as for making operational decision.

In the OTSG boiler tube U-bend, erosion wear predictions were obtained for operating conditions below and above the suggested API RP 14E velocity limits for two target materials i.e. A106C and P22. The API RP 14 E was inaccurate in representing the erosion limit velocity of system and it cannot provide further information on what the consequences will be if operating parameters are adjusted. For example, a change in operating flow velocity from 20 m/s to 22 m/s, which is below the API RP 14E predicted erosion velocity limits, may reduce the lifetime of the OTSG U-bend by 30% for all particle sizes considered in this study. It was also shown that an increase in the size of particles by a factor of 2 can cause failure time to be reduced by more than half at a given flow velocity. A comparison between the 3D CFD analysis and the empirical wear correlation of Parsi et al. [49] developed from a

2D parametric CFD study was also carried out. The Parsi et al. [49] model captures more wear-influencing variables than the API RP 14E and predicted closely the 3D CFD simulation results for the small particle sizes (10  $\mu\text{m}$ ). It is important to note that a 3D CFD analysis will still be required for investigating complex multiphase flows that occur in the OTSG e.g. presence of liquid film or droplets. It is also important to note that since erosion can constitute a significant damage mechanism in the OTSG, a controlled experiment to study pure erosion and pure corrosion in a lab/pilot scale facility at similar operating condition as the OTSG system is required. The investigation can provide the foundational insights on the synergistic effects of erosion-corrosion in the OTSG boiler tubes.

## References

- [1] E. I. Nduagu, I. D. Gates, Process analysis of a low emissions hydrogen and steam generation technology for oil sands operations, *Appl. Energy* 146 (2015) 184–195. URL: <http://dx.doi.org/10.1016/j.apenergy.2015.01.118>. doi:10.1016/j.apenergy.2015.01.118.
- [2] K.-w. Gwak, W. Bae, A Review of Steam Generation for In-Situ Oil Sands Projects, *Geosystems Eng.* 13 (2012) 11–118. doi:10.1080/12269328.2010.10541317.
- [3] A. Malik, A. Meroufel, Boiler Tubes Failures : A Compendium of Case Studies, *J. J. Anal. Preven.* 15 (2015) 246–250. doi:10.1007/s11668-015-9923-x.
- [4] M. R. Godfrey, P. Desch, L. Larocque, Erosion-Corrosion in Oil Field Once Through Steam Generators, in: 70th Annu. Int. Water Conf., volume 14, 2009, pp. 842–859.
- [5] B. Dooley, D. Lister, Flow-Accelerated Corrosion in Steam Generating Plants, *Powerpl. Chem.* 20 (2018) 194–244.
- [6] V. Kain, Flow Accelerated Corrosion : Forms , Mechanisms and Case Studies, *Procedia Eng.* 86 (2014) 576–588. URL: <http://dx.doi.org/10.1016/j.proeng.2014.11.083>. doi:10.1016/j.proeng.2014.11.083.
- [7] M. M. Stack, S. M. Abdelrahman, B. D. Jana, A new methodology for modelling erosion – corrosion regimes on real surfaces : Gliding down the galvanic series for a range

- of metal-corrosion systems, *Wear* 268 (2010) 533–542. URL: <http://dx.doi.org/10.1016/j.wear.2009.09.013>. doi:10.1016/j.wear.2009.09.013.
- [8] A. Neville, C. Wang, Erosion – corrosion mitigation by corrosion inhibitors — An assessment of mechanisms, *Wear* 267 (2009) 195–203. doi:10.1016/j.wear.2009.01.038.
- [9] S. Karimi, S. Shirazi, B. Mclaury, Effects of Fluid Viscosity and Impingement Angle on Submerged Jet Flowfields, in: Proc. ASME 2018 Fluids Eng. Div. Summer Meet., September, 2018, p. 83251. doi:10.1115/FEDSM2018-83251.
- [10] R. E. Vieira, M. Parsi, P. Zahedi, B. S. Mclaury, S. A. Shirazi, Electrical resistance probe measurements of solid particle erosion in multiphase annular flow, *Wear* 382-383 (2017) 15–28. URL: <http://dx.doi.org/10.1016/j.wear.2017.04.005>. doi:10.1016/j.wear.2017.04.005.
- [11] API RP 14E, Recommended Practice for Design and Installation of Offshore Production Platform Piping System, 5th editio ed., American Petroleum Institute, Washington DC, 1991.
- [12] C. B. Solnordal, C. Y. Wong, J. Boulanger, An experimental and numerical analysis of erosion caused by sand pneumatically conveyed through a standard pipe elbow, *Wear* 336-337 (2015) 43–57. URL: <http://dx.doi.org/10.1016/j.wear.2015.04.017>. doi:10.1016/j.wear.2015.04.017.
- [13] O. E. Adedeji, W. Yu, R. S. Sanders, Analysis of local wear variables for high-precision erosion modelling in complex geometries, *Wear* 426-427 (2019) 562–569. doi:10.1016/j.wear.2018.12.071.
- [14] C. A. R. Duarte, F. J. de Souza, V. F. dos Santos, Numerical investigation of mass loading effects on elbow erosion, *Powder Technol.* 283 (2015) 593–606. URL: <http://dx.doi.org/10.1016/j.powtec.2015.06.021>. doi:10.1016/j.powtec.2015.06.021.
- [15] D. R. Lester, L. A. Graham, J. Wu, High precision suspension erosion modeling, *Wear* 269 (2010) 449–457. doi:10.1016/j.wear.2010.04.032.
- [16] X. Chen, B. S. McLaury, S. A. Shirazi, Application and experimental validation of a computational fluid dynamics (CFD)-based erosion prediction model in elbows and

- plugged tees, *Comput. Fluids* 33 (2004) 1251–1272. doi:[10.1016/j.compfluid.2004.02.003](https://doi.org/10.1016/j.compfluid.2004.02.003).
- [17] A. Mansouri, A combined CFD-experimental method for developing an erosion equation for both gas-sand and liquid-sand flows, Phd thesis, University of Tulsa, 2016.
- [18] R. E. Vieira, A. Mansouri, B. S. McLaury, S. A. Shirazi, Experimental and computational study of erosion in elbows due to sand particles in air flow, *Powder Technol.* 288 (2016) 339–353. URL: <http://dx.doi.org/10.1016/j.powtec.2015.11.028>. doi:[10.1016/j.powtec.2015.11.028](https://doi.org/10.1016/j.powtec.2015.11.028).
- [19] H. Arabnejad, A. Mansouri, S. A. Shirazi, B. S. McLaury, Development of mechanistic erosion equation for solid particles, *Wear* 332-333 (2015) 1044–1050. doi:[10.1016/j.wear.2015.01.031](https://doi.org/10.1016/j.wear.2015.01.031).
- [20] S. Shirazi, B. McLaury, J. Shadley, E. Rybicki, Generalization of the API RP 14E Guideline for erosive services, *J. Pet. Technol.* (1995) 693–698. doi:[10.2118/28518-PA](https://doi.org/10.2118/28518-PA).
- [21] B. S. McLaury, J. Wang, S. A. Shirazi, SPE, J. R. Shadley, E. F. Rybicki, Solid Particle Erosion in Long Radius Elbows and Straight Pipes, *Annu. Spe Tech. Conf. (San Antonio, 10/5-8/97) Proc. [Production Oper. Eng. (1997)* 977–986.
- [22] H. Arabnejad, S. A. Shirazi, B. S. Mclaury, J. R. Shadley, T. Erosion, Calculation of Erosional Velocity Due to Liquid Droplets with Application to Oil and Gas Industry Production, in: *SPE Annu. Tech. Conf. Exhib.*, volume SPE 166423, New Orleans, USA, 2013.
- [23] M. Salama, E. Venkatesh, Evaluation of API RP 14E Erosional Velocity Limitations for Offshore Gas Wells, in: *Offshore Tecgnology Conf.*, 1983, pp. 371–376. doi:[10.4043/4485-ms](https://doi.org/10.4043/4485-ms).
- [24] F. Madani Sani, S. Huizinga, K. A. Esaklul, S. Nesic, Review of the API RP 14E erosional velocity equation: Origin, applications, misuses, limitations and alternatives, *Wear* 426-427 (2019) 620–636. URL: <https://doi.org/10.1016/j.wear.2019.01.119>. doi:[10.1016/j.wear.2019.01.119](https://doi.org/10.1016/j.wear.2019.01.119).

- [25] B. S. McLaury, S. A. Shirazi, An Alternate Method to API RP 14E for Predicting Solids Erosion in Multiphase Flow, *J. Energy Resour. Technol.* 122 (2002) 115. doi:[10.1115/1.1288209](https://doi.org/10.1115/1.1288209).
- [26] K. K. Botros, L. Jensen, S. Foo, Determination of erosion-based maximum velocity limits in natural gas facilities, *J. Nat. Gas Sci. Eng.* 55 (2018) 395–405. URL: <https://doi.org/10.1016/j.jngse.2018.05.013>. doi:[10.1016/j.jngse.2018.05.013](https://doi.org/10.1016/j.jngse.2018.05.013).
- [27] S. A. Shirazi, B. S. Mclaury, H. Arabnejad, T. Erosion, A Semi-Mechanistic Model for Predicting Sand Erosion Threshold Velocities in Gas and Multiphase Flow Production, *Soc. Pet. Eng. SPE-18147-* (2016).
- [28] Y. I. Oka, M. Nishimura, K. Nagahashi, M. Matsumura, Control and evaluation of particle impact conditions in a sand erosion test facility, *Wear* 250 (2001) 736–743.
- [29] Y. I. Oka, K. Okamura, T. Yoshida, Practical estimation of erosion damage caused by solid particle impact Part 1 : Effects of impact parameters on a predictive equation, *Wear* 259 (2005) 95–101. doi:[10.1016/j.wear.2005.01.039](https://doi.org/10.1016/j.wear.2005.01.039).
- [30] Y. I. Oka, H. Ohnogi, T. Hosokawa, M. Matsumura, The impact angle dependence of erosion damage caused by solid particle impact, *Wear* 203 (1997) 573–579.
- [31] DNV GL, Managing sand production and erosion, Technical Report August, 2015.
- [32] Y. Zhang, E. P. Reuterfors, B. S. McLaury, S. a. Shirazi, E. F. Rybicki, Comparison of computed and measured particle velocities and erosion in water and air flows, *Wear* 263 (2007) 330–338. doi:[10.1016/j.wear.2006.12.048](https://doi.org/10.1016/j.wear.2006.12.048).
- [33] N. Huber, M. Sommerfeld, Characterization of the cross-sectional particle concentration distribution in pneumatic conveying systems, *Powder Technol.* 79 (1994) 191–210.
- [34] M. Sommerfeld, N. Huber, Experimental analysis of modelling of particle-wall collisions, *Int. J. Multiph. Flow* 25 (1999) 1457–1489.
- [35] G. Grant, W. Tabakoff, Erosion Prediction in Turbomachinery Resulting from Environmental Solid Particles, *J. Aircr. - J Aircr.* 12 (1975) 471–478.

- [36] G. Haider, H. Arabnejad, S. A. Shirazi, B. S. Mclaury, A mechanistic model for stochastic rebound of solid particles with application to erosion predictions, *Wear* 376-377 (2017) 615–624. URL: <http://dx.doi.org/10.1016/j.wear.2017.02.015>. doi:10.1016/j.wear.2017.02.015.
- [37] C. A. R. Duarte, F. J. de Souza, R. V. Salvo, V. F. dos Santos, The role of inter-particle collisions on elbow erosion, *Int. J. Multiph. Flow* 89 (2017) 1–22. doi:10.1016/j.ijmultiphaseflow.2016.10.001.
- [38] M. Zamani, S. Seddighi, H. R. Nazif, Erosion of natural gas elbows due to rotating particles in turbulent gas-solid flow, *J. Nat. Gas Sci. Eng.* 40 (2017) 91–113. URL: <http://dx.doi.org/10.1016/j.jngse.2017.01.034>. doi:10.1016/j.jngse.2017.01.034.
- [39] D. Choudhury, Introduction to the Renormalization Group Method and Turbulence Modeling, Technical memorandum, Fluent Incorporated, 1973. URL: <https://books.google.ca/books?id=mKWEQwAACAAJ>.
- [40] S. A. Morsi, A. J. Alexander, An Investigation of Particle Trajectories in Two-Phase Flow Systems, *J. Fluid Mech.* 55 (1972) 193–208.
- [41] S. C. R. Dennis, S. N. Singh, D. B. Ingham, The Steady Flow Due to Rotating Sphere at Low and Moderate Reynolds Numbers, *J. Fluid Mech.* 101 (1980) 257–279.
- [42] A. Li, G. Ahmadi, Dispersion and Deposition of Spherical Particles from Point Sources in a Turbulent Channel Flow, *Aerosol Sci. Technol.* 16 (1992) 209–226.
- [43] G. P. Saffman, The Lift on a Small Sphere in a Slow Shear, *J. Fluid Mech.* 22 (1965) 385–400.
- [44] B. Oesterlé, T. Bui Dinh, Experiments on the Lift of a Spinning Sphere in the Range of Intermediate Reynolds Numbers, *Exp. Fluids* 25 (1998) 16–22.
- [45] ANSYS, ANSYS 17.0 Theory Guide, Technical Report, 2017. URL: <https://www.sharcnet.ca/Software/Ansys/17.0/en-us/help/flu{ }th/flu{ }th.html>.
- [46] R. S. Sanders, Fluid-Particle Systems and Application: Lecture notes, Technical Report, University of Alberta, Edmonton, Alberta, Canada, 2015.

- [47] S. A. Hashemi, A. Sadighian, S. I. A. Shah, R. S. Sanders, Solid velocity and concentration fluctuations in highly concentrated liquid–solid (slurry) pipe flows, *Int. J. Multiph. Flow* 66 (2014) 46–61. URL: <http://linkinghub.elsevier.com/retrieve/pii/S0301932214001153>. doi:10.1016/j.ijmultiphaseflow.2014.06.007.
- [48] A. Aguilar-Corona, R. Zenit, O. Masbernat, Collisions in a liquid fluidized bed, *Int. J. Multiph. Flow* 37 (2011) 695–705. URL: <http://dx.doi.org/10.1016/j.ijmultiphaseflow.2011.02.004>. doi:10.1016/j.ijmultiphaseflow.2011.02.004.
- [49] M. Parsi, D. N. V. Gl, H. Arabnejad, E/CRC, A. Al-sarkhi, K. Fahd, A New Correlation for Predicting Solid Particle Erosion Caused by Gas-Sand Flow in Elbows, in: *Offshore Technol. Conf.*, 2018.

# Conclusions and recommendations for future works

## 8.1 Summary of contributions and conclusions

There are numerous erosion wear-related challenges that face many particle-handling industries including the mining and oil sands industries. Ideally, industries want to predict erosion wear rate directly from measurements made on their own pipelines and equipment. However, this is not practical because there are many uncontrolled variables. It is, therefore, necessary to provide industries with tools to predict wear rates and take proactive steps to prevent failures. The primary objective of this thesis research is to conduct investigations that will provide industries with tools that will help improve the wear performance of their pipelines and equipment. This was achieved through advanced experimental and Computational Fluid Dynamics (CFD) analysis of slurry flow systems, erosion models, wear testing devices and the development of novel methodologies. The studies conducted in this thesis are divided into two parts:

1. The development of a cost-effective and efficient lab/bench-scale wear testing device as a slurry pipeline wear prediction tool. The investigations have been reported in Chapter 3, Chapter 4, and Chapter 5.
2. An investigation to improve the prediction performance of traditional erosion models in complex geometries e.g. bends, and to improve industrial process design and operation

through a proper erosion wear analysis. The respective studies have been reported in Chapter 6 and Chapter 7.

In the first part, the toroid wear tester (TWT) is the selected lab-scale device for the investigations. A preliminary study by Sarker [1] describes different slurry erosion tests using the TWT. Investigations like the effect of solids volume concentration, particle size, and operating speed on erosion rate were conducted. In a subsequent work by Zhang [2], a solids friction loss (Coulombic) model was presented to describe the load from the slurry bed in the TWT. Torque was measured in the experiments to show the sensitivity of Coulombic friction in the TWT to different operating conditions. In these studies, wear data from the TWT and a pipe at "similar" hydrodynamic conditions were compared, however, the results agreed poorly. Wear rate correlations presented in these studies also showed anomalous trends e.g. erosion rate increased with operating speed over a certain range but shows no increase (and sometimes, a decrease) at some other conditions. It was postulated from these investigations that the TWT, in fact, do not have hydrodynamics that can be compared directly to those in slurry pipeline, and that secondary flows exists in the TWT which introduce errors into measured wear. The research conducted in the first part of this PhD thesis answered some questions from these observations. The specific contributions are:

1. Flow behaviour in the TWT was characterized through CFD simulations, and for the first time, supported with experimental data. The flow visualization experiments and CFD simulations conducted were able to provide details about the flow fields in the TWT, which revealed regions of strong back flow and fluid rotation. Several torque (friction loss) measurement experiments were conducted for a range of TWT operating conditions using water-corn syrup mixtures. The torque data were used to confirm the prediction accuracy of the CFD model and indicate the strength of secondary flows in the TWT. Based on these findings, it is apparent that these secondary flows would influence the slurry bed in the TWT to behave very differently from those in a horizontal pipe; hence, introducing significant errors to wear measurements for certain conditions. Further consequences of these secondary flow effects require that specific operating range be defined for the TWT for which (1) wear tests can be confidently conducted with minimal uncertainties, and (2) proper scaling can be carried out, using suitable variables to interpret wear data between the TWT and a pipe.
2. To address the challenges identified from the TWT hydrodynamic study, flow visual-

ization, wear, solids-related torque (Coulombic friction) experiments were conducted in the TWT to study particle dynamics, and how they relate to measured wear rate. New sets of data for slurries prepared with glycerin-water mixtures (liquid) and sand particles were generated. Solids-related torque experiments were conducted to determine the Coulombic friction produced by the slurry. Flow visualization experiments were used to show the response of the slurry bed to different TWT operating conditions. Several wear measurements at similar conditions as the aforementioned experiments were also taken. From analysis of the data, the ratio of the TWT linear speed and particle terminal settling velocity ( $V/v_\infty$ ) was introduced as a new quantity to define slurry bed conditions inside this specific TWT. A region with  $V/v_\infty \leq 7$  was identified as a suitable condition for wear testing in the TWT. At this condition, the slurry bed is fully settled and wear rate correlates linearly with Coulombic friction. In other words, the anomalous trend in wear data previously seen in the TWT [1, 2], was shown not to exist when the TWT is operated at this fully settled condition.

3. For applications in slurry pipeline, the  $V/v_\infty \leq 7$  condition from the TWT study seems impractical for industrial operations. Also, wear damage in slurry pipelines results from a combination of kinematic and Coulombic friction-related mechanisms, and only the Coulombic friction-related part is comparable to the fully settled condition in the TWT. In order to use the TWT correlation for slurry pipeline application, the wear rate from Coulombic friction contribution in slurry pipelines must be determined. A novel method that combines CFD analysis and the formulation of the SRC two-layer model [3] was introduced and used to perform this task. In the development of the method, particle flux was predicted from the CFD simulations while the SRC two-layer model was used to calculate kinematic and Coulombic friction loss. Through a series of algebraic steps, the individual contributions of kinematic and Coulombic friction to the total wear damage were estimated for wear data from slurry pipeline tests [4, 5]. The results revealed that the estimated Coulombic friction-related wear rate showed a linear correlation similar to the one determined for the TWT. Clearly, an opportunity now exist to interpret wear data between the TWT and a pipe, however, this would be the subject for future investigations.

In the second part of this PhD research, the Oka et al. [6] erosion model, the API RP 14E guideline [7], CFD simulations, and wear data from a standard 90° elbow by Solnordal

et al. [8] were used in the investigations. Most single particle erosion models such as the Oka et al. [6] model were developed from direct impingement jet tester that do not capture the influence of secondary flows (local fluid rotation and swirls) that typically exist in complex geometries such as an elbow. The investigations conducted in the first part of this thesis revealed that a proper hydrodynamic analysis and characterization must be an integral part of erosion testing and model development. Particularly, the presence of secondary flows in a system can mislead wear data interpretation, which therefore means that single particle erosion models would not perform optimally in complex geometries. Also, reliance only on industry standards like the API RP 14E guideline for the design and operation of processes, especially ones that contain such complex geometries can result in very costly consequences. The research studies in the second part of this PhD thesis investigated appropriate tools and techniques to address these concerns and a summary of the contributions are:

1. Using CFD simulations and wear data analysis, a new geometry correction factor function (GCFF) was developed for a standard 90° elbow. The GCFF adapts to local positions on the elbow surface to correct wear rates predicted by traditional erosion models (Oka et al. [6] model in this case). In other words, the GCFF outputs different correction factors based on local positions on the elbow surface. This is a significant advancement over previous studies presented in McLaury et al. [9] and DNV GL [10] that reported a single factor to be used over the entire elbows surface. The CFD simulations were used to generate local wear variables such as the particle impact velocity and impact angle. Wear data from the elbow (by Solnordal et al. [8]) and the predicted variables from CFD simulations were analyzed and used to develop a geometry correction function (GCFF). The results showed the Oka et al. [6] wear model performed better when combined with the GCFF. It was also observed that regions on the elbow where there is direct impact, similar to the sand blast test from which the Oka et al. [6] model was developed did not require much correction i.e. the GCFF output was approximately equal to 1. However, regions that deviated from the direct flow path or are influenced by secondary flows in the elbow require significant correction. Another significant contribution from the CFD simulations revealed that particle rotation and wall roughness must be accounted for in order to predict accurate wear rate and wear map distribution.
2. A first look into the erosion damage caused by fine particles in the OTSG tubes was

conducted using CFD simulations. High density and very low concentration fine particles can be found in Once Through Steam Generator (OTSG) boiler tubes. The wear damage caused by these particles has not been evaluated. The visibly evident wear damage mechanisms in the OTSG are flow accelerated corrosion, thermal cracking, and erosion-corrosion [11, 12]. The severity of damage due to pure erosion wear or its contribution to erosion-corrosion synergy is often overlooked. Though there is no conspicuously visible evidence of pure erosion due to the presence of other masking wear damage mechanisms, the simulation results revealed that erosion damage contributes significantly to the failure in the OTSG. Further analysis was conducted to compare the durability of different materials for the construction of the OTSG boiler tubes. The CFD simulations were also used to show that the API RP 14E guideline currently being used by industries is not sufficient to define an operating envelope for the OTSG. The API RP 14E guideline does not capture the effects of wear-influencing variables like particles size and concentration which were shown to significantly affect the failure time of the OTSG.

## 8.2 Recommendations for future work

The next step in the development of the TWT as a wear prediction tool is to (1) interpret wear data between the TWT and a pipe, and (2) scale such data for use in industrial slurry pipeline operations. The following have been recommended for future investigators:

- An analysis of the local particle behaviour in the TWT slurry bed. Information such as the relative velocity, particle rotation, and bed oscillations observed during the experiments can provide more insight to connect Coulombic friction and wear between the TWT and a pipe. The Discrete Element Model (DEM) for particle modelling is likely the most suitable technique to carry out this investigation. The DEM approach is a four-way coupling method that allows all forces on the particle to be resolved; hence, it will provide more details about local interaction of the particles in the slurry.
- The leading edge effect due to the coupon-wall contact was shown to be a source of uncertainty in measured wear rate, which would affect the use of the TWT for pipeline wear prediction. A CFD analysis that accounts for the leading edge can provide more information about the non-uniform wear distribution observed and how it can be

effectively corrected. Additional wear measurement experiments to eliminate the leading-edge effect are needed. This is difficult as the edge effect is inherent in the design of TWT i.e. there is a 1 mm clearance between the coupon surface and the wall of the TWT that must be eliminated. The test coupons ideally would need to be flush mounted with the TWT wall. The coupons can either be radiused to the TWT wall, with a raised face or in an insert so that the leading edge effect is minimized.

- It would be of great value to visualize the  $V/v_{\infty}$  parameter in slurry pipelines. What does a similar value of  $V/v_{\infty}$  look like in the TWT and a pipe? This can tell what is physically meaningful when scaling wear data between the two geometries. Also, there is a TWT with larger channel dimensions at the Pipeline Transport Processes (PTP) Research Laboratory in which this same analysis can be performed. Though it is expected that the theory will hold, the behaviour of the slurry bed would differ. For example, the two TWT geometries can have the same  $V/v_{\infty}$  value at a given condition, however, the degree of turbulence determined from Reynolds number depends on the channel width. Similar consideration must be given to different pipe sizes.
- Wear data at experimental condition where Coulombic friction is dominant e.g. larger particle sizes, are needed from slurry pipeline wear tests. This would help create "equivalent" conditions between the TWT and a pipe for wear data comparison. However, there are concerns about the capacity of the recirculating pipe loop tester in handling such large particle sizes e.g. the clearance of the pump impeller.

For the geometry correction factor function (GCFF) developed, comparison was only done for one elbow geometry i.e. a standard elbow with curvature = 1.5, and also for one flow condition. More experiments at other flow conditions and for other elbow geometries i.e. with other curvature will be needed to further validate the GCFF. The initial GCFF study conducted here also suggests that GCFF is dependent only on variables that define the elbow geometry i.e. curvature and diameter. It should therefore, be applicable to larger size elbows and further validation on industrial scale elbows is recommended. Another future investigation is to improve the wear prediction accuracy in other geometries such as tees and cyclones by developing a GCFF for each of these geometries. Finally, the potential of the GCFF as a tool to translate wear rate between geometries should be explored.

Finally, the CFD model used to analyze the OTSG system was validated using another elbow system with gas-solid flow. Further experiments in U-bends and at conditions similar

to those in the OTSG will be needed to support the CFD simulations reported in this study. To match the OTSG conditions, the experimental system will be a high pressure steam-solid flow where corrosion has been minimized so as to quantify the effect of pure erosion damage. Sand which is easily accessible can be used in place of Aegerine for the experiments. Erosion models have been validated for different erodent-target materials combination, therefore, performance of Aegerine particle can be inferred from experiment with sand.

## References

- [1] N. R. Sarker, A Preliminary Study of Slurry Pipeline Erosion Using a Toroid Wear Tester, MSc thesis, University of Alberta, 2016.
- [2] L. Zhang, Relating slurry friction to erosion rate using a toroid wear tester, MSc thesis, University of Alberta, 2018.
- [3] R. G. Gillies, C. A. Shook, K. C. Wilson, An improved two layer model for horizontal slurry pipeline flow, *Can. J. Chem. Eng.* 69 (1991) 173–178. URL: <http://doi.wiley.com/10.1002/cjce.5450690120>. doi:10.1002/cjce.5450690120.
- [4] A. Sadighian, Investigating Key Parameters Affecting Slurry Pipeline Erosion, Ph.D. thesis, University of Alberta, 2016. doi:10.1017/CB09781107415324.004. arXiv:arXiv:1011.1669v3.
- [5] R. Jami, Investigation Using Polymer Additives to Mitigate Erosion in Multiphase Turbulent Pipe Flow, Master's thesis, University of Alberta, 2019.
- [6] Y. I. Oka, H. Ohnogi, T. Hosokawa, M. Matsumura, The impact angle dependence of erosion damage caused by solid particle impact, *Wear* 203 (1997) 573–579.
- [7] API RP 14E, Recommended Practice for Design and Installation of Offshore Production Platform Piping System, 5th editio ed., American Petroleum Institute, Washington DC, 1991.
- [8] C. B. Solnordal, C. Y. Wong, J. Boulanger, An experimental and numerical analysis of erosion caused by sand pneumatically conveyed through a standard pipe elbow,

Wear 336-337 (2015) 43–57. URL: <http://dx.doi.org/10.1016/j.wear.2015.04.017>.  
doi:10.1016/j.wear.2015.04.017.

- [9] B. S. McLaury, J. Wang, S. A. Shirazi, SPE, J. R. Shadley, E. F. Rybicki, Solid Particle Erosion in Long Radius Elbows and Straight Pipes, Annu. Spe Tech. Conf. (San Antonio, 10/5-8/97) Proc. [Production Oper. Eng. (1997) 977–986.
- [10] DNV GL, Managing sand production and erosion, Technical Report August, 2015.
- [11] B. Dooley, D. Lister, Flow-Accelerated Corrosion in Steam Generating Plants, Powerpl. Chem. 20 (2018) 194–244.
- [12] M. R. Godfrey, P. Desch, L. Larocque, Erosion-Corrosion in Oil Field Once Through Steam Generators, in: 70th Annu. Int. Water Conf., volume 14, 2009, pp. 842–859.

# Global References

- [1] R. G. Gillies, C. A. Shook, K. C. Wilson, An improved two layer model for horizontal slurry pipeline flow, *Can. J. Chem. Eng.* 69 (1991) 173–178. URL: <http://doi.wiley.com/10.1002/cjce.5450690120>. doi:10.1002/cjce.5450690120.
- [2] R. G. Gillies, Pipeline Flow of Coarse Particle Slurries, Ph.D. thesis, University of Saskatchewan, 1993.
- [3] R. G. Gillies, J. Schaan, R. J. Sumner, M. J. McKibben, C. A. Shook, Deposition velocities for newtonian slurries in turbulent flow, *Can. J. Chem. Eng.* 78 (2000) 704–708. URL: <http://doi.wiley.com/10.1002/cjce.5450780412>. doi:10.1002/cjce.5450780412.
- [4] B. Fotty, M. Krantz, J. Been, J. Wolodko, Development of a pilot-scale facility for evaluating wear in slurry pipeline systems, in: *Proc. Hydrotransp.* 18, September, Rio de Janeiro, Brazil, 2010, pp. 431–443.
- [5] L. L. Parent, D. Y. Li, Wear of hydrotransport lines in Athabasca oil sands, *Wear* 301 (2013) 477–482. doi:10.1016/j.wear.2013.01.039.
- [6] D. R. Lester, L. A. Graham, J. Wu, High precision suspension erosion modeling, *Wear* 269 (2010) 449–457. doi:10.1016/j.wear.2010.04.032.

- [7] Y. I. Oka, H. Ohnogi, T. Hosokawa, M. Matsumura, The impact angle dependence of erosion damage caused by solid particle impact, *Wear* 203 (1997) 573–579.
- [8] O. E. Adedeji, W. Yu, R. S. Sanders, Analysis of local wear variables for high-precision erosion modelling in complex geometries, *Wear* 426-427 (2019) 562–569. URL: <http://www.sciencedirect.com/science/article/pii/S0043164818316788>. doi:<https://doi.org/10.1016/j.wear.2018.12.071>.
- [9] P. Goosen, I. Malgas, An Experimental Investigation into Aspects of Wear in Boiler Ash Disposal Pipelines, in: *Proc. Hydrotransp.* 14, September, Maastricht, The Netherlands, 1999, pp. 8–10.
- [10] A. Sadighian, Investigating Key Parameters Affecting Slurry Pipeline Erosion, Ph.D. thesis, University of Alberta, 2016. doi:[10.1017/CB09781107415324.004](https://doi.org/10.1017/CB09781107415324.004). [arXiv:arXiv:1011.1669v3](https://arxiv.org/abs/1011.1669v3).
- [11] DNV GL, Managing sand production and erosion, Technical Report August, 2015.
- [12] B. S. McLaury, J. Wang, S. A. Shirazi, SPE, J. R. Shadley, E. F. Rybicki, Solid Particle Erosion in Long Radius Elbows and Straight Pipes, *Annu. Spe Tech. Conf. (San Antonio, 10/5-8/97) Proc. [Production Oper. Eng. (1997) 977–986*.
- [13] J. Been, F. Ju, Prediction of Wear of Tailings Pipelines in Oil Sands Slurries, Technical Report, Alberta Innovates Technology Futures, 2013.
- [14] R. Gupta, S. N. Singh, V. Sehadri, Prediction of uneven wear in a slurry pipeline on the basis of measurements in a pot tester, *Wear* 184 (1995) 169–178. doi:[10.1016/0043-1648\(94\)06566-7](https://doi.org/10.1016/0043-1648(94)06566-7).
- [15] C. A. Shook, M. McKibben, M. Small, Experimental investigation of some hydrodynamic factors affecting slurry pipeline wall erosion, *Can. J. Chem. Eng.* 68 (1990) 17–23. URL: <http://doi.wiley.com/10.1002/cjce.5450680102>. doi:[10.1002/cjce.5450680102](https://doi.org/10.1002/cjce.5450680102).
- [16] R. J. K. Wood, The sand erosion performance of coatings, *Mater. Des.* 20 (1999) 179–191. URL: [http://dx.doi.org/10.1016/S0261-3069\(99\)00024-2](http://dx.doi.org/10.1016/S0261-3069(99)00024-2). doi:[10.1016/S0261-3069\(99\)00024-2](https://doi.org/10.1016/S0261-3069(99)00024-2).

- [17] H. Arabnejad, A. Mansouri, S. A. Shirazi, B. S. McLaury, Development of mechanistic erosion equation for solid particles, *Wear* 332-333 (2015) 1044–1050. doi:[10.1016/j.wear.2015.01.031](https://doi.org/10.1016/j.wear.2015.01.031).
- [18] R. Cooke, G. Johnson, P. Goosen, Laboratory Apparatus for Evaluating Slurry Pipeline Wear, Technical Report March, SAIT Seminar, Calgary, 2000.
- [19] N. R. Sarker, A Preliminary Study of Slurry Pipeline Erosion Using a Toroid Wear Tester, MSc thesis, University of Alberta, 2016.
- [20] L. Zhang, Relating slurry friction to erosion rate using a toroid wear tester, MSc thesis, University of Alberta, 2018.
- [21] N. R. Sarker, D. E. S. Breakey, M. A. Islam, S. Sun, B. A. Fleck, R. S. Sanders, Performance and Hydrodynamics Analysis of a Toroid Wear Tester to Predict Erosion in Slurry Pipelines, *Wear* (2019) 203068. URL: <https://doi.org/10.1016/j.wear.2019.203068>. doi:[10.1016/j.wear.2019.203068](https://doi.org/10.1016/j.wear.2019.203068).
- [22] R. Jami, Investigation Using Polymer Additives to Mitigate Erosion in Multiphase Turbulent Pipe Flow, Master's thesis, University of Alberta, 2019.
- [23] API RP 14E, Recommended Practice for Design and Installation of Offshore Production Platform Piping System, 5th editio ed., American Petroleum Institute, Washington DC, 1991.
- [24] I. Finnie, Erosion of surfaces by solid particles, *Wear* 3 (1960) 87–103. doi:[10.1016/0043-1648\(60\)90055-7](https://doi.org/10.1016/0043-1648(60)90055-7). arXiv:[arXiv:1011.1669v3](https://arxiv.org/abs/1011.1669v3).
- [25] J. G. A. Bitter, A study of erosion phenomena part II, *Wear* 6 (1963) 169–190.
- [26] C. Huang, P. Minev, J. Luo, K. Nandakumar, A phenomenological model for erosion of material in a horizontal slurry pipeline flow, *Wear* 269 (2010) 190–196. URL: <http://dx.doi.org/10.1016/j.wear.2010.03.002>. doi:[10.1016/j.wear.2010.03.002](https://doi.org/10.1016/j.wear.2010.03.002).
- [27] Y. Zhang, E. P. Reuterfors, B. S. McLaury, S. a. Shirazi, E. F. Rybicki, Comparison of computed and measured particle velocities and erosion in water and air flows, *Wear* 263 (2007) 330–338. doi:[10.1016/j.wear.2006.12.048](https://doi.org/10.1016/j.wear.2006.12.048).

- [28] S. A. Shirazi, B. S. McLaury, H. Arabnejad, T. Erosion, A Semi-Mechanistic Model for Predicting Sand Erosion Threshold Velocities in Gas and Multiphase Flow Production, Soc. Pet. Eng. SPE-18147- (2016).
- [29] X. Chen, B. S. McLaury, S. A. Shirazi, Application and experimental validation of a computational fluid dynamics (CFD)-based erosion prediction model in elbows and plugged tees, *Comput. Fluids* 33 (2004) 1251–1272. doi:[10.1016/j.compfluid.2004.02.003](https://doi.org/10.1016/j.compfluid.2004.02.003).
- [30] C. B. Solnordal, C. Y. Wong, J. Boulanger, An experimental and numerical analysis of erosion caused by sand pneumatically conveyed through a standard pipe elbow, *Wear* 336-337 (2015) 43–57. URL: <http://dx.doi.org/10.1016/j.wear.2015.04.017>. doi:[10.1016/j.wear.2015.04.017](https://doi.org/10.1016/j.wear.2015.04.017).
- [31] C. A. R. Duarte, F. J. de Souza, R. V. Salvo, V. F. dos Santos, The role of inter-particle collisions on elbow erosion, *Int. J. Multiph. Flow* 89 (2017) 1–22. doi:[10.1016/j.ijmultiphaseflow.2016.10.001](https://doi.org/10.1016/j.ijmultiphaseflow.2016.10.001).
- [32] W. Yu, P. Fede, E. Climent, S. Sanders, Multi-fluid approach for the numerical prediction of wall erosion in an elbow, *Powder Technol.* 354 (2019) 561–583. URL:<http://www.sciencedirect.com/science/article/pii/S0032591019304504>. doi:<https://doi.org/10.1016/j.powtec.2019.06.007>.
- [33] M. Parsi, K. Najmi, F. Najafifard, S. Hassani, B. S. McLaury, S. A. Shirazi, A comprehensive review of solid particle erosion modeling for oil and gas wells and pipelines applications, *J. Nat. Gas Sci. Eng.* 21 (2014) 850–873. doi:[10.1016/j.jngse.2014.10.001](https://doi.org/10.1016/j.jngse.2014.10.001).
- [34] J. Wu, L. J. W. Graham, D. Lester, C. Y. Wong, T. Kilpatrick, S. Smith, B. Nguyen, An effective modeling tool for studying erosion, *Wear* 270 (2011) 598–605. doi:[10.1016/j.wear.2011.01.016](https://doi.org/10.1016/j.wear.2011.01.016).
- [35] L. J. W. J. W. Graham, D. Lester, J. Wu, Slurry Erosion in Complex Flows : Experiment and CFD, in: *Seventh Int. Conf. CFD Miner. Process Ind.*, December, 2009, pp. 1–6.
- [36] J. K. Edwards, B. S. McLaury, S. A. Shirazi, Modeling Solid Particle Erosion in Elbows and Plugged Tees, *J. Energy Resour. Technol.* 123 (2001) 277. doi:[10.1115/1.1413773](https://doi.org/10.1115/1.1413773).

- [37] X. Chen, B. S. McLaury, S. A. Shirazi, Numerical and experimental investigation of the relative erosion severity between plugged tees and elbows in dilute gas/solid two-phase flow, *Wear* 261 (2006) 715–729. doi:10.1016/j.wear.2006.01.022.
- [38] A. Gnanavelu, N. Kapur, A. Neville, J. F. Flores, An integrated methodology for predicting material wear rates due to erosion, *Wear* 267 (2009) 1935–1944. URL: <http://linkinghub.elsevier.com/retrieve/pii/S0043164809003986>. doi:10.1016/j.wear.2009.05.001.
- [39] O. E. Adedeji, L. Zhang, D. Breakey, R. S. Sanders, Investigation of abrasive wear in contact load-dominated slurry flows using a Toroid Wear Tester, *Manuscr. Submitt. to Wear* (2020).
- [40] M. Parsi, M. Kara, M. Agrawal, N. Kesana, A. Jatale, P. Sharma, S. Shirazi, CFD simulation of sand particle erosion under multiphase flow conditions, *Wear* 376-377 (2017) 1176–1184. URL: <http://dx.doi.org/10.1016/j.wear.2016.12.021>. doi:10.1016/j.wear.2016.12.021.
- [41] R. E. Vieira, M. Parsi, P. Zahedi, B. S. Mclaury, S. A. Shirazi, Electrical resistance probe measurements of solid particle erosion in multiphase annular flow, *Wear* 382-383 (2017) 15–28. URL: <http://dx.doi.org/10.1016/j.wear.2017.04.005>. doi:10.1016/j.wear.2017.04.005.
- [42] T. A. Sedrez, S. A. Shirazi, Y. R. Rajkumar, K. Sambath, H. J. Subramani, Experiments and CFD simulations of erosion of a 90° elbow in liquid-dominated liquid-solid and dispersed-bubble-solid flows, *Wear* 426-427 (2019) 570–580. URL: <https://doi.org/10.1016/j.wear.2019.01.015>. doi:10.1016/j.wear.2019.01.015.
- [43] B. Dooley, D. Lister, Flow-Accelerated Corrosion in Steam Generating Plants, *Powerpl. Chem.* 20 (2018) 194–244.
- [44] M. M. Stack, S. M. Abdelrahman, B. D. Jana, A new methodology for modelling erosion – corrosion regimes on real surfaces : Gliding down the galvanic series for a range of metal-corrosion systems, *Wear* 268 (2010) 533–542. URL: <http://dx.doi.org/10.1016/j.wear.2009.09.013>. doi:10.1016/j.wear.2009.09.013.

- [45] N. R. Sarker, L. Zhang, D. Breakey, B. A. Fleck, R. S. Sanders, Laboratory-Scale Erosive Wear Measurements Conducted with a Toroid Wear Tester (TWT), in: 8th Int. Conf. Transp. Sediment. Solid Part., September, 2017, pp. 295–303.
- [46] R. G. Gillies, C. A. Shook, Modelling high concentration slurry flows, *Can. J. Chem. Eng.* 78 (2000) 709–716. doi:[10.1002/cjce.5450780413](https://doi.org/10.1002/cjce.5450780413).
- [47] A. Bartosik, Influence of coarse-dispersive solid phase on the particles-wall shear stress in turbulent slurry flow with high solid concentration, *Arch. Mech. Eng.* LVII (2010) 1–16. URL: <http://yadda.icm.edu.pl/baztech/element/bwmeta1.element.baztech-article-BOS5-0024-0071>. doi:[10.2478/v10180-010-0003-1](https://doi.org/10.2478/v10180-010-0003-1).
- [48] A. Bragg, Development of the PDF kinetic approach for modelling inertial particle dispersion in turbulent boundary layers, Phd thesis, University of Nottingham Upon Tyne, 2011.
- [49] D. Besnard, F. Harlow, Turbulence in multiphase flow, *Int. J. Multiph. Flow* 14 (1988) 679–699. doi:[10.1016/0301-9322\(88\)90068-7](https://doi.org/10.1016/0301-9322(88)90068-7).
- [50] R. G. Gillies, C. A. Shook, J. Xu, Modelling Heterogeneous Slurry Flows at High Velocities, *Can. J. Chem. Eng.* 82 (2004) 1060–1065. doi:[10.1002/cjce.5450820523](https://doi.org/10.1002/cjce.5450820523).
- [51] M. Rhodes, Introduction to Particle Technology, second ed., John Wiley & Sons, Ltd., West Sussex, England, 2008. URL: <https://books.google.ca/books?id=P9Qgvh7kMP8C>.
- [52] R. S. Sanders, Fluid-Particle Systems and Application: Lecture notes, Technical Report, University of Alberta, Edmonton, Alberta, Canada, 2015.
- [53] C. A. Shook, M. C. Roco, Slurry flow: principles and practise, Butterworth-Heinemann, Boston, USA, 1991. doi:<http://dx.doi.org/10.1016/B978-0-7506-9110-9.50007-4>.
- [54] R. B. Spelay, S. A. Hashemi, R. G. Gillies, R. Hegde, R. S. Sanders, D. G. Gillies, Governing Friction Loss Mechanisms and the Importance of Off-Line Characterisation Test in the Pipeline Transport of Dense Coarse-Particle Slurries, in: ASME 2013 Fluids Eng. Div. Summer Meet., 2013, pp. V01CT20A013–V01CT20A013.

- [55] R. B. Spelay, R. G. Gillies, S. A. Hashemi, R. S. Sanders, Effect of pipe inclination on the deposition velocity of settling slurries, *Can. J. Chem. Eng.* 94 (2016) 1032–1039. doi:[10.1002/cjce.22493](https://doi.org/10.1002/cjce.22493).
- [56] R. G. Gillies, K. B. Hill, M. J. McKibben, C. A. Shook, Solids transport by laminar Newtonian flows, *Powder Technol.* 104 (1999) 269–277. doi:[10.1016/S0032-5910\(99\)00104-7](https://doi.org/10.1016/S0032-5910(99)00104-7).
- [57] K. C. Wilson, R. R. Horsley, T. Kealy, Direct prediction of fall velocities in non-Newtonian materials, *Int. J. Miner. Process.* 71 (2003) 17–30. doi:[10.1016/S0301-7516\(03\)00027-9](https://doi.org/10.1016/S0301-7516(03)00027-9).
- [58] K. C. Wilson, R. S. Sanders, R. G. Gillies, C. A. Shook, Verification of the near-wall model for slurry flow, *Powder Technol.* 197 (2010) 247–253. URL: <http://dx.doi.org/10.1016/j.powtec.2009.09.023>. doi:[10.1016/j.powtec.2009.09.023](https://doi.org/10.1016/j.powtec.2009.09.023).
- [59] J. Schaan, N. Cook, R. S. Sanders, On-line wear measurement for commercial-scale, coarse-particle slurry pipelines, in: 17th Int. Conf. Hydrotransp., Cape Town, South Africa, 2007, pp. 291–300.
- [60] P. Swamee, A. K. Jain, Explicit equations for pipe-flow problems, *ASCE J Hydraul Div* 102 (1976) 657–664.
- [61] S. W. Churchill, Friction factor equation spans all fluid flow regimes, *Chem. Eng. (New York)* 84 (1977) 91–92. URL: <https://www.scopus.com/inward/record.uri?eid=2-s2.0-0017769439{&}partnerID=40{&}md5=a878a518cf62db283094ff25416026fd>.
- [62] C. A. Shook, R. G. Gillies, R. S. Sanders, Pipeline hydrotransport: with applications in oil sand industry, SRC Pipe Flow Technology Centre, Saskatoon, Canada, 2002.
- [63] X. Song, Z. Xu, G. Li, Z. Pang, Z. Zhu, A new model for predicting drag coefficient and settling velocity of spherical and non-spherical particle in Newtonian fluid, *Powder Technol.* 321 (2017) 242–250. URL: <http://dx.doi.org/10.1016/j.powtec.2017.08.017>. doi:[10.1016/j.powtec.2017.08.017](https://doi.org/10.1016/j.powtec.2017.08.017).

- [64] A. Terfous, A. Hazzab, A. Ghenaim, Predicting the drag coefficient and settling velocity of spherical particles, *Powder Technol.* 239 (2013) 12–20. URL: <http://dx.doi.org/10.1016/j.powtec.2013.01.052>. doi:10.1016/j.powtec.2013.01.052.
- [65] G. Messa, S. Malavasi, Improvements in the numerical prediction of fully-suspended slurry flow in horizontal pipes, *Powder Technol.* 270 (2015) 358–367. URL: <http://dx.doi.org/10.1016/j.powtec.2014.10.027>. doi:10.1016/j.powtec.2014.10.027.
- [66] P. Doron, D. Barnea, Pressure drop and limit deposit velocity for solid-liquid flow in pipes, *Chem. Eng. Sci.* 50 (1995) 1595–1604. doi:10.1016/0009-2509(95)00024-Y.
- [67] A. D. Thomas, Predicting the deposit velocity for horizontal turbulent pipe flow of slurries, *Int. J. Multiph. Flow* 5 (1979) 113–129. doi:10.1016/0301-9322(79)90040-5.
- [68] R. S. Sanders, R. Sun, R. G. Gillies, M. J. McKibben, C. Litzenberger, C. A. Shook, Deposition velocities for particles of intermediate size in turbulent flow, in: *Hydrotransport*, volume 16, 2004, pp. 429–442.
- [69] K. C. Wilson, G. R. Addie, A. Sellgren, R. Clift, *Slurry Transport Using Centrifugal Pumps*, Springer ebook collection / Chemistry and Materials Science 2005-2008, Springer US, 2008. URL: <https://books.google.ca/books?id=YNEMPnBt-M0C>.
- [70] B. Bbosa, E. DelleCase, M. Volk, E. Ozbayoglu, A comprehensive deposition velocity model for slurry transport in horizontal pipelines, *J. Pet. Explor. Prod. Technol.* (2016). URL: <http://link.springer.com/10.1007/s13202-016-0259-1>. doi:10.1007/s13202-016-0259-1.
- [71] K. C. Wilson, J. K. P. Tse, Deposition limit for coarse particle transport in inclined pipes, in: *Proc. 9th Int. Conf. Hydraul. Transp. Solids Pipes*, 1984, pp. 149–161.
- [72] H. Hashimoto, K. Noda, T. Masuyama, T. Kawashima, Influence of pipe inclination on deposit velocity, in: *Proc. 7th Int. Conf. Hydraul. Transp. Solids Pipes*, 1980, pp. 231–244.
- [73] R. Durand, *Basic Relationships of the Transportation of Solids in Pipes-Experimental Research*, Intern. Assoc. Hydr. Res., 5th Congr. Minneapolis, 1953 (1953).

- [74] A. Gnanavelu, N. Kapur, A. Neville, J. F. Flores, N. Ghorbani, A numerical investigation of a geometry independent integrated method to predict erosion rates in slurry erosion, *Wear* 271 (2011) 712–719. URL: <http://dx.doi.org/10.1016/j.wear.2010.12.040>. doi:10.1016/j.wear.2010.12.040.
- [75] H. C. Meng, K. C. Ludema, Wear models and predictive equations: their form and content, *Wear* 181-183 (1995) 443–457. doi:10.1016/0043-1648(95)90158-2.
- [76] I. Finnie, Some Observations on the Erosion of Ductile Metals, *Wear* 19 (1972) 81–90.
- [77] I. Finnie, D. H. McFadden, On the velocity dependence of the erosion of ductile metals by solid particles at low angles of incidence, *Wear* 48 (1978) 181–190. URL: <http://www.sciencedirect.com/science/article/pii/0043164878901473>. doi:10.1016/0043-1648(78)90147-3.
- [78] Y. I. Oka, M. Nishimura, K. Nagahashi, M. Matsumura, Control and evaluation of particle impact conditions in a sand erosion test facility, *Wear* 250 (2001) 736–743.
- [79] Y. I. Oka, K. Okamura, T. Yoshida, Practical estimation of erosion damage caused by solid particle impact Part 1 : Effects of impact parameters on a predictive equation, *Wear* 259 (2005) 95–101. doi:10.1016/j.wear.2005.01.039.
- [80] M. C. Powers, A new roundness scale for sedimentary particles, *J. Sediment. Res.* 23 (1953) 117–119.
- [81] M. Parsi, D. N. V. Gl, H. Arabnejad, E/CRC, A. Al-sarkhi, K. Fahd, A New Correlation for Predicting Solid Particle Erosion Caused by Gas-Sand Flow in Elbows, in: *Offshore Technol. Conf.*, 2018.
- [82] DNV, Recommended Practise RP O501: Erosive Wear in Piping Systems, 2011.
- [83] C. Huang, S. Chiovelli, P. Mineev, J. Luo, K. Nandakumar, A comprehensive phenomenological model for erosion of materials in jet flow, *Powder Technol.* 187 (2008) 273–279. URL: <http://dx.doi.org/10.1016/j.powtec.2008.03.003>. doi:10.1016/j.powtec.2008.03.003.
- [84] I. M. Hutchings, A model for the erosion of metals by spherical particles at normal incidence, *Wear* 70 (1981) 269–281.

- [85] M. Melissa J., Wall Erosion in Slurry Pipelines, Phd, University of Saskatchewan, 1992.
- [86] H. M. Clark, L. C. Burmeister, The influence of the squeeze film on particle impact velocities in erosion, *Int. J. Impact Eng.* 12 (1992) 415–426. doi:[10.1016/0734-743X\(92\)90156-N](https://doi.org/10.1016/0734-743X(92)90156-N).
- [87] J. B. Zu, I. M. Ihtchings, G. T. Burstein, Design of a slurry erosion test rig, *Wear* 140 (1990) 331–344.
- [88] R. J. K. Wood, D. W. Wheeler, Design and performance of a high velocity air – sand jet impingement erosion facility, *Wear* 220 (1998) 95–112.
- [89] M. T. Benchaita, P. Griffith, E. Rabinowicz, Erosion of metallic plate by solid particles entrained in a liquid jet, *J. Eng. Ind.* 105 (1983) 215–222.
- [90] V. Javaheri, D. Porter, V.-t. Kuokkala, Slurry erosion of steel – Review of tests , mechanisms and materials, *Wear* 409 (2018) 248–273. doi:[10.1016/j.wear.2018.05.010](https://doi.org/10.1016/j.wear.2018.05.010).
- [91] A. Mansouri, S. A. Shirazi, B. S. Mclaury, FEDSM2014-21613 (2014) 1–10.
- [92] A. Mansouri, H. Arabnejad, S. A. Shirazi, B. S. Mclaury, A combined CFD / experimental methodology for erosion prediction, *Wear* 333 (2015) 1090–1097. URL: <http://dx.doi.org/10.1016/j.wear.2014.11.025>. doi:[10.1016/j.wear.2014.11.025](https://doi.org/10.1016/j.wear.2014.11.025).
- [93] A. Mansouri, A combined CFD-experimental method for developing an erosion equation for both gas-sand and liquid-sand flows, Phd thesis, University of Tulsa, 2016.
- [94] S. Karimi, A. Mansouri, B. S. Mclaury, S. A. Shirazi, Emperimental investigation oon the influence of particle size in a submerged slurry jet on erosion rates and pattermns, in: *Proc. ASME 2017 Fluids Eng. Div. Summer Meet.*, Hawaii, USA, 2019, pp. 1–11.
- [95] S. Karimi, S. Shirazi, B. Mclaury, Effects of Fluid Viscosity and Impingement Angle on Submerged Jet Flowfields, in: *Proc. ASME 2018 Fluids Eng. Div. Summer Meet.*, September, 2018, p. 83251. doi:[10.1115/FEDSM2018-83251](https://doi.org/10.1115/FEDSM2018-83251).

- [96] J. Owen, C. Ramsey, R. Barker, A. Neville, Erosion-corrosion interactions of X65 carbon steel in aqueous CO<sub>2</sub> environments, *Wear* 414-415 (2018) 376–389. URL: <https://doi.org/10.1016/j.wear.2018.09.004>. doi:10.1016/j.wear.2018.09.004.
- [97] A. Neville, C. Wang, Erosion – corrosion mitigation by corrosion inhibitors — An assessment of mechanisms, *Wear* 267 (2009) 195–203. doi:10.1016/j.wear.2009.01.038.
- [98] R. G. Gillies, R. Sun, M. Kosor, C. A. Shook, Laboratory Investigation of Inversion of Heavy Oil Emulsion, *Can. J. Chem. Eng.* 78 (2000) 757–763.
- [99] O. Urdahl, A. O. Fredheim, K. P. Loken, Viscosity measurements of water-in-crude-oil emulsions under flowing conditions: A theoretical and practical approach, *Colloids Surfaces A Physicochem. Eng. Asp.* 123-124 (1997) 623–634. doi:10.1016/S0927-7757(96)03801-0.
- [100] E. E. Johnsen, H. Fordedal, O. Urdahl, A simplified experimental approach for measuring viscosity for water-in-crude-oil emulsions under flowing conditions, *J. Dispers. Sci. Technol.* 22 (2001) 33–39.
- [101] S. T. Johansen, S. Mo, E. Meese, J. E. S. Oliveira, J. F. R. Reyes, J. N. E. Carneiro, CFD Simulations of Multiphase Flows Containing Large Scale Interfaces and Dispersed Phases with Selected Production Technology Applications, *OTC Bras.* (2015). URL: <http://www.onepetro.org/doi/10.4043/26303-MS>. doi:10.4043/26303-MS.
- [102] N. R. Sarker, M. A. Islam, R. S. Sanders, B. A. Fleck, CFD Analysis of the Hydrodynamics of an Air- Water Multiphase System in a Rotating Toroid Wheel, in: 23rd Annu. Conf. CFD Soc. Canada, April, Waterloo, ON, Canada, 2016.
- [103] R. C. Worster, D. F. Denny, Hydraulic transport of solid material in pipes, *Proc. Inst. Mech. Eng.* 169 (1955) 563–586.
- [104] V. V. Traynis, Parameters and flow regimes for hydraulic transport of coal by pipelines, Terraspace, Rockville. USA, 1977.
- [105] G. Henday, A comparison of commercial pipe materials intended for the hydraulic transport of solids, BHRA, 1988.

- [106] J. Blazek, Computational fluid dynamics: principles and applications, Elsevier publishing, 2001.
- [107] C. D. Rielly, J. Gimbut, Computational fluid mixing, in: Food Mix., Blackwell Publishing Ltd., Oxford, UK, 2009, pp. 125–174.
- [108] O. E. Adedeji, Computational fluid dynamics modelling of a left ventricular assist device, Msc, Loughborough University, 2014.
- [109] C. A. J. Fletcher, Computational techniques for fluid dynamics 1 (1988).
- [110] A. Ekambara, R. S. Sanders, K. Nandakumar, J. H. Masliyah, Hydrodynamic simulation of horizontal slurry pipeline flow using ANSYS-CFX, Ind. Eng. Chem. Res. 48 (2009) 8159–8171. doi:10.1021/ie801505z.
- [111] R. B. Bird, W. E. Stewart, E. N. Lightfoot, Transport phenomena. 1960, Madison, USA (1960).
- [112] H. K. Versteeg, W. Malalasekera, Computational fluid dynamics, finite Vol. method (1995).
- [113] A. Sayma, Computational Fluid Dynamics, 2009.
- [114] ANSYS, ANSYS 17.0 Theory Guide, Technical Report, 2017. URL: <https://www.sharcnet.ca/Software/Ansys/17.0/en-us/help/flu{ }th/flu{ }th.html>.
- [115] S. B. Pope, Turbulent Flows, Cambridge University Press, 2000. URL: <https://books.google.ca/books?id=HZsTw9SMx-0C>.
- [116] D. Choudhury, Introduction to the Renormalization Group Method and Turbulence Modeling, Technical memorandum, Fluent Incorporated, 1973. URL: <https://books.google.ca/books?id=mKWEQwAACAAJ>.
- [117] B. J. Daly, F. H. Harlow, Transport equations in turbulence, Phys. Fluids 13 (1970) 2634–2649.
- [118] F.-S. Lien, M. A. Leschziner, Assessment of turbulence-transport models including non-linear RNG eddy-viscosity formulation and second-moment closure for flow over a backward-facing step, Comput. Fluids 23 (1994) 983–1004.

- [119] M. M. Gibson, B. E. Launder, Ground effects on pressure fluctuations in the atmospheric boundary layer, *J. Fluid Mech.* 86 (1978) 491–511.
- [120] B. E. Launder, Second-moment closure and its use in modelling turbulent industrial flows, *Int. J. Numer. Methods Fluids* 9 (1989) 963–985.
- [121] S. Sarkar, L. Balakrishnan, Application of a Reynolds stress turbulence model to the compressible shear layer, in: *21st Fluid Dyn. Plasma Dyn. Lasers Conf.*, 1990, p. 1465.
- [122] G. H. Yeoh, J. Tu, *Computational techniques for multiphase flows*, Elsevier, 2009.
- [123] F. N. Krampa, *Two-Fluid Modelling of Heterogeneous Coarse Particles Slurry Flow*, Ph.D. thesis, University of Saskatchewan, 2009. doi:10.1017/CB09781107415324.004. arXiv:arXiv:1011.1669v3.
- [124] A. Abdulla, *Estimating Erosion in Oil and Gas Pipeline due to Sand Presence*, Msc, Blekinge Institute of Technology, Sweden, 2011.
- [125] R. Silva, F. A. P. Garcia, P. Faia, M. G. Rasteiro, Modelling Solid-Liquid Homogeneous Turbulent Flow of Neutrally Buoyant Particles using Mixture Model : A Study of Length scale and Closure Coefficients, *Multiph. Sci. Technol.* 26 (2014) 199–227.
- [126] G. J. Brown, Erosion prediction in slurry pipeline tee-junctions, *Appl. Math. Model.* 26 (2002) 155–170. URL: <http://www.sciencedirect.com/science/article/pii/S0307904X01000531>. doi:10.1016/S0307-904X(01)00053-1.
- [127] A. Vié, H. Pouransari, R. Zamansky, A. Mani, Particle-laden flows forced by the disperse phase: Comparison between Lagrangian and Eulerian simulations, *Int. J. Multiph. Flow* 79 (2016) 144–158. doi:10.1016/j.ijmultiphaseflow.2015.10.010.
- [128] D. R. Kaushal, T. Thinglas, Y. Tomita, S. Kuchii, H. Tsukamoto, CFD modeling for pipeline flow of fine particles at high concentration, *Int. J. Multiph. Flow* 43 (2012) 85–100. URL: <http://dx.doi.org/10.1016/j.ijmultiphaseflow.2012.03.005>. doi:10.1016/j.ijmultiphaseflow.2012.03.005.
- [129] C. M. Perez, *CFD Modelling of Laminar, Open-Channel Flows of Non-Newtonian Slurries*, Msc, University of Alberta, 2017.

- [130] F. Pourahmadi, J. A. C. Humphrey, Modelling solid-fluid turbulent flows with application to predicting erosive wear, *Math. Model.* 6 (1985) 82 –. URL: <http://www.sciencedirect.com/science/article/pii/0270025585900296>. doi:[http://dx.doi.org/10.1016/0270-0255\(85\)90029-6](http://dx.doi.org/10.1016/0270-0255(85)90029-6).
- [131] C. K. K. Lun, S. B. Savage, D. J. Jeffrey, N. Chepurniy, Kinetic theories for granular flow: inelastic particles in Couette flow and slightly inelastic particles in a general flowfield, *J. Fluid Mech.* 140 (1984) 223–256.
- [132] D. Gidaspow, R. Bezburuah, J. Ding, Hydrodynamics of circulating fluidized beds: kinetic theory approach, in: 7th Int. Conf. Fluid., Illinois Inst. of Tech., Chicago, IL (United States). Dept. of Chemical Engineering, Gold Coast, Australia, 1991.
- [133] L. Chen, Y. Duan, W. Pu, C. Zhao, CFD simulation of coal-water slurry flowing in horizontal pipelines, *Korean J. Chem. Eng.* 26 (2009) 1144–1154. doi:[10.1007/s11814-009-0190-y](https://doi.org/10.1007/s11814-009-0190-y).
- [134] G. V. Messa, G. Ferrarese, S. Malavasi, A mixed Euler-Euler/Euler-Lagrange approach to erosion prediction, *Wear* 342-343 (2015) 138–153. URL: <http://dx.doi.org/10.1016/j.wear.2015.08.015>. doi:[10.1016/j.wear.2015.08.015](https://doi.org/10.1016/j.wear.2015.08.015).
- [135] G. V. Messa, S. Malavasi, A CFD-based method for slurry erosion prediction, *Wear* 398-399 (2018) 127–145. URL: <https://doi.org/10.1016/j.wear.2017.11.025>. doi:[10.1016/j.wear.2017.11.025](https://doi.org/10.1016/j.wear.2017.11.025).
- [136] G. P. Saffman, The Lift on a Small Sphere in a Slow Shear, *J. Fluid Mech.* 22 (1965) 385–400.
- [137] A. Li, G. Ahmadi, Dispersion and Deposition of Spherical Particles from Point Sources in a Turbulent Channel Flow, *Aerosol Sci. Technol.* 16 (1992) 209–226.
- [138] B. Oesterlé, T. Bui Dinh, Experiments on the Lift of a Spinning Sphere in the Range of Intermediate Reynolds Numbers, *Exp. Fluids* 25 (1998) 16–22.
- [139] S. A. Morsi, A. J. Alexander, An Investigation of Particle Trajectories in Two-Phase Flow Systems, *J. Fluid Mech.* 55 (1972) 193–208.

- [140] E. K. Vakkilainen, M. Garcia Perez, T. Happanen, A brief overview of the drag laws used in the Lagrangian tracking of ash trajectories for boiler fouling CFD models, in: 26th Int. Conf. Impact Fuel Qual. Power Prod., September, Prague, 2016.
- [141] A. J. Karabelas, An Experimental Study of Pipe Erosion by Turbulent Slurry Flow, in: Proc. Hydrotransp. 5, May, Hannover, Germany, 1978, pp. 25–24.
- [142] V. B. Nguyen, Q. B. Nguyen, Z. G. Liu, S. Wan, C. Y. H. Lim, Y. W. Zhang, A combined numerical – experimental study on the effect of surface evolution on the water – sand multiphase flow characteristics and the material erosion behavior, *Wear* 319 (2014) 96–109. URL: <http://dx.doi.org/10.1016/j.wear.2014.07.017>. doi:10.1016/j.wear.2014.07.017.
- [143] B. K. Gandhi, S. Singh, V. Seshadri, Study of the parametric dependence of erosion wear for the parallel flow of solid – liquid mixtures, *Tribol. Int.* 32 (1999) 275–282.
- [144] W. Tsai, J. A. Humphrey, I. Cornet, A. V. Levy, Experimental measurement of accelerated erosion in a slurry pot tester, *Wear* 68 (1981) 289–303. doi:10.1016/0043-1648(81)90178-2.
- [145] J. F. Roca, J. N. E. Carneiro, J. E. S. Oliveira, S. Mo, M. Fossen, S. T. Johansen, CFD Simulation of The Two-Phase Flow of Different Mixtures in a Closed System Flow Wheel, in: 10th Int. Conf. CFD Oil Gas, Metallurgical Process Ind., June, SINTEF, Trondheim, Norway, 2014, pp. 253–259.
- [146] B. R. Munson, A. P. Rothmayer, T. H. Okiishi, *Fundamentals of Fluid Mechanics*, 7th Edition, Wiley, 2012. URL: <https://books.google.ca/books?id=GQMCAAAAQBAJ>.
- [147] B. E. Launder, G. J. Reece, W. Rodi, Progress in the development of a Reynolds-stress turbulence closure, *J. Fluid Mech.* 68 (1975) 537–566. doi:10.1017/S0022112075001814.
- [148] S. Jain, N. Singhal, S. N. Shah, Effect of Coiled Tubing Curvature on Friction Pressure Loss of Newtonian and Non-Newtonian Fluids - Experimental and Simulation Study, in: SPE Annu. Tech. Conf. Exhib., Society of Petroleum Engineers, Houston, Texas, 2004, p. 12. URL: <https://doi.org/10.2118/90558-MS>. doi:10.2118/90558-MS.

- [149] Y. Zhou, S. Shah, Fluid flow in coiled tubing: a literature review and experimental investigation, *J. Can. Pet. Technol.* 43 (2004).
- [150] M. C. Roco, G. R. Addie, Erosion wear in slurry pumps and pipes, *Powder Technol.* 50 (1987) 35–46. doi:10.1016/0032-5910(87)80081-5.
- [151] M. C. Roco, Wear Mechanisms in Centrifugal Slurry Pumps, *Corros. Eng.* 46 (1990) 424–431.
- [152] N. Barkoula, J. Karker-Kocsis, Processes and influencing parameters of the solid particle erosion of polymers and their composites, *J. Mater. Sci.* 37 (2002) 3807–3820. doi:10.1023/A.arXiv:0005074v1.
- [153] K. F. Adane, M. Huard, A. Fuhr, Modeling Abrasion-Corrosion in Horizontal Pipeline Slurry Flows, 2019. URL: <https://doi.org/>.
- [154] P. Rizkalla, D. F. Fletcher, Development of a Slurry Abrasion Model Using an Eulerian-Eulerian ‘Two-Fluid’ Approach, in: *Elev. Int. Conf. CFD Miner. Process Ind. CSIRO*, December, Melbourne, Australia, 2015, pp. 1–8.
- [155] G. Yang, D. Serate, K. Tsai, M. Wu, Wear Modeling of Dense Slurry Flow in Oil Sands Coarse Tailings (CT) Pipelines, 2018. URL: <https://doi.org/>.
- [156] Y. I. Oka, T. Yoshida, Practical estimation of erosion damage caused by solid particle impact Part 2 : Mechanical properties of materials directly associated with erosion damage, *Wear* 259 (2005) 102–109. doi:10.1016/j.wear.2005.01.040.
- [157] A. D. Burns, T. Frank, I. Hamill, J. M. Shi, The Favre averaged drag model for turbulent dispersion in Eulerian multi-phase flows, in: *5th Int. Conf. Multiph. Flow*, 392, Yokohama, Japan, 2004, pp. 1–17. URL: [http://www.drthfrank.de/publications/2004/Burns\\_{\\_}Frank\\_{\\_}ICMF\\_{\\_}2004\\_{\\_}final.pdf](http://www.drthfrank.de/publications/2004/Burns_{_}Frank_{_}ICMF_{_}2004_{_}final.pdf).
- [158] K. C. Wilson, A. Sellgren, Interaction of Particles and Near-Wall Lift in Slurry Pipelines (2003) 73–77.
- [159] F. A. Bikbaev, V. I. Krasnov, M. Z. Maksimenko, V. L. Berezin, I. B. Zhilinski, N. T. Otroshko, Main factors affecting gas abrasive wear of elbows in pneumatic conveying

- pipes, *Chem. Pet. Eng.* 9 (1973) 73–75. URL: <https://doi.org/10.1007/BF01139742>. doi:10.1007/BF01139742.
- [160] X. Song, P. Luo, S. Luo, S. Huang, Numerical simulation study on the influence of incident position on erosion characteristics of gas-particle two-phase flow in 90 degree elbow, *Adv. Mech. Eng.* 9 (2017) 1–18. doi:10.1177/1687814017733249.
- [161] A. T. Bourgoyne, Experimental Study of Erosion in Diverter Systems Due to Sand Production, *Soc. Pet. Eng.* (1989). doi:doi:10.2118/18716-MS.
- [162] K. Jordan, Erosion in Multiphase Production of Oil & Gas, in: *Corrosion, NACE International*, 1998.
- [163] Z. Johar, M. Jadid, P. Carigali, S. N. A. Shaffee, M. S. A. Zamberi, Experimental and CFD Erosion Modelling of Large Radius Pipe Elbows in, in: *Int. Pet. Technol. Conf.*, Kuala Lumpur, Malaysia, 2014, pp. 1–13.
- [164] M. Zamani, S. Seddighi, H. R. Nazif, Erosion of natural gas elbows due to rotating particles in turbulent gas-solid flow, *J. Nat. Gas Sci. Eng.* 40 (2017) 91–113. URL: <http://dx.doi.org/10.1016/j.jngse.2017.01.034>. doi:10.1016/j.jngse.2017.01.034.
- [165] S. C. R. Dennis, S. N. Singh, D. B. Ingham, The Steady Flow Due to Rotating Sphere at Low and Moderate Reynolds Numbers, *J. Fluid Mech.* 101 (1980) 257–279.
- [166] G. Grant, W. Tabakoff, Erosion Prediction in Turbomachinery Resulting from Environmental Solid Particles, *J. Aircr. - J Aircr.* 12 (1975) 471–478.
- [167] G. Haider, H. Arabnejad, S. A. Shirazi, B. S. Mclaury, A mechanistic model for stochastic rebound of solid particles with application to erosion predictions, *Wear* 376-377 (2017) 615–624. URL: <http://dx.doi.org/10.1016/j.wear.2017.02.015>. doi:10.1016/j.wear.2017.02.015.
- [168] M. Sommerfeld, N. Huber, Experimental analysis of modelling of particle-wall collisions, *Int. J. Multiph. Flow* 25 (1999) 1457–1489.
- [169] P. Patro, S. K. Dash, Prediction of acceleration length in turbulent gas – solid flows, *Adv. Powder Technol.* 25 (2014) 1643–1652. URL: <http://dx.doi.org/10.1016/j.apt.2014.05.019>. doi:10.1016/j.apt.2014.05.019.

- [170] M. Sommerfeld, S. Lain, Parameters Influencing Dilute - Phase Pneumatic Conveying Through Pipe Systems: A Computational Study by the Euler/Lagrange Approach, *Can. J. Chem. Eng.* 93 (2015) 1–17. doi:[10.1002/cjce.22105](https://doi.org/10.1002/cjce.22105).
- [171] N. Huber, M. Sommerfeld, Characterization of the cross-sectional particle concentration distribution in pneumatic conveying systems, *Powder Technol.* 79 (1994) 191–210.
- [172] C. A. R. Duarte, F. J. de Souza, V. F. dos Santos, Numerical investigation of mass loading effects on elbow erosion, *Powder Technol.* 283 (2015) 593–606. URL: <http://dx.doi.org/10.1016/j.powtec.2015.06.021>. doi:[10.1016/j.powtec.2015.06.021](https://doi.org/10.1016/j.powtec.2015.06.021).
- [173] G. C. Pereira, F. J. de Souza, D. A. de Moro Martins, Numerical prediction of the erosion due to particles in elbows, *Powder Technol.* 261 (2014) 105–117. URL: <http://dx.doi.org/10.1016/j.powtec.2014.04.033>. doi:[10.1016/j.powtec.2014.04.033](https://doi.org/10.1016/j.powtec.2014.04.033).
- [174] A. Uzi, Y. Ben Ami, A. Levy, Erosion prediction of industrial conveying pipelines, *Powder Technol.* 309 (2017) 49–60. URL: <http://dx.doi.org/10.1016/j.powtec.2016.12.087>. doi:[10.1016/j.powtec.2016.12.087](https://doi.org/10.1016/j.powtec.2016.12.087).
- [175] L. Xu, Q. Zhang, J. Zheng, Y. Zhao, Numerical prediction of erosion in elbow based on CFD-DEM simulation, *Powder Technol.* 302 (2016) 236–246. URL: <http://dx.doi.org/10.1016/j.powtec.2016.08.050>. doi:[10.1016/j.powtec.2016.08.050](https://doi.org/10.1016/j.powtec.2016.08.050).
- [176] ANSYS, ANSYS Fluent UDF Manual, Technical Report, 2013.
- [177] E. I. Nduagu, I. D. Gates, Process analysis of a low emissions hydrogen and steam generation technology for oil sands operations, *Appl. Energy* 146 (2015) 184–195. URL: <http://dx.doi.org/10.1016/j.apenergy.2015.01.118>. doi:[10.1016/j.apenergy.2015.01.118](https://doi.org/10.1016/j.apenergy.2015.01.118).
- [178] K.-w. Gwak, W. Bae, A Review of Steam Generation for In-Situ Oil Sands Projects, *Geosystems Eng.* 13 (2012) 11–118. doi:[10.1080/12269328.2010.10541317](https://doi.org/10.1080/12269328.2010.10541317).
- [179] A. Malik, A. Meroufel, Boiler Tubes Failures : A Compendium of Case Studies, *J. J. Anal. Preven.* 15 (2015) 246–250. doi:[10.1007/s11668-015-9923-x](https://doi.org/10.1007/s11668-015-9923-x).
- [180] M. R. Godfrey, P. Desch, L. Larocque, Erosion-Corrosion in Oil Field Once Through Steam Generators, in: 70th Annu. Int. Water Conf., volume 14, 2009, pp. 842–859.

- [181] V. Kain, Flow Accelerated Corrosion : Forms , Mechanisms and Case Studies, *Procedia Eng.* 86 (2014) 576–588. URL: <http://dx.doi.org/10.1016/j.proeng.2014.11.083>. doi:10.1016/j.proeng.2014.11.083.
- [182] R. E. Vieira, A. Mansouri, B. S. McLaury, S. A. Shirazi, Experimental and computational study of erosion in elbows due to sand particles in air flow, *Powder Technol.* 288 (2016) 339–353. URL: <http://dx.doi.org/10.1016/j.powtec.2015.11.028>. doi:10.1016/j.powtec.2015.11.028.
- [183] S. Shirazi, B. McLaury, J. Shadley, E. Rybicki, Generalization of the API RP 14E Guideline for erosive services, *J. Pet. Technol.* (1995) 693–698. doi:10.2118/28518-PA.
- [184] H. Arabnejad, S. A. Shirazi, B. S. Mclaury, J. R. Shadley, T. Erosion, Calculation of Erosional Velocity Due to Liquid Droplets with Application to Oil and Gas Industry Production, in: *SPE Annu. Tech. Conf. Exhib.*, volume SPE 166423, New Orleans, USA, 2013.
- [185] M. Salama, E. Venkatesh, Evaluation of API RP 14E Erosional Velocity Limitations for Offshore Gas Wells, in: *Ofsshore Tecgnology Conf.*, 1983, pp. 371–376. doi:10.4043/4485-ms.
- [186] F. Madani Sani, S. Huizinga, K. A. Esaklul, S. Nestic, Review of the API RP 14E erosional velocity equation: Origin, applications, misuses, limitations and alternatives, *Wear* 426-427 (2019) 620–636. URL: <https://doi.org/10.1016/j.wear.2019.01.119>. doi:10.1016/j.wear.2019.01.119.
- [187] B. S. McLaury, S. A. Shirazi, An Alternate Method to API RP 14E for Predicting Solids Erosion in Multiphase Flow, *J. Energy Resour. Technol.* 122 (2002) 115. doi:10.1115/1.1288209.
- [188] K. K. Botros, L. Jensen, S. Foo, Determination of erosion-based maximum velocity limits in natural gas facilities, *J. Nat. Gas Sci. Eng.* 55 (2018) 395–405. URL: <https://doi.org/10.1016/j.jngse.2018.05.013>. doi:10.1016/j.jngse.2018.05.013.
- [189] S. A. Hashemi, A. Sadighian, S. I. A. Shah, R. S. Sanders, Solid velocity and concentration fluctuations in highly concentrated liquid–solid (slurry) pipe flows, *Int. J.*

- Multiph. Flow 66 (2014) 46–61. URL: <http://linkinghub.elsevier.com/retrieve/pii/S0301932214001153>. doi:10.1016/j.ijmultiphaseflow.2014.06.007.
- [190] A. Aguilar-Corona, R. Zenit, O. Masbernat, Collisions in a liquid fluidized bed, Int. J. Multiph. Flow 37 (2011) 695–705. URL: <http://dx.doi.org/10.1016/j.ijmultiphaseflow.2011.02.004>. doi:10.1016/j.ijmultiphaseflow.2011.02.004.

# Appendices

## Experimental Data

### A.1 Liquid-related torque data

Table A.1: Liquid-only torque data: water

Speed, N ( <i>RPM</i> )	Viscosity, $\mu$ ( <i>mPa · s</i> )	Density, $\rho$ ( <i>kg/m<sup>3</sup></i> )	Torque, T ( <i>Nm</i> )
10	1	998	0.035
20			0.085
30			0.140
40			0.216
50			0.308
60			0.418
80			0.694
90			0.822

Table A.2: Liquid-only torque data: 20% corn syrup-water mixture

Speed, N ( <i>RPM</i> )	Viscosity, $\mu$ ( <i>mPa · s</i> )	Density, $\rho$ ( <i>kg/m<sup>3</sup></i> )	Torque, T ( <i>Nm</i> )
10	2.75	1072	0.034
20			0.077
30			0.147
40			0.239
50			0.369
60			0.526
80			0.872
90			1.104

Table A.3: Liquid-only torque data: 35% corn syrup-water mixture

Speed, N ( <i>RPM</i> )	Viscosity, $\mu$ ( <i>mPa · s</i> )	Density, $\rho$ ( <i>kg/m<sup>3</sup></i> )	Torque, T ( <i>Nm</i> )
10	5.28	1128	0.063
20			0.118
30			0.210
40			0.321
50			0.468
60			0.651
80			1.072
90			1.361

Table A.4: Liquid-only torque data: 20% glycerin-water mixture

Speed, N ( <i>RPM</i> )	Viscosity, $\mu$ ( <i>mPa · s</i> )	Density, $\rho$ ( <i>kg/m<sup>3</sup></i> )	Torque, T ( <i>Nm</i> )
10	2.27	1050	0.060
20			0.101
30			0.161
40			0.235
50			0.343
60			0.460
80			0.790
90			0.985

Table A.5: Liquid-only torque data: 40% glycerin-water mixture

Speed, N (RPM)	Viscosity, $\mu$ (mPa·s)	Density, $\rho$ (kg/m <sup>3</sup> )	Torque, T (Nm)
10	5.12	1103	0.077
20			0.123
30			0.190
40			0.283
50			0.409
60			0.558
80			0.910
90			1.146

## A.2 Solid-related torque data

Table A.6: Solid-related torque data (Nm): 4 mm gravel in water (1 mPa·s)

N (RPM)	C=10%	C=15%	C=20%
10	0.662	1.063	1.559
20	0.655	1.075	1.655
30	0.658	1.053	1.613
40	0.664	1.043	1.521
45	0.6675	1.0465	1.5015
50	0.672	1.061	1.511
60	0.683	1.096	1.551
80	0.717	1.182	1.679
90	0.735	1.222	1.737

Table A.7: Solid-related torque data (Nm): 2 mm gravel in water (1 mPa·s)

N (RPM)	C=10%	C=15%	C=20%
10	0.647	1.081	1.645
20	0.642	1.051	1.697
30	0.659	1.072	1.635
40	0.661	1.035	1.531
50	0.664	1.006	1.439
60	0.644	0.984	1.394
80	0.615	1.041	1.481
90	0.612	1.042	1.482

Table A.8: Solid-related torque data (Nm): 1 mm gravel in water (1 mPa·s)

N (RPM)	C=10%	C=15%	C=20%
10	0.673	1.053	1.725
20	0.666	1.028	1.713
30	0.661	1.018	1.627
40	0.641	0.982	1.539
50	0.606	0.927	1.34
60	0.569	0.858	1.187
80	0.563	0.913	1.329
90	0.544	0.902	1.278

Table A.9: Solid-related torque data (Nm): 0.425 mm sand in water (1 mPas)

N (RPM)	C=10%	C=15%	C=20%
10	0.634	1.007	1.6446
20	0.55	0.878	1.192
30	0.49	0.794	0.897
40	0.457	0.723	0.878
50	0.394	0.667	0.816
60	0.313	0.455	0.696
80	0.197	0.389	0.483
90	0.194	0.326	0.469

Table A.10: Solid-related torque data (Nm): 0.250 mm sand in water (1 mPa·s)

N (RPM)	C=10%	C=15%	C=20%
10	0.601	0.792	1.212
20	0.484	0.615	0.812
30	0.424	0.537	0.686
40	0.37	0.448	0.528
50	0.306	0.31	0.339
60	0.223	0.249	0.315
80	0.161	0.298	0.348
90	0.162	0.295	0.375

Table A.11: Solid-related torque data (Nm): 0.125 mm sand in water (1 mPa·s)

N (RPM)	C=10%	C=15%	C=20%
10	0.137	0.176	0.197
20	0.058	0.063	0.06
30	0.013	0.027	0.039
40	0.013	0.041	0.063
50	0.044	0.078	0.116
60	0.067	0.107	0.16
80	0.132	0.181	0.257
90	0.146	0.218	0.301

Table A.12: Solid-related torque data (Nm): 4 mm gravel in 20% glycerin-water mixture (2.3 mPa·s)

N (RPM)	C=10%	C=15%	C=20%
10	0.608	1.002	1.511
20	0.618	1.02	1.606
30	0.629	0.998	1.561
40	0.647	1.004	1.464
45	0.6595	1.0145	1.4485
50	0.673	1.033	1.455
60	0.69	1.079	1.503
80	0.695	1.133	1.595
90	0.685	1.144	1.619

Table A.13: Solid-related torque data (Nm): 2 mm gravel in 20% glycerin-water mixture (2.3 mPa·s)

N (RPM)	C=10%	C=15%	C=20%
10	0.688	1.068	1.522
20	0.654	0.997	1.478
30	0.625	0.983	1.385
40	0.64	0.983	1.261
50	0.661	0.983	1.252
60	0.688	1.026	1.325
80	0.677	1.063	1.367
90	0.66	1.036	1.324

Table A.14: Solid-related torque data (Nm): 1 mm gravel in 20% glycerin-water mixture (2.3 mPa·s)

N (RPM)	C=10%	C=15%	C=20%
10	0.615	1.043	1.678
20	0.627	1.003	1.605
30	0.604	0.949	1.477
40	0.58	0.867	1.251
50	0.576	0.839	1.115
60	0.586	0.878	1.191
80	0.545	0.831	1.136
90	0.507	0.748	0.993

Table A.15: Solid-related torque data (Nm): 0.425 mm sand in 20% glycerin-water mixture (2.3 mPa·s)

N (RPM)	C=10%	C=15%	C=20%
10	0.505	0.884	1.524
20	0.423	0.591	0.788
30	0.375	0.52	0.661
40	0.369	0.487	0.615
50	0.318	0.413	0.458
60	0.27	0.319	0.361
80	0.19	0.265	0.341
90	0.159	0.241	0.332

Table A.16: Solid-related torque data (Nm): 0.250 mm sand in 20% glycerin-water mixture (2.3 mPa·s)

N (RPM)	C=10%	C=15%	C=20%
10			0.754
20			0.449
30			0.323
40			0.192
50			0.193
60			0.231
80			0.277
90			0.279

Table A.17: Solid-related torque data (Nm): 0.125 mm sand in 20% glycerin-water mixture (2.3 mPa·s)

N (RPM)	C=10%	C=15%	C=20%
10			0.069
20			0.018
30			0.021
40			0.061
50			0.115
60			0.188
80			0.276
90			0.331

Table A.18: Solid-related torque data (Nm): 2 mm gravel in 40% glycerin-water mixture (5.12 mPa·s)

N (RPM)	C=10%	C=15%	C=20%
10	0.6047	0.953	1.546
20	0.615	0.935	1.489
30	0.586	0.847	1.265
40	0.588	0.825	1.149
50	0.595	0.855	1.203
60	0.588	0.86	1.223
80	0.557	0.825	1.152
90	0.507	0.755	1.046

Table A.19: Solid-related torque data (Nm): 1 mm gravel in 40% glycerin-water mixture (5.12 mPa·s)

N (RPM)	C=10%	C=15%	C=20%
10	0.574	1.052	1.676
20	0.534	0.976	1.532
30	0.509	0.759	1.123
40	0.516	0.792	1.007
50	0.52	0.831	1.074
60	0.498	0.795	1.028
80	0.451	0.672	0.853
90	0.404	0.597	0.742

Table A.20: Solid-related torque data (Nm): 0.425 mm sand in 40% glycerin-water mixture (5.12 mPa·s)

N (RPM)	C=10%	C=15%	C=20%
10	0.411	0.582	0.746
20	0.313	0.417	0.469
30	0.278	0.399	0.37
40	0.2	0.277	0.277
50	0.17	0.246	0.264
60	0.164	0.254	0.284
80	0.207	0.307	0.376
90	0.2	0.277	0.385

Table A.21: Solid-related torque data (Nm): 0.250 mm sand in 40% glycerin-water mixture (5.12 mPa·s)

N (RPM)	C=10%	C=15%	C=20%
10	0.269		0.405
20	0.199		0.251
30	0.106		0.158
40	0.072		0.143
50	0.093		0.176
60	0.114		0.234
80	0.174		0.338
90	0.174		0.365

Table A.22: Solid-related torque data (Nm): 20% v/v 2 mm glass beads

RPM	Water, 1 mPa·s	40% Water-Glycerine, 5.12 mPa·s
10	1.1	0.954
20	1.056	1.013
30	1.086	0.913
40	1.097	0.876
50	1.088	0.882
60	1.082	0.834
80	1.135	0.81
90	1.114	0.759

Table A.23: Solid-related torque data (Nm): 20% v/v 0.425  $Al_2O_3$  in 40% glycerine-water mixture(5.12 mPa·s)

RPM	T (Nm)
10	1.592
20	0.713
30	0.490
40	0.378
50	0.420
60	0.471
80	0.665
90	0.727

### A.3 TWT experimental wear data

Table A.24: Experimental wear data- New data plus data from Sarker (2016) and Zhang (2018)

$\rho_f$ ( $kg/m^3$ )	$\mu_f$ (mPa·s)	N (RPM)	C (v/v)	$d_p$ (mm)	ER (mm/yr)
998	1.00	30	0.1	1.000	0.200
998	1.00	30	0.15	1.000	0.199
998	1.00	30	0.2	1.000	0.480
998	1.00	30	0.1	2.000	0.190
998	1.00	30	0.15	2.000	0.316
998	1.00	30	0.2	2.000	0.475
998	1.00	30	0.15	2.000	0.329
998	1.00	30	0.2	2.000	0.475
998	1.00	30	0.2	0.420	0.079
998	1.00	45	0.2	4.000	2.180
998	1.00	45	0.1	4.000	1.870
1050	2.27	45	0.2	4.000	2.270
998	1.00	45	0.1	2.000	0.850
998	1.00	45	0.2	1.000	0.240
998	1.00	45	0.1	1.000	0.180
998	1.00	45	0.2	2.000	1.000
998	1.00	60	0.2	2.000	1.929
998	1.00	60	0.2	2.000	1.929
998	1.00	60	0.15	1.000	1.399
998	1.00	60	0.2	4.000	4.990
998	1.00	60	0.1	4.000	3.810
1050	2.27	60	0.2	4.000	4.750
998	1.00	60	0.1	0.250	0.015
998	1.00	60	0.15	0.420	0.136
998	1.00	60	0.1	0.420	0.075
998	1.00	60	0.2	0.420	0.129
1050	2.27	90	0.2	4.000	9.955
1050	2.27	90	0.1	4.000	6.290
998	1.00	90	0.2	4.000	10.220
998	1.00	90	0.1	4.000	7.180
1050	2.27	90	0.15	4.000	7.970
998	1.00	90	0.15	4.000	9.070

# Appendix B

## MATLAB codes

### B.1 SRC Two-Layer Model Code

This Appendix present the MATLAB code to implement the solution algorithm for the SRC two-layer model. The first code is the function file while the second code will be the run file. This will be followed by other function file which are called upon in the main/first code.

#### Function file code for SRC Two-Layer Model

---

```
1 %Function file for SRC two layer model solution algorithm
2 %This is the main funtion code which will call upon other subfunction ...
   in order to executue the algorithm
3 %Written by Oluwaseun E. Adedeji
4 %Copyright 2016
5 function [tauSRC,dPdzSRC,Vc,taulk,tau2k,tauc]=...
6 srctwolayer(U,D,d12,d50,Cr,Cmax,Cf,rhos,rhol,mul,k,g,nus)
7 %fines plus in-situ solids concentration
8 Ct=Cf+Cr;
9 %bulk fluid density in the presence of fines
10 rhof=(rhol*(1-Ct)+rhos*Cf)./(1-Ct+Cf);
11 %bulk fuilid viscosity using Thomas(1965) method
12 muf=thomasmu(Cf,mul);
13 %deposition velocity, see function below
```

```

14 Vc=dvelocity(d50,rhof,rhos,muf,g,D);
15 %terminal settling velocity, see function below
16 Vinf=terminalvelocity(d50,rhof,rhos,muf,g);
17 %layer 2 or limiting concentration correlation
18 C2= Cmax-(Cmax-Cr).*(0.074*(U./Vinf).^0.44).*(1-Cr).^0.189;
19 %contact load fraction correlation
20 Cc=Cr*exp((-0.062.*(U./Vinf).^0.81).*(sqrt(g.*D.*(rhos/rhof-1))./U).^0.38);
21
22 %Solution calculation begins
23 C1=Cr-Cc; %layer 1 solids concentration
24 rho1=rhof*(1-C1)+rhos*C1;
25 rho2f=(rhof*(1-C2)+rhos*C1)./(1-C2+C1);
26 A=pi.*(D.^2)/4;
27 A2=Cc.*A./(C2-C1); %bottom layer cross sectional area
28 A1=A-A2; %top layer cross sectional area
29 %Solving for beta. Note that alpha=2*beta
30 fA2=@(alpha) ((D.^2)/8).*(alpha-sin(alpha))-A2;
31 alpha=fzero(fA2,pi/3);
32 beta=alpha/2;
33 S12=D.*sin(beta);
34 S2=beta.*D;
35 S1=(pi-beta).*D;
36 d12D=d12/D;
37 if (d12D)>0.002
38 Y=5+1.86*log10(d12./D);
39 else
40 Y=0;
41 end
42
43 f12=(1+2*Y)./((4*log10(1/d12D)+3.36)^2);
44 FunTol=0.1;%function tolerance
45 n=500000;% maximum iterations
46 V1=zeros(1,n);
47 V2=zeros(1,n);
48 tau12=zeros(1,n);
49 tau1k=zeros(1,n);
50 tau2k=zeros(1,n);
51 dpdz1=zeros(1,n);
52 dpdz2=zeros(1,n);
53 j1=zeros(1,n);

```

```

54 j2=zeros(1,n);
55 for i=1
56 V1(i)=0;
57 end
58 for i=2:n
59 V2(i-1)=(A*U-A1*V1(i-1))./A2;
60 tau12(i-1)=0.5*f12.*(V1(i-1)-V2(i-1)).*abs(V1(i-1)-V2(i-1)).*rho1;
61 tau1k(i-1)=kfrictionloss(d50,D,rho1,rhos,muf,(V1(i-1)),k,C1,Cmax);
62 taucS2=0.5*g*(D.^2)*(rhos-rhof).*(C2-C1).*(sin(beta)-beta.*cos(beta))*nus;
63 tau2k(i-1)=kfrictionloss(d50,D,rho2f,rhos,muf,(V2(i-1)),k,C2-C1,Cmax);
64 dpdz1(i-1)=(tau1k(i-1).*S1+tau12(i-1).*S12)./A1;
65 dpdz2(i-1)=(-tau12(i-1).*S12+tau2k(i-1).*S2+taucS2)./A2;
66 j1(i-1)=dpdz1(i-1)./g./rho1;
67 j2(i-1)=dpdz2(i-1)./g./rho1;
68 V1(i)=0.0005+V1(i-1); %a step size of 0.0005 implemented
69 if abs(j1(i-1)-j2(i-1))<FunTol
70 break
71 else
72 continue
73 end
74
75 end
76 tau1k=tau1k(i-1);
77 tau2k=tau2k(i-1);
78 tau12=tau12(i-1);
79 V1=V1(i-1);
80 V2=V2(i-1);
81 dPdzSRC=(tau1k.*S1+tau2k.*S2+taucS2)./A;%Pa/m frictional pressure drop
82 tauSRC=D.*dPdzSRC/4;% Pa, Wall shear stress
83 tauc=taucS2./S2;%Coulombic stress
84 end

```

---

## Data for validation of for SRC Two-Layer Model code

Table B.1: Experimental data to test the SRC two layer model code in the run file that following

<b>Sample experimental data Gillies et al. 2004</b>					
C=0.1		C=0.2		Water	
<b>V (m/s)</b>	<b>dPdz (kPa/m)</b>	<b>V (m/s)</b>	<b>dPdz (kPa/m)</b>	<b>V (m/s)</b>	<b>dPdz (kPa/m)</b>
7.67	3.78	7.63	3.92	7.59	3.43
7.49	3.61	7.51	3.78	7.18	3.08
6.98	3.17	7.30	3.59	6.81	2.78
6.79	2.99	7.10	3.42	6.54	2.56
6.52	2.78	6.91	3.26	6.11	2.26
6.22	2.55	6.67	3.08	5.64	1.95
5.95	2.35	6.34	2.82	5.31	1.73
5.70	2.18	6.12	2.65	4.93	1.52
5.27	1.88	5.75	2.39	4.64	1.36
4.99	1.71	5.42	2.15	4.31	1.19
4.50	1.45	5.09	1.95	3.78	0.93
4.21	1.29	4.70	1.72	3.23	0.70
4.00	1.17	4.54	1.62	2.84	0.54
3.72	1.06	4.35	1.55	2.63	0.49
3.43	0.94	4.13	1.45	2.26	0.37
3.14	0.85	3.96	1.35	1.85	0.26
2.78	0.73	3.74	1.26	1.65	0.21
2.33	0.58	3.45	1.14	1.40	0.16
2.08	0.55	3.29	1.07	1.12	0.10
		2.98	0.98	0.89	0.06
		2.78	0.91		
		2.51	0.81		
		2.29	0.75		
		2.12	0.76		

## Run file code for SRC Two-Layer Model

---

```

1 %SRC wto layer model run file
2 % Validating Data from Gillies et al. (2004)

```

```
3 %Copyright Oluwaseun E Adedeji 2016 University of Alberta
4 clear
5 clc
6 tic %Solution start time
7 load('GilliesEtAl2004DataHeterod270microns') %loading data
8 Cf=0;%fines concentration
9
10 %Testing for 20% solids volume concentration
11 Cr=0.2;
12 U=U2C20;
13 dPdZExp=dPdZExp2;
14 z=length(U);
15 d12=d;
16 D=0.103;%Pipe diameter
17 d50=270e-6;% partice diameter (mass median)
18 Cmax=0.51;
19 rhos=2650;
20 rhol=997;
21 mul=0.89e-3;
22 k=0;
23 g=9.81;
24 nus=0.5;%coefficient of sliding friction
25
26 tau_fl=frictionloss(D,rhol,mul,UH20,k); %Wall shear stress for cartier ...
    fluid
27 dPdZ_fl=tau_fl*4/D/1000; %Pressure drop for cartier fluid
28 %creating zero vectors for storing of variables in the FOR LOOP
29 dPdZdata=zeros(z,1);
30 tauSRCdata=zeros(z,1);
31 tau1kdata=zeros(z,1);
32 tau2kdata=zeros(z,1);
33 taucdata=zeros(z,1);
34
35 for n=1:z
36 [tauSRC,dPdZSRC,Vc,tau1k,tau2k,tauc]=...
37 srctwolayer(U(n),D,d12,d50,Cr,Cmax,Cf,rhos,rhol,mul,k,g,nus);
38 dPdZdata(n,1)= dPdZSRC/1000;
39 tauSRCdata(n,1)=tauSRC;
40 tau1kdata(n,1)= tau1k;
41 tau2kdata(n,1)= tau2k;
```

```

42 taucdata(n,1)= tauc;
43 end
44 toc
45
46
47 figure(1)
48 subplot(1,2,1)
49 plot(U,dPdzExp,'s',U,dPdzdata,'-',UH20,dPdzExpH20,'o',...
50 UH20,dPdz_fl,'-', 'linewidth',2, 'color','k')
51 xlabel('V (m/s)'); ylabel('Frictional pressure drop, dP/dz (kPa/m)')
52 grid on
53 legend('Exp (Slurry)', 'Prediction (Slurry)', 'Exp (Water)', 'Prediction ...
      (Water)')
54 set(findall(gcf, '-property', 'FontSize'), 'FontSize', 14, ...
      'fontWeight', 'bold')
55
56 subplot(1,2,2)
57 plot(U,taucdata,'s', 'linewidth',2, 'color','k')
58 xlabel(' V (m/s)'); ylabel('Coulombic stress, \tau_c (Pa)')
59 grid on
60 set(findall(gcf, '-property', 'FontSize'), 'FontSize', 14, ...
      'fontWeight', 'bold')

```

---

## Other functions embedded in the SRC two layer model code

### Reynolds number

```

1 %Function file to calculate Reynolds number based on pipe diameter
2 %Written by Oluwaseun E. Adedeji
3 %Copyright 2016
4 function Re=reynoldsD(D,rhof,muf,U)
5 % D = Pipe diameter (m)
6 % rho = Fluid density (kg/m^3)
7 % mu = Fluid viscosity (Pa.s)
8 % U = Fluid flow velocity in pipe (m/s)
9 Re=D.*rhof.*U./muf;
10 end

```

---

---

**Solids linear concentration**

---

```
1 %Function file to calculate linear concentration for SRC model
2 %Written by Oluwaseun E. Adedeji
3 %Copyright 2016
4 function linconc=linconc(Cvmax,Cv)
5 % Cvmax = Maximum solids volume fraction
6 % Cv = Solids volume fraction
7 linconc=((Cv./Cvmax).^(-1/3)-1).^(-1);
8 end
```

---

**Archimedes number**

---

```
1 %Function file to calculate Archimedes number
2 %Written by Oluwaseun E. Adedeji
3 %Copyright 2016
4 function Ar=archimedes(d,rhof,rhos,mu,g)
5 % d = Particle diameter (m)
6 % rhof = Fluid density (kg/m^3)
7 % rhos = Particle density (kg/m^3)
8 % mu = Fluid viscosity (Pa.s)
9 % g = gravitational constant (m/s^2)
10 Ar=(4/3).*g.*(d.^3).*(rhos-rhof).*rhof./(mu.^2);
11 end
```

---

**Swamee-Jain friction factor**

---

```
1 %Function file to calculate fluid friction coefficient
2 %Written by Oluwaseun E. Adedeji
3 %Copyright 2016
4 function f=frictionfactor(D,rhof,muf,U,k)
5 % D = Pipe diameter (m)
6 % rhof = Fluid density (kg/m^3)
7 % mu = Fluid viscosity (Pa.s)
```

---

```

8 % k = roughness (m)
9 % U = Fluid flow velocity (m/s)
10 Re=reynoldsD(D, rhof, muf, U);
11 if Re<2000
12 %display('Flow is Laminar')
13 f=16./Re;
14 else
15 %display('Flow is Turbulent')
16 %Use Swamee-Jain equation
17 f=0.0625./(log10(k./D/3.7+5.74./Re.^0.9)).^2;
18 end
19 end

```

---

### Dimensionless particle diameter

---

```

1 %Function file to calculate dimensionless particle diameter for SRC model
2 %Written by Oluwaseun E. Adedeji
3 %Copyright 2016
4 function dpl=dplus(d,D, rhof, muf, U, k)
5 % d = Particle diameter (m)
6 % rhof = Fluid density (kg/m^3)
7 % mu = Fluid viscosity (Pa.s)
8 % k = Pipe wall roughness
9 % U = Fluid flow velocity (m/s)
10 f=frictionfactor(D, rhof, muf, U, k);
11 dpl=d.*U.*sqrt(f/2)./(muf./rhof);
12 end

```

---

### Solids friction factor

---

```

1 %Function file to calculate kinematic friction loss for SRC model
2 %Written by Oluwaseun E. Adedeji
3 %Copyright 2016
4 function fs=sfrictionfactor(d,D, rhof, muf, U, k, Cv, Cvmax)
5 % d = Particle diameter (m)

```

```

6 % rhof = Fluid density (kg/m^3)
7 % mu = Fluid viscosity (Pa.s)
8 % k = Wall roughness (m)
9 % U = Fluid flow velocity
10 % Cvmax = Maximum solids volume fraction
11 % Cv = Solids volume fraction
12
13 dpl=dplus(d,D,rhof,muf,U,k);
14 gamma=linconc(Cvmax,Cv);
15 if dpl<21
16 ko=-1.1e-4;k1=4.2e-4;
17 else
18 ko=-5.6e-5;k1=2.6e-4;
19 end
20
21 if dpl>100
22 fs=0;
23 else
24 fs=(gamma.^1.25).*(ko.*log(dpl)+k1);
25 end
26
27 end

```

---

## Fluid friction loss

```

1 %Function file to calculate fluid friction loss
2 %Written by Oluwaseun E. Adedeji
3 %Copyright 2016
4 function [tauw]=frictionloss(D,rhof,muf,U,k)
5 % D = Pipe diameter (m)
6 % rhof = Fluid density (kg/m^3)
7 % muf = Fluid viscosity (Pa.s)
8 % k = roughness (m)
9 % U = Fluid flow velocity
10 f=frictionfactor(D,rhof,muf,U,k);
11 tauw=0.5.*f.*rhof.*U.*abs(U);%Pa
12 end

```

---

## Solids friction loss

---

```

1 %Function file to calculate solids friction loss
2 %Written by Oluwaseun E. Adedeji
3 %Copyright 2016
4 function [tausws]=sfriictionloss(d,D,rhof,rhos,muf,U,k,Cv,Cvmax)
5 % D = Pipe diameter (m)
6 % rhof = Fluid density (kg/m^3)
7 % mu = Fluid viscosity (Pa.s)
8 % k = roughness (m)
9 fs=sfrictionfactor(d,D,rhof,muf,U,k,Cv,Cvmax);
10 tausws=0.5*fs*rhos.*U.*abs(U);%Pa
11 end

```

---

## Kinematic friction loss function

---

```

1 %Function file to calculate kinematic friction loss
2 %Written by Oluwaseun E. Adedeji
3 %Copyright 2016
4 function [tauwk]=kfrictionloss(d,D,rhof,rhos,muf,U,k,Cv,Cvmax)
5 % D = Pipe diameter (m)
6 % rhof = Fluid density (kg/m^3)
7 % rhos = Particle density (kg/m^3)
8 % muf = Fluid viscosity (Pa.s)
9 % k = Wall roughness (m)
10 % Cvmax = Maximum solids volume fraction
11 % Cv = Solids volume fraction
12 % U = Fluid velocity (m/s)
13 % d = Particle diameter
14 tausws=sfrictionloss(d,D,rhof,rhos,muf,U,k,Cv,Cvmax);
15 tauw=frictionloss(D,rhof,muf,U,k);
16 tauwk=tauw+tausws;
17 end

```

---

**Deposition velocity function**

---

```
1 %Function file to calculate deposition velocity
2 %Written by Oluwaseun E. Adedeji
3 %Copyright 2016
4 function Vc=dvelocity(d,rhof,rhos,mu,g,D)
5
6 % d = Particle diameter (m)
7 % rhof = Fluid density (kg/m^3)
8 % rhos = Particle density (kg/m^3)
9 % mu = Fluid viscosity (Pa.s)
10 % g = gravitational acceleration (m/s^2)
11 Ar=archimedes(d,rhof,rhos,mu,g);
12 if Ar>=125&&Ar<2690
13 a=1.27;b=0.049;
14 elseif Ar>=2690&&Ar<86000
15 a=2.35;b=-0.088;
16 elseif Ar>=86000
17 a=1.35;b=0;
18 elseif Ar<125
19 display('particle-system condition out of model range')
20 a=0;b=0;
21 end
22 Fr=a+b.*log(Ar);
23 Vc=Fr.*sqrt(g.*D.*(rhos-rhof)./rhof);
24 end
```

---

**Data for validation of for SRC deposition velocity model code. Data 1-10: Spelay et al. (2016), Data 11-22: Gillies (1993)**

SN	$\rho_s$ (kg/m <sup>3</sup> )	$\rho_f$ (kg/m <sup>3</sup> )	$\mu_f$ (Pas)	$D$ (m)	$d_{50}$ (m)	$C_r$	$C_{max}$	$Ar$	$V_c$ (m/s)
1	2650	999	0.00104	0.1036	0.00030	0.21	0.676	538.54	2.05
2	2650	999	0.00101	0.1036	0.00030	0.20	0.676	571.01	2.10
3	2650	999	0.00107	0.1036	0.00030	0.30	0.676	508.76	1.90
4	2650	1001	0.00111	0.1036	0.00030	0.31	0.676	473.13	2.00
5	2650	1011	0.00112	0.1036	0.00201	0.11	0.623	140310.44	1.75
6	2650	1032	0.00114	0.1036	0.00201	0.13	0.623	136472.27	1.75
7	2650	1057	0.00120	0.1036	0.00201	0.17	0.623	124200.74	1.80
8	2650	1027	0.00120	0.1036	0.00756	0.07	0.674	6541835.24	1.70
9	2650	1066	0.00149	0.1036	0.00756	0.10	0.674	4298460.85	1.70
10	2650	1124	0.00192	0.1036	0.00756	0.12	0.674	2629611.06	1.75
11	2650	1001	0.00120	0.0532	0.00055	0.15	0.550	2494.53	1.30
12	2650	1013	0.00160	0.0532	0.00055	0.30	0.550	1409.66	1.20
13	2650	1024	0.00330	0.0532	0.00055	0.40	0.550	332.73	1.30
14	2650	1003	0.00130	0.2630	0.00055	0.15	0.550	2127.18	3.40
15	2650	1010	0.00150	0.2630	0.00055	0.25	0.550	1602.06	3.20
16	2650	1009	0.00160	0.2630	0.00055	0.30	0.550	1407.52	3.10
17	2650	1007	0.00090	0.2630	0.00055	0.30	0.550	4445.06	3.20
18	2650	1041	0.00130	0.0532	0.00240	0.15	0.550	179209.71	1.20
19	2650	1173	0.00210	0.0532	0.00240	0.30	0.550	71036.47	1.20
20	2650	1029	0.00150	0.2630	0.00240	0.13	0.550	134047.07	2.60
21	2650	1068	0.00200	0.2630	0.00240	0.22	0.550	76376.40	2.40
22	2650	1058	0.00120	0.2630	0.00240	0.22	0.550	211498.70	2.60

**Terminal settling velocity function**

```

1 %Function file to calculate terminal velocity from archimedes number
2 %Written by Oluwaseun E. Adedeji
3 %Copyright 2016
4 function Vinf=terminalvelocity(d,rhof,rhos,muf,g)
5 % d = Particle diameter (m)
6 % rhof = Fluid density (kg/m^3)
7 % rhos = Particle density (kg/m^3)
8 % mu = Fluid viscosity (Pa.s)
9 % g = gravitational acceleration (m/s^2)
10 Ar=archimedes(d,rhof,rhos,muf,g);

```

```

11 if Ar ≤ 4.8
12 Rep=Ar./24;
13 elseif Ar > 4.8 && Ar < 4e5
14 Rel=0.00001; Reu=5e5;
15 Frep=@(Rep) 24.*Rep+3.6.*Rep.^1.687-Ar;
16 Rep=fzero(Frep, [Rel, Reu]);
17 %Rep=fzero(Frep, 100);
18 elseif Ar ≥ 4e5
19 Rep=sqrt(Ar./0.44);
20 end
21 Vinf=Rep.*muf./rhof./d;
22 end

```

---

## B.2 Coulombic friction code for the toroid wear tester

Script file to calculate the solids-related torque for the STWT. Data validated is for sand-in-water case in Zhang(2018)

---

```

1 %Script file to calculate solids-related torque for
2 %modified SRC model for the small Toroid wear tester(TWT)
3 %Model details found in Zhang (2018)
4 %Written by Oluwaseun E. Adedeji
5 %Copyright 2016
6
7 clear
8 clc
9 clf
10 % loading data. Data available in Zhang (2018)
11 load("TorqueMesData")
12
13
14 DS=(DT-0.12);
15 A1=Cv*W*pi*(DT.^2-DS.^2)/4/3;
16 nus=0.47;
17 R=0.304;
18 r=0.244;
19 Dh=2*W*(R-r)/(R-r+W);

```

```

20 Omega=2*pi*N./60;
21 V=Omega.*(R+r)./2;
22
23
24 for i=1:length(beta)
25 Ts(i)=torqueside(beta(i),theta(i),DT,rhos,rhofh20,nus,Cmax(i),g);
26 Tb(i)=torquebottom(beta(i),theta(i),DT,rhos,rhofh20,nus,Cmax(i),g,W);
27 T(i)=Tb(i)+2*Ts(i);
28 end
29 Tpredicted=T';
30
31 figure(1)
32 plot([0;TMeasured],[0;TMeasured],'-',[0;TMeasured],0.85.*([0;TMeasured])...,'--',[0;TMea
33 [0;Tpredicted],'o','color','k')
34 xlabel('Observed T(Nm)');
35 ylabel('Predicted T(Nm)');
36 grid on
37 xlim([0 2])
38 ylim([0 2])
39 set(findall(gcf,'-property','FontSize'),'FontSize',14,...
      'fontWeight','bold')
40
41 CFpred=Tpredicted./(rhos-rhofh20)./4./nus./g./V.^2;
42 CFmes=TMeasured./(rhos-rhofh20)./4./nus./g./V.^2;
43 VVnf=V./Vinf;
44
45 figure(2)
46 loglog(VVnf,CFpred,'s',VVnf,CFmes,'*','color','k')
47 ylabel('CF');
48 xlabel('V/V_{\infty}');
49 grid on
50 legend('Model','Experiment')
51 %xlim([0 2])
52 %ylim([0 2])
53 set(findall(gcf,'-property','FontSize'),'FontSize',14,...
      'fontWeight','bold')

```

---

function file to calculate torque due to the STWT channel side wall

---

---

```

1 %function file to calculate torque due to the TWT channel side wall
2 function funval=torqueside(beta,theta,DT,rhos,rhof,nus,Cmax,g)
3 funtc0=(rhos-rhof).*cos(theta).*nus.*Cmax.*g;
4 rmax=DT/2.*ones(size(beta));
5 rmin=rmax.*cos(beta);
6 funtc1=@(r) 2.*r.^3.*(1 - ...
    rmin.^2./r.^2).^ (1/2)-2.*rmax.*r.^2.*acos(rmin./r).*cos(beta);
7 funtc2=integral(funtc1,rmin,rmax);
8 funval=funtc0.*funtc2;
9 end

```

---

function file to calculate torque due to the STWT channel bottom wall

---

```

1 %function file to calculate torque due to the TWT channel bottom wall
2 function funval=torquebottom(beta,theta,DT,rhos,rhof,nus,Cmax,g,W)
3 funtc0=0.5*(rhos-rhof).*cos(theta).*nus.*Cmax.*g.*W.*(sin(beta) ...
4 -beta.*cos(beta)).*DT.^2;
5 rmax=DT/2;
6 funval=funtc0.*rmax;
7 end

```

---

## B.3 PipeMeshStarter MATLAB App Code

**Function files compile to build the App**

This is the main function file to calculate the first layer thickness for the pipe mesh

---

```

1 %Function file to calculate pipe mesh firstlayer thickness
2 %for a target yplus valus
3 %Written by Oluwaseun E. Adedeji, University of Alberta
4 %Copyright 2018
5 function [flt,slt,LE,LDRatio,Re]=flthick(D,rhof,muf,U,k,yplus)
6 % D = Pipe diameter (m)
7 % rhof = Fluid density (kg/m^3)
8 % muf = Fluid viscosity (Pa.s)
9 % k = pipe wall roughness (m)

```

```

10 % U = Fluid mean flow velocity (m/s)
11 % yplus = target wall yplus for your mesh
12 %LE =entrance length
13 %Re=reynolds number
14 %LDRaio=Length to diamater ratio
15 %laminar sublayer thickness
16 [LE,LDRatio,Re] = entrancelength(D, rhof, muf, U);
17 ust=ustar(D, rhof, muf, U, k);
18 kinVis=muf./rhof;
19 flt=yplus*kinVis/ust;
20 slt=lsbl(D, rhof, muf, U, k);
21 end

```

---

This is the function file to calculate the entrance length

---

```

1 %Function file to calculate entrance length for horizontal pipe
2 %Written by Oluwaseun E. Adedeji, University of Alberta
3 %Copyright 2018
4 function [LE,LDRatio,Re] = entrancelength(D, rhof, muf, U)
5 % D = Pipe diameter (m)
6 % rhof = Fluid density (kg/m^3)
7 % muf = Fluid viscosity (Pa.s)
8 % U = Fluid mean flow velocity (m/s)
9 %LE =entrance length
10 %Re=reynolds number
11 %LDRaio=Length to diamater ratio
12 Re=reynoldsD(D, rhof, muf, U);
13 if Re<2300
14 LE=0.06*D.*Re;
15 else
16 LE=4.4*D.*Re.^(1/6);
17 end
18 LDRatio=LE/D;
19 end

```

---

This is the function file to calculate the laminar sub-layer thickness

---

```

1 %Function file to calculate laminar sublayer thickness

```

---

```

2 %Written by Oluwaseun E. Adedeji
3 %Copyright 2018
4 function lamsublayer=lsbl(D,rhof,muf,U,k)
5 % D = Pipe diameter (m)
6 % rhof = Fluid density (kg/m^3)
7 % muf = Fluid viscosity (Pa.s)
8 % k = wall roughness (m)
9 % U = Fluid mean flow velocity in pipe (m/s)
10 ust=ustar(D,rhof,muf,U,k);
11 kinVis=muf./rhof;
12 lamsublayer=5*kinVis/ust;
13 end

```

---

This is the function file to calculate the shear velocity  $u^*$

---

```

1 %Function file to calculate turbulent (shear) velocity ustar
2 %Written by Oluwaseun E. Adedeji, University of Alberta
3 %Copyright 2018
4 function ust=ustar(D,rhof,muf,U,k)
5 % D = Pipe diameter (m)
6 % rhof = Fluid density (kg/m^3)
7 % muf = Fluid viscosity (Pa.s)
8 % k = wall roughness (m)
9 % U = Fluid mean flow velocity in pipe (m/s)
10 f=frictionfactor(D,rhof,muf,U,k);
11 ust=U.*sqrt(f/2);
12 end

```

---

Two other function i.e. for the fluid friction factor and for Reynolds number are required to complete this compilation. The codes for these functions have been provided in the previous section.

## PipeMeshStarter App GUI with Sample Calculations

The screenshot displays the PipeMeshStarter MATLAB App GUI. It is divided into two main sections: 'Inputs' and 'Results'.

**Inputs Section:**

- Density: 1000 kg/m<sup>3</sup>
- Viscosity: 0.001 Pas
- Pipe diameter: 0.05 m
- Wall roughness: 0 m
- Mean velocity: 5 m/s
- Yplus: 5

Buttons for 'Run' and 'Reset' are located below the input fields.

**Results Section:**

**First Cell Thickness:**

- Viscous sublayer thickness: 2.319e-05 m
- First cell thickness: 2.319e-05 m

**Entrance Length:**

- Reynolds number: 2.5e+05
- L/D Ratio: 34.92
- Entrance length: 1.746 m
- Recommended pipe length: 1.921 m
- Inlet Turbulence Intensity: 3.384 %

Figure B.1: MATLAB App (PipeMeshStarter) developed to estimate first layer thickness for a pipe mesh for a target  $y+$  value

## B.4 Contracer code for TWT surface profile contour

```

1 %Code to plot surface profile for both LTWT and STWT coupons
2 %Also estimate average wear rate from surface profile measure
3 %Estimate wear rate for a selected region on the TWT coupons
4 %Written by : Dr David Breakey
5 %Modification: Oluwaseun E. Adedeji
6 %Copyright 2019
7 %Pipeline Transport Processes (PTP) Research Group
8 %University of Alberta
9
10 function contracerProcess(varargin)
11 testhour = 47;

```

```

12 %Options
13 useXcorr = false;           %Use a correction for x-axis based on the ...
    uneroded sides
14 useYcorr = true;           %Use a correction for y-axis based on the ...
    uneroded leading+trailing end of coupon
15 XcorrRows= 2;             %Number of data rows to use for x-axis correction
16 YcorrRows= 2;             %Number of data rows to use for y-axis correction
17 enforce0 = 1 ;           %Enforce that no thickness loss is positive ...
    (subtract maximum value)1
18 smoothResult = true;     %Apply data smoothing to the final result
19
20 dy = 2;%mm %Distance between each profile file
21
22 %This allows you to select the folder to run in
23 if isempty(varargin)
24 shiftx = 0;
25 shifty = 0;
26 workdir = uigetdir(pwd);
27
28 if ~workdir
29 error('Must select a valid folder.')
30 end
31 elseif length(varargin)==1
32 workdir = varargin{1};
33 shiftx = 0;
34 shifty = 0;
35 else
36 shiftx = varargin{1};
37 shifty = varargin{2};
38 workdir = varargin{3};
39 end
40
41 folders = dir([workdir '/']);
42 folders = folders([folders.isdir] & ~strcmpi({folders.name}, '.') & ~...
    strcmpi({folders.name}, '..'));
43 if isempty(folders)
44 %Assume SWT
45 folders = {'.'};
46 elseif length(folders)≠2

```

```

47 error('There need to be two folders (one for the leading edge and one ...
    for trailing edge, in the selected folder.');
```

```

48 else %Try to figure out which folder is leading edge and which is ...
    trailing, then do leading first
49 folders = {folders.name}';
50 leading = contains(lower(folders), 'leading');
51 if any(leading)
52 folders = folders([find(leading) 3-find(leading)]);
53 else
54 front = contains(lower(folders), 'front');
55 folders = folders([find(front) 3-find(front)]);
56 end
57 end
58
59 folders = strcat(workdir, '/', folders);
60 cdir = pwd;
61 cd(folders{1}) %Go to the appropriate folder
62 Ny = length(dir('L*.dat')); %Find the data files
63 datFileName = sprintf('L%d.dat', 1);
64 fileCont = dlmread(datFileName, ',', 1, 0); %Open the first one
65 Nx = fileCont(1)+5; %Make room for files that may have a couple more ...
    data points
66 cd(cdir) %Move back to the original folder
67
68 Nxh = 1*Nx; %Resolution to resample surface at
69 Nyh = 1*Ny;
70
71 data = cell(length(folders), 1);
72 data(:) = {nan(Nx*Ny, 3)};
73
74 for fi = 1:length(folders)
75 folder = folders{fi};
76
77 cd(folder) %Go to the appropriate folder
78
79 %Read all the *.dat files sequentially and save input
80 currInd = 1;
81 for k = 3:Ny%1:Ny
82 datFileName = sprintf('L%d.dat', k);
83 if exist(datFileName, 'file')
```

```

84 %   reading *.dat file from 3rd line after the header
85 m = dlmread(datFileName, ',', 2, 0);
86 data{fi}((0:length(m)-1)+currInd, 1) = m(:, 1);
87 data{fi}((0:length(m)-1)+currInd, 2) = (k-1)*dy;
88 data{fi}((0:length(m)-1)+currInd, 3) = m(:, 2);
89 currInd = currInd+length(m);
90 else
91 % error report
92 fprintf('File %s does not exist.\n', datFileName);
93 end
94 end
95
96 cd(cdir) %Go back up
97
98 if fi==2 %(i.e. trailing edge)
99 data{fi}(:, 1) = -data{fi}(:, 1) + 160; %Length of LWT coupon
100 data{fi}(:, 2) = -data{fi}(:, 2) + 140; %Width of LWT coupon
101 end
102
103 data{fi}(:, 1) = data{fi}(:, 1) - min(data{fi}(:, 1)); %Set the x-axis to ...
      start at 0
104 data{fi}(:, 2) = data{fi}(:, 2) - min(data{fi}(:, 2)); %Set the y-axis to ...
      start at 0
105
106 %   figure(fi)
107 %   plot3(data{fi}(:, 1), data{fi}(:, 2), data{fi}(:, 3), 'k.')
108 %   xlabel('x')
109 %   ylabel('y')
110
111
112 end
113 %%
114
115 dxdata = data{fi}(:, 1);
116 dx = abs(median(diff(dxdata(¬isnan(dxdata))))); %Resolution for final ...
      resampling
117 dxFinal = dx;
118 dyFinal = dy;
119

```

```
120 S = cell(length(data),3);%Make a cell array to hold the resampled data ...
    structures
121
122 % Set up fitype and options for 2D surface fit
123 ft = 'cubicinterp';
124
125 for di = 1:length(data)
126 xdata = data{di}(:,1);
127 ydata = data{di}(:,2);
128 zdata = data{di}(:,3);
129
130 xdata = xdata(~isnan(zdata));
131 ydata = ydata(~isnan(zdata));
132 zdata = zdata(~isnan(zdata));
133
134 % Fit model to data.
135 [zfit, ~] = fit( [xdata ydata], zdata, ft );
136 % Use the uneroded regions to fit a model for uneven profile (accounts
137 % for x direction only)
138 unesel = (ydata<min(ydata)+XcorrRows*dy-dy/2 | ...
    ydata>max(ydata)-XcorrRows*dy+dy/2);
139 [zfite, ~] = fit( [xdata(unesel) ydata(unesel)], zdata(unesel), ft );
140
141 %Create a grid for interpolation
142 xg = linspace(min(xdata),max(xdata),Nxh);
143 yg = linspace(min(ydata),max(ydata),Nyh);
144 [xgg,ygg] = meshgrid(xg,yg);
145
146 %Estimate the thickness loss from the model (minus the baseline shape)
147 zgg = zfit(xgg,ygg) - zfite(xgg,ygg)*useXcorr;
148
149 %figure(10)
150 %plot3(xgg(:),ygg(:),zgg(:))
151
152 %Save to the cell array
153 S{di,1} = xgg;
154 S{di,2} = ygg;
155 S{di,3} = zgg;
156 end
157
```

```

158 switch fi
159 case 1%If there is only one profile (SWT)
160     fxg          = 0:dxFinal:70;
161     fyg          = 0:dyFinal:65;
162     [fxgg,fygg] = meshgrid(fxg,fyg);
163
164     %Add overlap zone and non-overlap zones
165     xdata = xgg(:);
166     ydata = ygg(:);
167     zdata = zgg(:);
168     figure(54)
169     plot3(xdata,ydata,zdata, '.');
170
171     %Create a fit again (This is a bit redundant, but it does incorporate
172     %the X correction if that option is selected
173     TLFit = fit( [xdata(~isnan(zdata)) ydata(~isnan(zdata))], ...
174                 zdata(~isnan(zdata)), ft );
175
176 case 2%If there are two profiles (LWT)
177     fxg          = 0:dxFinal:160;
178     fyg          = 0:dyFinal:140;
179     [fxgg,fygg] = meshgrid(fxg,fyg);
180
181     %And shift to the trailing edge
182     S{2,1} = S{2,1}+shiftx;
183     S{2,2} = S{2,2}+shifty;
184
185     %Show match between two profiles
186     figure(52)
187     clf
188     surf(S{1,1},S{1,2},S{1,3}, 'EdgeAlpha',0.1)
189     hold on
190     plot3(S{2,1}(:),S{2,2}(:),S{2,3}(:), 'k.', 'MarkerSize',0.1)
191     hold off
192
193     %Calculate a weight function to blend both measurements
194     wf = @(x) (x<min(S{2,1}(:)))*(1) + (x>min(S{2,1}(:)) & ...
195             x<max(S{1,1}(:)))* ( 1 - (x-min(S{2,1}(:)))/(max(S{1,1}(:)) - ...
196             min(S{2,1}(:)) ));

```

```

195 %         figure(53)
196 %         plot3(fxgg(:),fygg(:),wf(fxgg(:)));
197
198 %Overlap zone
199 wfxgg = wf(fxgg(:));
200 ozsel = wfxgg<1 & wfxgg>0;
201 fxggo = fxgg(ozsel);
202 fyggo = fygg(ozsel);
203 S1     = interp2(S{1,1},S{1,2},S{1,3},fxggo,fyggo);
204 S2     = interp2(S{2,1},S{2,2},S{2,3},fxggo,fyggo);
205 S12    = wf(fxggo).*S1 + (1-wf(fxggo)).*S2;
206
207 %Add overlap zone and non-overlap zones
208 xdata = [fxggo; S{1,1}(wf(S{1,1}(:))==1) ; S{2,1}(wf(S{2,1}(:))==0)];
209 ydata = [fyggo; S{1,2}(wf(S{1,1}(:))==1) ; S{2,2}(wf(S{2,1}(:))==0)];
210 zdata = [S12 ; S{1,3}(wf(S{1,1}(:))==1) ; S{2,3}(wf(S{2,1}(:))==0)];
211 %         figure(54)
212 %         plot3(xdata,ydata,zdata,'.');
213
214 %Create a fit
215 TLFit = fit( [xdata(~isnan(zdata)) ydata(~isnan(zdata))], ...
              zdata(~isnan(zdata)), ft );
216 end
217
218 %Create error fit based on uneroded area
219 xdata(isnan(zdata)) = median(fxg);%Make nans not the extreme values
220 unesel      = (xdata<min(xdata)+YcorrRows*dx-dx/2 | ...
                xdata>max(xdata)-YcorrRows*dx+dx/2) & ~isnan(zdata);
221 TLFite= fit( [xdata(unesel) ydata(unesel)], zdata(unesel), ft );
222
223 %Create final data
224 %TL     = zeros(size(fxgg));
225 TL     = (TLFit(fxgg,fygg) - useYcorr*TLFite(fxgg, fygg));
226 TL     = TL - enforce0*max(TL(:));
227 if useXcorr || useYcorr
228 TL(isnan(TL)) = 0;
229 end
230
231 %Smooth final data
232 if smoothResult

```

```
233 dfilt = [5 3];%Filter size (X x Y measurements)
234 filt = ones(dfilt)/prod(dfilt);
235 TL = conv2(TL,filt,'same');
236 end
237
238 %Plot as 3D plot and countour plot
239 figure(55)
240 plot3(fxgg(:),fygg(:),TL(:),'.');
241 figure(56)
242 contourf(fxgg,fygg,(TL-max(TL)).*8700./testhour,'.');
243 colorbar
244 xlabel('x direction (mm)','FontName','Calibri','FontSize',12);
245 ylabel('y direction (mm)','FontName','Calibri','FontSize',12);
246 zlabel('Erosion rate (mm/year)','FontName','Calibri','FontSize',12);
247 cb = colorbar;
248 %caxis([-25 0])
249 cb.Label.String = 'Erosion rate (mm/year)';
250 set(findall(gcf, '-property', 'FontSize'), 'FontSize', 14, ...
      'fontWeight', 'bold')
251
252 colormap jet
253 if enforce0 == 1
254 oldcmap = colormap;
255 colormap( flipud(oldcmap) )
256 end
257
258 if fi==2
259 xmin = 95;%95; %boundary for LWT
260 ymin = 16;
261 xmax = 106;
262 ymax = 102;
263 else
264 xmin = 0;%2; %SWT: boundary for eroded area
265 ymin = 0;
266 xmax = 65;
267 ymax = 65;
268 end
269
270
271 TLsel = fxgg > xmin & fxgg < xmax & fygg > ymin & fygg < ymax;
```

```
272
273 TLi = TL;
274 TLi(¬TLsel) = 0;
275
276 hest1 = abs(sum(sum(TLi,2))*dx*dy)/((ymax-ymin)*(xmax-xmin));
277 hest2 = abs(trapz(fxg,trapz(fyg,TLi),2))/((ymax-ymin)*(xmax-xmin));
278 if fi==2
279 Iest1 = abs(sum(sum(TLi,2))*dx*dy)/(114.5*114.5)*8760/testhour; %8760 ...
        is convertor between hour and year
280 Iest2 = abs(sum(sum(TLi,2))*dx*dy)/(114.5*114.5)*8760/testhour; %8760 ...
        is convertor between an hour and a year
281 else
282 Iest1 = abs(sum(sum(TLi,2))*dx*dy/65/65/testhour*8760; %8760 is ...
        convertor between hour and year
283 Iest2 = abs(sum(sum(TLi,2))*dx*dy/65/65/testhour*8760; %8760 is ...
        convertor between an hour and a year
284 end
285 fprintf('Wear rate 1 : %5.5f mm/year\n',Iest1)
286 fprintf('Wear rate 2 : %5.5f mm/year\n',Iest2)
287 fprintf('Thickness loss 1 : %5.5f mm^3\n',hest1)
288 fprintf('Thickness loss 2 : %5.5f mm^3\n',hest2)
```

---

## ANSYS UDF Codes

### C.1 Velocity profile inlet boundary condition

```
1  /*****  
2  /* UDF for specifying steady-state 3D velocity profile boundary ...  
   condition */  
3  /*****  
4  #include "udf.h"  
5  #define Umax 42 /* Maximum centerline velocity, m/s */  
6  #define R 0.1 /* Pipe radius, m */  
7  DEFINE_PROFILE(inlet_x_velocity, thread, position)  
8  {  
9     real pos[ND_ND];  
10    real xx;  
11    real yy;  
12    real zz;  
13    face_t f;  
14    begin_f_loop(f, thread)  
15    {  
16        F_CENTROID(pos, f, thread);  
17        yy = pos[1];  
18        zz = pos[2];  
19        F_PROFILE(f, thread, position) = Umax*(1-(yy*yy+zz*zz)/(R*R));  
20    }
```

```

21  end_f_loop(f, thread)
22  }

```

---

## C.2 Particle tracking for local wear variables and UDF erosion (DNV model)

```

1  /*****
2  User Defined Function (UDF) Code for calculating the Particle Impact ...
   Variables
3  and DNV erosion model
4  *****/
5  #include "udf.h"
6  #define NUM_UDM 11
7  /*begin definition of erosion model constants*/
8  #define RAD_TO_DEG(x) ((M_PI*180.0/x));
9  #define n=2.6;
10 #define A1 =9.37;
11 #define A2 =-42.295;
12 #define A3 =110.864;
13 #define A4 =-175.804;
14 #define A5 =170.137;
15 #define A6 =-98.398;
16 #define A7 =31.211;
17 #define A8 =-4.172;
18 #define K= 2.0e-9; /* material constant */
19 #define pt=7800; /* density of steel */
20 /*begin execute on loading function*/
21 static int udm_offset = UDM_UNRESERVED;
22 int p_impnumber=0;
23 DEFINE_EXECUTE_ON_LOADING(on_loading, libname)
24 {
25 if (udm_offset == UDM_UNRESERVED)
26 {
27 udm_offset=Reserve_User_Memory_Vars(NUM_UDM);
28 if (udm_offset == UDM_UNRESERVED)
29 {

```

```

30 Message("\nYou need to define up to %d extra UDMs in GUI and "
31 "then reload current library %s\n", NUM_UDM, libname);
32 }
33 else
34 {
35 Message("%d UDMs have been reserved by the current library ...
      %s\n", NUM_UDM, libname);
36 Set_User_Memory_Name(0, "Average Impact Velocity (m/s)");
37 Set_User_Memory_Name(1, "NUmber of Impacts");
38 Set_User_Memory_Name(2, "Average Impact Angle (deg)");
39 Set_User_Memory_Name(3, "PArtilcle Mass Rate (kg/m2-s)");
40 }
41 Message("\nUDM Offset for Current Loaded Library = %d", udm_offset);
42 }
43 }
44 DEFINE_DPM_EROSION(DNV_ER, particle, t, f, normal, theta, vel, mdot)
45 {
46 Domain *d; /* Get the domain using Fluent utility */
47 cell_t c0;
48 Thread *t0;
49 real erosion;
50 real f_alpha;
51 real V;
52 real A[ND_ND], area;
53 real imp_vel_mag;
54 int num_in_data;
55 real a;
56 F_AREA(A, f, t);
57 area = NV_MAG(A);
58 F_UDMI(f, t, 3) += (mdot/area);
59 c0 = F_C0(f, t);
60 t0 = THREAD_T0(t);
61 C_UDMI(c0, t0, 3) = F_UDMI(f, t, 3);
62 /*NV_V(imp_vel, =, P_VEL(particle));
63 /*imp_vel_mag=NV_MAG(imp_vel); */
64 imp_vel_mag=vel; /*point to impact velocity. Alternative method in last ...
      comment above*/
65 num_in_data = F_UDMI(f, t, 1);
66 /* Average velocity normal to wall of particles hitting the wall:*/
67 F_UDMI(f, t, 0) = (imp_vel_mag

```

```

68 + num_in_data * F_UDMI(f,t,0)
69 / (num_in_data + 1);
70 C_UDMI(c0,t0,0) = F_UDMI(f,t,0);
71 /* Average angle normal to wall of particles hitting the wall:*/
72 /*a = M_PI/2. - acos(MAX(-1.,MIN(1.,NV_DOT(normal,P_VEL(particle)))/
73 MAX(NV_MAG(P_VEL(particle)),DPM_SMALL)))); */
74 a=theta; /*point to impact angle in radians. Alternative method in last ...
       comment above*/
75 F_UDMI(f,t,2) = ((RAD_TO_DEG(a)) /*converting to degrees*/
76 + num_in_data * F_UDMI(f,t,2))
77 / (num_in_data + 1);
78 C_UDMI(c0,t0,2) = F_UDMI(f,t,2);
79 F_UDMI(f, t, 1) = num_in_data + 1;
80 C_UDMI(c0,t0,1) = num_in_data + 1;
81
82 /*define erosion equation*/
83 V=(pow(imp_vel_mag,n)); /* impact velocity of particle raised to ...
       constant n */
84 f_alpha=A1*a+A2*pow(a,2)+A3*pow(a,3)+A4*pow(a,4)+A5*pow(a,5)
85 +A6*pow(a,6)+A7*pow(a,7)+A8*pow(a,8); /*impact angle function*/
86 F_STORAGE_R(f,t,SV_DPMS_ACCRETION) += mdot / area; /*store accretion rate*/
87 erosion=(mdot*K*V*f_alpha/area); /*specify DNV erosion equation*/
88
89 F_STORAGE_R_XV(f, t, SV_DPMS_EROSION, EROSION_UDF)=erosion; /*erosion ...
       model output*/
90 }
91
92 DEFINE_ON_DEMAND(reset_udm)
93 {
94 reset_UDM_s(); /* This line will be executed only once, */
95 }
96 void
97 reset_UDM_s(void)
98 {
99 Domain *domain = Get_Domain(1);
100 Thread *t;
101 cell_t c;
102 face_t f;
103 int i;
104 /*er1=0.0;*/

```

```
105 Message("Resetting User Defined Memory...\n");
106 thread_loop_f(t, domain)
107 {
108   if (NNULLP (THREAD_STORAGE (t, SV_UDM_I)))
109   {
110     begin_f_loop(f,t)
111     {
112       for (i = 0; i < n_udm; i++)
113         F_UDMI(f,t,i) = 0.0;
114     }
115     end_f_loop(f, t)
116   }
117   else
118   {
119     Message("Skipping FACE thread no. %d..\n", THREAD_ID(t));
120   }
121 }
122 thread_loop_c(t, domain)
123 {
124   if (NNULLP (THREAD_STORAGE (t, SV_UDM_I)))
125   {
126     begin_c_loop(c,t)
127     {
128       for (i = 0; i < n_udm; i++)
129         C_UDMI(c,t,i) = 0.0;
130     }
131     end_c_loop(c,t)
132   }
133   else
134   {
135     Message(" Skipping CELL thread no. %d..\n", THREAD_ID(t));
136   }
137 } /* Skipping Cell Threads can happen if the user */
138 /* uses reset_UDM prior to initializing. */
139 Message(" --- Done.\n");
140 }
```

---

## Additional material

### D.1 Proof of Geometry Correction Factor

Consider two systems/geometries that are hydrodynamically different such that at similar inlet condition, the prediction of local wear variables will be different. From erosion studies, it is known that an erosion model developed in these systems will have different empirical coefficients and exponents that unique to these systems. Now let erosion wear rate for system 1, a supposed base system, be defined by

$$ER_1 = C_1 \dot{m}_{p1} V_{p1}^{n1} f_1(\alpha) \tag{D.1}$$

and the erosion wear rate for system 2 be defined by

$$ER_2 = C_2 \dot{m}_{p2} V_{p2}^{n2} f_2(\alpha) \tag{D.2}$$

Now if Equation D.2 is divided by Equation D.1, then the resulting expression is

$$\frac{ER_2}{ER_1} = \frac{C_2 \dot{m}_{p2} V_{p2}^{n2} f_2(\alpha)}{C_1 \dot{m}_{p1} V_{p1}^{n1} f_1(\alpha)} \tag{D.3}$$

It is possible that the variables in Equation D.2 can be represented by a factor (constants or

function) multiplied by the variables in Equation D.1 such that

$$C_2 = k_1 C_1 \quad (D.4a)$$

$$\dot{m}_{p2} = k_2 \dot{m}_{p1} \quad (D.4b)$$

$$V_{p2}^{n2} = k_3^{n1} V_{p1}^{n1} \quad (D.4c)$$

$$f_2(\alpha) = k_4 f_1(\alpha) \quad (D.4d)$$

then,

$$ER_2 = (k_1 k_2 k_3^{n1} k_4) \times ER_1 \quad (D.5)$$

The geometry correction factor (GCF) for erosion model  $ER_1$  (made from system 1) if it is to be used for system 2 is therefore defined by

$$G = k_1 k_2 k_3^{n1} k_4 \quad (D.6)$$

## D.2 OTSG failure mechanisms investigation steps

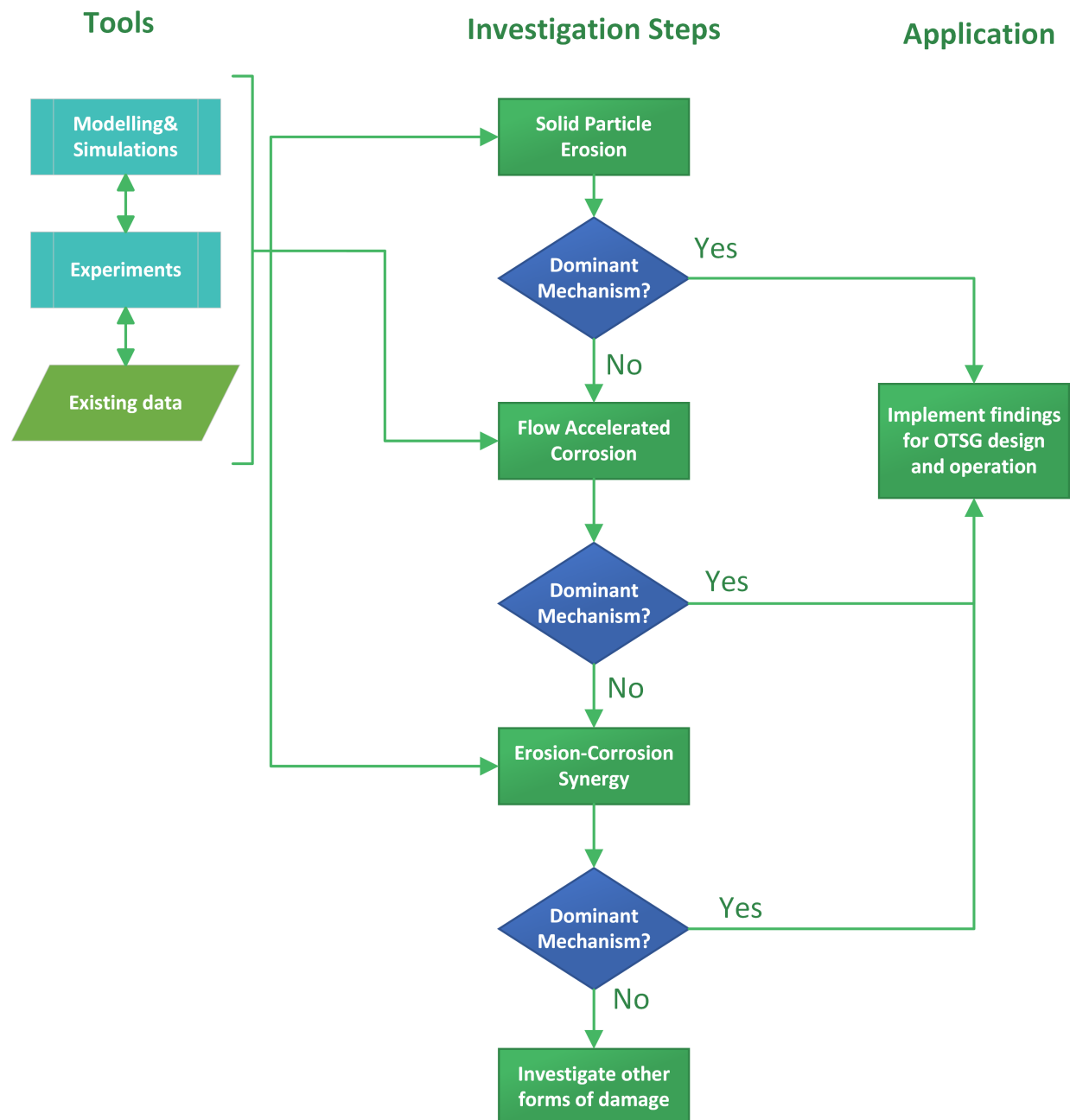


Figure D.1: Investigation steps for identifying the dominant wear mechanisms for the OTSG

